Universidade de Aveiro Departamento de Química
2017

Pedro Oliveira Lavrador

Desenvolvimento de nanomicelas poliméricas contendo fármacos para diferenciação osteogénica de células estaminais

Development of drug-loaded polymeric nanomicelles for stem cell osteogenic differentiation

Universidade de Aveiro Departamento de Química
2017

Pedro Oliveira Lavrador

Desenvolvimento de nanomicelas poliméricas contendo fármacos para diferenciação osteogénica de células estaminais

Development of drug-loaded polymeric nanomicelles for stem cell osteogenic differentiation

Dissertação apresentada à Universidade de Aveiro para cumprimento dos requisitos necessários à obtenção do grau de Mestre em Bioquímica Clínica, realizada sob a orientação científica do Doutor Vítor Gaspar e do Professor Doutor João Mano, Professor Catedrático do Departamento de Química da Universidade de Aveiro

o júri

presidente

Professor Doutor Pedro Miguel Dimas Neves Domingues
Professor Auxiliar do Departamento de Química da Universidade de Aveiro

Professor Doutor João Filipe Colardelle da Luz Mano
Professor Catedrático da Universidade de Aveiro

Professora Doutora Ana Paula Gomes Moreira Pêgo
Professora Associada no Instituto de Ciências Biomédicas Abel Salazar da Universidade do Porto

acknowledgments

First of all, I would like to express my thanks to Prof. Dr. João Mano for giving me the opportunity to work in his research group (COMPASS), for providing me access to all the activities that the COMPASS group participated in, from all the outstanding lectures and the international symposium, as well as for insightful discussions throughout the year. Secondly, I thank my supervisor Dr. Vítor Gaspar for everything he teached me during the year and making sure I always had every possible tool available necessary for my success. Mostly, for enthusiastically presenting me with a vast array of learning experiences in several areas both in laboratory techniques and writing expert advice. Also, I thank him for going beyond the supervisor's duties and extending his trust in my abilities, supporting me throughout the entire thesis, as well as providing me with incredible opportunities to guarantee the best possible outcome for my sprouting scientific career. If I am to become a good scientist in the future, it will definitely be influenced by his mentoring.

I am also grateful to all the members of the COMPASS group who have participated in helpful discussions throughout this thesis and have made the daily laboratory routine a pleasant experience. In particular, I extend my gratitude to the "old guard" of Master Students, namely Aukha, Cláudia, Carla, Diana, Lúcia, Sara and my comrade Luís for all the fun and unforgettable moments and support in the obligatory scientific failures, ultimately leading to a healthy environment for working and learning. I thank all my friends since the Biotechnology Bachelor's and in the Biochemistry's Masters, as well as my friends ever since elementary school. Your friendship is unforgettable and helped countless times throughout the year.

I thank all of my family, specially my Mother and Father for their unrelenting support and for all the sleepless nights throughout the year. This work would not be possible without their love and I profusely thank all the sacrifices they have made.

Finally, I would say that this thesis is not worth its weight in gold; in fact, it means so much more than that on a personal level. For all the experiences and knowledge accrued over this work, I thank all of those who, in some way or another, have helped me along this journey!

palavras-chave

Células estaminais, diferenciação osteogénica, entrega de fármacos, micelas poliméricas, Naringina

resumo

As doenças musculoesqueléticas afetam atualmente uma grande percentagem da população mundial sendo esperado que a sua prevalência venha a aumentar no futuro. De entre as abordagens terapêuticas atualmente aplicadas a nível clínico para as patologias ou danos ósseos, a utilização de terapias celulares baseadas em células estaminais mesenquimais humanas (hMSCs) surge como uma das mais promissoras devido à capacidade de diferenciação das hMSCs em células do tecido esquelético. No entanto, a diferenciação destas células em células osteoprogenitoras tem sido limitada pela relativa ineficácia e elevados custos das tecnologias de diferenciação. Para ultrapassar estas limitações, novas abordagens farmacológicas baseadas em compostos naturais como os flavonoides ou flavanonas têm sido exploradas para a diferenciação de hMSCs. A Naringina é uma flavanona natural, tipicamente presente em frutos do género *Citrus* que demonstrou bioatividade em várias patologias do osso e também capacidade de promover a diferenciação osteogénica de células estaminais. No entanto, este flavonoide hidrofóbico possui uma baixa biodisponibilidade e é metabolizado extensivamente, o que limita ao seu potencial terapêutico. Estas limitações podem ser colmatadas com o desenvolvimento de nanotransportadores especializados como as micelas poliméricas anfifílicas que alteram a farmacocinética/farmacodinâmica das flavanonas. Neste contexto, o trabalho de investigação apresentado nesta tese foca o desenvolvimento de micelas copoliméricas di-bloco para entrega controlada de Naringina a células osteoprogenitoras, com o objetivo de potenciar o efeito pro-osteogénico desta molécula natural. Inicialmente a síntese do copolímero anfifílico foi efetuada num passo através da reação de adição nucleofílica de Michael, entre o polímero hidrofílico metoxi-polietilenoglicol-maleimida (mPEG-MAL) e o polímero hidrofóbico poliácido láctido-tiol (PLA-SH). A caracterização do copolímero através de ressonância magnética nuclear de protão e de espectroscopia de infravermelho com transformada de Fourier em modo de atenuação total confirmaram a síntese do mPEG-MS-PLA. Através da utilização da técnica de nanoprecipitação o copolímero sintetizado formou micelas poliméricas monodispersas (70.69 ± 5.48 nm) e com uma elevada eficiência de encapsulação de Naringina (87.2 ± 4.6 %). A libertação controlada da Naringina encapsulada nas nanomicellas exibiu um perfil relativamente rápido a pH fisiológico (7.4) e acídico (5.5), atingindo 65 % de libertação às 24 h. As nanomicelas de mPEG-MS-PLA demonstraram também capacidade de internalização em pré-osteoblastos murinos (MC3T3-E1) e células mesenquimais estaminais derivadas do tecido adiposo humano (hASCs) tendo sido obtida uma correlação direta entre a dose e internalização. Para além destes resultados promissores, os estudos da avaliação da citotoxicidade da Naringina em forma livre ou encapsulada em nanomicelas revelou que em ambos os casos a viabilidade celular de hASCs foi mantida até 72 h. Posteriormente a bioatividade pro-osteogénica da Naringina na forma livre e formulada em nanomicelas foi investigada através da quantificação da fosfatase alcalina. Os resultados obtidos sugerem que a entrega controlada da Naringina promove a diferenciação osteogénica das hASCs e potenciou as suas propriedades pro-osteogénicas. No geral, os nanotransportadores micelares demonstraram ser um veículo promissor para a entrega controlada de Naringina a células reconhecidas pela sua difícil transfeção, estabelecendo-se assim como futuros candidatos para utilização em terapias osteogénicas com base em células estaminais.

keywords

Drug delivery, Naringin, osteogenic differentiation, polymeric micelles, stem cells

abstract

The incidence of musculoskeletal disorders is growing at an alarming rate and these diseases already affect a significant portion of the worldwide population. Among the therapeutic approaches currently employed in clinical settings for skeletal disorders or injuries, stem cell therapies exploring human mesenchymal stem cells (hMSCs) represent one of the most promising strategies due to the differentiation capacity of hMSCs into skeletal tissue cells. However current differentiation strategies into osteoprogenitor cells is hindered by the lack of effective pharmaceutic options as well as high costs associated with their use. Therefore, in order to overcome these limitations, there has been a shift to developing new pharmacological approaches based on natural products such as flavonoids or flavanones. Naringin is a natural flavanone typically found in *Citrus* fruits with described bioactivity in several bone disorders and capable of promoting osteogenic differentiation of stem cells. However, this hydrophobic flavonoid possesses low bioavailability and is extensively metabolized *in vivo*, which can limit its therapeutic effect. Nevertheless, these limitations can be overcome by developing specialized nanocarriers such as amphiphilic polymer micelles that can alter the pharmacokinetic/pharmacodynamic profile of entrapped flavanones. Considering this, the work here presented on this thesis focuses on the formulation of diblock copolymer micelles for controlled delivery of Naringin to osteoprogenitors, aiming to enhance the pro-osteogenic effect of this natural compound. Initially, the amphiphilic copolymer was synthesized in a one-pot Michael-type addition reaction between hydrophilic methoxypoly(ethylene glycol)-maleimide (mPEG-MAL) and hydrophobic thiol-poly(L-lactide) (PLA-SH) polymers. Copolymer characterization by proton nuclear magnetic resonance and attenuated total reflection Fourier transform infrared spectroscopy supported the successful synthesis of the mPEG-MS-PLA copolymer. The resulting copolymer self-assembled into monodisperse polymeric micelles (70.69 ± 5.48 nm) with a high Naringin encapsulation efficiency (87.2 ± 4.6 %) via nanoprecipitation. Naringin controlled release from nanomicelles followed a relatively fast release profile at physiological (pH =7.4) and acidic (pH = 5.5) conditions, achieving up to 65 % of released drug within 24 h. Cellular uptake evaluation of nanomicelles in human adipose-derived mesenchymal stem cells (hASCs) and murine pre-osteoblasts (MC3T3-E1) revealed a direct correlation between micelle dose and uptake. Moreover, besides previous promising results, cytotoxicity profile of free Naringin or Naringin-loaded nanomicelles in both cell lines showed no significant decrease of cell viability up to 72 h. Afterwards, the pro-osteogenic activity of free drug and nanomicelle-delivered drug was investigated by alkaline phosphatase assays. The obtained results suggest that the controlled delivery of Naringin promotes the osteogenic differentiation of hASCs over free drug administration. Overall, the nanomicelles demonstrated suitable properties for delivering flavanones into hard to transfect hASCs and are envisioned to be used in the future for stem cell-based osteogenic therapies.

Contents

List of Figures

1. Introduction

List of Tables

List of Abbreviations and Acronyms

AA	Ascorbic acid
ALP	Alkaline phosphatase
a.g.	Analytical grade
ASC	Adipose-derived mesenchymal stem cell
ATR - FTIR	Attenuated total reflectance fourier transformed infrared
BM	Basal growth medium
BMD	Bone mass density
BMP	Bone morphogenetic protein
BM-MSC	Bone marrow mesenchymal stem cell
BP	Bisphosphonate
BSP	Bone sialoprotein
$CDCl_3$	Deuterated chloroform
Col I / II	Collagen type I / II
Coum-6	Coumarin-6
CLSM	Confocal laser scanning microscopy
CMC	Critical micellar concentration
CML	Chronic myeloid leukemia
DEA	Diethanolamine
Dex	Dexamethasone
DLS	Dynamic light scattering
DMSO	Dimethylsulfoxide
dPBS	Dulbecco's phosphate buffered saline
dsDNA	Double-stranded DNA
EO/LA	Ethylene oxide/lactyl
EPR	Enhanced permeability and retention
ER	Estrogen receptor
ERK	Extracellular receptor kinase
Ph. Eur.	European Pharmacopeia
FBS	Fetal bovine serum
FCM	Flow cytometry
FDA	Food and Drug Administration
β-gly	β-glycerophosphate
^1H NMR	Proton nuclear magnetic resonance
hAFSC	Human amniotic fluid-derived stem cell
hASC	Human adipose-derived mesenchymal stem cell
hBM-MSC	Human bone marrow mesenchymal stem cell
HIF-1α	Hypoxia inducible factor-1α
hMSC	Human mesenchymal stem cell
hOB	Human fetal osteoblast
hPDLSC	Human periodontal dental ligament stem cell
H_r	Hydrodynamic radius
IL	Interleukin
IV	Intravenous
MAL	Maleimide
M-CSF	Macrophage colony-stimulating factor
MC3T3-E1	Murine pre-osteoblast cell

α-MEM	Minimum essential medium α-modification
MetOH	Methanol
MFI	Mean fluorescence intensity
M_n	Number average molecular weight
MOF	Metal-organic-framework
MPS	Mononuclear phagocyte system
mPEG	Methoxypoly(ethylene glycol)
MSC	Mesenchymal stem cell
MWCO	Molecular weight cut-off
NF-κB	Nuclear factor kappa B
4NPh	4-Nitrophenol
4NPhP	4-Nitrophenyl phosphate disodium salt hexahydrate
NSAIDs	Nonsteroidal anti-inflammatory drugs
OA	Osteoarthritis
OC	Osteocalcin
OM	Osteomyelitis
OP	Osteoporosis
OPG	Osteoprotegerin
OPN	Osteopontin
OS-Dex	Osteogenic differentiation medium with Dexamethasone
OVX	Ovariectomized
PBS	Phosphate buffered saline
PDI	Polydispersity index
PDGF	Platelet-derived growth factor
PEG	Poly(ethylene glycol)
PLA	Poly(L-lactide)
PM	Polymeric micelle
pOB	Murine primary fetal osteoblast
PPARɣ	Peroxisome proliferator activated receptor ɣ
PTH	Parathyroid hormone
RANKL	Receptor activator of nuclear factor kappa-B ligand
ROP	Ring-opening polymerization
rOS	Reduced osteogenic medium (AA + β-gly)
RT-PCR	Reverse transcription polymerase chain reaction
RT	Room temperature
RUNX2	Runt-related transcription factor 2
s.d.	Standard deviation
SEM	Scanning electron microscopy
$Sn(Oct)_2$	Stannous octoate
STEM	Scanning transmission electron microscopy
TCPS	Tissue culture polystyrene coverslip
TEA	Triethylamine
TEM	Transmission electron microscopy
TGF-β	Transforming growth factor-β
TNF-α	Tumor necrosis factor-α
TRAP	Tartrate-resistant alkaline phosphatase
USN	Unilateral sciatic neurectomy
UV-VIS	Ultraviolet-visible

VEGF	Vascular endothelial growth factor
WGA	Wheat germ agglutinin

List of Publications

I Review article: "*Bioinspired Bone Therapies using Naringin – Applications and Advances"*. Manuscript in preparation. Page **20**.

II Review article: *"Stimuli-Responsive Nanocarriers for Delivery of Bone Therapeutics – Barriers and Progresses"*. Manuscript currently under revision in Journal of Controlled Release. Page **48**.

III Article: *"Bioinstructive Naringin-loaded Micelles for Guiding Stem Cells Osteodifferentiation"*. Manuscript in preparation. Page **113**.

1 Introduction

1.1 Bone Microenvironment

Bone is a dynamic and integrating tissue comprised of living cells embedded in a mineralized connective tissue. It is considered the ultimate biological scaffold, with a sophisticated architecture with a nanoscale resolution. In fact, bone is structured from a series of hierarchically assembled building blocks, ranging from the macro- to the nanostructured intricate patterning (Figure 1) [1]. Seven levels of structural organization comprise this skeletal hierarchy: (i) bone tissue ~ 50 cm, (ii) osteons and Haversian canals ~100 mm, (iii) fibre patterns ~ 50 mm, (iv) fibril arrays ~10 mm, (v) mineralized collagen fibrils ~1 mm, (vi) tropocollagen ~ 300 nm, and (vii) amino acids ~1 nm [2]. At the nanoscale, bone is organized from the assembly and interaction of two major nanophases: (i) organic ~ 300 nm long collagen type I fibrils and (ii) inorganic 50 x 25 nm plate-shaped hydroxyapatite ($Ca_{10}(PO_4)_6(OH)_2$) nanocrystals, which are periodically arranged along the fibrils (Figure 1) [1]. These two intertwined nanophases represent nearly 95 % bone dry weight [1].

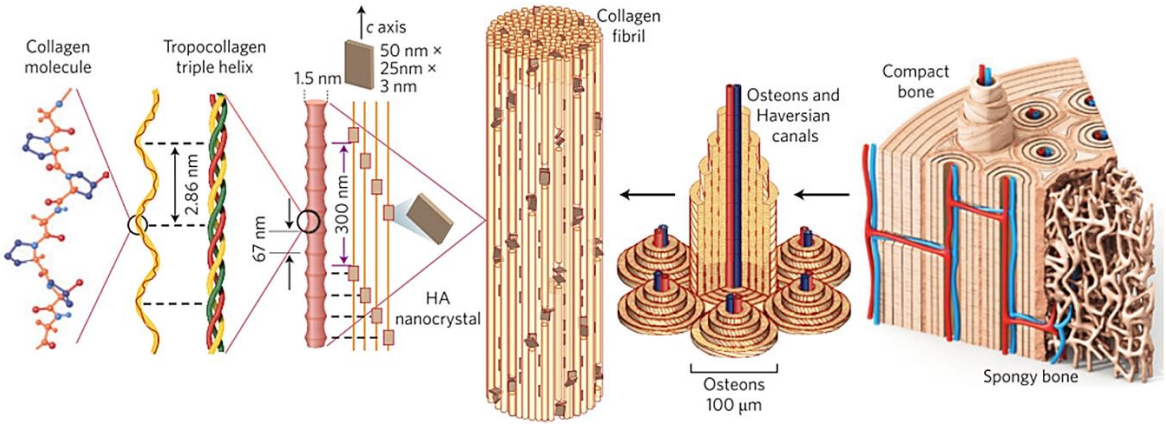

Figure 1. Hierarchical structure of bone and respective building blocks. Macroscale arrangements involve surface compact/cortical bone and trabecular/spongy bone in the interior. Compact bone is structured in lamellar osteons and Haversian canals enclosing blood vessels. The lamellae are mineralized collagen fibrils formed from intertwined helical tropocollagen with embedded hydroxyapatite nanocrystals. Adapted from reference [1].

At a molecular level, electrostatic interactions are considered the main driving force underlying the nanostructured organization of bone [3]. In fact, charged collagen amino acid residues determine potential nucleation sites for the binding of superficial Ca^{2+} and PO_4^{3-} ions from hydroxyapatite [3]. In addition, the collagen fibrils also rely on nearby water molecules to sustain the mechanical load [4]. The fine tuning of relatively weak interactions governing the macroscopic architecture of bone is responsible for the dynamic

physicochemical properties of bone, which results in a tough yet light-weight multifunctional material [1,3]. In the addition, this biomineralized structure is densely populated with a wide variety of cells embedded within its network, which further confers it with self-healing capacity, a unique feature that will be described in the following section [1].

1.2 Bone Remodeling Process and Cellular Mediators

Apart from its unique structural features, bone possesses an intrinsic capacity for self-healing with minimal formation of scar tissue [5]. Throughout life, bone tissue integrity is maintained through constant bone matrix resorption/deposition cycles. Such events prevent microcrack propagation and allows the tuning of bone strength and density to the patterns of mechanical loading that each individual is subjected to, a process known as bone remodeling [6]. In brief, the remodeling process encompasses a continuous cycle consisting in five main stages: (i) resting phase, (ii) resorption phase, (iii) reversal phase, (iv) bone formation phase, and (v) mineralization phase (Figure 2).

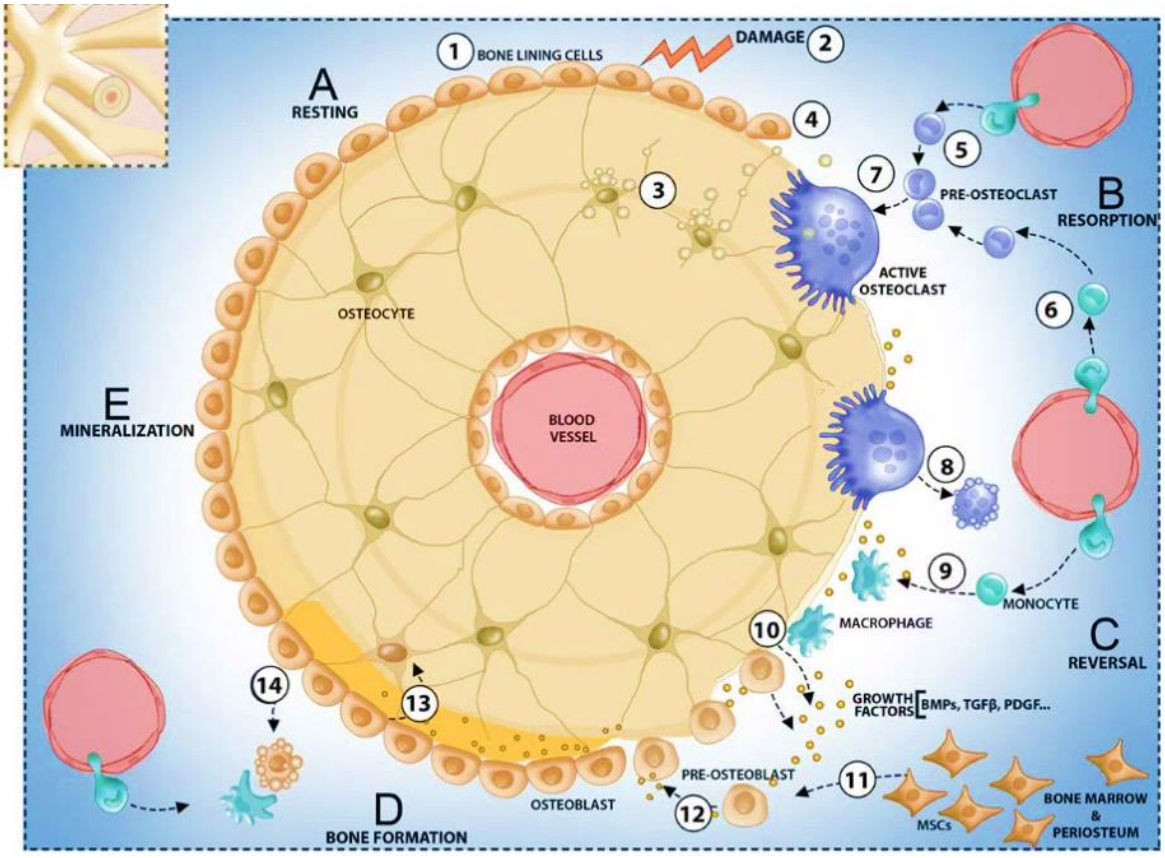

Figure 2. The physiologic cycle of bone remodeling. In Resting Phase **(A)**, bone surface is covered with bone lining cells (1). In response to microdamage (2), neighbouring osteocytes undergo apoptosis (3), signalling for bone lining cells detachment by communicating via the lacunocanalicular system, as well as

secreting RANKL for osteoclast recruitment (4), hence initiating the Resorption Phase **(B)**. Then, monocytes migrating from the marrow stroma differentiate into pre-osteoclasts (5, 6) and subsequently fuse into active osteoclasts (7) after exposure to secreted osteoclastogenic factors. Active osteoclasts are responsible for digesting the mineral and organic matrix during the bone resorption phase. Upon termination of their resorptive action, polarized osteoclasts detach from the bone surface and undergo apoptosis, initiating the Reversal Phase **(C)**. In this phase, local macrophages remove the remaining debris from resorbed surfaces, while locally secreting platelet-derived growth factor (PDGF) [7,8]. This mediator, coupled with other growth factors (e.g. bone morphogenetic proteins (BMPs) and transforming growth factor-β (TGF-β)) released from the resorbed matrix (10) are responsible for signalling human mesenchymal stem cells (hMSCs) local differentiation (11) into pre-osteoblasts that continue the release of growth factors for subsequent autocrine and paracrine signalling (12). At the beginning of Bone Formation Phase **(D),** osteoblasts deposit new osteoid and eventually incorporate into the new bone matrix as young osteocytes as this process continues (13). Meanwhile, mature osteoblasts can also undergo apoptosis (14) or become quiescent bone lining cells after the Mineralization Phase **(E).** Adapted from reference [9].

From a cellular perspective, the main hotspots of bone tissue remodeling are basic multicellular units and are mainly comprised by four different cell types: (i) osteoblasts, (ii) bone lining cells, (iii) osteocytes and (iv) osteoclasts [10] (Figure 3).

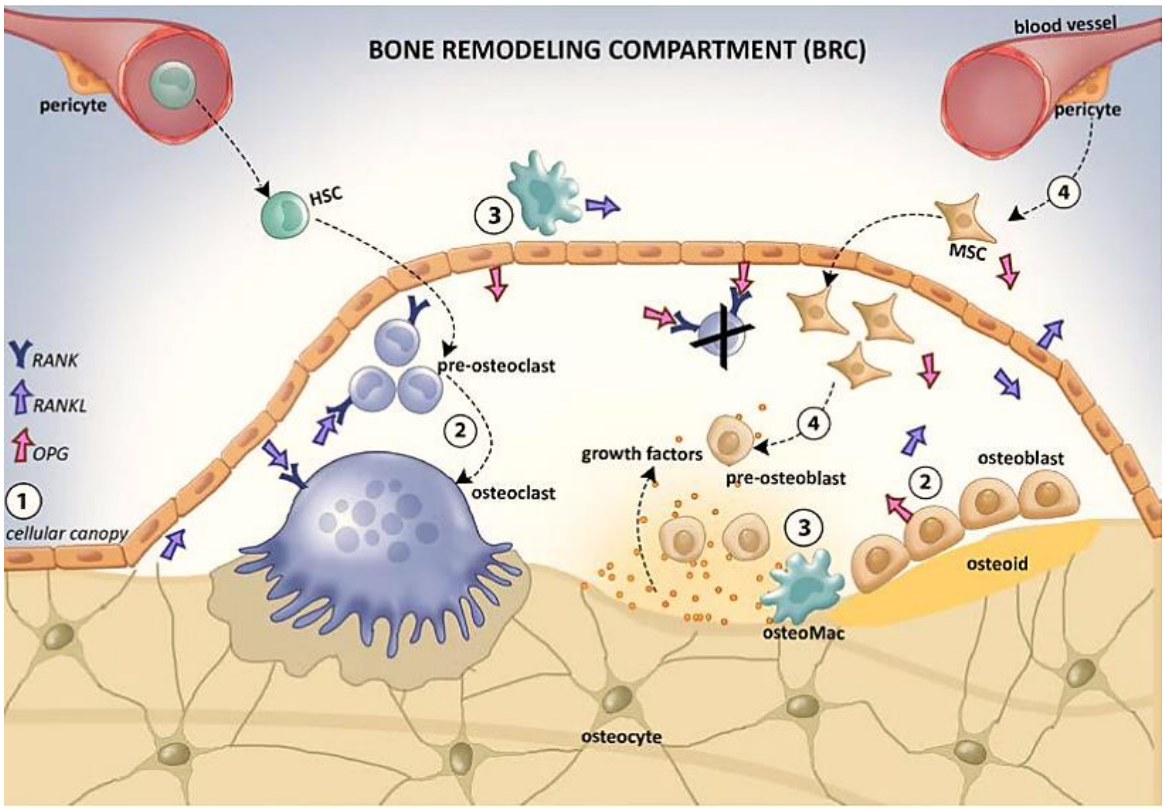

Figure 3. Bone remodeling process and its main cellular components (Osteoblasts, Bone lining cells, Osteocytes and Osteoclasts). **(1)** Osteocyte communication with bone lining cells forming the cellular canopy.

(2) Exposure of pre-osteoclasts to osteoclastogenic factors (e.g. RANKL and OPG) expressed by cells of the osteoblastic lineage (bone lining cells, pre- and osteoblasts, as well as osteocytes). **(3)** OsteoMacs express osteoclastogenesis markers such as RANKL and remove the remaining debris from resorbed bone. **(4)** hMSCs from the vicinity can differentiate into pre-osteoblasts and initiate new bone formation. The dynamic equilibrium between these cellular activities is responsible for maintaining a constant bone tissue renewal and ultimately bone health. Adapted from reference [9].

During the remodeling process, mature osteoblasts form a monolayer of cuboidal cells along the bone surface and are responsible for forming new bone [10]. They are mostly derived from human mesenchymal stem cells (hMSCs) originating from the hematopoietic stem cell niche in the marrow stroma [11]. Human bone marrow MSCs (hBM-MSCs) are committed towards the osteoprogenitor lineage through exposition to locally secreted factors, such as transforming growth factor-β (TGF-β), bone morphogenetic proteins (BMPs) and Wnt proteins [12]. Consecutively, these pathways trigger the expression of key transcriptional regulators of osteoblastic phenotypes, such as master switch Runt-related transcription factor 2 (RUNX2) and osterix, both of them critical stimuli for osteoblastic differentiation [10]. In the remodeling process, this event is followed by the upregulation of osteogenic markers, such as alkaline phosphatase (ALP), osteocalcin (OC), osteopontin (OPN), collagen type I (Col I) and bone sialoprotein (BSP), which establishes osteoprogenitors proliferation phase [10]. Afterwards, matrix vesicles (~300 nm) bud from osteoblasts and serve as nanoscaffolds for accumulating Ca^{2+} and PO_4^{3-} ions, where nucleation occurs and hydroxyapatite nanocrystals are subsequently formed [10]. Then, rupture occurs and the mineral nanocrystals are spread throughout the synthesized matrix. At this point, most (~ 60 %) mature osteoblasts undergo apoptosis while the rest differentiates into osteocytes or become quiescent bone lining cells [13].

The other cell type present during natural remodeling are bone lining cells. These cells are quiescent flat-shaped osteoblasts that cover bone surface regions where no bone formation or resorption takes place. The extent of their role in bone remodeling is not yet fully understood, but studies have shown that the thin barrier formed by these cells protects newly mineralized bone from osteoclastic resorption [10,13]. In addition, these cells can secrete OPG and express RANKL to signal osteoclast formation [10]. It is also suggested that this secretory activity can then initiate local bone resorption, via collagenase-mediated digestion of the protective layer and subsequent recruitment of osteoclasts [13]. Then, the detached bone

lining cells, together with nearby OsteoMacs, are capable of forming a cellular canopy delineating the remodeling area [9,13] (Figure 3).

Osteocytes are differentiated osteoblasts with dendritic-morphology encased within the mineralized bone matrix [14]. They represent the overwhelming majority of bone cells (~90 %) and act as mechanosensors as well as orchestrate bone formation/resorption via secretory activities of signalling molecules (e.g. sclerostin, nitric oxide or prostaglandins) directly delivered to the various bone cells via a vast intra-skeletal network [10,14]. Osteocytes extend their cytoplasmic processes throughout nanosized channels (canaliculi), forming the lacunocanalicular system, which allows for direct communication to other cells in the bone remodeling unit [3,10]. Microdamage in the skeletal matrix causes neighbouring osteocytes to undergo apoptosis, which in turn elicits osteocyte-mediated RANKL production [15]. Such initiates osteoclastic recruitment and subsequent bone remodeling at the injured site [10]. Thus, osteocytes play a major role in tightly coordinating remodeling cycles.

Another major mediator of the remodeling process are osteoclasts. These are bone resorbing, multinucleated, giant cells derived from hematopoietic cells, specifically arising from the fusion of mononuclear progenitors of the monocyte/macrophage family [16]. Osteoclastic differentiation is brought about by exposition to macrophage colony-stimulating factor (M-CSF) or RANKL, secreted by stromal cells or those of osteoblastic lineage [16]. In addition, osteoclastogenesis is also regulated by OPG secretion, which functions as decoy receptor for RANKL, therefore inhibiting osteoclastic formation [13]. Upon activation, osteoclasts polarize through cytoskeletal reorganization and form four distinct membrane domains, namely a ruffled border, sealing zone, functional secretory domain and a basolateral domain [3,10]. The sealing zone encloses the acidic resorptive microenvironment, responsible for digesting the mineral and organic phases of skeletal matrixes, respectively by enzymatic activities of carbonic anhydrase II and cathepsin K [16,17].

Bone remodeling therefore results from the concomitant destruction of old bone by bone-resorbing osteoclasts and deposition of new osteoid by osteoblasts, in an orchestrated communication among all bone cells in the basic multicellular unit, by using locally secreted signalling biomolecules (e.g. OPG, BMPs and TGF-β) [9] (Figure 2 and 3).

From this overview of the skeletal system hallmarks it becomes clear that bone is a tightly regulated tissue with important anatomical and physiological features that must be taken into consideration. In the following subchapter, different types of bone disorders will be

described and their current medical treatments critically discussed in the context of the development of advanced therapies for their management.

1.3 Bone Injuries and Disorders

1.3.1 Bone Fractures - Hallmarks of Fracture Healing

Bone tissue health can be affected by several types of injuries including trauma, infection or neoplasias [18]. Among trauma-related injuries, fractures are by far the most frequent and constitute a major cause of morbidity and mortality [19]. When a fracture occurs and the fracture ends are not in direct contact with each other, bone healing takes place via endochondral and intramembranous ossification [18,20]. This process is known as indirect fracture healing and represents the most common form of fracture healing [20]. Overall, this process encompasses six main stages: (i) acute inflammatory response, (ii) recruitment of progenitor cells, (iii) cartilaginous callus formation, (iv) fracture site revascularization, (v) cartilaginous callus resorption/mineralization, and (vi) bone remodeling [20] (Figure 4).

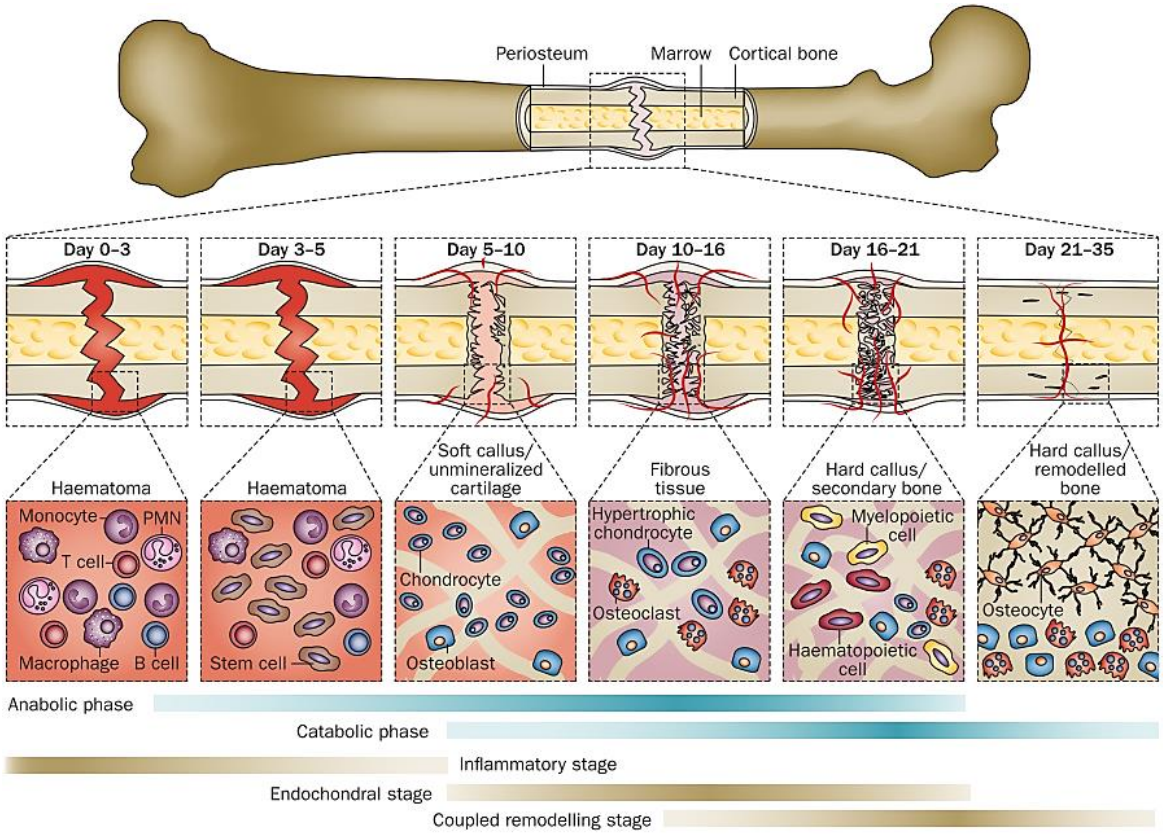

Figure 4. Physiology of femur fracture repair along time. Major metabolic phases of fracture healing, anabolic and catabolic (blue bars) are represented in the context of the three major biological stages, (i)

inflammatory, (ii) endochondral ossification and (iii) coupled remodeling, that orchestrate bone regeneration. Adapted from reference [21].

Acute inflammatory response (Figure 4, **day 0 - 3**). Immediately following a traumatic event, bone fracture as well as injury to surrounding soft tissues occurs. Blood from the neighbouring vasculature fills up the injured site and coagulates, leading to the formation of a characteristic hematoma which serves as a template for callus formation [20]. During this phase, platelets and monocytes/macrophages infiltrate the fracture site and initiate the acute inflammatory response by secreting proinflammatory cytokines, such as interleukin 1 and 6 (IL-1 and IL-6), platelet-derived growth factor (PDGF), TGF-β, prostaglandin E2 and tumor necrosis factor-α (TNF-α) [18,22]. The coordinated secretion of these bio-mediators peaks within the first 24 h post-trauma, and this timing is crucial for initiating bone healing [20,21].

Recruitment of progenitor cells (Figure 4, **day 3 - 5**). The cytokines (such as TNF-α and IL-6), as well as platelet-secreted chemokine stromal cell-derived factor-1, all play a key role in the recruitment of osteo- and chondroprogenitors from surrounding stem cell niches [18,21,23]. Stem cells are mainly recruited from the periosteum, but also from marrow stroma, endosteal envelope, from peripheral blood and adjacent myogenic progenitors [18,21]. It is worth noting that the recruitment from neighbouring or distant locations is known to be dependent on the extent and type of trauma [21]. For instance, in large open tibial fractures, nearly half the cells in the callus are derived from the surrounding muscle tissue [24]. Moreover, cytokines, as well as recruited hMSCs mediate immune functions by coordinating the removal of necrotic tissues and supressing immune cell populations, such as T cells [21]. A local increase in the number of induced T regulatory cells leads to immunosuppression of fracture sites, which is fundamental for the chondroprotection of recruited cells that are responsible for forming the cartilaginous template [21].

Cartilaginous callus formation (Figure 4, **day 5 - 10**). As aforementioned, the hematoma serves as a template for the synthesis of a cartilage scaffold [18]. In this region, angiogenesis cannot occur and an ischemic microenvironment is established [18]. This hypoxic gradient favours chondrogenesis over osteogenesis, thereby coordinating cartilage matrix formation via release of TGF-β_2, -β_3 and growth differentiating factor-5 from infiltrating platelets [18]. Afterwards, chondrocytes proliferate and synthesize the cartilaginous callus by secreting Col I and II as well as proteoglycans [18,22]. As the production of collagenous matrix proceeds, the synthesized template eventually covers the fracture gap, while hypoxia

inducible factor-1α (HIF-1α) is continuously secreted by recruited hMSCs [18,20]. This causes local chondrocytes to undergo hypertrophic differentiation which elicits vascular endothelial growth factor (VEGF) and type X collagen production, initiating localized revascularization and kickstarting the cartilage degradation process [25].

Fracture site revascularization (Figure 4, **day 10 - 16**). Neovascularization is essential for vascularizing the fracture callus and reversing cartilage formation [20]. This process is modulated by VEGF and angiopoietin-1 and -2 secreted by hypertrophic chondrocytes, as well as recruited hMSCs differentiating to osteoblastic lineages [20]. Irrigation of the avascular cartilaginous matrix provides a pathway for accumulation of osteoprogenitor cells and multiple factors (e.g. BMPs, TGF-β, insulin-like growth factor, OC, and collagen) signalling the conversion of cartilage to immature woven bone by calcifying the matrix [22].

Cartilaginous callus resorption/mineralization (Figure 4, **day 16 - 21**). At this stage, the anabolic phase is followed by a strong catabolic activity which ultimately reduces callus volume [21]. For further progressing into bone regeneration, the soft callus needs to be replaced by a hard callus [20]. As aforementioned, fracture site revascularization promotes the repopulation of the template region and originates a coordinated signalling cascade comprised by M-CSF, RANKL, OPG and TNF-α mediators that initiate mineralized cartilage resorption. Macrophages and osteoclasts are attracted to the soft callus vicinity and resorb matrix [18]. TNF-α may also be implicated in inducing hypertrophic chondrocyte apoptosis, releasing calcium granules to the extracellular matrix [20]. In parallel with the bone remodeling mineralization stage, these calcium nodes act as nucleation sites for generating apatite crystals [20]. At this point, while the collagenous template is continuously resorbed, additional vascular ingrowth continues as new bone tissue replaces the cartilage matrix, solidifying the fracture callus [21].

Bone remodeling (Figure 4, **day 21 - 35**). In order to restore original anatomical and biomechanical bone properties, a second woven bone remodeling is initiated with the aim of reforming lamellar bone with medullary cavity [18,20]. Although this process begins as early as 3 weeks post-trauma and overlaps with hard callus formation, it can take years until bone structures are fully regenerated. IL-1 and -6, TNF-α as well as BMPs are highly implicated in the biocoordination of this process [18,20]. In addition, the aforementioned vascular ingrowth is critical for a successful bone remodeling stage. Here, remodeling takes place according to Wolff's law; lamellar bone deposition by osteoblasts in high stress zones and hard callus

resorption in low stress regions [18]. Over time, the concomitant action of osteoclasts and osteoblasts forms a mature lamellar bone with characteristic medullar cavity [21].

In a holistic analysis, it is clear that bone is capable of regenerating most injuries via the complex regeneration cascade described above. However approximately 10 % of all fractures do not heal properly [21]. Moreover, trauma-related injuries can lead to critical size defects that are too large to fully heal and require more advanced treatments [26]. Furthermore, there are several clinical conditions such as chronic inflammation, diabetes mellitus, hypovitaminosis and polytrauma, associated with hindered bone repair [22]. In addition, other factors such as smoking or ageing incite unbalances in the hematopoietic stem cell niche, resulting in delayed responses to fracture injuries [22,27].

To address these issues, various strategies have been implemented in a clinical setting to enhance fracture healing, including (i) biophysical stimulation and (ii) local or systemic administration of bone therapeutics [21]. The first approach is based on the use of electromagnetic stimulation or low-intensity pulsed ultrasonography, however these approaches only yield a moderate to very low effect in fracture healing [21].

Alternatively, local stimulatory strategies have shown significant improvements over the previous approaches. Examples of this approach include the use of scaffolds comprised by PDGF subunit B embedded in β-tricalcium phosphate matrix, or the surgical implantation of Food Drug and Administration (FDA)-approved recombinant BMP-2 embedded in a collagen sponge [21]. However, some studies do indicate an increased cancer risk associated with BMP-2 treatments [21].

The studies investigating systemic administration of such therapeutics (e.g. Teriparatide (recombinant DNA form of parathyroid hormone (PTH)), and BMP-2 administration) indicate an improved fracture recovery following treatment, but also that the different underlying biological mechanisms lead to highly sensitive therapeutic outcomes, depending both on timing and treatment duration [21]. In fact, for Teriparatide, unfortunately the treatment is ineffective if the endogenous PTH levels are elevated from the normal threshold [18].

Apart from fractures bone acute bone diseases also contribute for significant patient morbidity, such major pathologies will be described in the following section.

1.3.2 Chronic Bone Diseases – Incidence and Current Medical Approaches

In the past decades, the increase in life expectancy has resulted in the growing prevalence of numerous age-related disorders. This reality is particularly evident for bone-associated diseases such as osteoporosis (OP), osteoarthritis (OA), osteomyelitis (OM) and Paget's disease whose prevalence is expected to increase continuously in the future [28]. More importantly, the prevalence of many of these conditions is already at its historical peak: (i) OP – in 2010 approximately 10.2 million adults in the United States aged 50 years and older had OP, with another 43.4 million adults under increased risk of developing OP due to low bone mass [29]; (ii) OA is now one of the leading causes of chronic disability and by the year 2020, 25% of the adult population in the United States will be affected by this disease [30]; (iii) OM – the elderly are naturally predisposed to chronic OM due to age-related immunodeficiency and increased fracture risk [31,32]. Preventing the burden of such disorders is important since they significantly impair patient's quality of life. However, despite several decades of progress, no definitive treatment options exist for OP or OA, [33]. Currently available treatment options for such disorders rely mostly on pharmacological-based therapies that are administered under various regimes according to each individual disease progression status [34].

Despite their recognizable therapeutic benefits, these approaches are still undermined by deleterious side effects that affect patients general health and daily quality of life. Moreover, due to the chronic nature of most of these disorders, frequent and long-term administration regimens are required, which can accentuate the appearance of associated side effects along time. For example, administration of FDA-approved recombinant PTH is limited to severe OP cases and for a maximum period of two years, owing to the increased risk of developing osteosarcoma as a side effect [35]. Similarly, even bisphosphonates (BPs), the most commonly used anti-osteoporotic class of drugs, remain controversial. Concerning this, there are several reports in the literature questioning BP long-term usage. In fact, Blum and colleagues suggest that there is a risk of atypical femur fractures associated with their long-term usage [36]. Similarly, oral therapy using BPs has been reported to induce gastritis, gastric ulcer and osteonecrosis of the jaw [37,38]. Apart from these examples, several other pharmaceutic formulations and active ingredients for bone pathologies such as OP have drawbacks associated with their administration [39,40] (Figure 5).

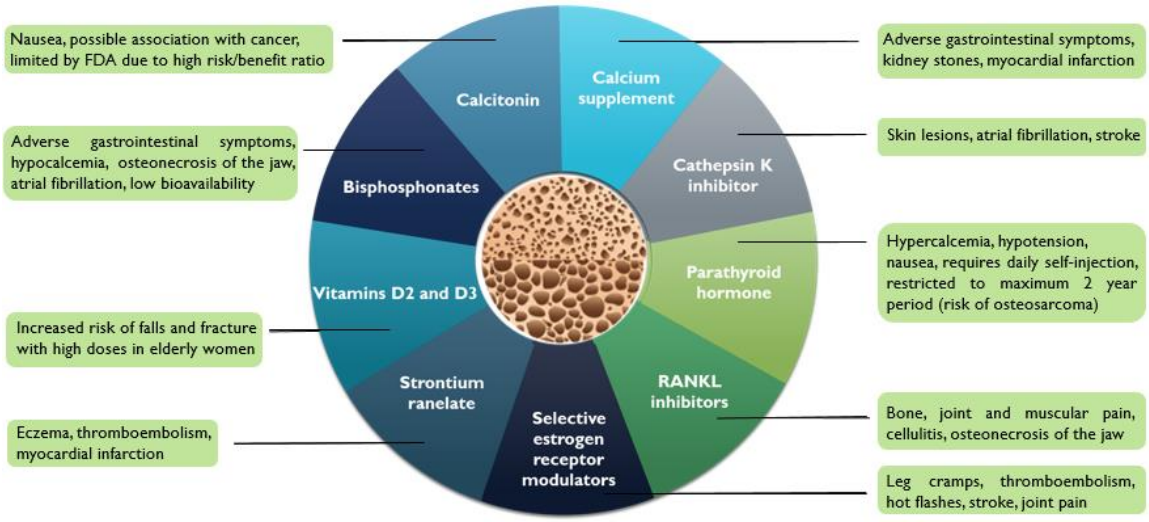

Figure 5. Overview of some of the currently available bone disease therapies and their off-target side-effects and limitations.

For OA, the current pharmaceutical treatments involve combinatorial therapy at different stages of disease progression with the aim of supressing the exaggerated inflammatory response [41]. The most common therapeutic approaches include acetaminophen, nonsteroidal anti-inflammatory drugs (NSAIDs) or corticosteroids [42]. Analgesic acetaminophen is considered first-line therapy and can be used for pain relief but does not affect swelling nor retard disease progression. Also, high doses of this drug can cause stomach ulcers. NSAIDs (e.g. ibuprofen, diclofenac, cyclooxygenase-2 inhibitors) are also considered first-line therapy and can reduce pain and swelling. However, there is a serious risk for gastrointestinal, renal or cardiovascular toxicity, and this risk increases with age [42]. On the other hand, the wide variety of side-effects associated with corticosteroid use is well known. Therefore, for OA there is also a need for effective disease-modifying agents, rather than only relying on pain and inflammation control [41]. In this context, studies exploring natural substances such as glucosamine, chondroitin sulfate and hyaluronic acid (via intra-articular injection) have been reporting beneficial effects, as well as suggesting potential disease-modifying effects [42].

In summary, it is clear that current pharmaceutic options for treating various skeletal disorders need considerable improvement. To overcome these issues regarding bone repair/remodeling disorders and chronic bone diseases, new approaches are exploiting the stem cell niche to enhance bone healing either: (i) via biomaterial-based scaffolds, or (ii) via induced stem cell differentiation toward osteogenic lineage by action of osteoinductive bioactive molecules. Both these approaches represent attractive therapeutic alternatives for

bone tissue engineering and regenerative medicine [26,43]. These approaches based on the use of stem cells will be addressed in the following sections.

1.4 Stem Cell-based Therapies for Bone Regeneration

Stem cells are a class of self-renewing progenitor cells capable of differentiating into different types of functional cells. They can be classified according to: (i) cell potency for differentiation – totipotent, pluripotent and multipotent; and (ii) origin – embryonic or adult [44]. While embryonic stem cells can differentiate into any cell type in the body, adult stem cells have limited potency and can be divided into different lineages, including hematopoietic, neural, epidermal and mesenchymal [44].

Mesenchymal stem cells (MSCs), also known as mesenchymal stromal cells, were originally discovered in the marrow stroma but currently these cells have been successfully isolated from several other tissues, such as trabecular bone, muscle, adipose, periosteum, the synovial membrane, articular cartilage, skin, periodontal ligament and umbilical cord [45]. These multipotent cells possess a fibroblast-like morphology and specifically differentiate towards the mesodermal lineage, namely to: (i) adipocytic, (ii) osteocytic and (iii) chondrocytic phenotypes (Figure 6) [46]. Also, transdifferentiation approaches have successfully directed them towards ectodermal (e.g. epithelial and neural), as well as endodermal lineages (e.g. muscle and lung) (Figure 6) [46].

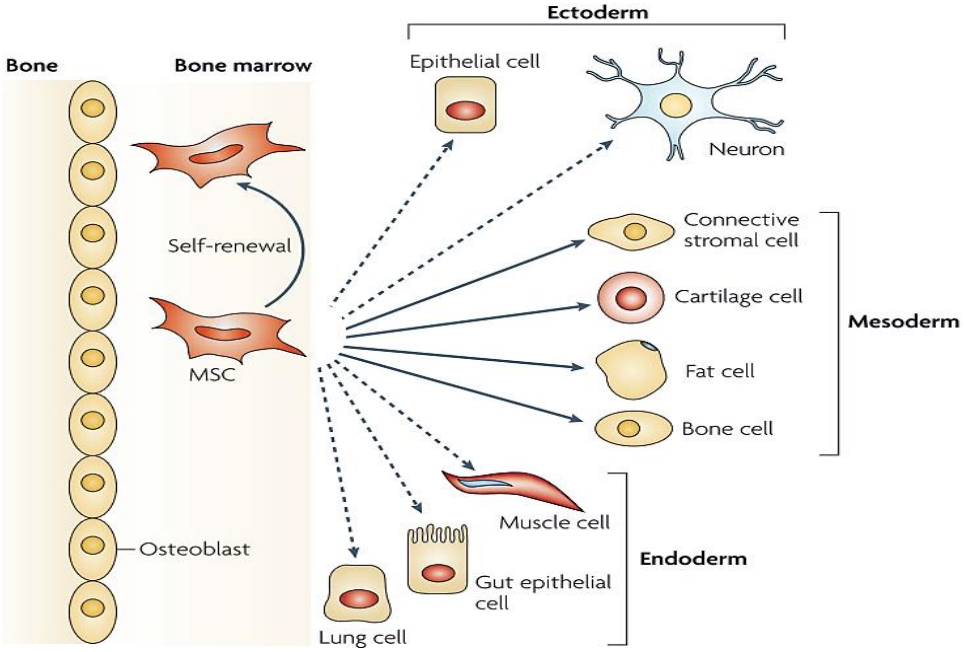

Figure 6. The multipotency of MSCs. In the marrow hematopoietic niche, MSCs are capable of self-renewing (curved arrow) and differentiate (straight, solid arrows) towards the mesodermal lineage. In addition,

the transdifferentiation (dashed arrows) capacity of MSCs towards ecto- and endodermal lineages *in vivo* is still controversial. Adapted from reference [46].

1.4.1 Mesenchymal Stem Cells Potential for Application in Tissue Engineering and Regenerative Medicine

The ubiquitous presence of hMSCs in niches throughout the body evidences their importance in providing maintenance and support in what regards the formation of mesenchymal tissues. As aforementioned, these cells are also able to migrate to injured sites and aid in the regeneration process [47]. In fact, systemic or local recruitment of hMSCs has been described in the context of myocardial infarction, as well as bone healing scenarios [47]. Such injury-mediated chemotactic response coupled with their key role in bone healing (building blocks for cartilage and bone regeneration), has inspired researchers to exploit their potential in tissue engineering and regenerative medicine. Migration to degenerated and inflamed sites also suggests that hMSCs-based therapies are promising alternatives not only for bone-erosive disorders but also for joint-degenerative disorders such as OA and rheumatoid arthritis [47]. Indeed, on the latter, *in vivo* hMSC recruitment to degenerating synovium has been demonstrated in osteoarthritic patients.

In addition, *in vitro* and *in vivo* studies suggest that hMSCs capacity to promote tissue repair goes beyond merely differentiating into mature osteoblasts or chondrocytes [48]. In fact, hMSCs are truly 'living factories', producing important growth factors and cytokines that mediate tissue regeneration or resident tissue precursors (e.g. osteo- and chondroprogenitors) differentiation via paracrine action [49]. Unsurprisingly, hMSCs have been successfully employed in a clinical setting to augment tissue regeneration, with positive outcomes in spinal fusion, hip avascular necrosis, non-union fracture healing or distraction osteogenesis [46,49]. Currently, the most used hMSCs for bone regeneration include human BM-MSCs (hBM-MSCs) and human adipose-derived MSCs (hASCs).

1.4.2 Adipose-derived Mesenchymal Stem Cells - An Emerging Alternative over hBM-MSC-based Strategies

So far, hBM-MSCs are the most explored osteoprogenitor cell line, with numerous studies upholding its potential for enhancing *in vivo* bone healing in both animal models and humans [45]. Moreover, some literature reports suggest that BM-MSCs and periosteum-derived MSCs exhibit superior osteogenic activity than ASCs, although this phenomenon is controversial

in vivo [45,50]. In spite of this, the application of these cells in tissue engineering has been significantly decaying, with only 2 out of 33 clinical trials involving them in bone repair applications [51].

Hurdles for clinical translation of hBM-MSCs in cell-based therapies can be related to several factors. First, harvesting of hBM-MSCs from bone marrow is an invasive procedure associated with patient discomfort and donor site morbidity [45]. Frequently, general or spinal anaesthesia are required to perform this procedure [52]. Secondly, harvesting of sufficient numbers of viable autologous hBM-MSCs is not always possible, especially considering the proportion of these cells in bone marrow (1 in every 10^4 to 10^5 mononuclear cells) [53]. Such scarcity raises the need for an *ex vivo* expansion in order to obtain sufficient cell titers for clinical administration [45]. This not only significantly increases the time of the envisioned administration to patients, but can also lead to other variabilities, particularly in terms of phenotypic changes upon long-term *in vitro* cell culture [51]. Furthermore, ageing is characterized with a marrow stromal shift towards adipocyte differentiation of hBM-MSCs, as well as a significant decrease in their proliferative and pro-osteogenic potential [45,49]. Considering the age-related incidence of fractures and musculoskeletal degenerative diseases, this represents a significant obstacle for clinical translation, especially taking into account the even higher scarcity of these cells in older patients (1 in every 2 x 10^6 cells, approximately a 200-fold reduction) [45,54].

Considering this reality, autologous human ASCs (hASCs) have been steadily gathering attention over the last years as exciting candidates for tissue engineering and regenerative medicine. While hBM-MSCs are particularly rare, hASCs are present in significant quantities within the stromal vascular fraction of human adipose tissues [48]. Therefore, hASCs can be harvested in large numbers by means of subcutaneous lipoaspiration, which is also less invasive in comparison with the bone marrow aspiration procedure. Moreover, hASCs constitute a more valuable option over hBM-MSCs for tissue engineering and regenerative medicine applications in younger patients. Such subjects possess an enhanced osteogenic activity but with fewer amounts of autologous bone available, whereas adipose tissue is readily available [51]. In this context, a clinical case report by Lendeckel and colleagues described the successful repair of a critical post-traumatic calvarial defect in a 7-year old girl by using autologous hASCs [55].

In addition, hASCs are characterized by their low immunogenicity, immunosuppresive and anti-inflammatory properties, excellent characteristics for posterior implantation in injured sites [56]. These properties are maintained even after culturing in xeno-free media, which are a pre-requisite for future clinical application [57]. Regarding their *ex vivo* expansion, hASCs can proliferate faster and for extended periods with lower senescence in comparison to hBM-MSCs [50]. Furthermore, hASCs maintain comparable osteogenic potential in either younger (36 years old), or elderly (71 years old) patients, whereas hBM-MSCs osteogenic capacity markedly declines with age, as aforementioned [58].

Presently, it is important to clarify if the promising results of pre-clinical studies involving hASCs for bone regeneration are related to "quantity over quality" in terms of producing bone matrix as discussed by Fisher and colleagues [51]. Well-designed head-to-head comparison studies between hASCs and hBM-MSCs are required to evaluate bone tissues anatomy/physiology when produced by each type of osteoprogenitor cells. The superior osteogenic capacity of hBM-MSCs is well described and secretomes are markedly different between these two cells (e.g. only hASCs express adipokines with bone remodeling capacity) [59]. Both hBM-MSCs and hASCs secrete the VEGF proangiogenic growth factor [48,59]. However, VEGF expression is much higher in hBM-MSCs than in hASCs [60]. Considering the importance of angiogenesis in bone healing and effective hard callus remodeling, this can lead to important differences in bone biological function over time. Such particularities must be taken into consideration during treatment design stages. It is clear that in many scenarios, the differences between hASCs/hBM-MSCs biological performance can be ascribed to different donor sites, processing method, donor age, gender and diet [45,48,51,61].

Future hASC-based cell therapies should be further optimized in terms of the methodologies for osteogenic differentiation to unravel their full potential for application in tissue engineering, regenerative medicine and treatment of other bone pathologies. Some of the strategies currently employed for stem cells differentiation will be briefly addressed in the following subchapter.

1.4.3 Strategies for Stem Cells Differentiation into Osteogenic Lineage

Currently glucocorticoid Dexamethasone (Dex) and recombinant BMP-2 are the gold standard osteoinductive molecules employed for inducing differentiation into osteogenic lineages in cell-based therapies. However, Dex systemic administration is characterized by

a plethora of deleterious side-effects and simultaneously induces stem cell adipogenesis even in osteogenic conditions [62,63]. On the other hand, although BMPs are remarkable candidates for eliciting bone formation, they usually require supraphysiological doses to obtain the desired osteoinductive effects, which can result in ectopic bone formation.[64] Besides, recombinant BMPs have high production costs, could be denatured *in vivo* and are partitioned in other tissues not being able to be specifically delivered to the target site, such limits their applicability [65].

Consecutively, the search for safer, cost-effective and more potent osteoinductive agents has lead researchers to exploring the potentials of natural-based compounds commonly found in nature. The main driving force behind this paradigm shift is the discovery of drugs with fewer side-effects and more specific biological targets that induce total osteogenic commitment of stem cells, therefore potentially enhancing the therapeutic effect. Also, safer drugs can improve patient compliance, which has been a difficult issue to tackle arising from the side effects and ineffectiveness associated with the current conventional treatment/osteoinducing options.

In the following section, the potential of a naturally available flavanone compound is described in terms of its unique pro-osteoinductive capacity, but also its potential to be used for bone disorders such as OP and OA.

References

1. Wegst, U. G. K., Bai, H., Saiz, E., Tomsia, A. P. & Ritchie, R. O. Bioinspired structural materials. *Nat. Mater.* **14,** 23–36 (2014).
2. Ritchie, R. O. The conflicts between strength and toughness. *Nat. Mater.* **10,** 817–822 (2011).
3. Behzadi, S., Luther, G. A., Harris, M. B., Farokhzad, O. C. & Mahmoudi, M. Nanomedicine for safe healing of bone trauma: Opportunities and challenges. *Biomaterials* **146,** 168–182 (2017).
4. Parratt, K. & Yao, N. Nanostructured Biomaterials and Their Applications. *Nanomaterials* **3,** 242–271 (2013).
5. Jeon, O. H. & Elisseeff, J. Orthopedic tissue regeneration: cells, scaffolds, and small molecules. *Drug Deliv. Transl. Res.* **6,** 105–120 (2016).
6. Duque, G. & Troen, B. R. Understanding the Mechanisms of Senile Osteoporosis: New Facts for a Major Geriatric Syndrome. *J. Am. Geriatr. Soc.* **56,** 935–941 (2008).
7. Wu, A. C., Raggatt, L. J., Alexander, K. A. & Pettit, A. R. Unraveling macrophage contributions to bone repair. *Bonekey Rep.* **2,** 1–7 (2013).
8. Shah, P., Keppler, L. & Rutkowski, J. A Review of Platelet Derived Growth Factor Playing Pivotal Role in Bone Regeneration. *J. Oral Implantol.* **40,** 330–340 (2014).
9. Matsumoto, M., Biguetti, C., Fonseca, A. & Saraiva, P. Bone Tissue Healing Dynamics: From damage to reconstruction. *J. Mol. Signal. Updat.* **1,** 33–40 (2016).
10. Florencio-Silva, R., Sasso, G. R. da S., Sasso-Cerri, E., Simões, M. J. & Cerri, P. S. Biology of Bone Tissue: Structure, Function, and Factors That Influence Bone Cells. *Biomed Res. Int.* **2015,** 1–17 (2015).
11. Nombela-Arrieta, C. *et al.* Quantitative imaging of haematopoietic stem and progenitor cell localization and hypoxic status in the bone marrow microenvironment. *Nat. Cell Biol.* **15,** 533–543

(2013).
12. Weilbaecher, K. N., Guise, T. A. & McCauley, L. K. Cancer to bone: a fatal attraction. *Nat Rev Cancer* **11,** 411–425 (2011).
13. Y., A., Valds-Flores, M., Orozco, L. & Velzquez-Cruz, R. in *Topics in Osteoporosis* (InTech, 2013). doi:10.5772/54905
14. Lin, C. *et al.* Sclerostin Mediates Bone Response to Mechanical Unloading Through Antagonizing Wnt/β-Catenin Signaling. *J. Bone Miner. Res.* **24,** 1651–1661 (2009).
15. Kennedy, O. D., Laudier, D. M., Majeska, R. J., Sun, H. B. & Schaffler, M. B. Osteocyte apoptosis is required for production of osteoclastogenic signals following bone fatigue in vivo. *Bone* **64,** 132–137 (2014).
16. Teitelbaum, S. L. Bone Resorption by Osteoclasts. *Science (80-.).* **289,** 1504–1508 (2000).
17. Søe, K., Merrild, D. M. H. & Delaissé, J. M. Steering the osteoclast through the demineralization-collagenolysis balance. *Bone* **56,** 191–198 (2013).
18. Sathyendra, V. & Darowish, M. Basic Science of Bone Healing. *Hand Clin.* **29,** 473–481 (2013).
19. Bliuc, D. & Center, J. R. Determinants of mortality risk following osteoporotic fractures. *Curr. Opin. Rheumatol.* **28,** 413–419 (2016).
20. Marsell, R. & Einhorn, T. A. The biology of fracture healing. *Injury* **42,** 551–555 (2011).
21. Einhorn, T. A. & Gerstenfeld, L. C. Fracture healing: mechanisms and interventions. *Nat. Rev. Rheumatol.* **11,** 45–54 (2014).
22. Borrelli, J. *et al.* Physiological Challenges of Bone Repair. *J. Orthop. Trauma* **26,** 708–711 (2012).
23. Massberg, S. *et al.* Platelets secrete stromal cell–derived factor 1α and recruit bone marrow–derived progenitor cells to arterial thrombi in vivo. *J. Exp. Med.* **203,** 1221–1233 (2006).
24. Liu, R. *et al.* Myogenic progenitors contribute to open but not closed fracture repair. *BMC Musculoskelet. Disord.* **12,** 288 (2011).
25. van der Kraan, P. M. & van den Berg, W. B. Chondrocyte hypertrophy and osteoarthritis: role in initiation and progression of cartilage degeneration? *Osteoarthr. Cartil.* **20,** 223–232 (2012).
26. Agarwal, R. & García, A. J. Biomaterial strategies for engineering implants for enhanced osseointegration and bone repair. *Adv. Drug Deliv. Rev.* **94,** 53–62 (2015).
27. Sloan, A., Hussain, I., Maqsood, M., Eremin, O. & El-Sheemy, M. The effects of smoking on fracture healing. *Surg.* **8,** 111–116 (2010).
28. Rodan, G. A. & . Therapeutic Approaches to Bone Diseases. *Science (80-.).* **289,** 1508–1514 (2000).
29. Wright, N. C. *et al.* The Recent Prevalence of Osteoporosis and Low Bone Mass in the United States Based on Bone Mineral Density at the Femoral Neck or Lumbar Spine. *J. Bone Miner. Res.* **29,** 2520–2526 (2014).
30. Chen, D. *et al.* Osteoarthritis : toward a comprehensive understanding of pathological mechanism. *Nat. Publ. Gr.* (2017).
31. Huang, C., Tsai, K., Weng, S., Lin, H. & Huang, H. Chronic osteomyelitis increases long-term mortality risk in the elderly : a nationwide population-based cohort study. *BMC Geriatr.* 1–7 (2016).
32. Ensrud, K. E. Epidemiology of Fracture Risk With Advancing Age. *J Gerontol A Biol Sci Med Sci* **68,** 1236–1242 (2013).
33. Gu, W., Wu, C., Chen, J. & Xiao, Y. Nanotechnology in the targeted drug delivery for bone diseases and bone regeneration. *Int. J. Nanomedicine* **8,** 2305–2317 (2013).
34. Feurer, E. & Chapurlat, R. Emerging drugs for osteoporosis. *Expert Opin. Emerg. Drugs* **19,** 385–395 (2014).
35. Vahle, J. L. *et al.* Skeletal changes in rats given daily subcutaneous injections of recombinant human parathyroid hormone (1-34) for 2 years and relevance to human safety. *Toxicol. Pathol.* **30,** 312–321 (2002).
36. Blum, L. *et al.* Atypical femur fractures in patients receiving bisphosphonate therapy: etiology and management. *Eur. J. Orthop. Surg. Traumatol.* (2016).
37. Nase, J. B. & Suzuki, J. B. Osteonecrosis of the jaw and oral bisphosphonate treatment. *J.Am.Dent.Assoc.* **137,** 1115–1119 (2006).
38. Graham, D. Y. What the gastroenterologist should know about the gastrointestinal safety profiles of bisphosphonates. *Dig. Dis. Sci.* **47,** 1665–1678 (2002).
39. Low, S. A. & Kopeček, J. Targeting polymer therapeutics to bone. *Adv. Drug Deliv. Rev.* **64,** 1189–1204 (2012).
40. Kyllönen, L., D'Este, M., Alini, M. & Eglin, D. Local drug delivery for enhancing fracture healing in osteoporotic bone. *Acta Biomater.* **11,** 412–434 (2015).
41. González-Rodríguez, M. L., Fernández-Romero, A. M. & Rabasco, A. M. Towards the antioxidant

therapy in Osteoarthritis: Contribution of nanotechnology. *J. Drug Deliv. Sci. Technol.* (2017).
42. Glass, G. G. Osteoarthritis. *Disease-a-Month* **52,** 343–362 (2006).
43. Frese, L., Dijkman, P. E. & Hoerstrup, S. P. Adipose Tissue-Derived Stem Cells in Regenerative Medicine. *Transfus. Med. Hemotherapy* **43,** 268–274 (2016).
44. Choumerianou, D. M., Dimitriou, H. & Kalmanti, M. Stem Cells: Promises Versus Limitations. *Tissue Eng. Part B Rev.* **14,** 53–60 (2008).
45. J. Panetta, N., M. Gupta, D. & T. Longaker, M. Bone Regeneration and Repair. *Curr. Stem Cell Res. Ther.* **5,** 122–128 (2010).
46. Uccelli, A., Moretta, L. & Pistoia, V. Mesenchymal stem cells in health and disease. *Nat. Rev. Immunol.* **8,** 726–736 (2008).
47. Jakob, F. *et al.* Biology of Mesenchymal Stem Cells. *Curr. Rheumatol. Rev.* **4,** 148–154 (2008).
48. Barba, M., Cicione, C., Bernardini, C., Michetti, F. & Lattanzi, W. Adipose-Derived Mesenchymal Cells for Bone Regereneration: State of the Art. *Biomed Res. Int.* **2013,** 1–11 (2013).
49. Kiernan, J., Davies, J. E. & Stanford, W. L. Concise Review: Musculoskeletal Stem Cells to Treat Age-Related Osteoporosis. *Stem Cells Transl. Med.* **6,** 1930–1939 (2017).
50. Liao, H.-T. Osteogenic potential: Comparison between bone marrow and adipose-derived mesenchymal stem cells. *World J. Stem Cells* **6,** 288 (2014).
51. Fisher, J. N., Peretti, G. M. & Scotti, C. Stem Cells for Bone Regeneration: From Cell-Based Therapies to Decellularised Engineered Extracellular Matrices. *Stem Cells Int.* **2016,** 1–15 (2016).
52. Zuk, P. A. *et al.* Multilineage Cells from Human Adipose Tissue: Implications for Cell-Based Therapies. *Tissue Eng.* **7,** 211–228 (2001).
53. Li, X., Zhang, Y. & Qi, G. Evaluation of isolation methods and culture conditions for rat bone marrow mesenchymal stem cells. *Cytotechnology* **65,** 323–334 (2013).
54. Freemont, A. & Hoyland, J. Morphology, mechanisms and pathology of musculoskeletal ageing. *J. Pathol.* **211,** 252–259 (2007).
55. Lendeckel, S. *et al.* Autologous stem cells (adipose) and fibrin glue used to treat widespread traumatic calvarial defects: case report. *J. Cranio-Maxillofacial Surg.* **32,** 370–373 (2004).
56. Leto Barone, A. A., Khalifian, S., Lee, W. P. A. & Brandacher, G. Immunomodulatory Effects of Adipose-Derived Stem Cells: Fact or Fiction? *Biomed Res. Int.* **2013,** 1–8 (2013).
57. Patrikoski, M. *et al.* Different Culture Conditions Modulate the Immunological Properties of Adipose Stem Cells. *Stem Cells Transl. Med.* **3,** 1220–1230 (2014).
58. Chen, H.-T. *et al.* Proliferation and differentiation potential of human adipose-derived mesenchymal stem cells isolated from elderly patients with osteoporotic fractures. *J. Cell. Mol. Med.* **16,** 582–592 (2012).
59. Makridakis, M., Roubelakis, M. G. & Vlahou, A. Stem cells: Insights into the secretome. *Biochim. Biophys. Acta - Proteins Proteomics* **1834,** 2380–2384 (2013).
60. Du, W. J. *et al.* Heterogeneity of proangiogenic features in mesenchymal stem cells derived from bone marrow, adipose tissue, umbilical cord, and placenta. *Stem Cell Res. Ther.* **7,** 163 (2016).
61. Lamontagne, V., Akoum, S. El, Cloutier, I. & Tanguay, J.-F. High-Fat Diets-Induced Metabolic Alterations Alter the Differentiation Potential of Adipose Tissue-Derived Stem Cells. *Open J. Endocr. Metab. Dis.* **3,** 197–207 (2013).
62. Hempen, C., Weiss, E. & Hess, C. F. Dexamethasone treatment in patients with brain metastases and primary brain tumors: do the benefits outweigh the side-effects? *Support. Care Cancer* **10,** 322–328 (2002).
63. Ghali, O. *et al.* Dexamethasone in osteogenic medium strongly induces adipocyte differentiation of mouse bone marrow stromal cells and increases osteoblast differentiation. *BMC Cell Biol.* **16,** 9 (2015).
64. Dimitriou, R., Jones, E., McGonagle, D. & Giannoudis, P. V. Bone regeneration: current concepts and future directions. *BMC Med.* **9,** 66 (2011).
65. El Bialy, I., Jiskoot, W. & Reza Nejadnik, M. Formulation, Delivery and Stability of Bone Morphogenetic Proteins for Effective Bone Regeneration. *Pharm. Res.* **34,** 1152–1170 (2017).

1.5 Nature-based Osteoinductive Bioactive Molecules

Subchapter 1.5.

This subchapter is based on the review article entitled
"*Bioinspired Bone Therapies using Naringin – Applications and Advances*"
(manuscript in preparation)

Bioinspired Bone Therapies using Naringin – Applications and Advances

Lavrador, P.[1], Gaspar, V.M.[1], and Mano, J.F.[1#]

[1]Department of Chemistry, CICECO – Aveiro Institute of Materials, University of Aveiro, Campus Universitário de Santiago, 3810-193, Aveiro, Portugal

[#]Corresponding author:
João F. Mano
E-mail: jmano@ua.pt

Abstract

The use of natural compounds to develop new treatments for chronic bone diseases and injuries is receiving an emerging focus due to their cost-effectiveness, availability and unique bioactivity. Among natural-based small molecules, Naringin, a flavanone glycoside, represents one of the most promising candidates due to its multifaceted effect on bone tissues as recently emphasized by numerous pre-clinical *in vitro* and *in vivo* studies. This review provides an up-to-date overview on Naringin applications in the treatment of bone disorders, such as osteoporosis, and further highlights its potential to be used for stem cell pro-osteogenic differentiation therapies. A critical perspective on different aspects that still hinder Naringin clinical translation is also provided. Such topic is discussed in light of recently developed biomaterial-based approaches that potentiate Naringin bioavailability and bioactivity. Overall, the reported pro-osteogenic, anti-resorptive and anti-adipogenic properties establish this flavanone as an exciting candidate for application in bone tissue engineering and regenerative medicine.

Keywords: Biomaterials, bone disorders, Naringin, osteogenic differentiation, tissue engineering

1. Introduction

Currently bone diseases and injuries represent a significant healthcare burden at a worldwide scale due to the ineffectiveness of currently applied medical treatments for various skeletal disorders [1]. In fact, to date, a fully curative treatment for diseases such as osteoporosis (OP), osteoarthritis (OA), osteomyelitis (OM) or Paget's disease has yet to be developed. Such reality is further accentuated in what concerns critical size bone injuries that are unable to self-regenerate [2]. For these cases, current strategies involve the use of bone grafts with embedded osteogenic growth factors to accelerate bone healing [2]. However currently used osteogenic molecules are frequently associated with high production costs or deleterious side-effects limiting wide applicability and therapeutic efficacy [3]. In an effort to discover new approaches that increase the toolbox of effective treatments for bone pathologies, a great focus has been put on the pursuit of natural-based products due to their availability, cost-effectiveness and biological activity.

Plant-based derivatives and marine-derived compounds represent one of the most cost-effective sources of new bioactive molecules with promising therapeutic effects for different diseases including those of skeletal tissues [4]. In this context, various natural formulations (e.g. *Drynaria fortunei* or *Erythrina variegata*) have presented a remarkable potential for improving joint-related (e.g. OA) osteoarticular degradation, or for treating bone injuries and bone-related disorders, such as OP [4,5]. Typically, these formulations can modulate multiple signaling pathways and exert an effect in different cellular targets [6]. Such is extremely valuable in the context of bone diseases considering their multi-factorial pathogenesis, particularly in the case of OA and OP [7]. In addition, their capacity for improving osteoporotic bone healing is highly related to its pro-osteogenic effect in both osteoprogenitor cells as well as stem cells [4]. Hence, research interest in this pro-osteogenic potential has been steadily growing for applications in stem cell-based therapies for tissue engineering.

Currently, the application for these naturally small molecules in bone is particularly focused in OP and on the pro-osteogenic differentiation of mesenchymal/stromal stem cells. Regarding the latter, such bioinspired approaches have recently shown promising pro-osteogenic potential for tissue engineering and regenerative medicine applications [4].

For example, a catechin hydrate-coated substrate markedly enhanced the osteogenic differentiation and mineralization of hASCs [8]. In addition, catechin-coated polycaprolactone nanofiber scaffolds implanted in a critical-size calvarial defect prompted a significant

improvement in bone formation and density, as well as collagen deposition [8]. Another natural compound, Icariin, a prenylated flavonol glycoside, has exhibited equally promising properties for bone tissue engineering [4]. In a mouse calvarial defect model, Icariin was transplanted in calcium phosphate cement and resulted in enhanced bone and blood vessel formation [9]. Other *in vivo* studies have reported significant cartilage repair in mice bearing osteochondral defects, as well as bone formation and anti-adipogenic behavior ameliorating osteoporotic status of ovariectomized (OVX) mice [10,11].

In addition, Resveratrol, Formononetin and Ginsenosides have all markedly improved *in vivo* bone formation and mineralization, in both defect and OVX animal models [4]. Also, Oleanolic acid as well as green tea polyphenols have exhibited beneficial effects by reducing bone erosion and inflammation-induced bone loss *in vivo* [4,12]. Moreover, oral administration of Quercetin-loaded solid lipid nanoparticles increased Quercetin levels by 3.5-fold of free drug and effectively reversed the osteoporotic status of OVX rats to Sham levels [13].

Therefore, current research into natural small molecules suggests that they are a desirable source of potentially innovative pharmaceutics. In the toolbox of naturally available compounds for treatment of bone disorders, Naringin, a flavanone glycoside, is currently gathering special attention in pre-clinical studies and represents one of the most promising candidates for treating various bone diseases and promoting stem cells differentiation towards a pro-osteogenic phenotype.

2. Naringin - A Flavonoid with Multiple Therapeutic Targets in Bone Tissues

Naringin, also known as Naringenin 7-O-neohesperidose, is a natural flavonoid present in several fruits of the *Citrus* genus. Commercial grapefruit (*Citrus paradisi*) juice is the richest source of Naringin (43.5 mg / 100 mL), where this compound is significantly more concentrated than in their hand-squeezed equivalents (23.0 mg / 100 mL) [14]. Similarly, industrial bergamot (*Citrus bergamia*) juice represents another valuable source of this compound, with Naringin contents around 26.1 mg / 100 mL [14]. Furthermore, this compound is present in moderate quantity in *Citrus aurantium* (1.97 mg / mL) and even in certain commercial orange juices (2.13 mg / 100 mL) [14]. In addition, Naringin is also considered the main effective component in the basket fern *Drynaria fortunei*, a traditional Chinese medicine for OP [15].

Naringin-enriched natural-sources have been found to hold remarkable potential for various biomedical applications. In fact, *Citrus paradisi* juice has been described to increase the bioavailability of various drugs by decreasing first-pass metabolism, either via inhibition of cytochrome P-450 3A4 drug-metabolizing intestinal enzyme, or by inhibiting the P-glycoprotein induced efflux from the enterocytes [16]. Industrial bergamot juice has also shown antiproliferative activity in human hepatocellular carcinoma (HepG2 cells), and plays a protective role in the treatment of rheumatoid arthritis due to its anti-oxidant and anti-inflammatory activity. Interestingly it is also capable of mimicking the mechanism of statins, exerting significant hypolipidemic and hypocholesterolemic effects in humans [17–19].

Naturally, these findings raised attention towards understanding the molecular effects of the main bioactives present in these sources, such as the flavanone Naringin. Numerous pre-clinical studies investigating Naringin bioactivity support promising applications in different diseases (Figure 1) [15,20].

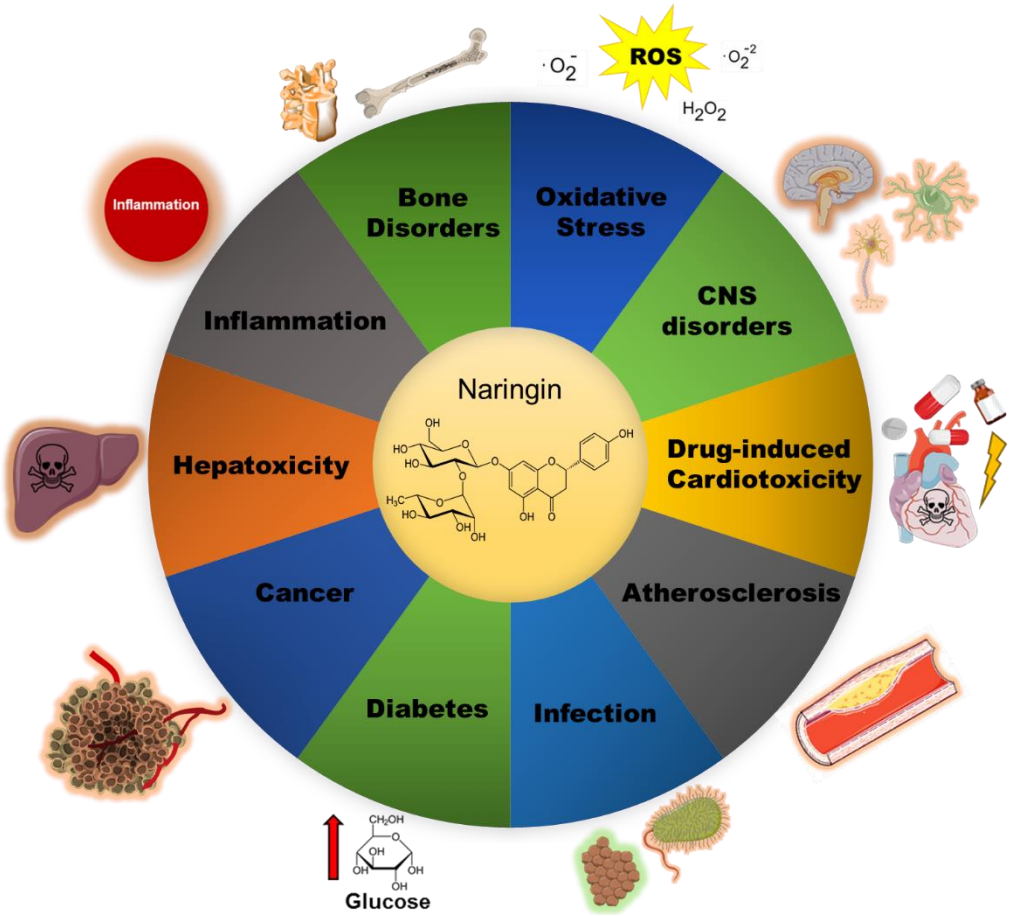

Figure 1. Overview of various conditions in which Naringin has been described to display protective / therapeutic effects. For a more general description of the activity of Naringin in these conditions, please see reference [20]. ROS – reactive oxygen species. CNS – central nervous system.

Among the different applications of Naringin, recent research has been focusing on the pro-osteogenic effects of Naringin in OP, or as a naturally-inspired compound for directing mesenchymal/stromal cells osteogenic differentiation. This unique biological activity in the context of bone disorders will be further discussed in the context of recent *in vitro* and *in vivo* pre-clinical reports.

2.1 Pre-clinical *in vitro* Studies

The pro-osteogenic effect of Naringin is well described in the literature, suggesting potential applications as bone therapeutic or as mediator of MSCs osteogenic lineage differentiation [15]. Different studies have shown that Naringin has a significant effect in the proliferation or differentiation of osteoprogenitor cells such as murine pre-osteoblasts (MC3T3-E1), and cells with osteoblastic phenotype, including human and murine primary fetal osteoblasts (respectively, hOB and pOB) [21,22]. Fan and his team found that Naringin dose-dependently improved the proliferation of rabbit BM-MSCs, and that Naringin (1 µM) significantly increased the mRNA expression of OC, ALP and Col I across studied time points (3, 7, 14, 21 days) [23]. Moreover, the authors observed that Naringin improved cells osteogenic commitment by inhibiting peroxisome proliferator activated receptor ɣ (PPARɣ) expression, a key regulator in promoting MSCs adipogenesis. The Naringin-induced downregulation of PPARɣ levels was linked to the corresponding upregulation of microRNA-20a expression [23]. The effect of Naringin on the expression of the previous markers (OC and PPARɣ) was effectively reversed by transfecting the BM-MSCs with anti-microRNA-20a antibody. Alternatively, in rat BM-MSCs, Naringin increased the proliferation over 9 days in a dose dependent manner (up to 10 µg/mL) [24]. In these cells, the highest dose (100 µg/mL) was shown to decrease proliferation over long culture periods (9 days). After Naringin treatment, there was a 5 to 7-day delay before ALP expression peak was observed, where the dose of 10 µg/mL exhibited the best osteogenic performance. These findings were supported by OC cell immunostaining after Naringin treatment, in which 10 µg/mL led to the highest increase in OC expression (Figure 2A). Another study performed by Yu and co-workers further expands the knowledge regarding Naringin-mediated activation of signaling pathways that are related to proliferation or osteogenesis [25]. These researchers found that Naringin promotes rat BM-MSCs osteogenesis via activation of the Notch signaling pathway [25]. Naringin significantly enhanced the mRNA levels of osteogenic markers (ALP, BSP and core-binding factor a1), while it decreases adipogenic regulator

(PPARγ2) both in a dose-dependent manner (Figure 2B). In addition, increased calcium node deposition in cultured cells also followed a dose-dependent behavior (Figure 2C). Interestingly, treatment with Notch-inhibitor DAPT partly reduced Naringin-induced ALP activity stimulation, calcium deposits and osteogenic mRNA transcript levels, whilst suppressing the inhibitory effect on PPARγ2. Such findings strongly support the use of Naringin as a pro-osteogenic natural compound. This is highly important in the context of stem cell-based therapies since up to date the main pharmaceutical approach has been the use of Dex to guide lineage differentiation [26]. However, this glucocorticoid has been described to strongly induce adipogenesis even in osteogenic medium, which can be counterproductive for the final application of such therapies [27]. The described simultaneous anti-adipogenic and osteogenic activity of Naringin, suggest a tremendous potential of this natural compound for stem cell-based therapies.

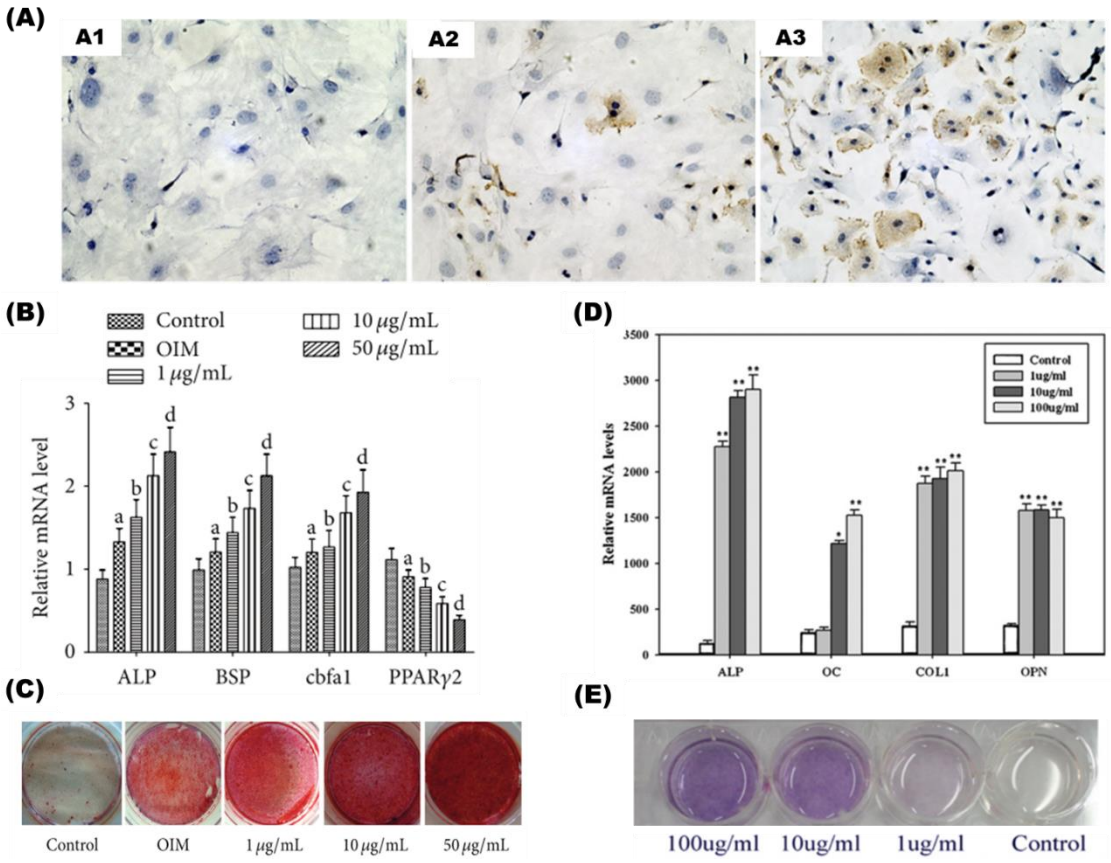

Figure 2. Naringin increases the expression of osteogenic markers, leading to an enhanced mineralization. **(A)** OC immunostaining of rat BM-MSCs after induction with different Naringin doses for 6 days, A1 – control, A2 – 1 μg/mL, A3 – 10 μg/mL. **(B)** RT-PCR gene expression analysis of osteogenic markers after a 14-day treatment of rat BM-MSCs with different Naringin doses. Data represented in mean ± s.d. (n=5). $^{a}p < 0.05$ versus control group; $^{b}p < 0.05$ versus the OIM group; $^{c}p < 0.01$ versus the 1 μg/mL group; $^{d}p < 0.01$ versus

the 10 µg/mL. **(C)** Alizarin Red S staining of calcium deposits formed in rat BM-MSCs after incubation with various doses of Naringin (1, 10 and 50 µg/mL) for 21 days. **(D)** RT-PCR gene expression analysis of osteogenic markers after a 7-day treatment of hBM-MSCs with different Naringin doses. Data represented in mean ± s.d. (n=6). *p < 0.05 and **p < 0.01 compared with the control group (n=6). **(E)** ALP staining of hBM-MSCs 7 days after drug administration. Adapted from references [24,25,28].

In the context of stem cell based bone therapies the osteogenic effect of Naringin was also assessed in hBM-MSCs. Peng-Zhang and his team observed a dose-dependent proliferative and osteogenic activity of Naringin in hBM-MSCs up to 100 µg/mL.[28] The effect of the highest doses (10 and 100 µg/mL) on ALP activity was significant after only a 24 h incubation period and increased over 7 days. In addition, all Naringin-treated groups exhibited a remarkable improvement in the expression of osteogenic markers ALP, OC, Col I and OPN (Figure 2D). Moreover, Von Kossa staining of calcium nodes and ALP staining following Naringin treatment further supported the dose-dependent effect of this flavonoid (Figure 2E).

Numerous studies have investigated the role of different signaling pathways in determining the osteogenic activity of Naringin in other cell types, such studies are important since different cell types can respond differently to the flavonoid [25,28,29]. Liu and co-workers found that Naringin-induced osteogenic activity in human amniotic fluid-derived stem cells (hAFSCs) was related to stimulation of the BMP and Wnt/β-catenin signaling pathways[30]. These pathways play a crucial role in osteogenesis regulation, adipogenesis repression and prevention of osteoblastic apoptosis [31]. Similar to previous studies, the authors demonstrated a dose-dependent increase in proliferative and osteogenic activities of this flavonoid (1 to 100 µg/mL), but not at the highest dose (200 µg/mL). Accordingly, calcium content after 28 days of Naringin treatment was markedly increased at 100 µg/mL. Reverse transcription polymerase chain reaction (RT-PCR) gene expression analysis of Naringin-treated cells revealed significant upregulation of osteogenic marker genes (OPN and Col I) and a remarkable increase in OPG expression, once again suggesting a dual-effect of Naringin in both promoting osteogenic proliferation/differentiation while inhibiting osteoclastogenesis. Interestingly, the expression levels of BMP-related regulators (RUNX2 and BMP-4), as well as Wnt-related genes (β-catenin and cyclin D1) were upregulated in Naringin-treated cells, and the ALP activities were significantly reduced in the presence of inhibitors for these pathways (accordingly, noggin for BMP and DKK-1 for Wnt-signaling).

Also, Pang and colleagues confirmed the significant osteogenic role of Naringin in UMR 106 osteoblast-like cells via estrogen receptor (ER)-dependent pathways [32]. Importantly, this study demonstrated that Naringin exerts tissue-selective oestrogenic effects on bone and possibly in adipose tissue, but not in the uterus. It was proposed that this selective behavior is determined by differential phosphorylation of ERα and ERE-dependent transcriptional activity. In addition, the authors observed that Naringin (10 nM) markedly enhanced OPG mRNA expression, and that this effect was reversed in the presence of an ER-antagonist (ICI 182780). OPG secretion is linked to inhibition of osteoclastogenesis, which suggests a potential anti-resorptive capacity of Naringin.

In fact, besides its known pro-osteogenic effect, Naringin is has demonstrated to be capable of inhibiting bone resorption *in vitro* via osteoclasts [29,33]. In this case, the anti-inflammatory effect of Naringin appears to play a role in its anti-resorptive activities. Such is supported by OPG and nuclear factor kappa B (NF-κB) pathway involvement in osteoclastogenesis [5].

In this context, Ang and co-workers observed that Naringin inhibits osteoclastogenesis and bone resorption by suppressing RANKL-induced NF-κB activation and phosphorylation of extracellular receptor kinase (ERK) [29]. Notably, the flavonoid was able to reduce the bone resorption area whilst maintaining the cell number of osteoclast-like cells (Figure 3A, B). It is also worth noting that murine macrophage RAW 264.7 cells, which were used to generate osteoclast-like cells, showed a remarkable tolerance against Naringin dosages, with only 10% apoptosis after a 24 h treatment with 1 mM of Naringin (approximately 580 μg/mL). Nevertheless, another study achieved significant bone resorption inhibition at much lower dosages of the flavonoid [33]. In this study, Xu and colleagues investigated the Naringin effect in repressing osteoclastogenesis of a rat calvarial bone culture, after incubation with different Naringin doses (1, 10 and 100 mg/L). The tartrate-resistant alkaline phosphatase (TRAP) staining of osteoclasts after treatment with different Naringin doses for 10 days revealed a dose-dependent inhibition of osteoclastogenesis (Figure 3C). Moreover, Naringin markedly suppressed osteoclastogenesis in a time-dependent manner, from 1 to 10 days of *in vitro* 2D culture (Figure 3D). After incubation with different Naringin concentrations, the authors observed a 74 % (100 mg/L), 52 % (10 mg/L) and 41 % (1 mg/L) reduction in the number of TRAP-stained osteoclasts.

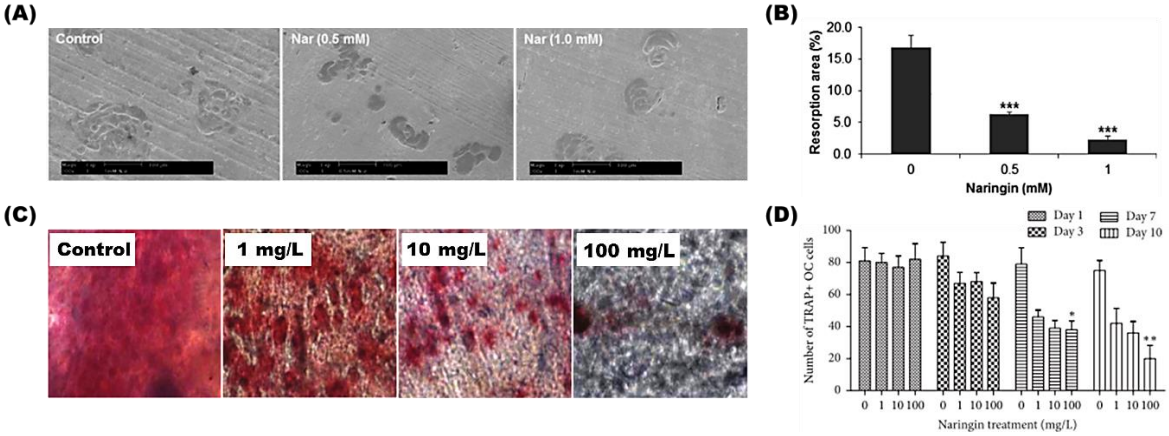

Figure 3. Naringin effectively inhibits bone resorption *in vitro*. **(A)** Representative scanning electron microscopy (SEM) micrographs of bone resorption pits induced by osteoclast-like cells in bovine bone slices after incubation with different Naringin doses (0, 0.5 and 1 mM) for 24 h. **(B)** Total resorption pit areas of each treatment group as measured under SEM. **(C)** Microscopic view of TRAP-stained osteoclasts in rat calvarial bone cultures treated with different doses of Naringin for 10 days. **(D)** Number of TRAP-stained osteoclast cells treated with different doses of Naringin for 1, 3,7 and 10 days. *p < 0.05, **p < 0.01, ***p < 0.001. All data above is represented in mean ± s.d. (n=3). Adapted from references [29,33].

The above findings demonstrate that Naringin is capable of significantly repressing osteoclastogenesis and reduce bone resorption areas. This is an important finding for applications in bone degenerative disorders, such as post-menopausal OP, characterized with osteolytic degradation due to markedly increased bone turnover. Taken together, the pre-clinical *in vitro* studies highlight a tremendous potential for Naringin applications as a bone therapeutic and for committing stem cells into the osteoblastic lineage.

2.2 Pre-clinical *in vivo* Studies

The former examples provide an important body of knowledge regarding the potential of Naringin for treating different bone disorders. Adding to this, various *in vivo* studies that will be discussed in the following paragraphs provide further evidence of Naringin realistic potential to be used as therapeutic alternative in a foreseeable future.

In laboratory animal models (such as rat and mouse), Naringin has improved overall bone health in both healthy and gonadectomized animal models *in vivo*. In healthy mice, Naringin daily oral administration significantly enhanced femoral bone mass by increasing both trabecular and cortical bone [34]. In another study in healthy mice, Yin and co-workers achieved the first validation of successful stem cell-based therapy involving Naringin for improving bone formation *in vivo*. Initially, human periodontal dental ligament stem cells

(hPDLSCs) were seeded in a nanohydroxyapatite scaffold and cultured in Naringin-containing (1 μM) medium for 1 week, before implantation into healthy mice. The transplant was harvested 8 weeks later and Naringin-treated group exhibited improved trabecular bone maturity surrounding the scaffold, as well as locally increased OPN and OC expression by 50 % [35].

Currently, most *in vivo* studies involving Naringin have been performed in OVX mice. Pang and colleagues demonstrated that treatment of OVX mice with Naringin (200 mg/kg and 400 mg/kg per day) for 6 weeks significantly improved bone quality at the distal femur, proximal tibia and lumbar spine [32]. In addition, Naringin suppressed the OVX-induced increase in urinary calcium excretion as well as losses in bone mass and strength. However, Naringin treatment failed to significantly decrease urinary deoxypyridoline level in OVX mice, a collagen degradation product that reflects bone resorption rate. In another study, OVX mice were daily treated with various Naringin doses (60, 300 and 1500 mg/kg) via oral gavage, leading to effective recovery of OVX-induced bone loss [24]. The authors found that Naringin at 300 mg/kg provided an optimal increase in bone mass density (BMD), bone volume as well as trabecular thickness, while decreasing trabecular space. Furthermore, Naringin treatment did not change the uterus weight significantly, suggesting that Naringin did not elicit off-target estrogenic effects. Interestingly, a study by Sun and colleagues investigated the effect of a combination regimen of oral Naringin (300 mg/kg) with treadmill exercise in OVX rats for 60 days [36]. Authors found that Naringin + exercise regime led to stronger effects on OP than either monotherapy on bone mass preservation and improved bone strength (Figure 4A). In a different report, Wang and colleagues observed an improved bone strength in OVX mice even at lower doses (5 mg/kg) of Naringin (Figure $4B_1$) [37]. This dose markedly improved ALP, RUNX2 and Col I expression *in vivo* (Figure $4B_2$). In particular, the authors observed that co-administration of AMPK and Akt inhibitors partly reversed Naringin effects *in vivo*, suggesting that the osteogenic activity of this flavonoid is in part via its stimulation Wnt/β-catenin signaling upon interaction with AMPK and Akt. Moreover, OVX mice achieved equally increased cell proliferation when treated with Naringin or conventional PTH, but Naringin-treated mice were characterized with the highest enhancement in ALP activity (Figure $4B_3$). Adding to this evident potential, a recent study found that Naringin (100 and 200 mg/kg) significantly inhibited the OVX-induced reduction in bone marrow microvessels, regulating the function of endothelial cells while

promoting angiogenesis in bone (Figure 4C) [38]. In parallel, Naringin has recently been shown to promote the vascularization of the callus in osteoporotic fractures in OVX rats, by significantly improving the expression of VEGF and VEGF receptor-2 [39]. In turn, this lead to an increase in vessel numbers and larger neovascularization areas, therefore resulting in accelerated bone healing at 2, 4 and 8 weeks post-fracture, in a dose dependent manner (40, 100 and 300 mg/kg). The development of bone vasculature is particularly relevant for both the treatment of OP but also in the context of tissue engineering and regenerative medicine. In particular, angiogenesis is fundamental for engineering a clinically relevant-sized tissue, which requires a vascular network for properly supplying cells beyond the diffusional limit for oxygen and nutrients [40].

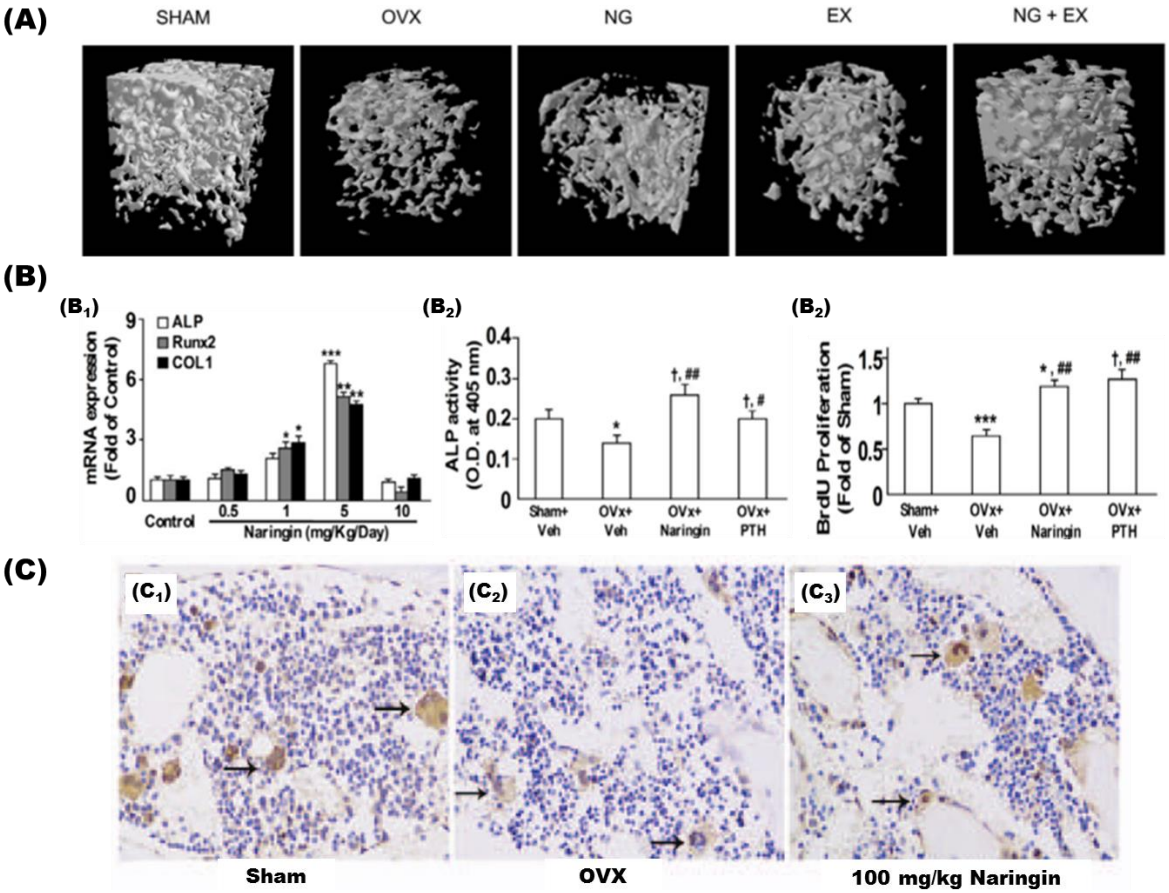

Figure 4. Pro-osteogenic and pro-angiogenic protective activities of Naringin *in vivo*. **(A)** 3D reconstruction of trabecular microarchitecture within the distal femoral metaphyseal region in Sham, OVX, Naringin (NG) or exercise (EX) monotherapy or combination regimen groups. **(B1)** Optimal Naringin-induced osteogenic gene (ALP, RUNX2, Col I) expression at 5 mg/kg (n=5). *p < 0.05; **p < 0.01; ***p <0.001 compared to control group. **(B2, B3)** Naringin-induced (5 mg/kg) increase in ALP activity and osteoblastic cell proliferation. Data represented in mean ± SEM (n=5 and n=3, respectively). #p < 0.05; ##p < 0.01 compared

with the OVX group. **(C)** Naringin markedly inhibited (100 mg/kg) the OVX-induced reduction in bone marrow microvessels (black arrows). Adapted from references [36–38].

These findings regarding the pro-angiogenic activity of Naringin are supported by the previous *in vitro* study demonstrating Naringin-induced osteogenic differentiation of BM-MSCs via activation of the Notch signaling pathway [25]. Endothelial Notch activity plays a key role in simultaneously promoting bone angiogenesis and osteogenesis and therefore, could be one of the main mechanisms behind the osteoprotective effect of Naringin [41].

Alternatively, other studied animal models support the above findings regarding the clinical potential of Naringin in improving bone health status. Wei and co-workers demonstrated the anti-osteoporotic activity of Naringin in a retinoic acid-induced OP rat model [42]. Naringin treatment with different doses (20, 40, 100 mg/kg) led to improvement in bone weight index, length and diameter of the femur bone, as well as bone ash content and levels of calcium and phosphorus. In orchidectomized rats, treatment with Naringin at 200 ppm for 2 months significantly increased serum IGF-I, femoral bone density and calcium content, as well as suppressed plasma TRAP activity, associated with bone resorption [43]. Alternatively, subcutaneous administered Naringin (10 mg/kg) is also described to promote bone formation in a titanium particle-induced diabetic murine calvarial osteolytic model [44]. Naringin embedded in a collagen bone graft also promoted bone formation in a rabbit bone defect model [45].

Naringin exhibited the most therapeutic potential in disuse-induced OP animal models, caused by mechanical unloading and characteristic in bedridden or low-mobility patients, as well as astronauts [46]. A study by Ma and co-workers investigated Naringin-treatment in denervated bone induced by sciatic neurectomy [47]. Disuse-induced bone loss in rats was induced by sciatic-neurectomy, resulting in reduced BMD and trabecular microarchitecture in the distal femur, as well as increased urinary deoxypyridoline levels. The authors confirmed the dose-dependent (30, 100, 300 mg/kg) recovery induced by Naringin treatment in restoring trabecular microarchitecture as well as bone formation rates to Sham-levels (Figure 5A). Moreover, the highest Naringin dose had a profound effect in improving osteogenesis and inhibiting osteoclastogenesis *in vivo*, as indicated by OC and TRAP immunohistochemistry analysis in the distal femoral metaphysis (Figure 5B), as well as reducing urinary deoxypyridoline. Naringin-treatment also successfully prevented biomechanical deterioration of ipsilateral femur in immobilized rats (Figure 5B). This

protective effect is thought to be modulated via Naringin-induced increase in Semaphorin 3A expression *in vivo*, a local factor of the bone microenvironment that simultaneously promotes bone formation while reducing bone resorption [47]. These studies suggest that Naringin could be a promising therapeutic alternative in treating disuse OP.

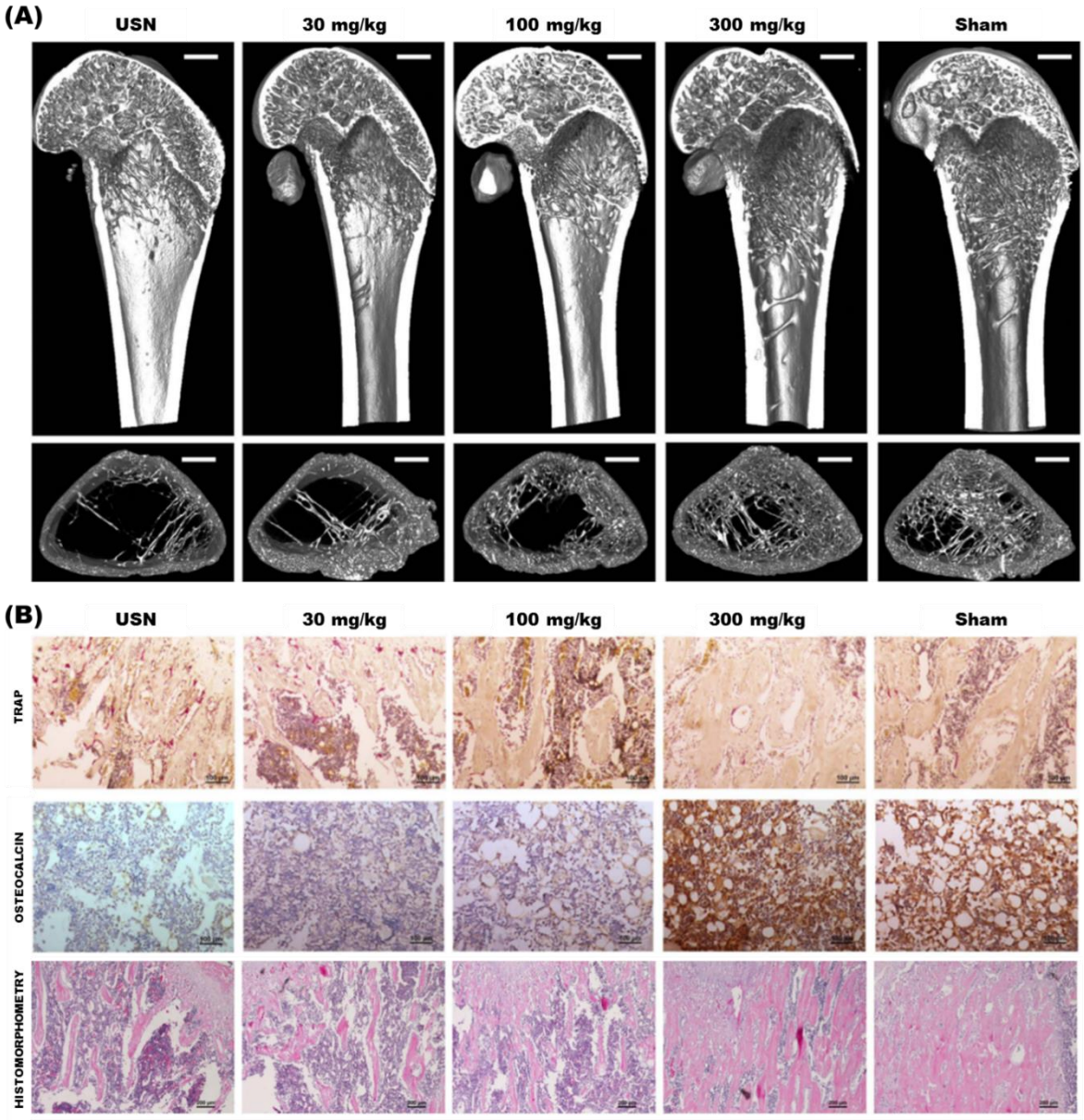

Figure 5. Naringin therapeutic activity in disuse OP induced by unilateral sciatic neurectomy (USN) in rats. **(A)** Representative 3D images showing the trabecular microarchitecture in the distal femoral metaphysis of each group. **(B)** Immunohistochemical staining of OC and osteoclasts (via TRAP) in the distal femoral metaphysis, as well as histomorphometric analysis of Naringin-prevented deterioration of the ipsilateral femurs due to immobilization. Adapted from reference [47].

Overall, the above pre-clinical studies evidence that Naringin has a significant multifactorial osteostimulative effect on bone fractures healing and overall bone health. It is worth noting that bone remodeling is a product of concomitant interaction between bone formation and resorption, meaning that disruption of this balance leads to bone dysfunction [47]. In this context, clinically available therapeutics such as antiresorptive BPs and anabolic PTH can simultaneously inhibit bone formation and promote bone resorption, which might explain why combination therapy approaches between clinical therapeutics or with mechanical-loading have been investigated with the aim of improving bone quality [48,49]. Furthermore, long-term disuse OP has been described as less sensitive to BP treatment than other OP [50]. Alternatively, bone formation is significantly reduced with ageing, mostly attributed to a shift from osteogenesis to predominant adipogenesis in the marrow stroma, leading to senile OP [51].

Taken together, the simultaneous antiresorptive, osteostimulative and antiadipogenic role of Naringin ultimately play a role in improving bone health and establish this flavonoid as a valuable candidate for pursuing alternative clinical treatment options for some of the most common bone disorders or injuries due to fractures.

3. Current Obstacles in Naringin Clinical Translation

Despite its promise for therapeutic action in several pathologies, in particular for preventing degenerative diseases and improving bone health status, Naringin is yet to be approved for clinical administration, either as a single therapy or combination with other bioactives. This fact is mainly correlated with flavonoids extensive *in vivo* metabolism, a critical factor that limits their therapeutic efficacy [52]. In addition, Naringin exhibits low bioavailability (8.8 %) following oral administration due to its poor water solubility and dissolution rates [53,54]. In fact, the poor water solubility of Naringin is considered the rate-limiting step for its absorption in the body, thus leading to inferior therapeutic efficacy [54]. Moreover, this drug is extensively degraded in acidic pH and enzymatically cleaved by β-glucosidases in the gut, inherent to intestinal microflora [55].

The effects of Naringin have been mainly explored via oral absorption, however its absorption in the gastrointestinal tract is slow and irregular [56]. Moreover, the intestinal microbiota plays a crucial role in defining the bioavailability of flavonoids such as Naringin. It is important to emphasize that this microbiome is characterized by substantial inter-individual heterogeneity, hence, ultimately the microbiome defines the clinical efficacy of

dietary flavonoids [52]. On account of these limitations, recently there have been some *in vitro* attempts for improving flavonoids bioavailability and absorption, by increasing its solubility and dissolution rates, as well as protection from intestinal degradation upon encapsulation in nanoparticles, microparticles or water-soluble fibers [54,56–58]. It has been suggested that minimal absorption rates of such drugs can severely restrict their clinical applications [13].

Adding to this, Naringin can also be degraded during blood circulation if administered via intravenous (IV) route. Indeed, flavonoids such as Naringin are unstable during circulation and easily undergo oxidation both in serum, and in the liver, where they are generally degraded by hepatic β-glucosidases [55]. It is also reported that Naringin spontaneously interacts with bovine serum albumin under physiological conditions, an aspect that can play a major role in defining its pharmacokinetic profile, facilitating excretion and hence influencing its bioavailability [59]. Such parameter is also influenced by the decreased solubility of flavanones under physiological conditions (pH = 7.4), due to degradation into chalcone structures [54]. So far, no attempts have been made towards formulating intravenously administrable nanocarriers for the controlled delivery of Naringin. As recognized from previously highlighted studies with other natural compounds (e.g. Quercetin), controlled delivery via nanocarriers can significantly alter their *in vivo* therapeutic effect [13]. There have been some recent developments concerning the formulation of Naringin within suitable carriers for oral absorption, but research is still at an early stage and studies are yet to validate this approach *in vivo*. Concerning the parenteral route of administration, literature is still scarce and there is a great untapped potential to be exploited on this approach.

Nanotechnology-based drug delivery systems allow for the improvement of solubility, bioavailability and pharmacokinetics of entrapped pharmaceutics, protecting them from degradation and unspecific interactions while prolonging their circulation times [60]. Furthermore, these nanocarriers can provide a sustained release profile and can be modified with specific targeting moieties for improving accumulation at the desired locations [61]. Hence, the bioavailability of Naringin could be vastly improved by inclusion in a nanocarrier, ultimately leading to locally increased concentrations in the bone microenvironment.

Recognizing the potential of nanotechnology for flavonoid delivery, the following chapters will address the development of nanocarriers for drug delivery to bone tissues. A

critical discussion regarding the barriers encountered by these nanomedicines upon systemic administration and the precision chemistry-based modifications that can be imprinted in their structure to endow them with stimuli-responsive cargo release are also provided.

4. Biomaterial-based Platforms for Naringin Incorporation

As aforementioned, Naringin has low bioavailability and undergoes extensive metabolism *in vivo*. Such has motivated researchers to explore biomaterial-based platforms for immobilizing or protecting Naringin from degradation, and for achieving a sustained spatiotemporally controlled release with the aim of improving its therapeutic effect. The most relevant examples of such platforms are summarized in Figure 6.

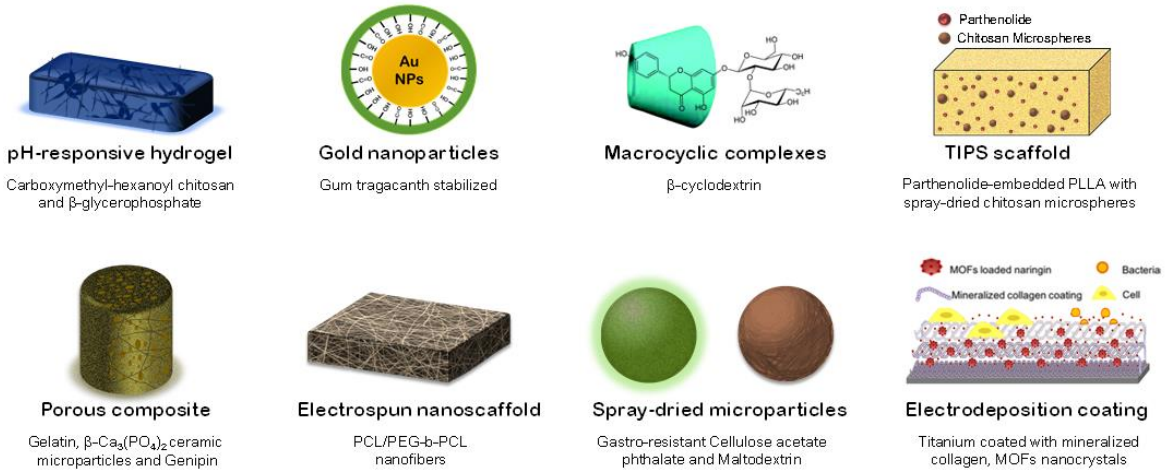

Figure 6. Overview of current strategies for Naringin incorporation into specialized biomaterial-based platforms. Representative images of literature reports are presented, except for the electrodeposition coating approach which was adapted from the respective reference [62]. TIPS – Thermal-induced phase separation. MOF – Metal-organic framework.

Regarding the production of Naringin-biomaterial hybrids Ji and co-workers incorporated the flavanone within an electrospun nanoscaffold comprised of polycaprolactone (PCL) and poly(ethylene glycol)-b-polycaprolactone (PEG-b-PCL) nanofibers (~ 242 nm) to serve as a bone regenerating implant [63]. PCL/PEG-b-PCL/Naringin nanoscaffolds elicited an increased MC3T3-E1 proliferation, as well as enhanced osteogenic differentiation (evaluated via ALP activity) after 14 days of culture in medium with no osteogenic supplements. Moreover, for cells cultured in these nanoscaffolds, Alizarin Red S staining showed improved calcium mineralization nodules after only 10 days. In addition, the authors studied the effect of the Naringin nanoscaffold in suppressing osteoclastogenesis in a critical size defect model of

mouse calvarial bone. After 14 days of implantation, the defects treated with PCL/PEG-b-PCL/Naringin nanoscaffolds showed a significant decrease in TRAP staining when compared to treatment with blank PCL nanoscaffolds (Figure 7A). These results corroborate Naringin-induced osteoclastogenesis suppression and suggest potential applications of this drug-loaded nanofiber scaffold in bone tissue engineering. Regarding this application, Chen and co-workers developed a porous biodegradable composite comprised by Genipin crosslinked Gelatin, and β-$Ca_3(PO_4)_2$ ceramic microparticles (GGT) mixed with Naringin (10 mg/mL). These composites were formulated with the aim to enhance bone repair *in vivo* in a rabbit calvarial defect model [64]. The obtained radiographic analysis (Figure $7B_1$) and histological H&E staining (Figure $7B_2$) revealed that, 8 weeks post-implantation, Naringin-loaded GGT composites promoted a significant deposition of new bone formation when compared to GGT controls. Moreover, complete osseointegration of the biodegradable implant could be readily observed, with newly formed bone replacing a significant amount of the Naringin-loaded GGT composites (Figure 7B).

Recently, Guo and colleagues developed a porous poly(L-lactide) (PLLA) scaffold incorporating anti-inflammatory drug Parthenolide and spray-dried Naringin-loaded chitosan microspheres in the matrix [65]. The regenerative performance of this dual drug delivery scaffold was studied in a rat model of periodontal fenestration defects. Analysis of μ-CT data revealed that 8 weeks post-implantation, the dual delivery scaffold significantly enhanced bone volume and decreased inflammatory response in the defect, when compared to the PLLA group (Figure 7C). Histological H&E analysis corroborated the superior performance of the dual delivery scaffold in improving periodontal tissue regeneration. Also, IL-6 immunostaining showed that the dual delivery scaffold achieved the least positive staining areas for the cytokine, highlighting its anti-inflammatory activity. The authors therefore suggest a possible application as an adjuvant for the treatment of periodontitis. However, it should be noted that MC3T3-E1 cell proliferation assays showed that both the dual delivery scaffold and the Parthenolide-loaded group significantly decreased cells proliferation in comparison with the Naringin-loaded group. These results suggest that this flavanone can partially rescue the observed cytotoxic effect of anti-inflammatory drug Parthenolide.

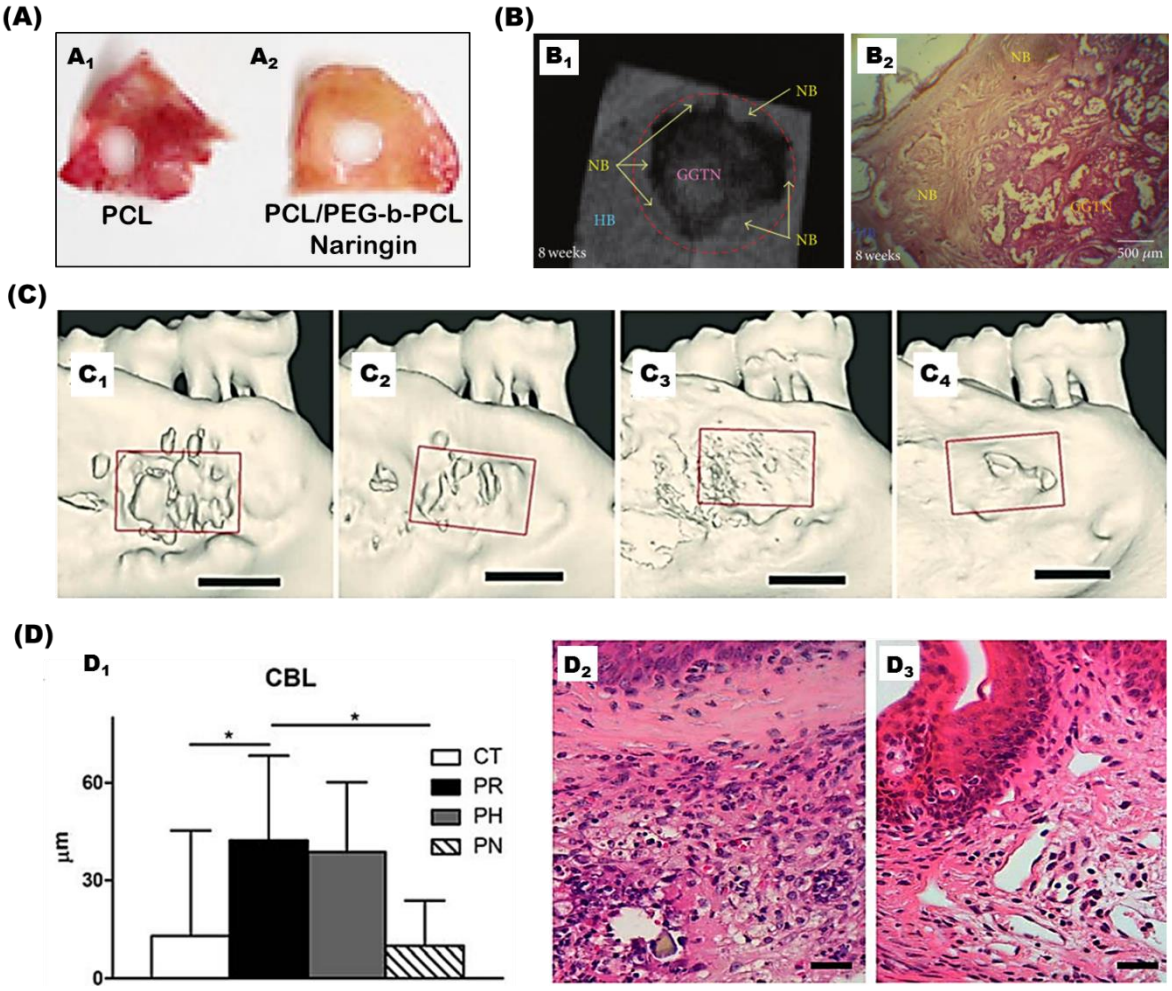

Figure 7. Application of Naringin-biomaterial hybrids. **(A)** TRAP staining of mouse calvarial bone sections highlighting the anti-osteoclastogenic activity of Naringin nanoscaffold after 14 days. **(B)** Radiographic **(B_1)** and H&E staining **(B_2)** images showing significant new bone formation surrounding the Naringin-loaded porous gelatin composite 8 weeks post-implantation in calvarial bone defects. **(C)** μCT 3D reconstruction images of periodontal bone repair 4 weeks **(C_1, C_3)** and 8 weeks **(C_2, C_4)** after PLLA scaffold **(C_1, C_2)** and dual delivery scaffold **(C_3, C_4)** implantation. **(D)** Biological performance of Naringin-loaded pH-responsive hydrogel in treating an acute periodontitis mice model. **(D_1)** Change in periodontal bone level (CBL) across control (CT), untreated periodontitis (PR), periodontitis treated with blank hydrogel (PH) and periodontitis treated with Naringin hydrogel (PN) 7 days after periodontitis induction (n=10). **(D_2, D_3)** Degradation of the extracellular matrix following inflammatory cell infiltration was evident in PR and PH groups **(D_2)** but was significantly halted in the PN group **(D_3)**. Adapted from references [63–66].

In parallel, Chang and colleagues have recently developed a Naringin-loaded (0.85 %) pH-responsive hydrogel for periodontitis treatment, taking advantage of the characteristic pH reduction hallmark in inflammation sites [66]. In this study, the authors formulated a hydrogel comprised by carboxymethyl-hexanoyl chitosan, β-glycerophosphate and glycerol via a thermally induced sol-to-gel transition. Notably, the hydrogel underwent instant sol-

to-gel transition at 37 ºC. Interestingly, a 2-fold higher amount Naringin was released in acidic conditions (pH = 5.5) when compared to physiological conditions (pH = 7.4), accordingly 51 % versus 24 % of total Naringin released in the first 4 h. Here, a silk-induced acute periodontitis mice model was used to evaluate the hydrogel biological performance. The Naringin-loaded hydrogel markedly attenuated local inflammation and periodontal breakdown after 7 days (Figure 7D). Gene expression analysis also showed a remarkable downregulation of Toll-like receptor 2, TNF-α and RAGE expression, but not myd88, which is why the authors suggested that this therapeutic activity might be achieved via a LPS-mediated myd88-independent mechanism. Overall, these studies suggest promising future applications for Naringin delivered through biomaterials.

5. Conclusions

The search for safer and more suitable osteoinductive agents has lead researchers to explore the potential of natural-based compounds such as Naringin. As highlighted by the numerous pre-clinical studies investigating this flavanone's therapeutic activities, there is unquestionable potential in Naringin application for bone diseases or for instructing stem cells osteogenic differentiation. Indeed, Naringin has shown promise for applications in skeletal disorders for which current pharmaceutic strategies are lacking, while also providing a relatively safe option for osteoinduction, particularly when compared to other commonly used osteoinductive drugs. Studies investigating Naringin controlled release formulations are rapidly emerging. The studies involving the loading and controlled release of this flavanone could pave the way for future biomedical applications. Such could potentially lead to the establishment of nature-derived products as valuable sources for new pharmaceutics that find application in cell-based therapies for tissue engineering and regenerative medicine.

References

1. Rodan, G. A. & . Therapeutic Approaches to Bone Diseases. *Science.* **289,** 1508–1514 (2000).
2. Roberts, T. T. & Rosenbaum, A. J. Bone grafts, bone substitutes and orthobiologics. *Organogenesis* **8,** 114–124 (2012).
3. Dimitriou, R., Jones, E., McGonagle, D. & Giannoudis, P. V. Bone regeneration: current concepts and future directions. *BMC Med.* **9,** 66 (2011).
4. Che, C.-T., Wong, M. & Lam, C. Natural Products from Chinese Medicines with Potential Benefits to Bone Health. *Molecules* **21,** 239 (2016).
5. An, J. *et al.* Natural products for treatment of bone erosive diseases: The effects and mechanisms on inhibiting osteoclastogenesis and bone resorption. *Int. Immunopharmacol.* **36,** 118–131 (2016).
6. An, J. *et al.* Natural products for treatment of osteoporosis: The effects and mechanisms on promoting osteoblast-mediated bone formation. *Life Sci.* **147,** 46–58 (2016).
7. Brandi, M. L. *et al.* Genetic markers of osteoarticular disorders : facts and hopes. *Arthritis Res. Ther.* **3,** 270–280 (2001).

8. Lee, J. S. *et al.* Plant Flavonoid-Mediated Multifunctional Surface Modification Chemistry: Catechin Coating for Enhanced Osteogenesis of Human Stem Cells. *Chem. Mater.* **29,** 4375–4384 (2017).
9. Zhao, J. *et al.* Icariin: A Potential Osteoinductive Compound for Bone Tissue Engineering. *Tissue Eng. Part A* **16,** 233–243 (2010).
10. Wang, P. *et al.* Flavonoid Compound Icariin Activates Hypoxia Inducible Factor-1α in Chondrocytes and Promotes Articular Cartilage Repair. *PLoS One* **11,** e0148372 (2016).
11. Liu, H. *et al.* Icariin improves osteoporosis, inhibits the expression of PPARγ, C/EBPα, FABP4 mRNA, N1ICD and jagged1 proteins, and increases Notch2 mRNA in ovariectomized rats. *Exp. Ther. Med.* **13,** 1360–1368 (2017).
12. Weaver, C. M., Alekel, D. L., Ward, W. E. & Ronis, M. J. Flavonoid Intake and Bone Health. *J. Nutr. Gerontol. Geriatr.* **31,** 239–253 (2012).
13. Ahmad, N. *et al.* Quercetin-loaded solid lipid nanoparticles improve osteoprotective activity in an ovariectomized rat model: a preventive strategy for post-menopausal osteoporosis. *RSC Adv.* **6,** 97613–97628 (2016).
14. Gattuso, G., Barreca, D., Gargiulli, C., Leuzzi, U. & Caristi, C. Flavonoid composition of citrus juices. *Molecules* **12,** 1641–1673 (2007).
15. Chen, R., Qi, Q.-L., Wang, M.-T. & Li, Q.-Y. Therapeutic potential of naringin: an overview. *Pharm. Biol.* **54,** 3203–3210 (2016).
16. Dahan, A. & Altman, H. Food–drug interaction: grapefruit juice augments drug bioavailability—mechanism, extent and relevance. *Eur. J. Clin. Nutr.* **58,** 1–9 (2004).
17. Ferlazzo, N. *et al.* NF-κB mediates the antiproliferative and proapoptotic effects of bergamot juice in HepG2 cells. *Life Sci.* **146,** 81–91 (2016).
18. Marino, A. *et al.* Role of natural antioxidants and potential use of bergamot in treating rheumatoid arthritis. *PharmaNutrition* **3,** 53–59 (2015).
19. Janda, E. *et al.* Molecular mechanisms of lipid- and glucose-lowering activities of bergamot flavonoids. *PharmaNutrition* **4,** S8–S18 (2016).
20. Bharti, S., Rani, N., Krishnamurthy, B. & Arya, D. S. Preclinical evidence for the pharmacological actions of naringin: A review. *Planta Med.* **80,** 437–451 (2014).
21. Li, L., Zeng, Z. & Cai, G. Comparison of neoeriocitrin and naringin on proliferation and osteogenic differentiation in MC3T3-E1. *Phytomedicine* **18,** 985–989 (2011).
22. Wu, J. Bin *et al.* Naringin-induced bone morphogenetic protein-2 expression via PI3K, Akt, c-Fos/c-Jun and AP-1 pathway in osteoblasts. *Eur. J. Pharmacol.* **588,** 333–341 (2008).
23. Fan, J., Li, J. & Fan, Q. Naringin promotes differentiation of bone marrow stem cells into osteoblasts by upregulating the expression levels of microRNA-20a and downregulating the expression levels of PPARγ. *Mol. Med. Rep.* **12,** 4759–4765 (2015).
24. Li, N., Jiang, Y., Wooley, P. H., Xu, Z. & Yang, S. Y. Naringin promotes osteoblast differentiation and effectively reverses ovariectomy-associated osteoporosis. *J. Orthop. Sci.* **18,** 478–485 (2013).
25. Yu, G. *et al.* Naringin Stimulates Osteogenic Differentiation of Rat Bone Marrow Stromal Cells via Activation of the Notch Signaling Pathway. *Stem Cells Int.* **2016,** 1-8 (2016).
26. Rickard, D. J., Sullivan, T. A., Shenker, B. J., Leboy, P. S. & Kazhdan, I. Induction of Rapid Osteoblast Differentiation in Rat Bone Marrow Stromal Cell Cultures by Dexamethasone and BMP-2. *Dev. Biol.* **161,** 218–228 (1994).
27. Ghali, O. *et al.* Dexamethasone in osteogenic medium strongly induces adipocyte differentiation of mouse bone marrow stromal cells and increases osteoblast differentiation. *BMC Cell Biol.* **16,** 9 (2015).
28. Peng-Zhang *et al.* Effects of naringin on the proliferation and osteogenic differentiation of human bone mesenchymal stem cell. *Eur. J. Pharmacol.* **607,** 1-5 (2009).
29. Ang, E. S. M. *et al.* Naringin abrogates osteoclastogenesis and bone resorption via the inhibition of RANKL-induced NF-kB and ERK activation. *FEBS Lett.* **585,** 2755–2762 (2011).
30. Liu, M., Li, Y. & Yang, S.-T. Effects of naringin on the proliferation and osteogenic differentiation of human amniotic fluid-derived stem cells. *J. Tissue Eng. Regen. Med.* **11,** 276–284 (2014).
31. Krishnan, V., Byrant, H. U. & MacDougald, O. A. Regulation of bone mass by Wnt signaling. *J. Clin. Invest.* **116,** 1202–1209 (2006).
32. Pang, W.-Y. *et al.* Naringin improves bone properties in ovariectomized mice and exerts oestrogen-like activities in rat osteoblast-like (UMR-106) cells. *Br. J. Pharmacol.* **159,** 1693–1703 (2010).
33. Xu, T. *et al.* The Function of Naringin in Inducing Secretion of Osteoprotegerin and Inhibiting Formation of Osteoclasts. *Evidence-Based Complement. Altern. Med.* **2016,** 1–7 (2016).
34. Hirata, M., Matsumoto, C., Takita, M., Miyaura, C. & Inada, M. Naringin Suppresses Osteoclast Formation and Enhances Bone Mass in Mice. *J. Heal. Sci.* **55,** 463–467 (2009).

35. Yin, L. *et al.* Effects of Naringin on Proliferation and Osteogenic Differentiation of Human Periodontal Ligament Stem Cells In Vitro and In Vivo. *Stem Cells Int.* **2015,** 1–9 (2015).
36. Sun, X. *et al.* The Effects of Combined Treatment with Naringin and Treadmill Exercise on Osteoporosis in Ovariectomized Rats. *Sci. Rep.* **5,** 13009 (2015).
37. Wang, D. *et al.* Stimulation of Wnt/β-Catenin Signaling to Improve Bone Development by Naringin via Interacting with AMPK and Akt. *Cell. Physiol. Biochem.* **36,** 1563–1576 (2015).
38. Shangguan, W. *et al.* Naringin inhibits vascular endothelial cell apoptosis via endoplasmic reticulum stress‐ and mitochondrial‐mediated pathways and promotes intraosseous angiogenesis in ovariectomized rats. *Int. J. Mol. Med.* **40,** 1741–1749 (2017).
39. Song, N. *et al.* Naringin promotes fracture healing through stimulation of angiogenesis by regulating the VEGF/VEGFR-2 signaling pathway in osteoporotic rats. *Chem. Biol. Interact.* **261,** 11–17 (2017).
40. Rouwkema, J. & Khademhosseini, A. Vascularization and Angiogenesis in Tissue Engineering: Beyond Creating Static Networks. *Trends Biotechnol.* **34,** 733–745 (2016).
41. Ramasamy, S. K., Kusumbe, A. P., Wang, L. & Adams, R. H. Endothelial Notch activity promotes angiogenesis and osteogenesis in bone. *Nature* **507,** 376–380 (2014).
42. Wei, M., Yang, Z., Li, P., Zhang, Y. & Sse, W. C. Anti-osteoporosis activity of naringin in the retinoic acid-induced osteoporosis model. *Am. J. Chin. Med.* **35,** 663–667 (2007).
43. Mandadi, K. *et al.* Citrus bioactive compounds improve bone quality and plasma antioxidant activity in orchidectomized rats. *Phytomedicine* **16,** 513–520 (2009).
44. Zhou, X., Zhang, P., Zhang, C. & Zhu, Z. Promotion of bone formation by naringin in a titanium particle-induced diabetic murine calvarial osteolysis model. *J. Orthop. Res.* **28,** 451-456 (2009).
45. Wong, R. W. K. & Rabie, A. B. M. Effect of naringin collagen graft on bone formation. *Biomaterials* **27,** 1824–1831 (2006).
46. Lin, C. *et al.* Sclerostin Mediates Bone Response to Mechanical Unloading Through Antagonizing Wnt/β-Catenin Signaling. *J. Bone Miner. Res.* **24,** 1651–1661 (2009).
47. Ma, X. *et al.* Naringin ameliorates bone loss induced by sciatic neurectomy and increases Semaphorin 3A expression in denervated bone. *Sci. Rep.* **6,** 24562 (2016).
48. Cosman, F. Combination therapy for osteoporosis: a reappraisal. *Bonekey Rep.* **3,** 1–8 (2014).
49. Camargos, G. V *et al.* Mechanical competence of ovariectomy-induced compromised bone after single or combined treatment with high-frequency loading and bisphosphonates. *Sci. Rep.* **5,** 10795 (2015).
50. Li, C. Y. *et al.* Long-Term Disuse Osteoporosis Seems Less Sensitive to Bisphosphonate Treatment Than Other Osteoporosis. *J. Bone Miner. Res.* **20,** 117–124 (2004).
51. Duque, G. & Troen, B. R. Understanding the Mechanisms of Senile Osteoporosis: New Facts for a Major Geriatric Syndrome. *J. Am. Geriatr. Soc.* **56,** 935–941 (2008).
52. Cassidy, A. & Minihane, A.-M. The role of metabolism (and the microbiome) in defining the clinical efficacy of dietary flavonoids. *Am. J. Clin. Nutr.* **105,** 10–22 (2017).
53. Manach, C., Williamson, G., Morand, C., Scalbert, A. & Rémésy, C. Bioavailability and bioefficacy of polyphenols in humans. I. Review of 97 bioavailability studies. *Am. J. Clin. Nutr.* **81,** 230S–242S (2005).
54. Kanaze, F. I. *et al.* Dissolution enhancement of flavonoids by solid dispersion in PVP and PEG matrixes: A comparative study. *J. Appl. Polym. Sci.* **102,** 460–471 (2006).
55. Walle, T. Absorption and metabolism of flavonoids. *Free Radic. Biol. Med.* **36,** 829–837 (2004).
56. Lauro, M. R., De Simone, F., Sansone, F., Iannelli, P. & Aquino, R. P. Preparations and release characteristics of naringin and naringenin gastro-resistant microparticles by spray-drying. *J. Drug Deliv. Sci. Technol.* **17,** 119–124 (2007).
57. Pai, D. A., Vangala, V. R., Ng, J. W., Ng, W. K. & Tan, R. B. H. Resistant maltodextrin as a shell material for encapsulation of naringin: Production and physicochemical characterization. *J. Food Eng.* **161,** 68–74 (2015).
58. Rao, K. *et al.* Gum tragacanth stabilized green gold nanoparticles as cargos for Naringin loading: A morphological investigation through AFM. *Carbohydr. Polym.* **174,** 243–252 (2017).
59. Roy, A. S. A spectroscopic study of the interaction of the antioxidant naringin with bovine serum albumin. *J. Biophys. Chem.* **1,** 141–152 (2010).
60. Singh, R. & Lillard, J. W. Nanoparticle-based targeted drug delivery. *Exp. Mol. Pathol.* **86,** 215–223 (2009).
61. Low, S. A. & Kopeček, J. Targeting polymer therapeutics to bone. *Adv. Drug Deliv. Rev.* **64,** 1189–1204 (2012).
62. Yu, M. *et al.* Controlled release of naringin in metal-organic framework-loaded mineralized collagen coating to simultaneously enhance osseointegration and antibacterial activity. *ACS Appl. Mater.*

Interfaces **9,** 19698–19705 (2017).
63. Ji, Y. *et al*. Controlled-release naringin nanoscaffold for osteoporotic bone healing. *Dent. Mater.* **30,** 1263–1273 (2014).
64. Chen, K.-Y., Lin, K., Chen, Y. & Yao, C. A Novel Porous Gelatin Composite Containing Naringin for Bone Repair. *Evidence-Based Complement. Altern. Med.* **2013,** 1–10 (2013).
65. Guo, Z. *et al.* Sequential controlled-released dual-drug loaded scaffold for guided bone regeneration in a rat fenestration defect model. *J. Mater. Chem. B* **5,** 7701–7710 (2017).
66. Chang, P.-C. *et al.* Inhibition of Periodontitis Induction Using a Stimuli-Responsive Hydrogel Carrying Naringin. *J. Periodontol.* **88,** 190–196 (2017).

1.6 Classes of Nanocarriers for Bone Drug Delivery

The bone microenvironment is comprised of a myriad of functional cells, as well as of respective precursors, and is surrounded by an extracellular matrix with equal diversity. Each of these distinct components represent unique opportunities for targeting of nanocarriers to skeletal tissue. Lately, there has been tremendous progress in this area, with development of new bone-specific peptides, aptamers or BP-derived moieties that greatly enhance the active targeting to bone. Among bone-targeting molecules explored to date, BPs, aptamers and peptides (e.g. aspartate-based oligopeptides), have been extensively employed to modify the surface of bone-targeted nanocarriers [1–3]. Interestingly, some of these peptides even possess inherent osteogenic properties, while others are capable of minimizing aggregation in biological media [2,4]. Readers interested in bone-seeking strategies are pointed to these excellent reviews discussing the topic at hand [3,5,6].

Incorporating small bioactive molecules capable of promoting bone regeneration, inhibiting bone resorption or treatment of bone tumors within nanocarriers modified with bone-seeking properties, represent attractive possibilities for improving the pharmacokinetic/pharmacodynamic profiles of currently available drugs. In addition, emerging siRNA therapeutics have recently showed potential for bone regeneration and could greatly benefit from enhanced intracellular delivery via nanocarriers [7–9].

This next section addresses the advances in nanocarriers formulation for bone drug delivery, including those with active targeting moieties for this tissue. Amongst several nanocarrier classes (Figure 7), one of the most frequently explored for bone are polymeric micelles (PMs), and as such, will be the focus of the following section.

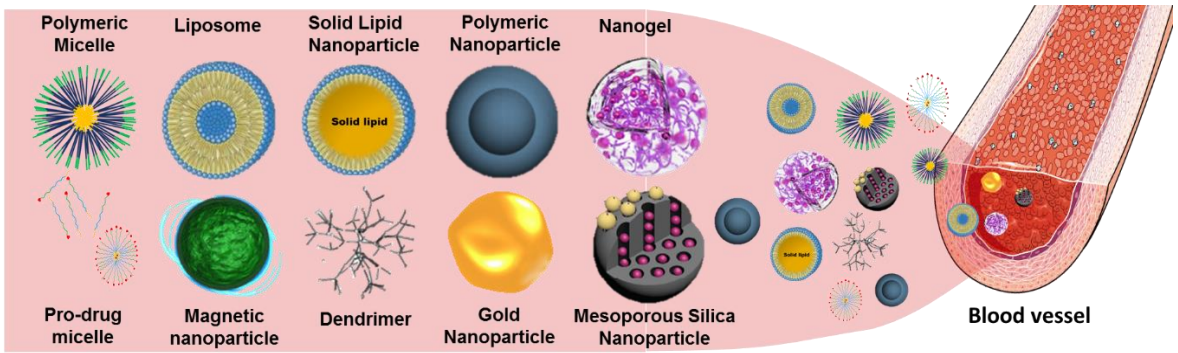

Figure 7. Schematic representation of some of the most frequently employed classes of nanocarriers for systemic delivery. Some nanocarrier vectors were adapted from references [10,11].

Polymeric Micelles as Versatile Nanocarriers for Therapeutic Delivery

Polymeric micelles (PMs) are promising nanocarriers widely explored in several therapeutic areas, with some formulations currently entering clinical trials [12]. Typically ranging from 10 to 100 nm, PMs are generally comprised of amphiphilic blocks that self-assemble into core-shell type nanostructures in aqueous media at concentrations above their critical micellar concentration (CMC) (Figure 8) [13]. Their amphiphilic nature results in a unique core-shell type structure where the inner hydrophobic core allows high drug loading of hydrophobic pharmaceuticals and the outer hydrophilic shell imprints a water-soluble character to these nanocarriers. In addition, the ability to circulate in blood for long periods can be assigned to PMs by using hydrophilic polymers such as PEG or poly(2-ethyl-2-oxazoline) (PEOz) in their shell [14]. Such polymers can provide steric hindrance and effectively shield PMs by preventing opsonization and limiting non-specific plasma proteins adsorption (i.e., limiting the formation of a protein corona) [15]. These properties make PMs valuable candidates for IV administration.

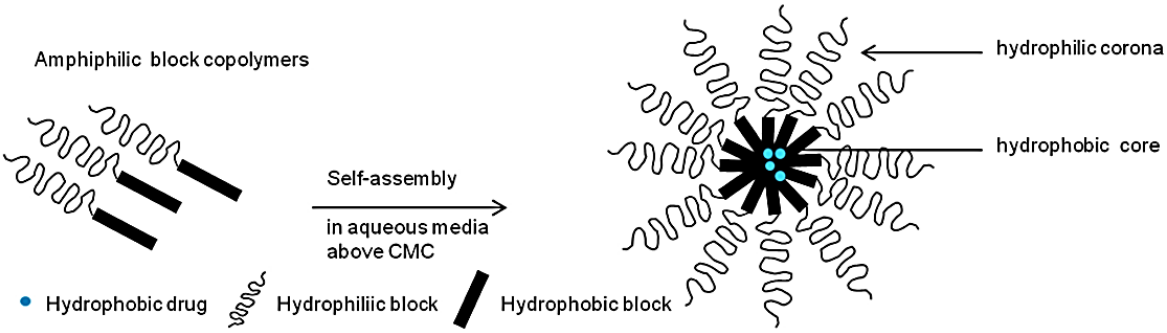

Figure 8. PMs formation via self-assembly in aqueous solutions. Adapted from reference [16].

Micelles main advantages for drug delivery stem from their tunable physicochemical properties namely: (i) particle size, (ii) surface charge, (iii) biocompatibility and (iv) chemical functionalization via inclusion of targeting moieties on the micellar hydrophilic shell [17]. These properties significantly influence PMs *in vivo* fate and consequently the overall therapeutic effect [18]. Small sized and long-circulating nanocarriers such as micelles, are important for increasing drug bioavailability in different tissues, such as bone, to which pharmaceuticals have generally low affinity.

To increase bone targeting specificity currently developed PMs are typically surface functionalized with osteotropic moieties, such as alendronate. By taking advantage of this approach, Mu and his team co-encapsulated Ponatinib and SAR302503 within poly(lactide)

(PLA)-PEG-alendronate micelles for treating therapy-resistant chronic myeloid leukaemia (CML) [19]. Dynamic light scattering (DLS) analysis showed a particle size of 26.4 ± 6.9 nm and ζ-potential of -22.8 ± 2.1 mV. The *in vivo* bone affinity was accessed after injection in female BALB/c mice of either DiR or Coumarin-6 (Coum-6) labelled micelles. Interestingly, Coum-6 labelled micelles with 40 % alendronate coating were found in bone marrow cavities of the mouse femur, but not in cortical bone. Moreover, *in vivo* pharmacokinetic results show that Ponatinib concentrations in the femur after micelle injection (5 mg/kg) were around 2-fold when compared to the untargeted control. Notably, half the initial dosage (2.5 mg/kg) achieved the same drug availability relatively to the untargeted control formulation at a higher dosage (5 mg/kg). Interestingly, while SAR302503 concentration rapidly decreased in the controls, the PLA-PEG-alendronate formulation enhanced drug accumulation in femur by 2- to 3-fold at 2 and 8 h, respectively, after IV injection. The *in vivo* therapeutic efficacy of PLA-PEG-alendronate was studied by an inoculated murine model of leukaemia (BaF3/T315I cells) and it was shown that treatment of mice with PLA-PEG-alendronate containing both drugs significantly prolonged survival across all groups. Therefore, this IV injectable bone-seeking micellar formulation may be a promising therapeutic strategy for treating therapy-resistant CML [19].

Despite of relatively low CMC when compared to surfactant micelles, some classes of PMs with low molecular weight hydrophobic moieties still suffer from poor *in vivo* stability while trafficking in the bloodstream, mainly due to dilution after administration, as well as binding of block copolymers to plasma serum proteins [20]. Concerning these limitations, hydrophobic core crosslinking via chemical bonds or hydrophobic interactions can improve micelle stability with several methods being employed with success: (i) radical polymerization, (ii) bifunctional agents and (iii) disulfide bridges (bioreducible bonds) [20]. These delivery systems encapsulate bioactive molecules in the crosslinked core, improving nanocarrier *in vivo* stability but simultaneously creating a different dilemma regarding a tight control over the spatiotemporal cargo release. In fact, core crosslinking may potentially reduce cargo release below the threshold of therapeutic concentration, which is why robust stimuli-responsive micelles could improve drug delivery by allowing a triggered cargo release under relevant physiological conditions [21]. This particular topic will be further discussed in the following sections.

References

1. Hirabayashi, H. & Fujisaki, J. Bone-Specific Drug Delivery Systems Approaches via Chemical Modification of Bone-Seeking Agents. *Clin. Pharmacokinet.* **42,** 1319–1330 (2003).
2. Aoki, K., Alles, N., Soysa, N. & Ohya, K. Peptide-based delivery to bone. *Adv. Drug Deliv. Rev.* **64,** 1220–1238 (2012).
3. Dang, L. *et al.* Targeted Delivery Systems for Molecular Therapy in Skeletal Disorders. *Int. J. Mol. Sci.* **17,** 428 (2016).
4. Nowinski, A. K., White, A. D., Keefe, A. J. & Jiang, S. Biologically inspired stealth peptide-capped gold nanoparticles. *Langmuir* **30,** 1864–1870 (2014).
5. Carbone, E. J. *et al.* Osteotropic nanoscale drug delivery systems based on small molecule bone-targeting moieties. *Nanomedicine Nanotechnology, Biol. Med.* **13,** 37–47 (2017).
6. Xinluan, W., Yuxiao, L., Helena, N. H., Zhijun, Y. & Ling, Q. Systemic Drug Delivery Systems for Bone Tissue Regeneration – A Mini Review. *Curr. Pharm. Des.* **21,** 1575–1583 (2015).
7. Ghadakzadeh, S., Mekhail, M., Aoude, A., Hamdy, R. & Tabrizian, M. Small Players Ruling the Hard Game: SiRNA in Bone Regeneration. *J. Bone Miner. Res.* **31,** 475–487 (2016).
8. Lu, Z.-R. pH-sensitive siRNA delivery systems. *J. Drug Deliv. Sci. Technol.* **22,** 55–63 (2012).
9. Cheng, R. *et al.* Glutathione-responsive nano-vehicles as a promising platform for targeted intracellular drug and gene delivery. *J. Control. Release* **152,** 2–12 (2011).
10. Yang, K.-N. *et al.* pH-responsive mesoporous silica nanoparticles employed in controlled drug delivery systems for cancer treatment. *Cancer Biol. Med.* **11,** 34–43 (2014).
11. Karimi, M., Zangabad, P. S., Ghasemi, A. & Hamblin, M. R. Smart External Stimulus-Responsive Nanocarriers for Drug and Gene Delivery. (2015).
12. Cabral, H. & Kataoka, K. Progress of drug-loaded polymeric micelles into clinical studies. *J. Control. Release* **190,** 465–476 (2014).
13. Torchilin, V. P. Micellar nanocarriers: Pharmaceutical perspectives. *Pharm. Res.* **24,** 1–16 (2007).
14. Gaspar, V. M. *et al.* Bioreducible poly(2-ethyl-2-oxazoline)–PLA–PEI-SS triblock copolymer micelles for co-delivery of DNA minicircles and Doxorubicin. *J. Control. Release* **213,** 175–191 (2015).
15. Kataoka, K., Harada, A. & Nagasaki, Y. Block copolymer micelles for drug delivery: Design, characterization and biological significance. *Adv. Drug Deliv. Rev.* **47,** 113–131 (2001).
16. Jhaveri, A. M. & Torchilin, V. P. Multifunctional polymeric micelles for delivery of drugs and siRNA. *Front. Pharmacol.* **5,** 1–26 (2014).
17. Torchilin, V. P. Structure and design of polymeric surfactant-based drug delivery systems. *J. Control. Release* **73,** 137–172 (2001).
18. Hu, Q. *et al.* Tailoring the physicochemical properties of core-crosslinked polymeric micelles for pharmaceutical applications. *J. Control. Release* (2016).
19. Mu, C.-F., Xiong, Y., Bai, X., Sheng, Y.-J. & Cui, J. Codelivery of Ponatinib and SAR302503 by Active Bone-Targeted Polymeric Micelles for the Treatment of Therapy-Resistant Chronic Myeloid Leukemia. *Mol. Pharm.* **14,** 274–283 (2017).
20. Talelli, M. *et al.* Core-crosslinked polymeric micelles: Principles, preparation, biomedical applications and clinical translation. *Nano Today* **10,** 93–117 (2015).
21. Fleige, E., Quadir, M. A. & Haag, R. Stimuli-responsive polymeric nanocarriers for the controlled transport of active compounds: Concepts and applications. *Adv. Drug Deliv. Rev.* **64,** 866–884 (2012).

1.7 Stimuli-Responsive Nanocarriers for Delivery of Bone Therapeutics – Barriers and Progresses

Subchapter 1.7.

This subchapter is based on the review article entitled
"*Stimuli-Responsive Nanocarriers for Delivery of Bone Therapeutics – Barriers and Progresses*"
currently under revision in Journal of Controlled Release

Stimuli-Responsive Nanocarriers for Delivery of Bone Therapeutics – Barriers and Progresses

Lavrador, P.[1*], Gaspar, V.M.[1*], and Mano, J.F.[1#]
[1]Department of Chemistry, CICECO – Aveiro Institute of Materials, University of Aveiro, Campus Universitário de Santiago, 3810-193, Aveiro, Portugal

[#]Corresponding author:
João F. Mano
E-mail: jmano@ua.pt

*Authors Contributed Equally

Abstract

The development of stimuli-responsive nanomedicines with tunable cargo release is gathering an increased applicability in bone regeneration and precision biomedicine. Yet, the formulation of nanocarriers that explore skeletal-specific stimuli remains remarkably challenging to materialize due to several endogenous and disease-specific barriers that must be considered during particle design stages. Such anatomo-physiological constrains ultimately hinder nanocarriers bioavailability in target bone tissues and impact the overall therapeutic outcome. This review aims to showcase and critically discuss the hurdles encountered upon responsive nanocarriers delivery in the context of skeletal diseases or tissue regeneration scenarios. Such focus is complemented with an in-depth and up-to-date analysis of advances in the development of stimuli-responsive, bone-focused delivery systems. In a holistic perspective, a deeper knowledge of human osteology combined with advances in materials functionalization via simple precision-chemistry is envisioned to incite the manufacture of stimuli-triggered nanomedicines with more realistic potential for clinical translation.

Keywords: Bone biological barriers, controlled release, drug delivery, nanocarriers, stimuli-responsive

1. Introduction

The continuous improvement in human life-expectancy in the past decades has contributed for an increased incidence of numerous skeletal diseases and age-related bone abnormalities such as osteoporosis, osteoarthritis, osteomyelitis or bone cancer [1]. Regardless of several decades of scientific and medical progress, still no definitive treatment options exist for any of these pathologies [2].

Currently available treatment options for such disorders rely mostly on pharmacological-based therapeutics that are administered under various regimes according to each individuals disease progression status [3]. Despite their recognizable therapeutic benefits, these approaches are still undermined by deleterious side effects that affect patients general health and daily quality of life. This issue is clearly evident for various therapies that are currently employed in the clinics [4]. For example, the administration of FDA-approved recombinant parathyroid hormone (PTH) is limited to severe cases of osteoporosis and for a maximum period of 2 years, owing to the increased risk of developing osteosarcoma as a side effect [5]. Likewise, the oral administration of antiresorptive bisphosphonates has been reported to induce gastric ulcer and osteonecrosis of the jaw [6,7]. In the case of bone diseases that require immediate treatment such as osteosarcoma, the access of systemically administered pharmaceutics to the tumor is also physically hindered due to the existence of a denser osteoid. Such limitation adds on to the common side-effects underlying chemotherapeutics systemic administration [8].

The challenge of administering bioactive molecules to diseased bone tissues lies in attaining an optimal compromise between: (i) pharmacokinetic/pharmacodynamic (PK/PD) parameters, (ii) the administered dose, (iii) the existence of off-target side-effects (e.g. nephrotoxicity, cardiotoxicity, etc), (iv) the overall treatment efficacy and, more importantly, (v) the short or long-term therapeutic outcome.

To overcome such issues, the development of advanced nanosized carriers formulated for delivery of bone therapeutics *via* different administration routes has been extensively explored in the past decade [9–12]. Such nanocarriers have so far been engineered to modify drugs pharmacokinetics to improve their local concentration, whilst reducing unspecific tissue partitioning. Ensuing nanoformulated bone therapeutics bioavailability following minimally IV administration is a crucial parameter to address during pre-clinical design stages, especially considering that some bone sections are poorly perfused and that its highly

hierarchic structure naturally restricts particles access [13]. Numerous *in vitro* and *in vivo* studies highlight the potential of nanocarriers for delivery of bioactive molecules to treat different bone disorders, but so far, very few have managed to actually reach clinical trials. One example is the Phase II trial (NCT03140657 – currently at recruitment stage), which aims to evaluate the use of nanoformulated curcumin for the treatment of patients diagnosed with Ankylosing spondylitis. Other interesting clinical trial focusing on bone regeneration was recently completed in China Medical Hospital (NCT01323894). This study involved the use of stem cells transfected with hydroxyapatite-based nanoparticles as a strategy to improve human mesenchymal/stromal stem cells (hMSCs) osteoblastogenesis. It is important to highlight that both trials employ pristine nanoparticles with no specific selectivity for bone tissue or bone tissue progenitor cells. In fact, as the knowledge on the complexity of bone disease/remodeling dynamics deepens, there is an ever-increasing notion that simply relying on increased drug accumulation in bone tissues and passive diffusion from nanocarriers may not be enough to achieve a selective and clinically significant therapeutic effect [14,15].

The functionalization of nanocarriers with bone targeting moieties is particularly valuable for improving accumulation in bone-specific cells or in dynamic bone-disease scenarios. Among the different molecules explored to date, bisphosphonates, aptamers and peptides (e.g. aspartate-based oligopeptides), have been the most used to functionalize nanocarriers surface and endow them with bone-targeting properties [16–18]. Interestingly, some of these peptides are capable of minimizing particle aggregation in biological media, while others possess inherent osteogenic properties [17,19]. The latter could be interesting to formulate bone nanotherapeutics that take advantage of drug-peptide combination therapies as means to achieve a synergistic osteo-regenerative effect.

Apart from the desirable increase in nanomedicines bone selectivity, the controlled release of therapeutics is also a major aspect that is yet to be fully controlled *in vivo*.

Stimuli responsive nanocarriers have been investigated in the last years as an approach to circumvent the characteristic burst-type release profile of nano-formulated therapeutics or the residual release during parenteral administration. To achieve this control, these so-termed smart delivery systems, can be precisely tailored to respond to internal, external, or physiological triggering conditions as means to promote a fine tuning of bioactive molecules release [20]. Specifically, stimuli-responsive nanocarriers have been engineered to respond to

triggers such as: (i) pH gradients, (ii) redox conditions; (iii) light; (iv) ultrasound (v) magnetic fields; (vi) temperature or (vii) enzymes [20]. The majority of these have significant potential to be used in the context of bone regeneration or skeletal diseases. In fact, the progression of some chronic bone disorders is characterized by changes in the biological microenvironment, resulting in pathophysiological induced shifts (e.g. pH, enzymes, temperature) that can activate nanotherapeutics release.

From this standpoint, this review aims to showcase state-of-the-art stimuli-responsive nanocarriers applied in bone-related therapies, as well as their unique designs and properties. The different biological barriers encountered during nanosized particles systemic delivery is also addressed in a disease-specific mode as this should be a determinant factor during pre-clinical design and testing stages. As an overarching concept the loading of osteo-regenerative/resorptive drugs or bone chemotherapeutics within nanocarriers, combined with the inclusion of sensitive stimuli-responsive linkages should enhance their efficacy while minimizing off-target cytotoxic effects.

2. Biological Barriers to Nanocarrier-mediated Delivery of Bone Therapeutics

Upon parenteral administration, the accumulation of pristine or targeted stimuli-responsive delivery systems in bone is hindered by its unique anatomic structure. In essence, mature bone is a complex calcified tissue primarily composed of: 50-70 % mineral hydroxyapatite (HA), 20 - 40 % collagen matrix, 5-10 % water and 1-5 % lipidic contents [14]. Hierarchically, it consists of: (i) cortical bone, a compact shell with rapid tissue turnover that is comprised of well aligned Haversian systems, also termed Osteons, which run in parallel along the structure, and (ii) cancellous (trabecular) bone, a highly porous core that consists of an intertwined microarchitecture with bone marrow-filled free spaces. Both these structures represent 80 % and 20 % of total bone mass, respectively [21–23]. The Osteon is particularly interesting as it harbors nerves and arterial/venous blood vessels. In this system, Haversian canals run longitudinally and Volkmann canals branch out radially, endowing the entire osteon with an intricate vascular network [24]. The osteon is also comprised by concentric lamellae with embedded osteocytes, interconnected through canaliculi channels with approximately 100 - 300 nm in diameter [25,26]. From a therapeutic perspective such may

be an important size threshold for successful delivery of nanomedicines to osteocyte cells in different disease scenarios.

Since bone is a highly complex and dynamic tissue from both at an anatomical and physiological level, the question arises as how are nanoparticles capable of accumulating within the bone matrix and be internalized in deregulated bone cells.

Recently, several reports have been detailing nanocarriers *in vivo* fate and focusing on major biological barriers or tissue accumulation issues encountered upon parenteral administration [27-29]. However, the barriers encountered upon particles IV administration and during accumulation in bone tissues have been poorly described so far. Such is evident both in the context of non-malignant bone diseases and in bone regeneration scenarios. Having a fundamental knowledge about skeletal anatomo-physiological barriers is paramount to design more effective bone-specific nanotherapeutics.

There are several biological barriers that may hinder nanocarriers delivery via systemic route to different tissues including bone. In an overview, following IV injection, nanotherapeutics must first travel in the bloodstream for sufficient time to promote accumulation in bones, either by probabilistic passive accumulation, or by active targeting to cell-specific moieties. The latter could be achieved by designing nanocarriers targeted to specific bone cell receptors such as Periostin, or neighboring extracellular matrix components (reviewed in detail elsewhere [4,30,31]). To achieve sufficient circulation time for accumulation in the desired tissues, nanocarriers must also be formulated to avoid opsonisation and sequestration by the components of the mononuclear phagocyte system (MPS) including phagocytic cells of the liver (e.g. Kupffer cells), spleen (e.g. Splenocytes), as well as kidney excretion (< ~5 nm) (reviewed in detail in [27]).

Once in the vicinity of skeletal tissues, nanocarriers are transported by the nutrient arteries that penetrate the bone cortex and give rise to cortical capillaries that connect to the medullar vascular capillaries. These capillaries form a dense blood network inside the bone marrow. While vessels in cortical bone are characterized by a continuous lining of endothelial cells with no phago-endocytic activity, the microvascular bed in bone marrow sinusoids possesses phago-endocytic activity and several intercellular gaps often appearing to have an incomplete basement membrane [24,32].

Upon reaching the bone marrow vessels, nanocarriers can then transverse it by extravasating either *via* (i) intercellular gaps (paracellular pathway), or (ii) by phago-endocytic uptake throughout the endothelium (transcellular pathway) [33] (Figure 1).

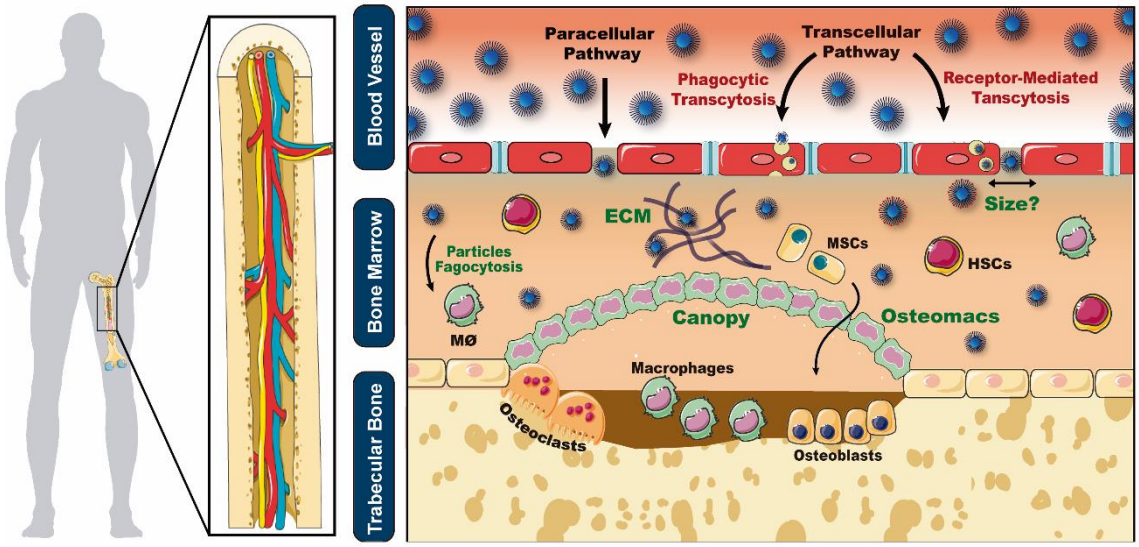

Figure 1. Schematics of nanocarriers biological barriers and routes of extravasation from the sinusoidal vasculature into the extravascular space. Green text represents major barriers to nanocarrier delivery to bone cells (bone marrow ECM, macrophage-mediated phagocytosis, unknown fenestration size, bone canopy and its osteomacs (generally present in bone remodeling/regeneration stages)).

In general, the mechanisms of accumulation across the marrow-blood vessel barrier have been poorly explored so far and further insights on their influence in nanotherapeutics accumulation are necessary for improving their potential.

To better understand and explore nanoparticle accumulation in bone trough the paracellular pathway two main aspects must be discussed. First, the existence of different types of gaps throughout the endothelium of bone marrow capillaries is unclear. In a detailed review performed by Sarin, the bone marrow endothelium is described as non-fenestrated, except when hematopoietic cells are traversing through it and creating transient openings [32]. The author suggests that the primary route of biomacromolecules transport to marrow interstitial space is via phago-endocytic uptake (molecules > 5 nm) and macula occludens inter-endothelial junctions (lipid-insoluble molecules ≤ 5 nm in diameter) [32]. Other reports define bone marrow capillaries as being discontinuous/sinusoidal, with large sinusoidal gaps between endothelium cells, but with no diaphragm [34]. Therefore, it seems that there is some ambiguity regarding the classification of this particular set of capillaries. Providing further

insights on these structures could aid in the design of the next-generation of nanotherapeutics.

The presence of diaphragms and their role in the extravasation of nanoparticles via these intercellular spaces is also not yet clear. The possible presence of diaphragms in marrow fenestrae likely reduces flexibility/permeability and may further constrain therapeutics transport. In comparison with other preferential particle accumulation organs such as the liver, the boundaries of hepatic open fenestrae lack a considerable amount of glycocalyx matrix fibers rendering these fenestrae less restrictive [32]. It is unknown whether this pattern of glycocalyx is similar in marrow fenestrae [32]. Overall, the presence of the diaphragm in fenestrae and adjacent patterning of glycocalyx matrix fibers could play a role in delineating the physiologic upper limit of pore size and affect particles accumulation. The type of capillaries also varies between red (hematopoietic) and yellow (stromal) bone marrow. While vessels in red marrow are characterized by flat reticulum cells with many diaphragmed fenestrations and no basal membrane, in yellow bone marrow the vessels are closed and continuous, akin to those present in other tissues such as the muscle [35]. Interestingly, this may help explain the biodistribution pattern that Sou and coworkers observed after intravenously administration of bone marrow-specific liposomes (216 ± 21 nm) in non-human primates [36]. Besides achieving 70 % of the administered dose accumulated in the bone marrow, these researchers observed that liposomes biodistribution in rhesus monkeys was similar to that of the pattern of red marrow in humans. Because red marrow is highly irrigated with sinusoid capillaries, one can hypothesize that this reflects the importance of sinusoids in nanocarriers bone marrow accumulation.

The second aspect that must be considered in the paracellular accumulation pathway is the exact marrow fenestrae dimension in humans, particularly in non-malignant disease, since this is currently unknown to the best of our knowledge. The reported size fenestrae ranges in the literature are extrapolated from a multitude of studies performed only in animal models and should be updated with robust information from human studies. The existing differences in bone vascular microarchitecture between species may impact the analysis of the biological performance of nanocarriers and impair their successful clinical translation in the long run. In fact, there is a clear disparity between the organization of cortical vascularization in long bones among species, with rodents lacking well-developed Harvesian remodeling systems when compared to larger mammals [37]. This type of remodeling is a

significant source of cortical porosity and age-related bone loss, being thus important for therapeutics delivery in aged individuals [37]. Also, rodent marrow and cortical vasculature are thought to be in series, contrasting with parallel vascular networks in humans [24]. In other species, such as rabbit and marmoset (but not humans), perisinal macrophages populate the marrow stroma adjacent to bone sinus endothelium, often extending cytoplasmic processes into the lumen and monitoring circulation [38]. These perisinal macrophages are an active component of the marrow-blood barrier and play a key role in the uptake of triglyceride-rich macromolecules.

It is important to emphasize that these vascular and cellular barriers are altered in bone-specific diseases including bone cancer/metastasis, inflammation or during bone remodeling/regeneration processes. In bone regeneration scenarios, after transposing blood vessels and entering the marrow stroma/extravascular space nanocarriers encounter a complex bone extracellular matrix that hinders diffusion (Figure 1, ECM). Adding to this, nanotherapeutics need to subsequently overcome phagocytosis by macrophages and unspecific uptake by hematopoietic/mesenchymal stem cells. In bone remodeling areas and regeneration scenarios nanocarriers also need to overcome osteomac-based cellular canopy isolating bone remodeling pockets from marrow compartments and get internalized for example by target osteoblasts (Figure 1, canopy) *via* the various cellular uptake pathways (reviewed in detail by Hillaireau and co-workers [39]). All these events depend on the dynamics of bone blood perfusion as it will be discussed.

2.1. Influence of Bone Physiological Blood Flow on Nanocarriers Accumulation

Skeletal perfusion is a fundamental parameter following nanocarriers parenteral administration and influences bone therapeutics accumulation dynamics. Interestingly, the values of blood flow vary significantly amongst different skeletal regions. For instance, trabecular bone experiences approximately 4-fold increased blood perfusion when compared to cortical bone [25]. This vascular diversity should result in different exposures to nanocarriers. Several pathological conditions have been associated with impaired blood flow and subsequent bone loss, such as osteonecrosis, postmenopausal-osteoporosis (in both women and ovariectomized mice) and glucocorticoid-induced osteoporosis, which may be linked with increased conversion of the more vascularized red marrow to yellow marrow

[37,40,41]. The vessels in fatty bone marrow are closed and less vascularized than those of the red marrow [42], such can limit nanoparticle extravasation. Patients suffering from myelodysplastic syndromes also present an abnormal expansion of sinusoidal compartments. Nanotherapeutics could potentially benefit from facilitated access across the bone-marrow barrier in these scenarios akin to what is normally proposed by the enhanced permeability and retention (EPR) effect in cancer [43]. However, the latter should be addressed carefully as this phenomenon is quite variable from patient to patient and its true impact in therapeutics accumulation is yet to be fully elucidated in a clinical setting [44,45]. Strategies to augment the EPR through vascular modulators (e.g. nitric oxide, bradykinin [46]) have been investigated so far for cancer with some promising pre-clinical *in vivo* data [47]. To the best of our knowledge such has not been explored for other bone disorders that could benefit from this strategy. One can postulate that dynamic studies addressing this may provide important insights to increase the performance of disease-specific nanocarriers.

A recent study performed by Ramasamy and co-workers is one of the few that investigated the fundaments of blood flow dynamics in bone by using *in vivo* fluorescence intravital imaging. The reported results indicate that blood velocity in type H capillaries is about 6-fold higher than that of sinusoidal type L vessels (Figure 2) [41].

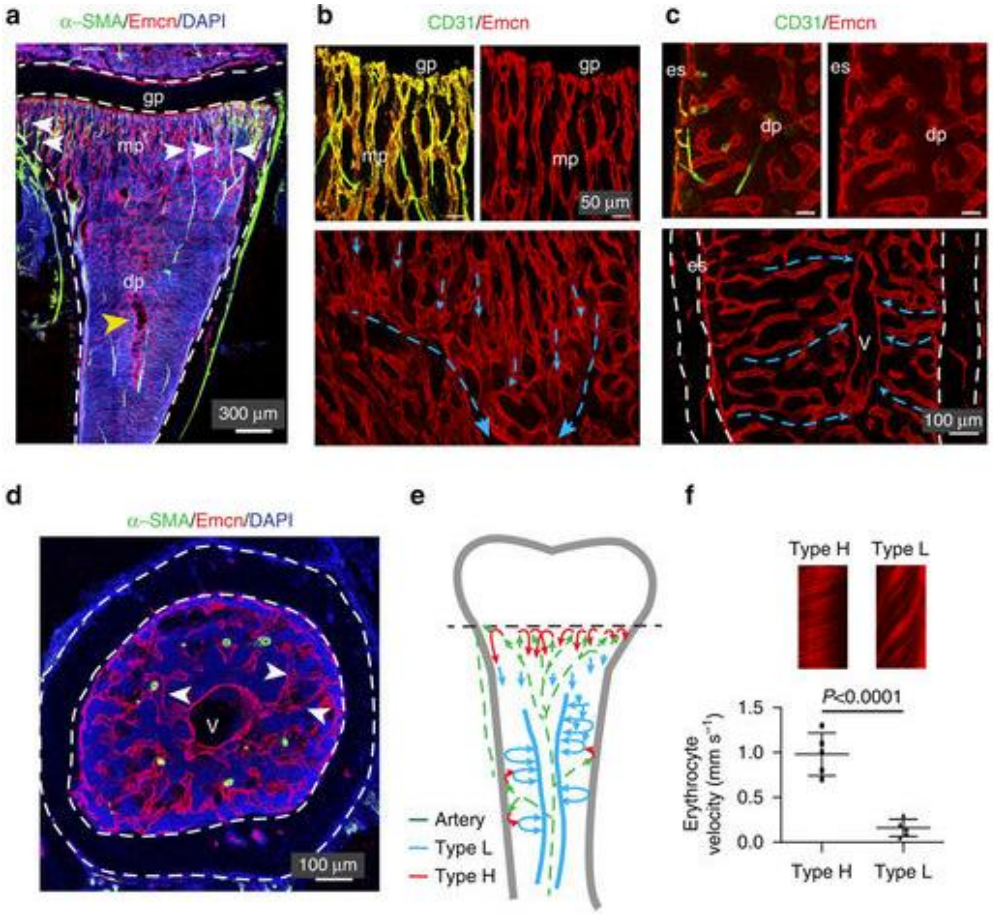

Figure 2. Fluorescence microscopy imaging of 4-week-old tibial C57BL/6J mice vasculature. **(A)** Immunostaining of smooth muscle actin containing arteries (α-SMA positive cells, green channel), Endomucin (Emcn, red channel) and cell nuclei (DAPI, blue channel). mp-represents metaphyseal plate; gp- represents growth plate. White arrows indicate α-SMA cells connection to metaphyseal H-type vessels. **(B, C)** Confocal images proximal to the growth plate (b, top panel) or to diaphysis (c, top). CD31+ and Emcn-arteries terminate in type H vessels in metaphysis (CD31+ and Emcn+) and endosteum (es). No interaction with L-type vessels in diaphysis was observed. Blue arrows indicate blood flow from metaphyseal vessel columns **(B)** and endosteum **(C)**, respectively. **(D)** Transversal tibial sections where sinusoidal L-type vessels (arrowheads) connect to the large central vein (v). Dashed lines represent compact bone. From these images it is clear that CD31+ Emnc-arteries containing multiple smooth muscle cells cross the diaphysis. **(E)** Schematics of arterial (green arrows), H-type (red arrows) and sinusoidal/venous blood flow (blue arrows) of murin long bones. **(F)** Erythrocytes velocity data demonstrating the differences between type H and type L vessels. Adapted from [41] under Creative Commons Attribution 4.0 International License.

Considering that osteoporosis and aging diminish bone perfusion, associated with the reduction of type H capillaries, these aspects must be taken into consideration during particles pre-clinical design and investigation of optimal dose/treatment regime. Age-induced increase in vascular stiffness and calcification of muscle vessels has also shown to

contribute to an impaired vascular function in humans [48]. Such is corroborated by ultrasound doppler data that indicates a 30 % lower femoral artery blood flow in aged human male patients (average of 64 years) in comparison with those of young men in their mid-twenties [49]. It is therefore clear that bone vascular complexity and the blood-marrow interface pose significant barriers for nanotherapeutics delivery. To overcome these barriers various particles physicochemical parameters should be optimized, including surface charge, shape and size. The latter is one of the most important aspects that needs to be considered to improve therapeutics pharmacokinetics and performance in the bone blood-marrow microenvironment.

2.2. Nanocarriers Size-dependent Bone Accumulation

Regarding nanocarriers size-dependent bone accumulation there are some literature reports that suggest optimal bone delivery for nanocarriers under 80 nm, motivated by the detailed work of Howlett and co-workers on avian tibia microstructures[50]. It is important to emphasize that up-to-date there is a scarcity in human and non-human primate studies regarding this topic [50]. Considering the disparity between the physiological upper limit of pore size in human hepatic sinusoids (180 nm) versus rodents (280 nm), one could expect that bone microvasculature could also be slightly different across mammals [32]. In fact, differences between avian and mammalian erythropoiesis could convey important differences in the organization of the bone sinusoids traversing the marrow. In mammals, erythropoiesis is extravascular, whereas in birds is intravascular and involves no marrow-blood barrier [51]. More studies on the ultrastructure of bone microvasculature across species are necessary to shed light into the optimal design of nanocarriers.

The size of rabbit bone marrow fenestrae was reported to range from 85 nm to 150 nm [52]. This is supported by the work of Porter and colleagues, that studied the accumulation of poloxamer 407-coated polystyrene particles (sizes of 60, 150 and 250 nm) in rabbit femoral bone marrow [53]. The obtained results indicate that nanoparticles with sizes of 150 nm and below, effectively avoided liver and spleen clearance and were predominantly located within bone marrow sinus endothelial cells after 24 h. Such was evident by the formation of dense bodies consisting of particle clusters. Importantly, in this study no evidence of transcytosis to the marrow extravascular space was observed [53]. However, it was also not clear if the 250 nm nanoparticles were not efficiently accumulated in bone due to size limitations of the nanocarrier or due to increased MPS uptake in spleen and liver, as these particles had less

density of stealth polymer coating when compared to smaller formulations. Bone marrow targeting by these poloxamer 407-coated nanoparticles is a phenomenon reportedly only in rabbit-based animal models [38]. This observation is not related to the exclusive perisinal macrophage population present in rabbit marrow, because the authors claimed that these macrophages were unable to interact with the poloxamer particles, perhaps due to the steric barrier provided by the hydrophilic moieties of poloxamer-407. Not only does this emphasizes the key role of nanocarrier composition in marrow uptake, but reinforces the differences between different animal models. Conversely, non-targeted liposomal formulations of several sizes (136 - 318 nm) were unable to significantly accumulate in rabbit bone marrow in a biodistribution study following IV administration [52]. Another study performed by Mann and colleagues exploited the unique expression of E-selectin in bone marrow endothelium by using nanoparticle-loaded, E-selectin functionalized, porous silica microcarriers administrated intravenously in mice [54]. Remarkably, the targeted microparticles (~1.6 µm) were capable of delivering Paclitaxel-loaded nanoliposomes (25 - 35 nm) within bone marrow endothelium, as demonstrated by fluorescence microscopy analysis [54]. Some studies also suggest that nanocarrier dosage could play a role in bone marrow uptake. When administering liposomal dosages above 50 mg/kg in rabbits, the bone marrow appears to be the first tissue to become saturated, followed by increased uptake in the liver and spleen [52]. These reports further highlight the importance of fully characterizing nanocarriers surface chemistry and targeting moieties type and density; since these parameters play key roles in the outcomes of biodistribution studies [55,56]. Ideally, it is important to also evaluate nanocarriers protein 'hard' and 'soft' corona and its influence in *in vivo* particles targeting performance [34]. The sole functionalization of stimuli-responsive nanocarriers with osteotropic bone moieties may not confer bone selectivity if the bound protein corona temporarily or permanently shields these linkers, as it was already observed for transferrin functionalized nanoparticles [57,58].

On this topic, some emerging imaging technologies could prove useful in clarifying nanocarriers bone accumulation. Sun and his team developed a bone imaging toolkit containing several clinically relevant fluorescent probes, which could be useful for further investigation of bone physio-pharmacology (Figure 3A) [59]. Using a different strategy, Peck and colleagues exploited synthavidin technology to design highly biocompatible pre-assembled probes with affinity for high turnover living bone regions [60]. Notably this probe

maintained high stability even after 24 h past administration (Figure 3B). The probe does suffer from squaraine self-quenching in aqueous solutions, but binding to bone surfaces inhibits this effect, an exciting observation that may be useful in the future for improving signal/noise ratio (Figure 3C).

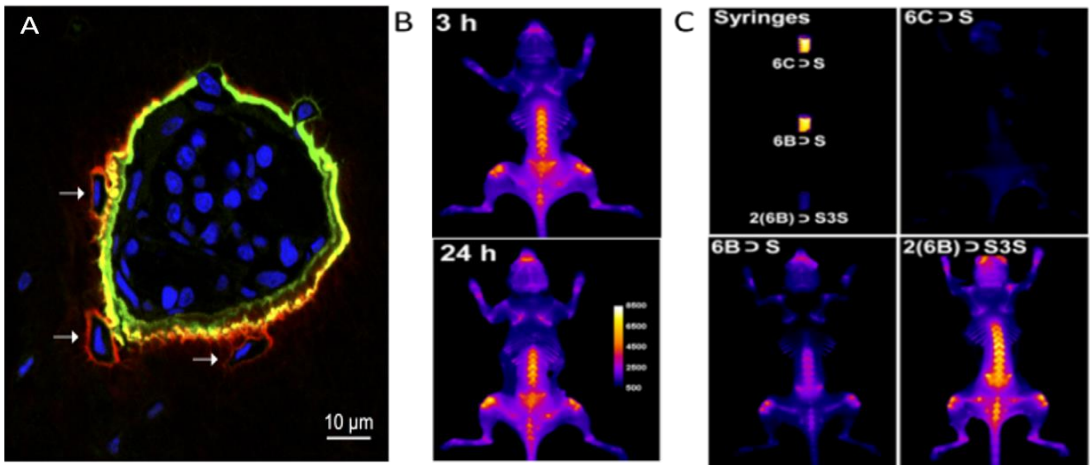

Figure 3. Advanced bone imaging technologies. (A) Pocket of bone marrow surrounded by fluorescently labelled bone matrix (red - low HA affinity probe; green - high HA affinity probe) with DAPI (blue) stained nuclei. Adapted from [59] with permission from the American Chemical Society. (B) Evidence of probe high stability on living mice skeleton. (C) Fluorescence enhancement caused by probe unfolding when binding to bone. Adapted from [60] with permission from the American Chemical Society.

The advances in disease-specific imaging and cell tracking techniques in bone tissues are expected to contribute for a more robust pre-clinical validation of nanotherapeutics. These techniques will be particularly valuable to follow the release of drugs and biomacromolecules from stimuli-responsive nanocarriers in complex *in vivo* environments. Such follow-up remains a challenging aspect in the assessment of smart delivery systems biological performance. In the following section, we will present and discuss up-to-date reports on stimuli-sensitive nanocarriers that exploit different stimuli in an attempt to achieve a therapeutically relevant release of bioactive molecules.

3. Stimuli-responsive Nanocarriers for the Delivery of Bioactive Molecules to Bone Tissues

Bone is one of the most dynamic tissues being in constant adsorption/remodeling during lifetime. Naturally, a myriad of biomolecular cues and hotspot microenvironments render bone an interesting organ in which to explore stimuli-responsive delivery at both homeostatic or pathological scenarios. The latter is particularly interesting since during the

onset and progression of different bone disorders many of skeletal microenvironment hallmarks and cellular functions become profoundly deregulated. Each of these disease-specific features represent unique barriers, but also unique opportunities for nanocarrier-mediated stimuli-responsive release of therapeutics. To date several types of non-responsive nanocarriers have been explored for bone therapeutics delivery, reviewed in detail elsewhere [30]. Yet, the majority is unable to achieve a realistic spatiotemporally controlled release of their payload at the target site. This is observed for various types of cargo including small molecule drugs, nucleic acids or proteins (e.g. bone morphogenetic proteins).

In general, there are several interesting biological characteristics within bone tissues and alterations found in different skeletal pathologies that can been exploited for stimuli-responsive delivery of bone therapeutics (Figure 4).

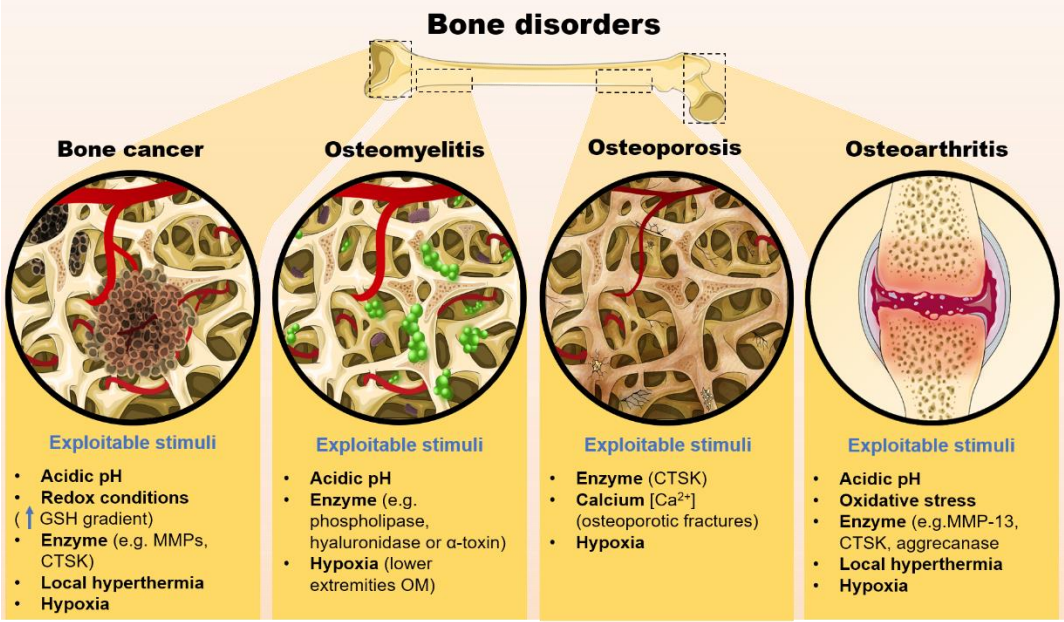

Figure 4. Schematics of different stimuli that can be explored to promote the release of therapeutics from nanocarriers engineered for different bone-specific disorders.

In the context of bone regeneration scenarios, the existence of specific enzymes involved in the bone remodeling process, such as cathepsin K (CTSK), certain matrix metalloproteinases (e.g. MMPs -2, -9, -13, -14 and -16), vacuolar H^+ ATPase (an osteoclastic enzyme that contains a unique 116-kD subunit which may also be exploited for specific targeting), are valuable triggers to be exploited. Tartrate-resistant acid phosphatase (TRAP), normally present within the bone milieu is also an interesting endogenous target for stimuli-responsive delivery [1,61,62].

On the other hand, certain bone disorders are characterized by specific biological modifications in the bone vicinity that could trigger cargo release. For example, an hallmark of osteomyelitis is the reduction in local pH due to bacterial infection [63]. On the other hand, in osteoarthritis there is a slight localized temperature increase (~2.0 – 3 ºC), due to joint inflammation [64]. In osteolytic cancer there is a markedly decreased pH due to exaggerated osteoclastic activity that can be explored as trigger, amongst other more common exploitations in cancers such as redox-based stimuli within the tumor microenvironment [65,66]. In this context, the following subchapters highlight the different strategies currently being explored for the design of stimuli-responsive nanocarriers aimed to be used for different bone disorders.

3.1 Enzyme-responsive Nanocarriers

Enzyme-responsive nanocarriers take advantage of intrinsic enzymatic activity at the target tissues. Such stimuli can be explored in certain pathologies or during tissue remodeling/repair where enzyme activity can be upregulated, thus making it an interesting biological trigger to promote the release of bioactive molecules from nanocarriers at specific sites [20]. Typically, the most commonly explored instances of enzyme-responsive delivery take advantage of altered expression profiles of proteases, phospholipases and oxireductases underlying various scenarios such as wound healing, infectious pathogens, neurodegeneration, diabetes or tumor invasion [67]. Particularly in the bone milieu, CTSK is one of the most valuable enzyme-based stimulus to be explored.

CTSK production is associated with the bone remodeling dynamics, particularly bone catabolism. In this process, osteoclasts (multinucleated cells responsible for resorbing bone), are localized within the resorption lacunae, an acidic sealed area (pH ~4), where these cells release CTSK and HCl to digest the collagenous organic matrix and HA crystals, respectively. Apart from osteoclast-mediated expression, breast cancer skeletal metastases are also known to overexpress this specific proteinase [68]. Also, CTSK expression has been reported in fibrotic lung tissues [69]. Hence during pre-clinical analysis of CTSK-responsive nanocarriers aimed for bone therapies, one should take into consideration possible unspecific particle accumulation in these organs and undesired drug release. Directing CTSK-responsive particles to target skeletal tissues is therefore crucial to maximize their efficacy and reduce side-effects.

Various researchers have explored the incorporation of specific peptides as CTSK-cleavable linkers in the design of stimuli-responsive nanocarriers for delivery to osteoclastic bone resorbing zones, including those occurring in osteoporosis.

Peptide sequences that are CTSK substrates such as the GGP-Nle, GGGMGPSGPWGGK and HPGGPQ have been extensively employed for enzyme-responsive delivery in various studies [70–72]. Clearly, there are immediately two ways to exploit this cleavage-dependent delivery: (i) incorporating sensitive moieties in polymeric nanocarrier backbone, eliciting its disruption upon enzyme exposure; (ii) or attaching the drug to the nanocarrier through CTSK sensitive linkers, prompting drug release from nanoparticles via enzyme cleavage. The latter approach has been used with success in a study by Pan and co-workers which showed the induction of bone formation *in vivo* in ovariectomized Sprague-Dawley rats after administration of prostaglandin E_1 attached to a Asp_8-HPMA copolymer via a CTSK-sensitive oligopeptide sequence (GGP-Nle) [70]. Also, a particularly elegant approach by Wang and co-workers exploited the CTSK-mediated cleavage to increase the cellular uptake of charge shifting nanocarriers and improve chemotherapeutics delivery to bone metastasis [72]. In this study, PEG and poly(trimethylene carbonate) diblock copolymer (PEG-b-PTMC) were synthesized via ring-opening polymerization of trimethylene carbonate (TMC) and then PEG blocks were functionalized with a chimeric peptide, prior to doxorubicin (DOX) anti-cancer drug loading. This multifunctional peptide consisted of three components: i) the exposed anionic aspartate repetitions (Asp_8), responsible for bone targeting; ii) the CTSK substrate (HPGGPQ) sequence linking the two adjacent domains; and iii) the cationic residue linked to the surface of the diblock copolymer, responsible for increasing cellular uptake upon CSTK-cleavage (Figure 5). This hybrid biomaterial was able to self-assemble into micelles in aqueous solution via dialysis under mild conditions (size: 75 ± 10 nm, ζ-potential −18.5 ± 1.9 mV).

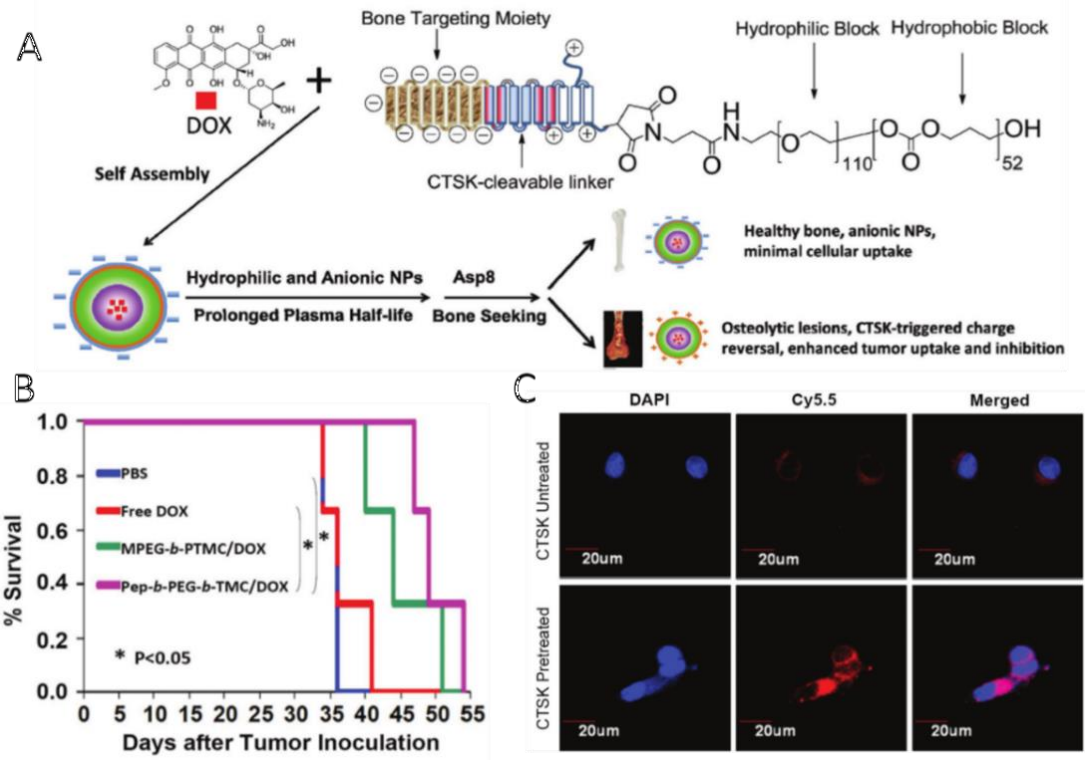

Figure 5. Mechanism of action of CTSK-triggered charge reversal micelles for targeted *in vivo* bone metastasis treatment. Kaplan–Meier survival curves of mice following tumor injection and treatment. Adapted from [72] with permission from Royal Society of Chemistry.

The negatively charged micelles then experience a charge-reversal upon reaching osteolytic lesion sites overexpressing CTSK, due to enzymatic cleavage of the anionic block, which exposes the cationic moiety and triggers a charge reversal from negative to positive (-18.5 mV to +15.2 mV), markedly increasing *in vitro* cellular uptake in MCF-7 breast cancer cells after 30 min incubation with CTSK, when compared to absence of CTSK conditions (Figure 5C). Interestingly, following IV injection, these enzyme-sensitive PMs prolonged the survival of 4TGM1 mice bearing bone metastatic myeloma in comparison to free DOX and non-responsive formulations. In addition, serum IgG 2b levels were the lowest for the CTSK-responsive nanomicelles, which correlates with reduced tumor burden across all controls.

Another enzyme-based trigger mechanism that can be explored relies on extracellular matrix-degrading enzymes, specifically matrix metalloproteinases (MMPs). These zinc-dependent proteinases are actively implicated in bone remodeling and are also involved in bone cancer dissemination via degradation of the extracellular matrix [73]. Osteoclasts are known to express various MMPs including MMP-14, MMP-12 and MMP-9 [74], while

osteoblasts are reported to express MMP-13 [75]. Regarding MMP-9, some reports describe the formulation of smart nanocarriers endowed with MMP-9 sensitivity, however these are yet to be applied for bone-specific delivery [76,77]. Since MMP-9 is highly expressed in regenerating bone tissues (e.g. upon fracture), the stimuli-responsive carriers could enhance bone regeneration when loaded with appropriate osteoinductive/pro-regenerative factors [78]. In the context of bone malignancies, Liu and his team developed MMP-7-sensitive photodynamic molecular beacons that achieved tumor reduction in a vertebral model of osteolytic bone metastasis [79].

Hyaluronic acid-based nanocarriers may also be explored for stimuli-responsive release in a disease-specific mode since hyaluronidase is present in some bone disorders. This enzyme is secreted by *Staphylococcus aureus*, a bacteria that is the responsible pathogen for osteomyelitis. The infectious microenvironment of osteomyelitis is characterized by a marked reduction in local pH, as well as the local presence of specific glycosidases, phosphatases, lipases and toxins, all inherent to the excessive proliferation of infecting bacteria [63,80]. To treat this disease, Baier and co-workers developed biocompatible hyaluronic acid-based nanocapsules (size: 320 nm, ζ-potential: -17 mV) carrying polyhexanide, a known antimicrobial agent. The obtained results indicate that enzyme-responsive formulations had significantly lower minimal inhibitory concentration against *S. aureus and methicillin resistant S. aureus* (ATCC 29213 and 43300) when compared to non-hyaluronidase degradable nanocarriers [81]. As evidenced by Baier, taking advantage of microorganisms hyaluronidase secretion to trigger the release of encapsulated antibiotics is a valuable strategy to eradicate bacterial infections not only in bone but also in other tissues.

Despite being valuable examples, more information regarding the kinetics of enzymes under/over-expression in each patient and at each disease progression stage is necessary. Adding to this, fundamental *in vitro* studies regarding the efficacy of enzyme-based release at very low colony forming units (CFUs) should also be addressed, as the quantity of produced enzymes could be insufficient to prompt bioactive molecules release. Such research is envisioned to aid in the determination of the optimal enzyme-sensitive nanocarriers administration regime and the adaptation of therapy to each patient and bacterial strain in a more personalized mode.

3.2 Thermo-responsive Nanocarriers

Thermo-responsive nanocarriers frequently comprise a thermolabile moiety such as the extensively explored material poly(N-isopropyl acrylamide) (PNIPAM) or temperature-sensitive lipids such as dipalmitoyl phosphatidylcholine and lysolipids [20,33]. Temperature sensitivity is correlated with materials ability to change their properties with temperature, often in a nonlinear and sharp mode. The low critical solution temperature (LCST) of different materials used for nanocarriers assembly is as key parameter to tailor the temperature-mediated release profile of these delivery systems. Owing to their biological characteristics, healthy humans have thermoregulatory mechanisms that guarantee constant body temperature over time. However, some pathophysiological scenarios, including inflammation and tumors are characterized by higher temperatures than healthy tissues [82]. This thermal difference between cancer and normal tissues has been extensively explored for developing thermo-responsive nanocarriers with application in cancer treatment, as shown below. However, because not all tumors behave equally in locally increased temperature this selective delivery could be further improved by externally heating the tumor site either through ultrasound, alternating magnetic fields or temperature-controlled water sacks [20,33]. Yet, we should carefully address the validity of such approaches in the context of tumors, since the overexpression of heat-shock proteins (e.g. Hsp-70, Hsp-90 [83]) may further contribute for cells thermal resistance along time and counteract the cytotoxic effect of released chemotherapeutics. Some combinatorial strategies for silencing HSPs and releasing cytotoxic drugs have been under development to circumvent this resistance mechanism [84].

For the particular case of bone tissues, Staruch and co-workers were able to achieve magnetic resonance imaging (MRI)-guided drug deposition in bone through the administration of thermo-responsive liposomes containing DOX (ThermoDox®) [85]. Focused ultrasound heating after liposomal administration in New Zealand white rabbits resulted in 8.2 and 16.8-fold increased DOX concentration in bone marrow and bone adjacent muscles, respectively, in comparison with non-heated tissues. On a similar note, Song and colleagues developed thermo-responsive pamidronate (PA)-functionalized liposomes containing DOX for treatment of bone tumor metastases [86]. These liposomes exhibited a strong binding affinity to hydroxyapatite and a complete release of DOX was observed within 10 min at 42 ºC. Blank liposomes showed relatively low cytotoxicity to A549 cells, regardless of PA-functionalization. However, it is important to underline that in this study, the heating effect

on cell viability with blank liposomes was not explored. For DOX concentrations over 5 μM, PA-functionalized liposomes clearly showed higher cytotoxicity than non-targeted liposomes. Pre-heating PA-coated liposomes at 42 ºC prior to *in vitro* administration induced higher cytotoxicity than the same formulation at 37 ºC, validating the superior therapeutic effect of the thermo-sensitive liposomes.

Apart from increased temperature in bone cancers, other bone diseases such as osteoarthritis present at late stages significant joint inflammation, resulting in a mild increase on local temperature [64]. Such environment can also be exploited with thermo-responsive nanocarriers for improving therapeutics spatiotemporal delivery and the overall therapeutic outcome. Current studies on osteoarthritis, such as that of Poh and colleagues exploit (N,N′-bis(acryloyl)cystamine) disulfide crosslinked, PEGylated poly(N-isopropylacrylamide-2-acrylamido-2-methyl-1-propanesulfonate) nanoparticles (NGPEGSS) to load the anti-inflammatory peptide KAFAK (size: 223 ± 9.7 nm, ζ-potential: -3.81 ± 2.01 mV). Particles formulation was promoted through temperature and disulfide crosslinking assembly, while drug loading was achieved through passive diffusion below the LCST. Such particles then rely on intracellular stimuli (pH and redox) for therapeutics spatiotemporally controlled release [87]. In the context of bone disorders, the KAFAK peptide delivery is promising for osteoarthritis due to its suppression of TNF-α and IL-6 production. Despite being already an interesting system, the performance of these nanocarriers could be further improved by external heating so as to enhance the delivery at intended joints or inflamed areas in the knee [88]. In addition, it is well known that osteoarthritis progression is related with increased oxidative stress. For example, previously reported citrate-based thermo-responsive nanocarriers with intrinsic antioxidant properties could be used in the future to improve osteoarthritis treatment [89].

From the available body of literature, it is clear that there are still significant challenges to be overcome in the development of bone-specific thermo-responsive nanocarriers to achieve maximum therapeutic efficacy *in vivo*. This is particularly challenging for scenarios where there is no significant increase of internal temperature, thus requiring external heating as stimuli. In this context, one of the most important aspects is the ability to assure an externally focused heating to bone disease sites without affecting neighboring healthy tissues.

3.3 Ultrasound-responsive Nanocarriers

Ultrasound is based on the use of low or high intensity acoustic energy and is widely used in clinic for non-invasive biomedical imaging [90]. Ultrasound-responsive systems have been widely explored for delivery of bioactive therapeutics, typically by exploiting liposomal and micellar nanocarrier [91]. In the context of drug delivery, this external stimulus induces cavitation microbubble contrast agents (small gas bubbles) loaded within nanocarriers hydrophobic reservoirs. The incidence of ultrasound leads to expansion and ultimately can fragment carriers structure.

Echogenic liposomes have been previously designed to allow multiple stimuli-responsiveness and enhance the release of bioactive molecules. Nahire and co-workers developed MMP-9 responsive echogenic liposomes comprised of 1-palmitoyl-2-oleoyl- sn-glycero-3-phosphocholine with a triple-helical lipopeptide (size: 190 ± 35 nm) [92]. In this study, an increased payload release from liposomes upon simultaneous application of diagnostic-used ultrasound frequency (3 MHz) was obtained. More recently, Crasto and his team developed PEGylated liposomes (size: 145 ± 20 nm) that released recombinant human BMP-2 (rhBMP-2) upon ultrasound exposure (1 MHz) (Figure 6) [93]. By using this strategy, the researchers were able to increase localized bone matrix formation in a Swiss Webster mice muscle pouch model, representing the first *in vivo* validation of ultrasound-triggered delivery of rhBMP-2 and consequently have issued a patent on this technology [94].

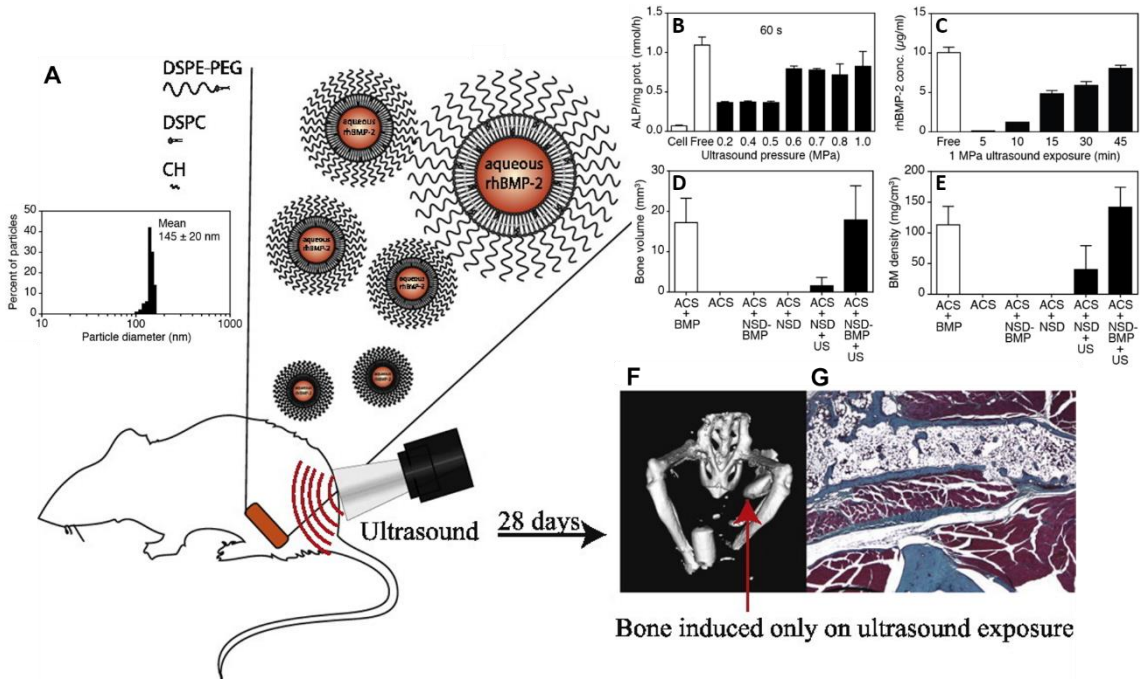

Figure 6. Ultrasound-responsive liposomes characterization. **(A)** Dynamic light scattering analysis of PEGylated nanoliposomes loaded with rhBMP-2; **(B)** ALP assay in C2C12 cell line following rhBMP-2 released from from nanoparticles for sonodisruptable delivery containing rhBMP-2 (NSD-BMP) exposed to increasing ultrasound pressures for 60 s (N=3, *n*=2); Free refers to an assayed amount of soluble rhBMP-2 predicted to be contained within NSD-BMP-2 of the same sample size. **(C)** Evaluation of ultrasound exposure in rhBMP-2 release profile, i.e, ultrasound duration dependence of rhBMP-2 release from NSD-BMP in phantom tissue (5 – 45 min at 1 MPa), quantified by ELISA (N=3, n=2); **(D)** Bone volume data acquired from µCT; ACS + BMP, standard rhBMP-2 implant (no ultrasound), ACS, implant sponge only (no rhBMP-2, no ultrasound), ACS + NSD- BMP, NSD-BMP nanocomplexes with rhBMP-2 payload applied to ACS implant (no ultrasound), ACS + NSD, nanoparticles without rhBMP-2 payload, on ACS implant (no ultrasound), ACS + NSD + US, nanoparticles without rhBMP-2 payload, on ACS implant (ultrasound applied 24 h after implantation surgery), ACS + NSD-BMP + US, nanocomplexes with rhBMP-2 payload applied to ACS implant (ultrasound applied 24 h after implantation surgery) **(E)** Bone mineral density analysis of different formulations. ACS – represents collagen implant. NSD – PEGylated nanoliposomes; NSD-BMP- PEGylated nanoliposomes loaded with rhBMP-2. US- ultrasound (applied 24 h following surgery). **(F)** µCT reconstruction, group subjected to ultrasound exposure. This induced bone formation by using the ACS+NSD-BMP formulation. **(G)** Masson's trichrome staining of perifemoral section showing the extent of bone induction by using ACS implant with NSD-BMP formulations and administering ultrasound 24 h post-surgery. Adapted from [93] with permission from Elsevier.

Despite achieving promising results, it must be emphasized that this study involved liposome impregnation within a collagen sponge, a delivery route that is invasive and may entail further surgery associated problems. Apart from standard ultrasound stimulation, low intensity pulsed ultrasound stimulation (LIPUS) is also valuable in the scope of bone disorders with recent reports from different researchers emphasizing the ability to enhance bone regeneration during fracture healing and callus distraction [95]. In addition to its pro-osteogenic potential, Nagao and his team recently investigated the anti-inflammatory effects of LIPUS on MC3T3-E1 mouse calvarial cell line, where it was discovered that LIPUS was able to suppress the nuclear translocation of NF-kB activation induced by lipopolysaccharide, while also inhibiting the upregulation of toll-like receptor 4 and inflammatory cytokine IL-1 [96]. Moreover, this effect was found to be mediated by an increased expression of mechanosensitive angiotensin receptor type I upon LIPUS application. We thus hypothesize that this stimulus could potentially be used in the future as a tool to treat inflammatory bone diseases such as periodontitis or osteoarthritis. Combining LIPUS with ultrasound-responsive nanocarriers, could be a valuable strategy to design a stimuli-responsive nanomedicine-based therapeutic approach where not only drug release

could be spatiotemporally controlled, but also where the triggering stimuli itself has therapeutic activity. Despite being a promising approach for the future it should be taken into account that LIPUS potential for bone therapy may vary with a multitude of factors, ranging from medical history of previous treatments, site of application, type of fracture or nature of bone loss, treatment regime and patients age [97].

3.4 Magnetic-responsive Nanocarriers

Magnetic-responsive nanoparticles respond to magnetic fields and find application in various areas including bioimaging namely through MRI and as guidance systems that allow cell or particle magnetic guidance. In this approach, magnetic forces are used to move nanocarriers towards the intended anatomical sites [20]. Then, the locally increased drug concentration due to nanocarrier retention is expected to translate into sustained doses released within the therapeutic window. However, this strategy is always dependent on the passive release of therapeutics from carriers. Moreover, because this guidance requires a localized magnetic force, this approach is not very promising for the treatment of systemic bone disorders such as osteoporosis, that logically require a widespread delivery to bone tissues. Nevertheless, magnetic delivery systems may be valuable to direct chemotherapeutics toward target osteosarcoma tumor hotspots and achieve localized malignant cells ablation [98]. In the context of bone regeneration particles can be directed to localized defects such as fractures and be used to deliver bioactive molecules that prompt regeneration and the development of fully functional tissue [99]. The design of magnetic-responsive drug release by nanocarriers is of uttermost importance and highly desirable to control the therapeutic effect overtime. Magnetic-responsive nanocarriers span beyond the scope of simply being magnetically guided, since external alternating magnetic fields (AMFs) can be used to disrupt their colloidal structure, thus providing the possibility to spatiotemporally control drug release in an on-demand mode [100].

An extensive literature analysis revealed that so far only cationic magnetic liposomes were explored for magnetic on-demand drug delivery in bone, namely in mouse and hamster osteosarcoma models, both with successful outcomes [101,102]. These examples take advantage of magnetically induced temperature increase. Typically, the diffusion of loaded drugs from liposomal carriers core increases with bilayer permeability, which in turn is generally dictated by lipids melting temperature (T_m). The value of T_m can be tailored depending on the lipid composition, and by tuning the high-frequency AMF pulses. This promotes lipid

bilayer disruption by surpassing the intrinsic T_m and thereby prompts cargo release [103,104]. Despite being an attractive design, the application of these smart-release systems in bone regeneration or other bone disorders is still scarce when compared to its use in cancer therapy, where there are numerous studies upholding its potential. This could be due to bone characteristic anatomic location since its localized deep within the body, constituting a major biophysical barrier that is responsible for a rapid drop in magnetic field strength with increasing depth. Moreover, the before mentioned intertwining bone vasculature poses a major barrier in nanocarriers guidance [105]. To overcome the former barrier, recently, a magnetic spatial localization strategy has been developed in which magnetic field density can be focused at a distance from the pole. This may overcome magnetic attenuation and be used for both magnetic guidance and on-demand magnetic-mediated therapeutics release [106].

3.5 pH-responsive Nanocarriers

Therapeutics delivery from nanocarriers via pH stimuli can be explored mainly in two different modes. The first one involves the design of a nanocarriers with a pH-sensitive release profile resulting from existence of carboxylic acids or amines (including tertiary amines) within the nanocarrier backbone/structure [14,107]. Changes in the medium pH then results in different protonation/deprotonation states of these ionizable groups and to a shift in nanocarriers properties. This behavior can thus be explored for spatiotemporally controlled delivery of entrapped drugs within polymeric nanocarriers in specific microenvironments. The second alternative involves drug attachment to pH-sensitive moieties such as polyketals, acetals or hydrazide linkers that act as anchoring spots for binding the drug to the nanocarrier until pH-mediated hydrolysis occurs [10,90,108].

To date nanocarriers pH-sensitivity has been mainly explored for cancer therapy due to the characteristic acidic pH in tumors microenvironment (pH 6.5 - 7.2) [109,110]. The characteristic acidic tumor microenvironment is further accentuated in osteolytic cancers (e.g. bone Ewing's sarcoma) due to an excessive osteoclastic activity that acts in concert with cancer cells to further contribute to bone tumors acidity [66]. Owing to these exploitable characteristics it becomes clear why a significant body of literature involves the development of pH-responsive carriers for cancer therapy. On this topic, some interesting multifunctional pH-responsive delivery systems have been recently developed. Ferreira and colleagues prepared alendronate-coated liposomes for pH-responsive release of DOX in female nude BALB/c mice bearing bone metastases established through injection of MDA-MB-231

breast cancer cells on mice tibia [111]. The presence of 1,2-dioleoylglycero-3-phosphatidylethanolamine (DOPE) and cholesteryl hemisuccinate (CHEMS) lipids endowed the liposome with pH sensitivity, whereas alendronate-targeting moiety was responsible for nanocarriers active binding to hydroxyapatite. The liposome sizes ranged from 150 to 185 nm and exhibited a sharp DOX release at pH = 5 when compared to pH = 7.4, highlighting the pH-responsiveness of the formulation. Furthermore, encapsulated DOX maintained its cytotoxicity with a significant dose-dependent effect against the MDA-MB-231 cell line, while also markedly reducing drug cardiac uptake. Biodistribution studies indicated a 4-fold increase in chemotherapeutics accumulation in tumor tissues when compared to that of the free drug.

In a different approach, Wang and his team developed biodegradable and pH-responsive selenium-doped hydroxyapatite nanoparticles (Se-HANs) for the treatment of osteosarcoma (Figure 7A) [112]. These rod-shaped HANs (size: 78.55 ± 0.20 nm, ζ-potential of -37.13 ± 0.63 mV) elicited 4 to 5-fold increase in selenium release under acidic conditions (pH = 5) when compared to that obtained at physiological conditions (Figure 7B). As evidenced by FITC-labeled nanocarriers the amount of encapsulated selenium significantly affected Se-HANs degradation in the lysosome, with higher selenium content resulting in a faster, pH-mediated degradation. *In vitro* results in human MNNG/HOS osteosarcoma cells, showed that the 10 % Se-HANs formulation had the highest cytotoxic effect on osteosarcoma cells, with their administration resulting in 83 % cell death after 18 h. This cytotoxic activity was found to be associated with the intracellular generation of reactive oxygen species (ROS) mediated by the selenium cargo. More importantly, Se-HANs induced tumor apoptosis and reduced systemic toxicity *in vivo*, in a BALB/c nude mice osteosarcoma model. Following nanocarriers intratumoral administration 2- and 3-fold reduction in tumor weight and volume was obtained. Additionally, serum biochemical analysis of nanocarrier injected mice found that 10 % Se-HANs had the lowest systemic toxicity when compared to a mixture of equal selenium content (HANs / 16 mM Na_2SeO_3), suggesting a controlled release profile at local tumor and reduced leakage at normal tissues. However, further studies involving nanocarriers parenteral delivery could be performed to fully characterize the biological performance of these carriers.

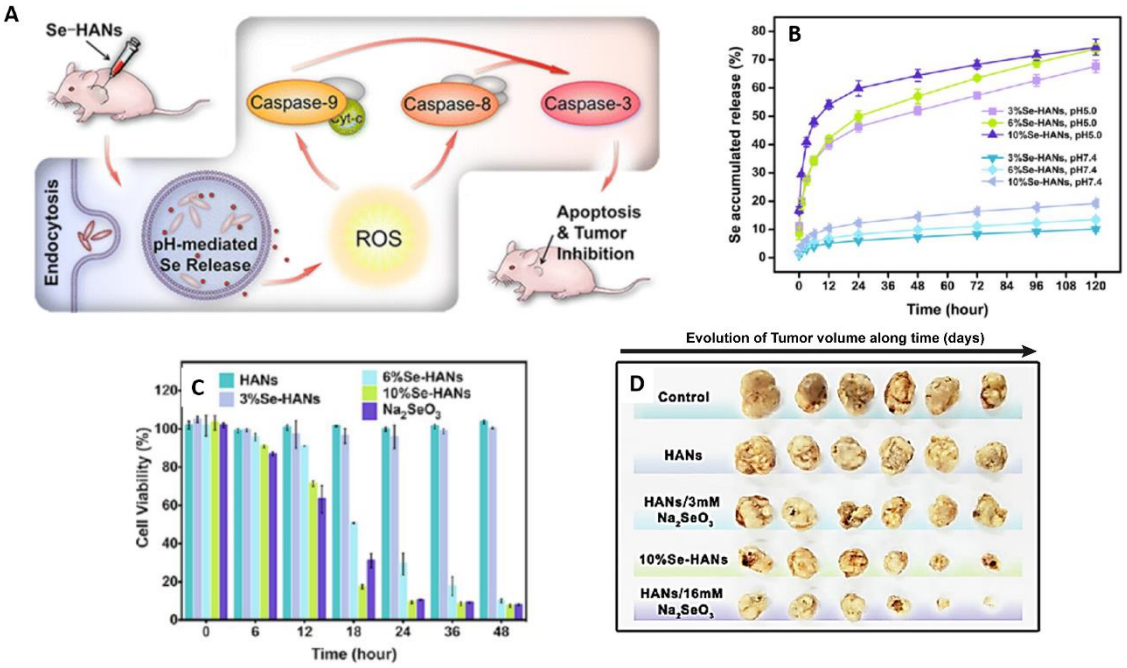

Figure 7. (A) *In vivo* treatment of mice-bearing osteosarcoma with pH-responsive release of Se-HANs. Internalized Se-HANs by nonspecific endocytosis are rapidly degraded in acidic lysosomes to release selenium. **(B)** Selenium release from Se-HANs exhibited a pH-responsive release profile at pH = 5.0 versus pH = 7.4. **(C)** CCK-8 assay of MNNG/HOS osteosarcoma cells showed that viability was highly associated with selenium content and degradation of Se-HANs. **(D)** *In vivo* evaluation of anti-osteosarcoma activity of Se-HANs after intratumoral injection on a xenograft osteosarcoma model. Compounds with higher selenium content, including 10 %Se-HANs and HANs/16 mM Na_2SeO_3 exhibited efficient inhibition of tumor growth as evidenced by the reduction of tumor size (left). Adapted from [112] with permission from the American Chemical Society.

Exploring pH-responsiveness to elicit improved nanocarrier cytotoxicity may also be valuable for bone therapy, particularly in bone cancer. Alpaslan and colleagues showcased the potential of dextran-coated cerium oxide nanoparticles (nanoceria) (size: 45 nm (pH = 7) and 29 nm (pH = 6), ζ-potential: 16.68 ± 3.98 mV (pH = 6)), which exhibit antioxidant activity at physiological pH values, but shifts to an oxidizing profile at slightly acidic pH conditions [113]. These nanoceria allow for a selective increase in ROS generation in osteosarcoma microenvironment. In this study, nanoceria particles incubated at pH = 6 showed maximum cytotoxicity against osteosarcoma MG-63 cells. In healthy osteoblasts *in vitro* cultures (pH = 6), no significant ROS generation was observed at any nanoceria concentration, thus confirming the proposed ROS-dependent cancer-killing mechanism. After 5 days at pH = 6, the osteosarcoma IC50 value was found to be 100 µg/mL, as opposed to 500 µg/mL for normal osteoblasts [113]. In addition, nanoceria particles maintain their

selective cancer-killing effect even at physiological pH, being observed that after a 5-day treatment, the IC50 values for healthy osteoblasts were well above 1000 µg/mL, in contrast with IC50 values of 250 µg/mL for MG-63 osteosarcoma cells.

In the context of tissue engineering and regenerative medicine, Gan and co-workers developed pH-responsive chitosan-capped MCM-41 mesoporous silica nanoparticles (Chi-MSNs) (size: 130 nm, ζ-potential: +22.5 mV) for delivery of BMP-2 and Dexamethasone (Dex) to enhance bone regeneration (Figure 8) [114]. Chitosan (Chi) functionalization of MSNs surface endowed the nanocarrier with pH-responsiveness due Chi primary amine protonation states at different pH (pKa ~ 6.5). In this sense Chi functioned as a nanovalve for controlled release of MCM-41 mesopores-loaded Dex upon intracellular uptake. Dex release followed a pH-responsive behavior, achieving 85 % release within 60 min at pH = 6.0, while almost no Dex was released at physiological pH conditions (pH = 7.4). In addition, the outer chitosan layer also functioned as matrix for BMP-2 incorporation, with results showing that BMP-2 release profile is unaffected by the culture medium pH, resulting in an immediate release under physiological conditions (80 % BMP-2 release after 6 h). On one hand, this is beneficial as BMP-2 requires binding to specific cell-surface receptors, but on the other hand, because BMPs have low bioavailability, this release profile is not the most adequate for systemic administration, which is why the authors opted for the implantation with Gelfoam® (absorbable gelatin sponge). Nevertheless, this nanocarrier has shown particular promise in promoting *in vitro* osteogenesis, with the combinatorial effect of Dex/BMP-2 dual-loaded chi-MSNs exhibiting significantly higher ALP activity of rat bone mesenchymal stem cells (BM-MSCs) than single Dex or BMP-2 MSNs loaded formulations. Moreover, Alizarin Red S staining further confirmed that bone marrow mesenchymal stromal/stem cells (BM-MSCs) incubated with Dex/BMP-2@chi-MSNs have greater mineralization nodules when compared to controls. The *in vivo* osteogenic capacity of this formulation was evaluated via ectopic bone formation in a male mice thigh muscle pouch model. By using 3D µCT analysis the authors demonstrate that after 4 weeks there is an increase in tissue mineral density of both dual-loaded formulations when compared to the free therapeutics control groups.

Even though such nanovehicle has not been formulated for minimally invasive IV administration, this example highlights the potential of pH-responsive delivery of

pharmaceuticals for bone regeneration, an area where parenteral routes of administration have been poorly explored so far.

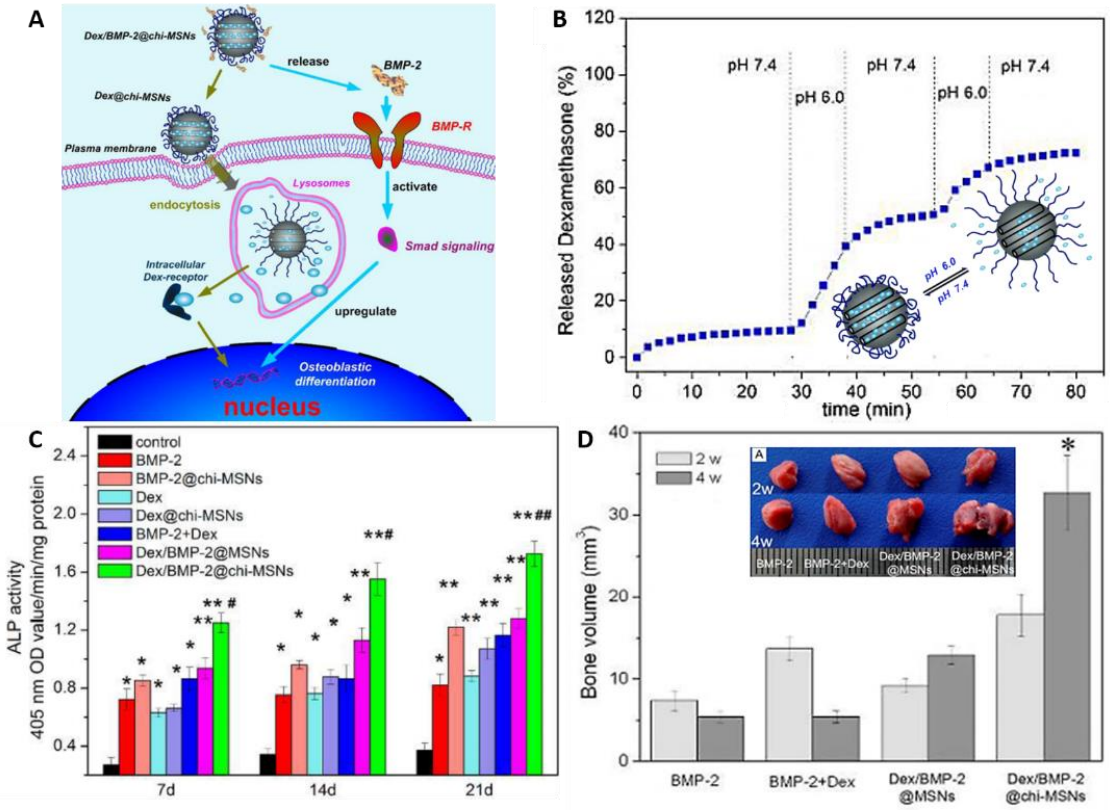

Figure 8. Physicochemical characterization and biological performance of silica-based pH-responsive nanocarriers. **(A)** Schematic diagram of Dex/BMP-2@chi-MSNs on osteoblast differentiation. First, BMP-2 is quickly released and then activates the downstream Smad signaling by binding to specific cell surface BMP receptors. Secondly, Dex is delivered intracellularly through a pH-responsive release within lysosomes. **(B)** The capping effect of chitosan in the pH-responsive release of Dex from chi-MSNs. **(C)** Effect of different nanocarriers formulations BM-MSCs ALP activity cultured **(D)** *In vivo* ectopic bone formation induced by BMP-2 and Dex with different implants after 2 and 4 weeks post-implantation. Quantitative analysis of regenerated bone volume from 3D μCT images. Adapted from [114] with reprint permission from Royal Society of Chemistry.

Apart from the former examples, there are also other bone disorders for which pH-responsive nanocarriers could be valuable as on-demand delivery systems. In osteomyelitis, the production of acid by osteoclasts and infecting bacteria metabolism tends to reduce pH in the site of inflammation [63]. Such acidic environment, could allow for selective release of bioactive molecules (e.g. antibiotics) in the affected bone milieu.

To treat bone bacterial infections Ferreira and co-workers developed a pH-responsive liposomal theranostic platform (DOPE, CHEMS, PEG2K-DSPE) containing technetium-

99m-labeled ceftizoxime, a 3rd generation cephalosporin antibiotic. The liposomal carriers (size: 169.1 ± 8.4 nm, ζ potential: 2.2 ± 1.1 mV) were able to accumulate in bone infected *foci* in a male Wistar rat model of acute osteomyelitis following IV administration [115]. These liposomes undergo structural destabilization in acidic medium, locally releasing the radiotracer and thereby allowing accurate infection imaging and treatment. The obtained results indicate that radioactivity level in the infected tibia was 1.5-fold higher than in healthy tibia. Although this study demonstrated the positive effect of such theranostic liposomes, from the perspective of clinical application the use of radiotracers could entail some restrictions due to their known toxicity. With the advent of multimodal imaging technologies and non-radioactive probes such concept could be further investigated.

More recently, alendronate-coated PEG-poly(lactic acid-co-glycolic acid) (PLGA) micelles targeted to were used for bone-targeted delivery of the antibiotic vancomycin [116]. These micellar carriers showed faster vancomycin release profiles at pH = 5.0 when compared to that obtained under physiological conditions. Interestingly, the binding affinity to HA was unaffected by external pH and therefore these micelles may constitute a suitable nanocarrier for stimuli-responsive treatment of osteomyelitis. However, it is important to emphasize that for early stage osteomyelitis, the acidic environment may not be sufficient to be used as a drug release trigger, thus limiting drugs therapeutic efficacy before disease progression.

Such could be overcome by engineering highly sensitive pH-responsive systems as those recently developed by Sethuraman and co-workers. These researchers produced a two component pH-mediated charge-shifting nanocarrier comprised by: (i) PLA-b-PEG diblock co-polymers conjugated to TAT cell penetrating peptide and (ii) pH-sensitive diblock copolymer poly(L-cystine bisamide-g-sulfadiazine)-b-PEG (PCBS23K-b-PEG5K) [117]. At physiological pH, sulfadiazine is negatively charged and shields the TAT-micelle by electrostatic interactions. Upon a decrease in pH, sulfadiazine becomes neutral and detaches from the TAT-micelle, exposing TAT for interaction with nearby cells, while the PCBS moiety is degraded by glutathione (GSH). This PMs markedly enhanced DOX cytotoxicity within 0.2 pH units below of pH 7.2 [117]. This remarkably sensitive block may be an interesting design tweak for improving stimuli sensitivity during the initial onset of osteomyelitis.

3.6 Redox-responsive Nanocarriers

Redox sensitive nanocarriers are very interesting due to their ability to respond to oxidative-reductive environments including those dependent on GSH, thioredoxin, or human serum albumin (HAS-SH) concentration [118,119]. Redox-responsive nanocarriers are designed to disassemble in the cytosol and release their bioactive cargo. Such is an important aspect for skeletal disorders considering that some bioactive therapeutics for bone cells have intracellular molecular targets [14,120]. Human cells intracellular compartments contain a high GSH concentration (2-10 mM), which is about 10^3-fold higher than that found in the extracellular matrix and blood plasma (2-20 μM) [121]. However, some studies suggest that reductive conditions may already be present at the endosome during receptor-mediated endocytosis [122]. This difference in redox-potential inside cells is typically exploited by designing nanocarriers containing reduction-sensitive linkers that are cleaved upon cellular uptake, thus releasing cargo only in intracellular conditions. The disulfide bond is the most commonly used redox-sensitive linker. However, the library of redox-responsible chemical modifications that can be imprinted in nanocarriers structure is increasing with other responsive moieties such as diseleinide, ditellurium [123] and maleimide-arylthiol bonds gaining increased attention in recent years [124,125]. Such chemical imprinting of redox-responsive moieties in nanocarriers structure can be achieved by three main ways: (i) grafting of bioreducible linkers on the repeating monomers of polymeric backbones, which readily prompt nanocarrier intracellular disintegration; (ii) grafting disulfide bonds as terminal crosslinkers between different polymer blocks in copolymer-based nanocarriers, that can lead to micelles disassembly [125] and (iii) precision chemical modification of polymer monomeric units with redox-responsive moieties linked to drugs (polymer-drug conjugate), which upon the stimulus are promptly released. These strategies have been extensively used for formulation of redox-responsive PMs for delivery of pharmaceutics under redox-conditions, either through core or shell disulfide-based crosslinking, which can greatly improve PMs stability [126]. However, it is important to emphasize few redox-responsive carriers have been used for the treatment of bone diseases other than cancer.

For treatment of osteosarcoma, Maciel and colleagues designed a facile method for preparing redox-responsive alginate nanogels by crosslinking with cystamine through mini-emulsion [127]. Then, cytotoxic drug loading was achieved by incorporating DOX in aqueous solution with nanogels, resulting in high encapsulation efficiency (95.2 ± 4.7%). These

biocompatible nanogels significantly increased DOX intracellular concentration and enhanced cytotoxicity in osteosarcoma cells (CAL-72). Another interesting approach for bone cancer is that proposed by Yao and co-workers which designed glutathione-responsive self-assembled micelles (size: 169.8 nm, ζ-potential: +20.23 mV) based on disulfide crosslinked stearyl cationic polypeptide copolymers containing arginine and histidine for co-delivery of DOX and microRNA-34a to androgen-independent prostate cancer cells both *in vitro* and *in vivo* [128]. These micelles reduced anthracycline cardiotoxicity and promoted a synergistic anti-tumoral effect upon drug-gene co-delivery (DOX/microRNA-34a). In particular, because microRNA-34a has shown an important role in myeloid and bone-related cancers (namely myeloma, leukemia, osteosarcoma and Ewing's sarcoma), it might be interesting to pursue further studies in bone with these micelles [129].

For the treatment of osteoarthritis other researchers developed PEGylated poly(N-isopropylacrylamide-2-acrylamido-2-methyl-1-propanesulfonate) nanoparticles with a disulfide crosslinker (N, N'-bis(acryloyl)cystamine) (NGPEGSS)) for delivery of the anti-inflammatory peptide KAFAK to an *ex vivo* model [130]. These disulfide nanocarriers exhibited enhanced extracellular stability and improved KAFAK loading, as well as enhanced release under reducing conditions. Strikingly, they selectively infiltrate inflamed cartilage and were internalized by chondrocytes, which are recognized as a hard to transfect cell type. The KAFAK-loaded NGPEGSS nanoparticles were able to significantly decrease cytokine IL-6 production over time both in chondrocytes and macrophages, demonstrating its potential to act as an intra-articular injected nanocarrier for the treatment of osteoarthritis [87,130].

It is without doubt that the unique reversibility and responsiveness of disulfide linkages as a ubiquitous stimulus contributed to the engineering of redox-responsive nanocarriers with efficient on-demand release of therapeutics for various bone diseases. Yet, to fulfil their potential for clinical translation some aspects such as the effect of cell surface thiols in their cellular uptake and intracellular trafficking of such carriers should be further investigated and optimized [121].

5. Conclusion and Perspectives

From an-in-depth analysis of available literature reports focusing on stimuli-responsive nanocarriers it is clear that their overwhelming majority aims for bone cancer treatment and takes advantage of cancer-specific stimuli (e.g. redox, pH, temperature). The motivation for

such focus stems mostly from tumors increasing prevalence, but also from the relative understanding of their major hallmarks and microvasculature [55,82,110,131,132].

Apart from this pathology, non-regenerating acute bone injuries (e.g. critical size fractures), bone diseases (e.g. osteomyelitis, osteoporosis) and joint degeneration problems (e.g. osteoarthritis) are increasing in incidence and the development of more effective treatments tailored for these disorders is evermore required in a clinical setting. However, the translation of stimuli-responsive nanocarriers into clinical practice remains highly challenging.

To date, few stimuli-responsive nanocarriers reached clinical stages across all areas, an aspect that is particularly evident for bone disorders. This could be in part assigned to insufficient nanocarriers bioavailability and selectivity to bone tissues. But can be mainly attributed to our poor understanding of more fundamental aspects regarding the unique biological barriers posed by the skeletal architecture. An increased information of how intravenously administered nanocarriers can reach bone tissues and what optimal characteristics in terms of size, shape, surface charge and blood stability they should possess is fundamental and should receive a renewed focus. Intravenous administration is in fact highly attractive when compared to localized delivery via micro- or macro-sized implants, that while interesting for some bone disorders, do not warrant enough coverage to reach every bone tissue in a similar manner [10], a major aspect in osteoporosis. Furthermore, the procedures for implant introduction are costly, laborious and highly invasive, not to mention the possible complications or infections arising from surgery.

In a critical perspective, it is clear that a stimuli-mediated control over therapeutics release provides significant advances over the current shortcomings regarding premature leakage and burst release, yet, future generations of responsive carriers must be rationally engineered. Achieving a balance between complexity and biological performance is an underlying issue in the drug delivery field since the trend in the past years has been to develop perhaps overengineered stimuli-responsive multifunctional carriers in detriment of more simple systems as recently emphasized [133]. Such trend could be restrictive in the context of cost-effectiveness and realistic industrial production.

Yet, the design of more complex, multifunctional carriers could have an added benefit in the context of bone pathologies/injuries that feature more than one physicochemical/biochemical features as compared with healthy bone. Hence, the

manufacture of dual/multi-stimuli responsive systems (pH+temperatute, pH+redox, light+pH, etc) could offer synergistic non-linear responses that could enhance the therapeutic outcome of such nanobiomaterials [134]. Envisioning future advances, the next-generation of such systems could combine also physical and morphological properties such as shape, topography and mechanical properties which are known to influence cellular behavior and carriers biological performance [135].

Alongside with this, in the design of multifunctional carriers aimed for parenteral delivery different strategies other than the widely used PEGylation as shielding mechanism should be encouraged and pursued, particularly following the myriad of recent reports highlighting some pitfalls in such approach [136]. In fact, with the latest developments regarding alternatives to endow nanocarriers with stealth character we will for sure assist to the proposal of smarter nanocarriers for systemic bone treatments. However, parallel efforts should be done in order to comply with regulatory guidelines to seriously consider the final application of such systems.

We envision that having an open mindset on these fundamental challenges could contribute for the formulation of responsive nanocarriers with more potential for future commercialization and realistic clinical application.

References

[1] G.A. Rodan, T.J. Martin, Therapeutic Approaches to Bone Diseases, *Science*. **289,** 1508–1514 (2000).

[2] W. Gu, C. Wu, J. Chen, Y. Xiao, Nanotechnology in the targeted drug delivery for bone diseases and bone regeneration, *Int. J. Nanomedicine.* **8,** 2305–2317 (2013).

[3] E. Feurer, R. Chapurlat, Emerging drugs for osteoporosis, *Expert Opin. Emerg. Drugs*. **19,** 385–395 (2014).

[4] E.J. Carbone, K. Rajpura, B.N. Allen, E. Cheng, B.D. Ulery, K.W.H. Lo, Osteotropic nanoscale drug delivery systems based on small molecule bone-targeting moieties, *Nanomedicine Nanotechnology, Biol. Med.* **13,** 37–47 (2017).

[5] J.L. Vahle, M. Sato, G.G. Long, J.K. Young, P.C. Francis, J. a Engelhardt, M.S. Westmore, Y. Linda, J.B. Nold, Skeletal changes in rats given daily subcutaneous injections of recombinant human parathyroid hormone (1-34) for 2 years and relevance to human safety. *Toxicol. Pathol*. **30,** 312–321 (2002).

[6] J.B. Nase, J.B. Suzuki, Osteonecrosis of the jaw and oral bisphosphonate treatment, *J.Am.Dent.Assoc*. **137,** 1115–1119 (2006).

[7] D.Y. Graham, What the gastroenterologist should know about the gastrointestinal safety profiles of bisphosphonates, *Dig. Dis. Sci*. **47,** 1665–1678 (2002).

[8] A. Luetke, P.A. Meyers, I. Lewis, H. Juergens, Osteosarcoma treatment - Where do we stand? A state of the art review, *Cancer Treat. Rev*. **40,** 523–532 (2014).

[9] M. Farokhi, F. Mottaghitalab, M.A. Shokrgozar, K.L. Ou, C. Mao, H. Hosseinkhani, Importance of dual delivery systems for bone tissue engineering, *J. Control. Release*. **225,** 152–169 (2016).

[10] M.R. Newman, D.S.W. Benoit, Local and targeted drug delivery for bone regeneration, *Curr. Opin. Biotechnol.* **40,** 125–132 (2016).

[11] E.R. Balmayor, Targeted delivery as key for the success of small osteoinductive molecules, *Adv. Drug Deliv. Rev*. **94,** 13–27 (2015).

[12] Y.-H. Kim, Y. Tabata, Dual-controlled release system of drugs for bone regeneration, *Adv. Drug Deliv. Rev.* **94,** 28–40 (2015).

[13] G. Basha, M. Ordobadi, W.R. Scott, A. Cottle, Y. Liu, H. Wang, P.R. Cullis, Lipid Nanoparticle Delivery of siRNA to Osteocytes Leads to Effective Silencing of SOST and Inhibition of Sclerostin In Vivo, Mol. *Ther. Acids*. **5,** e363 (2016).

[14] I.S. Alencastre, D.M. Sousa, C.J. Alves, L. Leitão, E. Neto, P. Aguiar, M. Lamghari, Delivery of pharmaceutics to bone: Nanotechnologies, high-throughput processing and in silico mathematical models, *Eur. Cells Mater*. **31,** 355–381 (2016).

[15] L. Yang, T.J. Webster, Nanotechnology controlled drug delivery for treating bone diseases., *Expert Opin. Drug Deliv*. **6,** 851–864 (2009).

[16] H. Hirabayashi, J. Fujisaki, Bone-Specific Drug Delivery Systems Approaches via Chemical Modification of Bone-Seeking Agents, *Clin. Pharmacokinet*. **42,** 1319–1330 (2003).

[17] K. Aoki, N. Alles, N. Soysa, K. Ohya, Peptide-based delivery to bone, *Adv. Drug Deliv. Rev*. **64,** 1220–1238 (2012).

[18] L. Dang, J. Liu, F. Li, L. Wang, D. Li, B. Guo, X. He, F. Jiang, C. Liang, B. Liu, S. Badshah, B. He, J. Lu, C. Lu, A. Lu, G. Zhang, Targeted Delivery Systems for Molecular Therapy in Skeletal Disorders, *Int. J. Mol. Sci*. **17,** 428 (2016).

[19] A.K. Nowinski, A.D. White, A.J. Keefe, S. Jiang, Biologically inspired stealth peptide-capped gold nanoparticles, *Langmuir*. **30,** 1864–1870 (2014).

[20] S. Mura, J. Nicolas, P. Couvreur, Stimuli-responsive nanocarriers for drug delivery, *Nat. Mater*. **12,** 991–1003 (2013).

[21] H. Yi, F. Ur Rehman, C. Zhao, B. Liu, N. He, Recent advances in nano scaffolds for bone repair, *Bone Res*. **4,** 16050 (2016).

[22] C.W. Cheng, L.D. Solorio, E. Alsberg, Decellularized tissue and cell-derived extracellular matrices as scaffolds for orthopaedic tissue engineering, *Biotechnol. Adv*. **32,** 462–484 (2014).

[23] B. Clarke, Normal Bone Anatomy and Physiology, *Clin. J. Am. Soc. Nephrol*. **3,** (2008) S131–S139.

[24] S.C. Cowin, L. Cardoso, Blood and interstitial flow in the hierarchical pore space architecture of bone tissue, *J. Biomech*. **48,** 842–854 (2015).

[25] I. McCarthy, The physiology of bone blood flow: a review., *J. Bone Joint Surg. Am*. **88–A,** 4–9 (2006).

[26] S.C. Cowin, G. Gailani, M. Benalla, Hierarchical poroelasticity: movement of interstitial fluid between porosity levels in bones., *Philos. Trans. A. Math. Phys. Eng. Sci*. **367,** 3401–3444 (2009).

[27] E. Blanco, H. Shen, M. Ferrari, Principles of nanoparticle design for overcoming biological barriers to drug delivery., *Nat. Biotechnol*. **33,** 941–951 (2015).

[28] S.M. Kim, P.H. Faix, J.E. Schnitzer, Overcoming key biological barriers to cancer drug delivery and efficacy, *J. Control. Release*. (2017).

[29] M. Moros, S.G. Mitchell, V. Grazu, The fate of nanocarriers as nanomedicines in vivo: important considerations and biological barriers to overcome, *Curr. Med. Chem*. **20,** 2759–2778 (2013).

[30] H. Cheng, A. Chawla, Y. Yang, Y. Li, J. Zhang, H.L. Jang, A. Khademhosseini, Development of nanomaterials for bone-targeted drug delivery, *Drug Discov. Today*. **22,** (9) (2017).

[31] T. Cobo, C.G. Viloria, L. Solares, T. Fontanil, E. González-Chamorro, F. De Carlos, J. Cobo, S. Cal, A.J. Obaya, Role of periostin in adhesion and migration of bone remodeling cells, *PLoS One*. **11,** 1–19 (2016).

[32] H. Sarin, Physiologic upper limits of pore size of different blood capillary types and another perspective on the dual pore theory of microvascular permeability, *J. Angiogenes. Res*. **2,** 1–19 (2010).

[33] V.P. Torchilin, Multifunctional, stimuli-sensitive nanoparticulate systems for drug delivery., *Nat. Rev. Drug Discov.* **13,** 813–827 (2014).

[34] M.I. Setyawati, C.Y. Tay, D. Docter, R.H. Stauber, D.T. Leong, Understanding and exploiting nanoparticles' intimacy with the blood vessel and blood., Chem. Soc. Rev. **44,** 8174–8199 (2015).

[35] E.A. Williams, R.H. Fitzgerald Jr., P.J. Kelly, 8 - Microcirculation of Bone A2 - Mortillaro, Nicholas A. BT - The Physiology and Pharmacology of the Microcirculation, in: Physiol. Pharmacol. Microcirc., Academic Press. 267–323 (1984).

[36] K. Sou, B. Goins, M.M. Leland, E. Tsuchida, W.T. Phillips, Bone marrow-targeted liposomal carriers: a feasibility study in nonhuman primates., *Nanomedicine (Lond).* **5,** 41–49 (2010).

[37] M.-H. Lafage-Proust, B. Roche, M. Langer, D. Cleret, A. Vanden Bossche, T. Olivier, L. Vico, Assessment of bone vascularization and its role in bone remodeling., *Bonekey Rep*. **4,** 662 (2015).

[38] S.M. Moghimi, Exploiting bone marrow microvascular structure for drug delivery and future therapies, *Adv. Drug Deliv. Rev*. **17,** 61–73 (1995).

[39] H. Hillaireau, P. Couvreur, Nanocarriers' entry into the cell: relevance to drug delivery, *Cell. Mol. Life Sci*. **66,** 2873–2896 (2009).

[40] R.S. Weinstein, Glucocorticoid-Induced Osteoporosis and Osteonecrosis, *Endocrinol. Metab. Clin. North Am*. **41,** 595–611 (2012).

[41] S.K. Ramasamy, A.P. Kusumbe, M. Schiller, D. Zeuschner, M.G. Bixel, C. Milia, J. Gamrekelashvili, A. Limbourg, A. Medvinsky, M.M. Santoro, F.P. Limbourg, R.H. Adams, G. Karsenty, E.F. Wagner, H.M. Kronenberg, Y. Wang, I. Eshkar-Oren, H.P. Gerber, C. Maes, C. Maes, A.P. Kusumbe, S.K. Ramasamy, R.H. Adams, S.K. Ramasamy, A.P. Kusumbe, L. Wang, R.H. Adams, H. Xie, R.H. Adams, K. Alitalo, M. Potente, H. Gerhardt, P. Carmeliet, M. Hellstrom, I.B. Lobov, J. Ridgway, S. Suchting, S. Nicoli, K. Yashiro, H. Shiratori, H. Hamada, M.A. Gimbrone, J.N. Topper, T. Nagel, K.R. Anderson, G. Garcia-Cardena, K.J. Whitehead, M.C. Smith, D.Y. Li, I. McCarthy, M.T. Vogt, J.A. Cauley, L.H. Kuller, M.C. Nevitt, D.A. Hanley, T. Atsumi, Y. Kuroki, J. Trueta, C. Wan, R.E. Tomlinson, M.J. Silva, A. Limbourg, F.C. Seifert, M. Banker, B. Lane, U. Bagge, C.E. Anagnostopoulos, D.T. Nash, K. Tanaka, P. Carmeliet, F. De Smet, S. Loges, M. Mazzone, L.K. Phng, H. Gerhardt, D.E. Conway, E. Tzima, G.S. Duncan, R. Benedito, H. Han, K. Tanigaki, T. Honjo, A.P. Kusumbe, R.D. Prisby, L.C. Murtaugh, B.Z. Stanger, K.M. Kwan, D.A. Melton, J.D. Hoeck, M.T. Drake, B.L. Clarke, S. Khosla, L.I. Plotkin, M. Acar, P.E. Boulais, P.S. Frenette, Y. Kunisaki, S.J. Morrison, D.T. Scadden, C. Maes, S. Stegen, N. van Gastel, G. Carmeliet, A.D. Berendsen, B.R. Olsen, J. Klein-Nulend, A.D. Bakker, R.G. Bacabac, A. Vatsa, S. Weinbaum, E. Kozhemyakina, A.B. Lassar, E. Zelzer, N. Ohashi, A.G. Robling, D.B. Burr, C.H. Turner, I. Noguera-Troise, A.F. Siekmann, N.D. Lawson, M. Corada, M.F. Morini, E. Dejana, J.E. Fish, J.D. Wythe, S. Obi, D. Morrow, J.P. Cullen, P.A. Cahill, E.M. Redmond, E.D. Jahnsen, O. Watson, I.B. Lobov, A.C. Chang, P.A. Murphy, I. MacIntyre, S. Imai, Y. Matsusue, M.J. Hilton, F. Engin, P. Liu, G. Marotti, H.J. Snippert, Y. Wang, M.A. Serrat, Blood flow controls bone vascular function and osteogenesis, *Nat. Commun*. **7,** 13601 (2016).

[42] J.F. Griffith, D.K. Yeung, P.H. Tsang, K.C. Choi, T.C. Kwok, A.T. Ahuja, K.S. Leung, P.C. Leung, Compromised Bone Marrow Perfusion in Osteoporosis, *J. Bone Miner. Res*. **23,** 1068–1075 (2008).

[43] M.D. Ewalt, D. Gratzinger, Selective quantitation of microvessel density reveals sinusoidal expansion in myelodysplastic syndromes, *Leuk. Lymphoma*. **57,** 2923–2926 (2016).

[44] H. Maeda, Toward a full understanding of the EPR effect in primary and metastatic tumors as well as issues related to its heterogeneity, *Adv. Drug Deliv. Rev*. **91,** 3–6 (2015).

[45] F. Danhier, To exploit the tumor microenvironment: Since the EPR effect fails in the clinic, what is the future of nanomedicine?, *J. Control. Release.* **244,** 108–121 (2016).

[46] H. Maeda, K. Tsukigawa, J. Fang, A Retrospective 30 Years After Discovery of the Enhanced Permeability and Retention Effect of Solid Tumors: Next-Generation Chemotherapeutics and Photodynamic Therapy—Problems, Solutions, and Prospects, *Microcirculation.* **23,** (2016) 173–182.

[47] R. Kinoshita, Y. Ishima, V.T.G. Chuang, H. Nakamura, J. Fang, H. Watanabe, T. Shimizu, K. Okuhira, T. Ishida, H. Maeda, Improved anticancer effects of albumin-bound paclitaxel nanoparticle via augmentation of EPR effect and albumin-protein interactions using S-nitrosated human serum albumin dimer, *Biomaterials.* **140,** 162–169 (2017).

[48] M. Marenzana, T.R. Arnett, The Key Role of the Blood Supply to Bone, *Bone Res.* **1,** 203–215 (2013).

[49] F.A. Dinenno, H. Tanaka, B.L. Stauffer, D.R. Seals, Reductions in basal limb blood flow and vascular conductance with human ageing: role for augmented α-adrenergic vasoconstriction, *J. Physiol.* **536,** 977–983 (2001).

[50] C.R. Howlett, M. Dickson, A.K. Sheridan, The fine structure of the proximal growth plate of the avian tibia: vascular supply., *J. Anat.* **139,** 115–132 (1984).

[51] M. Tavassoli, The marrow-blood barrier., *Br. J. Haematol*. **41,** 297–302 (1979).

[52] K. Sou, B. Goins, B.O. Oyajobi, B.L. Travi, W.T. Phillips, Bone marrow-targeted liposomal carriers., *Expert Opin. Drug Deliv*. **8,** 317–328 (2011).

[53] C.J. Porter, S.M. Moghimi, L. Illum, S.S. Davis, The polyoxyethylene / polyoxypropylene selectively redirects intravenously injected microspheres to sinusoidal endothelial cells of rabbit bone marrow, *FEBS Lett*. **305,** 62–66 (1992).

[54] A.P. Mann, T. Tanaka, A. Somasunderam, X. Liu, D.G. Gorenstein, M. Ferrari, E-selectin-targeted porous silicon particle for nanoparticle delivery to the bone marrow, *Adv. Mater*. **23,** 278–282 (2011).

[55] A. Albanese, P.S. Tang, W.C.W. Chan, The Effect of Nanoparticle Size, Shape, and Surface Chemistry on Biological Systems, *Annu. Rev. Biomed. Eng.* **14,** 1–16 (2012).

[56] C. He, Y. Hu, L. Yin, C. Tang, C. Yin, Effects of particle size and surface charge on cellular uptake and biodistribution of polymeric nanoparticles, *Biomaterials*. **31,** 3657–3666 (2010).

[57] A. Salvati, A.S. Pitek, M.P. Monopoli, K. Prapainop, F.B. Bombelli, D.R. Hristov, P.M. Kelly, C. Aberg, E. Mahon, K.A. Dawson, Transferrin-functionalized nanoparticles lose their targeting capabilities when a biomolecule corona adsorbs on the surface, *Nat Nano*. **8,** 137–143 (2013).

[58] S. Milani, F. Baldelli Bombelli, A.S. Pitek, K.A. Dawson, J. Rädler, Reversible versus Irreversible Binding of Transferrin to Polystyrene Nanoparticles: Soft and Hard Corona, *ACS Nano*. **6,** 2532–2541 (2012).

[59] S. Sun, K.M. BŁazewska, A.P. Kadina, B.A. Kashemirov, X. Duan, J.T. Triffitt, J.E. Dunford, R.G.G. Russell, F.H. Ebetino, A.J. Roelofs, F.P. Coxon, M.W. Lundy, C.E. McKenna, Fluorescent Bisphosphonate and Carboxyphosphonate Probes: A Versatile Imaging Toolkit for Applications in Bone Biology and Biomedicine, *Bioconjug. Chem.* **27,** 329–340 (2016).

[60] E.M. Peck, P.M. Battles, D.R. Rice, F.M. Roland, K.A. Norquest, B.D. Smith, Pre-Assembly of Near-Infrared Fluorescent Multivalent Molecular Probes for Biological Imaging, *Bioconjug. Chem*. **27,** 1400–1410 (2016).

[61] A.R. Hayman, Tartrate-resistant acid phosphatase (TRAP) and the osteoclast/immune cell dichotomy., *Autoimmunity*. **41,** 218–223 (2008).

[62] K.B.S. Paiva, J.M. Granjeiro, Bone tissue remodeling and development: Focus on matrix metalloproteinase functions, *Arch. Biochem. Biophys*. **561,** 74–87 (2014).

[63] V. Uskokovic, Nanostructured platforms for the sustained and local delivery of antibiotics in the treatment of osteomyelitis., *Crit. Rev. Ther. Drug Carrier Syst*. **32,** 1–59 (2015).

[64] P.F. Tsai, K. Richards, I. Tatom, The association between knee temperature and pain in elders with osteoarthritis of the knee: A pilot study, J. Adv. Nurs. **42,** 373–381 (2003).

[65] M. Upreti, A. Jyoti, P. Sethi, Tumor microenvironment and nanotherapeutics, *Transl. Cancer Res*. **2,** 309–319 (2013).

[66] T. Yoneda, M. Hiasa, Y. Nagata, T. Okui, F.A. White, Acidic microenvironment and bone pain in cancer-colonized bone., *Bonekey Rep*. **4,** 690 (2015).

[67] Q. Hu, P.S. Katti, Z. Gu, Enzyme-responsive nanomaterials for controlled drug delivery, *Nanoscale*. **6** 12273–12286 (2014).

[68] C. Le Gall, A. Bellahcène, E. Bonnelye, J. a Gasser, V. Castronovo, J. Green, J. Zimmermann, P. Clézardin, A cathepsin K inhibitor reduces breast cancer induced osteolysis and skeletal tumor burden., *Cancer Res*. **67,** 9894–9902 (2007).

[69] F. Bühling, C. Röcken, F. Brasch, R. Hartig, Y. Yasuda, P. Saftig, D. Brömme, T. Welte, Pivotal Role of Cathepsin K in Lung Fibrosis, *Am. J. Pathol.* **164,** 2203–2216 (2004).

[70] H. Pan, M. Sima, S.C. Miller, P. Kopečková, J. Yang, J. Kopeček, Efficiency of high molecular weight backbone degradable HPMA copolymer-Prostaglandin E1 conjugate in promotion of bone formation in ovariectomized rats, *Biomaterials*. **34,** 6528–6538 (2013).

[71] C.W. Hsu, R.M. Olabisi, E.A. Olmsted-Davis, A.R. Davis, J.L. West, Cathepsin K-sensitive poly(ethylene glycol) hydrogels for degradation in response to bone resorption, *J. Biomed. Mater. Res.* - Part A. **98A,** 53–62 (2011).

[72] X. Wang, Y. Yang, H. Jia, W. Jia, S. Miller, B. Bowman, J. Feng, F. Zhan, Peptide Decoration of Nanovehicles to Achieve Active Targeting and Pathology-Responsive Cellular Uptake for Bone Metastasis Chemotherapy., *Biomater. Sci*. **2,** 961–971 (2014).

[73] C.C. Lynch, Matrix metalloproteinases as master regulators of the vicious cycle of bone metastasis, *Bone*. **48,** 44–53 (2011).

[74] P. Hou, T. Troen, M.C. Ovejero, T. Kirkegaard, T.L. Andersen, I. Byrjalsen, M. Ferreras, T. Sato, S.D. Shapiro, N.T. Foged, J.-M. Delaissé, Matrix metalloproteinase-12 (MMP-12) in osteoclasts: new lesson on the involvement of MMPs in bone resorption, *Bone.* **34,** 37–47 (2017).

[75] L.J. Raggatt, N.C. Partridge, Cellular and molecular mechanisms of bone remodeling, *J. Biol. Chem*. **285,** 25103–25108 (2010).

[76] N. Sarkar, J. Banerjee, A.J. Hanson, A.I. Elegbede, T. Rosendahl, A.B. Krueger, A.L. Banerjee, S. Tobwala, R. Wang, X. Lu, S. Mallik, D.K. Srivastava, Matrix metalloproteinase-assisted triggered release of liposomal contents, *Bioconjug. Chem*. **19,** 57–64 (2008).

[77] P.S. Kulkarni, M.K. Haldar, R.R. Nahire, P. Katti, A.H. Ambre, W.W. Muhonen, J.B. Shabb, S.K.R. Padi, R.K. Singh, P.P. Borowicz, MMP-9 responsive PEG cleavable nanovesicles for efficient delivery of chemotherapeutics to pancreatic cancer, *Mol. Pharm*. **11,** 2390–2399 (2014).

[78] A. Page-McCaw, A.J. Ewald, Z. Werb, Matrix metalloproteinases and the regulation of tissue remodelling., *Nat. Rev. Mol. Cell Biol*. **8,** 221–233 (2007).

[79] T.W. Liu, M.K. Akens, J. Chen, B.C. Wilson, G. Zheng, Matrix metalloproteinase-based photodynamic molecular beacons for targeted destruction of bone metastases *in vivo*, *Photochem. Photobiol. Sci.* **15,** 375–381 (2016).

[80] J. Hatzenbuehler, T.J. Pulling, Diagnosis and Management of Osteomyelitis, *Am Fam Physician*. **84** 1027–1033 (2011).

[81] G. Baier, A. Cavallaro, K. Vasilev, V. Mailander, A. Musyanovych, K. Landfester, Enzyme Responsive Hyaluronic Acid Nanocapsules Containing Polyhexanide and Their Exposure to Bacteria To Prevent Infection, *Biomacromolecules.* **14,** 1103–1112 (2013).

[82] F. Danhier, O. Feron, V. Préat. To exploit the tumor microenvironment: Passive and active tumor targeting of nanocarriers for anti-cancer drug delivery, *J. Control. Release*. **148,** 135–146 (2010).

[83] S.K. Calderwood, J. Gong, Heat Shock Proteins Promote Cancer: It's a Protection Racket, *Trends Biochem. Sci*. **41,** 311–323 (2016).

[84] D. Liu, L. Ma, Y. An, Y. Li, Y. Liu, L. Wang, J. Guo, J. Wang, J. Zhou, Thermoresponsive Nanogel-Encapsulated PEDOT and HSP70 Inhibitor for Improving the Depth of the Photothermal Therapeutic Effect, *Adv. Funct. Mater.* **26,** 4749–4759 (2016).

[85] R. Staruch, R. Chopra, K. Hynynen, Hyperthermia in Bone Generated with MR Imaging-controlled Focused Ultrasound: Control Strategies and Drug Delivery, *Radiology*. **263,** 117–127 (2012).

[86] H. Song, J. Zhang, X. Liu, T. Deng, P. Yao, S. Zhou, W. Yan, Development of drug loaded nanoparticles binding to hydroxyapatite based on a bisphosphonate modified nonionic surfactant, *Pharm. Dev. Technol.* **21,** (6) 1-8 (2015).

[87] S. Poh, J.B. Lin, A. Panitch, Release of Anti-inflammatory Peptides from Thermosensitive Nanoparticles with Degradable Cross-Links Suppresses Pro-inflammatory Cytokine Production, *Biomacromolecules.* **16,** 1191–1200 (2015).

[88] N. Cetin, A. Aytar, A. Atalay, M.N. Akman. Comparing hot pack, short-wave diathermy, ultrasound, and TENS on isokinetic strength, pain, and functional status of women with osteoarthritic knees: a single-blind, randomized, controlled trial., *Am. J. Phys. Med. Rehabil*. **87,** 443–451 (2008).

[89] J. Yang, R. Van Lith, K. Baler, R.A. Hoshi, G.A. Ameer, A thermoresponsive biodegradable polymer with intrinsic antioxidant properties, *Biomacromolecules.* **15,** 3942–3952 (2014).

[90] E. Fleige, M.A. Quadir, R. Haag, Stimuli-responsive polymeric nanocarriers for the controlled transport of active compounds: Concepts and applications, *Adv. Drug Deliv. Rev*. **64,** 866–884 (2012).

[91] A.-Z. Zardad, Y. Choonara, L. du Toit, P. Kumar, M. Mabrouk, P. Kondiah, V. Pillay, A Review of Thermo- and Ultrasound-Responsive Polymeric Systems for Delivery of Chemotherapeutic Agents, *Polymers.* **8,** 359 (2016).

[92] R. Nahire, S. Paul, M.D. Scott, R.K. Singh, W.W. Muhonen, J. Shabb, K.N. Gange, D.K. Srivastava, K. Sarkar, S. Mallik, Ultrasound enhanced matrix metalloproteinase-9 triggered release of contents from echogenic liposomes, *Mol. Pharm.* **9,** 2554–2564 (2012).

[93] G.J. Crasto, N. Kartner, N. Reznik, M. V. Spatafora, H. Chen, R. Williams, P.N. Burns, C. Clokie, M.F. Manolson, S.A.F. Peel, Controlled bone formation using ultrasound-triggered release of BMP-2 from liposomes, *J. Control. Release* (2016).

[94] G.J. Crasto, H. Chen, N. Kartner, N. Reznik, S.A.F. Peel, Ultrasound triggered delivery of growth factors from liposomes for tissue regeneration (2016).

[95] S. Sawant, R. Shegokar, Chapter 5 - Bone scaffolds: What's new in nanoparticle drug delivery research? A2 - Grumezescu, Alexandru Mihai BT - Nanobiomaterials in Hard Tissue Engineering, in: William Andrew Publishing, 155–187 (2016).

[96] M. Nagao, N. Tanabe, S. Manaka, M. Naito, K. Nakai, T. Takayama, T. Kawato, G. Torigoe, J. Sekino, N. Tsukune, M. Maeno, N. Suzuki, S. Sato, LIPUS suppressed LPS-induced IL-1α through the inhibition of NF-κB nuclear translocation via AT1-PLCβ pathway in MC3T3-E1, *J. Cell. Physiol*. (2017).

[97] R. Puts, J. Albers, A. Kadow-Romacker, S. Geissler, K. Raum, Influence of Donor Age and Stimulation Intensity on Osteogenic Differentiation of Rat Mesenchymal Stromal Cells in Response to Focused Low-Intensity Pulsed Ultrasound, *Ultrasound Med. Biol*. **42,** 2965–2974 (2016).

[98] X.-S. Li, W.-Q. Li, W.-B. Wang, Using targeted magnetic arsenic trioxide nanoparticles for osteosarcoma treatment., *Cancer Biother. Radiopharm*. **22,** 772–778 (2007).

[99] T. Matsuo, T. Sugita, T. Kubo, Y. Yasunaga, M. Ochi, T. Murakami, Injectable magnetic liposomes as a novel carrier of recombinant human BMP-2 for bone formation in a rat bone-defect model., *J. Biomed. Mater. Res.* A. **66,** 747–754 (2003).

[100] E. Guisasola, A. Baeza, M. Talelli, D. Arcos, M. Moros, J.M.D. La Fuente, M. Vallet-regí, E. Guisasola, A. Baeza, M. Talelli, D. Arcos, M. Moros, J.M. De, Magnetic-responsive Release

Controlled by Hot Spot Effect Magnetic-responsive Release Controlled by Hot Spot Effect, *Langmuir.* **31,** 12777–12782 (2015).

[101] Y. Shido, Y. Nishida, Y. Suzuki, T. Kobayashi, N. Ishiguro, Targeted hyperthermia using magnetite cationic liposomes and an alternating magnetic field in a mouse osteosarcoma model., *J. Bone Joint Surg. Br*. **92,** 580–585 (2010).

[102] F. Matsuoka, M. Shinkai, H. Honda, T. Kubo, T. Sugita, T. Kobayashi, Hyperthermia using magnetite cationic liposomes for hamster osteosarcoma, *Biomagn. Res. Technol*. **2,** (2004).

[103] E. Amstad, J. Kohlbrecher, E. Müller, T. Schweizer, M. Textor, E. Reimhult, Triggered release from liposomes through magnetic actuation of iron oxide nanoparticle containing membranes, *Nano Lett*. **11,** 1664–1670 (2011).

[104] J.C. Kraft, J.P. Freeling, Z. Wang, R.J.Y. Ho, Emerging research and clinical development trends of liposome and lipid nanoparticle drug delivery systems, *J. Pharm. Sci*. **103,** 29–52 (2014).

[105] S.C. McBain, H.H.P. Yiu, J. Dobson, Magnetic nanoparticles for gene and drug delivery, *Int. J. Nanomedicine.* **3,** 169–180 (2008).

[106] Z. Huang, N. Pei, Y. Wang, X. Xie, A. Sun, L. Shen, S. Zhang, X. Liu, Y. Zou, J. Qian, J. Ge, Deep magnetic capture of magnetically loaded cells for spatially targeted therapeutics, *Biomaterials.* **31,** 2130–2140 (2010).

[107] M. Kanamala, W.R. Wilson, M. Yang, B.D. Palmer, Z. Wu, Mechanisms and biomaterials in pH-responsive tumour targeted drug delivery: a review, *Biomaterials*. **85,** 152–167 (2016).

[108] X. Pang, Y. Jiang, Q. Xiao, A.W. Leung, H. Hua, C. Xu, pH-responsive polymer–drug conjugates: design and progress, *J. Control. Release*. **222,** 116–129 (2016).

[109] D. Schmaljohann, Thermo- and pH-responsive polymers in drug delivery, *Adv. Drug Deliv. Rev*. **58,** 1655–1670 (2006).

[110] V. Torchilin, Tumor delivery of macromolecular drugs based on the EPR effect, *Adv. Drug Deliv. Rev.* **63,** 131–135 (2011).

[111] D. dos S. Ferreira, S.D. Faria, S.C. de A. Lopes, C.S. Teixeira, A. Malachias, R. Magalhães-Paniago, J.D. de Souza Filho, B.L. Oliveira de Jesus Pinto, A.R. Guimarães, P. Caravan, L.A.M. Ferreira, R.J. Alves, M.C. Oliveira, Development of a bone-targeted pH-sensitive liposomal formulation containing doxorubicin: Physicochemical characterization, cytotoxicity, and biodistribution evaluation in a mouse model of bone metastasis, *Int. J. Nanomedicine*. **11,** 3737–3751 (2016).

[112] Y. Wang, J. Wang, H. Hao, M. Cai, S. Wang, J. Ma, Y. Li, C. Mao, S. Zhang, *In Vitro* and *in Vivo* Mechanism of Bone Tumor Inhibition by Selenium-Doped Bone Mineral Nanoparticles, *ACS Nano*. **10,** 9927–9937 (2016).

[113] E. Alpaslan, H. Yazici, N.H. Golshan, K.S. Ziemer, T.J. Webster, pH-Dependent Activity of Dextran-Coated Cerium Oxide Nanoparticles on Prohibiting Osteosarcoma Cell Proliferation, *ACS Biomater. Sci. Eng***. 1,** 1096–1103 (2015).

[114] Q. Gan, J. Zhu, Y. Yuan, H. Liu, J. Qian, Y. Li, C. Liu, A dual-delivery system of pH-responsive chitosan-functionalized mesoporous silica nanoparticles bearing BMP-2 and dexamethasone for enhanced bone regeneration, *J. Mater. Chem. B*. **3,** 2056–2066 (2015).

[115] S.M.Z.M.D. Ferreira, G.P. Domingos, D.D.S. Ferreira, T.G.R. Rocha, R. Serakides, C.M. De Faria Rezende, V.N. Cardoso, S.O.A. Fernandes, M.C. Oliveira, Technetium-99m-labeled ceftizoxime loaded long-circulating and pH-sensitive liposomes used to identify osteomyelitis, *Bioorganic Med. Chem. Lett*. **22,** 4605–4608 (2012).

[116] Cong, Y.; Quan, C.; Liu, M.; Liu, J.; Huang, G.; Tong, G.; Yin, Y.; Zhang, C.; Jiang, Q. Alendronate-Decorated Biodegradable Polymeric Micelles for Potential Bone-Targeted Delivery of Vancomycin. *J. Biomater. Sci. Polym. Ed*. **26,** (11) 629–643 (2015).

[117] V.A. Sethuraman, M.C. Lee, Y.H. Bae, A biodegradable pH-sensitive micelle system for targeting acidic solid tumors, *Pharm. Res*. **25,** 657–666 (2008).

[118] C. Wu, S. Wang, L. Bruelisauer, J. Leroux, M.A. Gauthier, Broad control of disulfide stability through microenvironmental effects and analysis in complex redox environments, *Biomacromolecules*. **14,** 2383–2388 (2013).

[119] L. Turell, R. Radi, B. Alvarez, Free Radical Biology and Medicine The thiol pool in human plasma: The central contribution of albumin to redox processes, *Free Radic. Biol. Med*. **65,** 244–253 (2013).

[120] M.T. Drake, B.L. Clarke, S. Khosla, Bisphosphonates: Mechanism of Action and Role in Clinical Practice, *Mayo Clin. Proc*. **83,** 1032–1045 (2008).

[121] R. Cheng, F. Feng, F. Meng, C. Deng, J. Feijen, Z. Zhong, Glutathione-responsive nano-vehicles as a promising platform for targeted intracellular drug and gene delivery, J. Control. Release**. 152,** 2–12 (2011).

[122] J. Yang, H. Chen, I.R. Vlahov, J.-X. Cheng, P.S. Low, Evaluation of disulfide reduction during receptor-mediated endocytosis by using FRET imaging., Proc. Natl. Acad. Sci. U. S. A. **103,** 13872–13877 (2006).
[123] X. Zhang, L. Han, M. Liu, K. Wang, L. Tao, Q. Wan, Y. Wei, Recent progress and advances in redox-responsive polymers as controlled delivery nanoplatforms, Mater. Chem. Front. **1,** (2017) 807–822.
[124] A.D. Baldwin, K.L. Kiick, Reversible maleimide–thiol adducts yield glutathione-sensitive poly(ethylene glycol)–heparin hydrogels, Polym. Chem. **4,** 133–143 (2012).
[125] H. Sun, F. Meng, R. Cheng, C. Deng, Z. Zhong, Reduction-responsive polymeric micelles and vesicles for triggered intracellular drug release., Antioxid. Redox Signal. **21,** 755–767 (2014).
[126] M. Talelli, M. Barz, C.J.F. Rijcken, F. Kiessling, W.E. Hennink, T. Lammers, Core-crosslinked polymeric micelles: Principles, preparation, biomedical applications and clinical translation, Nano Today**. 10,** 93–117 (2015).
[127] D. Maciel, P. Figueira, S. Xiao, D. Hu, X. Shi, J. Rodrigues, H. Tomás, Y. Li, Redox-responsive alginate nanogels with enhanced anticancer cytotoxicity, Biomacromolecules. **14,** (2013) 3140–3146.
[128] C. Yao, J. Liu, X. Wu, Z. Tai, Y. Gao, Q. Zhu, J. Li, L. Zhang, C. Hu, F. Gu, J. Gao, S. Gao, Reducible self-assembling cationic polypeptide-based micelles mediate co-delivery of doxorubicin and microRNA-34a for androgen-independent prostate cancer therapy, J. Control. Release**. 232,** 203–214 (2016).
[129] X.J. Li, Z.J. Ren, J.H. Tang, MicroRNA-34a: a potential therapeutic target in human cancer., Cell Death Dis. **5,** e1327 (2014).
[130] J.B. Lin, S. Poh, A. Panitch, Controlled release of anti-inflammatory peptides from reducible thermosensitive nanoparticles suppresses cartilage inflammation., Nanomedicine. **12,** 2095–2100 (2016).
[131] W.A. Flavahan, E. Gaskell, B.E. Bernstein, Epigenetic plasticity and the hallmarks of cancer, Science. **357,** eaal2380 (2017).
[132] D. Hanahan, R.A. Weinberg, Hallmarks of cancer: the next generation, Cell. **144,** 646–674 (2011).
[133] J. Leroux, Drug Delivery: Too Much Complexity, Not Enough Reproducibility?, Angew. Chemie Int. Ed. (2017).
[134] J.F. Mano, Stimuli-Responsive Polymeric Systems for Biomedical Applications, Adv. Eng. Mater. **10,** 515–527 (2008).
[135] A.C. Lima, C. Alvarez-Lorenzo, J.F. Mano, Design Advances in Particulate Systems for Biomedical Applications, Adv. Healthc. Mater. **5,** 1687–1723 (2016).
[136] T.J. Anchordoquy, D. Simberg, Watching the gorilla and questioning delivery dogma., J. Control. Release Off. J. Control. Release Soc. **262,** 87 (2017).

2 Aims

The global aim of this thesis was to develop monodisperse nanomicelles capable of efficiently encapsulating the flavonoid Naringin for controlled intracellular delivery in hASCs in order to potentiate or promote their osteogenic differentiation. The specific aims of this master thesis were the following:

- Synthesis and characterization of mPEG-PLA amphiphilic diblock copolymer;
- Synthesis and characterization of mPEG-MS-PLA amphiphilic diblock copolymer;
- Preparation of mPEG-PLA and mPEG-MS-PLA nanomicelles via nanoprecipitation;
- Physicochemical characterization of mPEG-PLA and mPEG-MS-PLA nanomicelles;
- Naringin encapsulation in mPEG-MS-PLA micelles and characterization of *in vitro* drug release profile;
- Investigation of the intracellular uptake of nanomicelles via fluorescence microscopy and flow cytometry studies in MC3T3-E1 and hASCs;
- Evaluation of the cytotoxic profile of free Naringin, blank and Naringin-loaded nanomicelles in MC3T3-E1 and hASCs;
- Study of the proliferative capacity of free Naringin in hASCs;
- Evaluation of the pro-osteogenic potential of free Naringin and Naringin-loaded nanomicelles in hASCs in different osteogenic conditions;
- Execution of mineralization assays of free Naringin and Naringin-loaded nanomicelles in hASCs.

3 Materials and Methods

3.1 Materials

Methoxypoly(ethylene glycol) (mPEG-OH) (M_n 5000), Methoxypoly(ethylene glycol)-maleimide (mPEG-MAL) (M_n 5000, >90 % purity), thiol-poly(L-lactide) (PLA-SH) (M_n 5000, PDI < 1.2), 3,6-Dimethyl-1,4-dioxane-2,5-dione (L-Lactide), stannous octoate ($Sn(Oct)_2$), anhydrous toluene, dichloromethane, diethanolamine (puriss American Chemical Society), 4-Nitrophenyl phosphate disodium salt hexahydrate (4NPhP), 4-Nitrophenol 10 mM (4NPh), phosphate buffered saline (PBS), formaldehyde, Coumarin-6 (Coum-6), Naringin (> 95 % purity), β-glycerophosphate disodium salt hydrate BioUltra (β-gly), Alizarin Red S, Triton X-100 BioXtra, dimethylsulfoxide (DMSO, sterile) and Amicon® Ultra-4 mL (3000 NMWL) were all purchased from Laborspirit (Lisbon, Portugal). Spectra/Por 1 dialysis tubing (6000 - 8000 Da MWCO) and Float-A-Lyzer G2 (3500 - 5000 Da MWCO) dialysis cassettes were purchased from Reagente 5 (Oporto, Portugal). Liquid paraffin (GPR Rectapur®) and L-ascorbic acid 2-phosphate magnesium salt (AA) were purchased from VWR (Lisbon, Portugal). Deuterated chloroform ($CDCl_3$), methanol (MetOH, 99.8% analytical grade - a.g.), di-Sodium hydrogen phosphate dihydrate (a.g.), Sodium di-hydrogen phosphate monohydrate (reagent European Pharmacopeia - Ph. Eur.), EDTA disodium salt dihydrate (Ph. Eur.) and diethyl ether (Labsolve®) were all purchased from JMGS Lda. (Odivelas, Portugal). Magnesium chloride hexahydrate was kindly gifted by Fernando Sá. Acetone (99-100 %) was purchased from Enzymatic S.A. (Loures, Portugal). Murine pre-osteoblast cell line subclone-4 (MC3T3-E1, *Mus Musculus*, ATCC® CRL-2593™) and human adipose-derived mesenchymal stem cells (hASCs, *Homo Sapiens*, ATCC® PCS-500-011™) were purchased from LGC Standards S.L.U. (Barcelona, Spain). Minimum Essential Medium α-modification (α-MEM, -nucleosides, +L-glutamine), fetal bovine serum (FBS, E.U. approved, South American origin), antibiotic mixture penicillin-streptomycin (10 000 U/mL penicillin-G and 100 mg/mL streptomycin), TrypLE™ Xpress Enzyme with phenol red(1X), Quant-iT™ PicoGreen® dsDNA Assay Kit, AlamarBlue™, 1-Step™ NBT/BCIP Substrate Solution, and Wheat germ agglutinin (WGA) Alexa Fluor® 594 conjugate dye and DAPI were purchased from Alfagene (Lisbon, Portugal). Dexamethasone (Dex, 96% purity, ACROS Organics™) and Dulbecco's PBS were purchased from Thermo Fisher Scientific (Oeiras, Portugal).

3.2 Methods

3.2.1 Synthesis of mPEG-PLA Diblock Copolymer via Ring-opening Polymerization

The synthesis of mPEG(5K)-PLA diblock copolymer was obtained via ring-opening polymerization (ROP) of L-Lactide by using $Sn(Oct)_2$ as catalyst and the Ω-end hydroxyl group (-OH) of mPEG-OH polymer as the initiator (Figure 9). Prior to ROP-based synthesis the L-Lactide monomer and mPEG-OH were dried for 4 days in an oven at 70 ºC and 37 ºC, respectively.

For block co-polymer synthesis L-Lactide (3.469 mmol) and mPEG-OH initiator (0.05 mmol, 50 % w/w L-Lactide) were added to a three-neck round bottom flask under N_2 inert atmosphere and dissolved in dry toluene (10 mL). The resulting solution was stirred at 800 rpm (MR Hei-End with PT1000 sensor, VWR, Lisbon, Portugal) and heated in an oil bath to 100 ºC under reflux, before the $Sn(Oct)_2$ catalyst (0.193 mmol, 62.5 µL), in dry toluene (2.5 mL), was added to the flask. Following this addition, the polymerization proceeded for 8 h at 120 ºC, under reflux. Subsequently, the reaction was cooled to room temperature (RT) and toluene was evaporated under a N_2 gas flow line. The resulting yellowish crude product was then dissolved in dichloromethane before being precipitated in excess cold MetOH in order to recover the synthesized mPEG-PLA copolymer. The precipitated white product was then dialyzed in a dialysis membrane (6000 - 8000 Da MWCO), for 72 h against deionized water. Then, it was frozen at -80 ºC and freeze-dried (approximately -74 ºC condenser temperature, 0.014 mbar vacuum, Telstar LyoQuest Plus, purchased from VWR, Lisbon, Portugal) for storage.

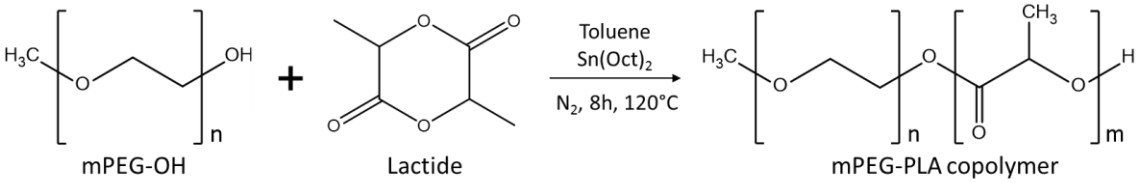

Figure 9. Synthesis route of mPEG-PLA diblock copolymer via ROP of L-Lactide.

3.2.2 Synthesis of mPEG-MS-PLA Diblock Copolymer

For the synthesis of amphiphilic block copolymer under more environmentally friendly conditions methoxypoly(ethylene glycol)-maleimide (mPEG-MAL, 5000 Da) was

conjugated to thiol-poly(L-lactide) (PLA-SH, 5000 Da) via a Michael-type addition [1] (Figure 10). Maleimides are reported to selectively react with thiols in the pH range of 6.5 - 7.5 to afford thiol-ether bonds.[2] For copolymer synthesis mPEG-MAL (0.04 mmol) was added by molar excess (1.5 mPEG/PLA molar ratio) to a three-neck round bottom flask in order to improve the overall reaction yield. After adding PLA-SH (0.0267 mmol), the polymers were dissolved in acetone (V = 15 mL, v/v ratio = 0.43) and sodium phosphate buffer (pH = 7.2, 100 mM, V = 20 mL, v/v ratio = 0.57) containing EDTA (5 mM) in order to minimize the oxidation of free PLA thiols (-SH) before conjugation with the maleimide (-MAL) end group [3]. The mixture was then flushed with a N_2 flow and then magnetically stirred at 400 rpm under inert conditions for 2 days (400 rpm) at RT. Afterwards, the resulting crude mixture was completely dried in a rotary evaporator (Buchi, Rotavapor® R-300, Reagente 5, Oporto, Portugal). The dried solid within the flask was dissolved in dichloromethane and precipitated in an excess volume of cold (4 ºC) diethyl ether. Following this, the precipitated polymer was dried with a N_2 gas flow and re-suspended in deionized water before being transferred to a dialysis membrane (6000 – 8000 Da MWCO) and exhaustively dialyzed against deionized water in sink conditions for 72 h. Then, the product was frozen in -80ºC before being freeze-dried for storage.

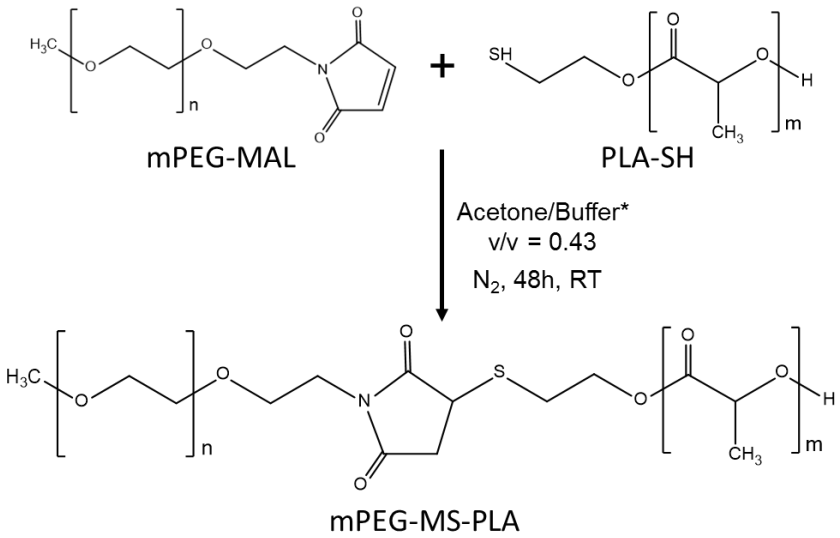

Figure 10. Synthesis route of mPEG-MS-PLA diblock copolymer via a Michael-type addition. *Phosphate buffer 100mM, pH = 7.2, containing 5 mM EDTA.

3.2.3 Spectroscopy Characterization

The successful synthesis of the various copolymers was characterized by different spectroscopy techniques. Proton nuclear magnetic resonance (^{1}H NMR) spectra were recorded on a Bruker Advance III 400 MHz spectrometer. Prior to spectra acquisition, samples were dissolved in 700 µL of $CDCl_3$ and transferred to 300 MHz NMR glass tubes (Sigma-Aldrich, Sintra, Portugal). Employed parameters for spectra acquisition consisted in 18 s relaxation delay, 256 scans and 32 dummy scans. Data processing was performed in the MestReNova v6.0.2 software, and spectra were normalized according to the established $CDCl_3$ solvent singlet at 7.26 ppm. Fourier Transformed Infrared spectra were collected on dried samples by the attenuated total reflectance (ATR-FTIR) method using a Brucker Tensor 27 spectrometer. The spectra of all samples were recorded at a 4 cm^{-1} resolution for a total of 256 scans in the spectral width of 4000 to 350 cm^{-1}. The spectra were obtained and processed in OPUS software.

3.2.4 Self-assembly of Nanosized Polymeric Micelles

Polymeric micelles (PMs) were prepared by the solvent exchange technique, also known as nanoprecipitation. For the self-assembly based formulation of mPEG-MS-PLA micelles the polymer powder (5 mg) was dissolved in 1.0 mL of freshly prepared acetone containing Naringin (10% w/w of copolymer) and placed in an ultrasonic bath for 5 min (80 Hz, pulsed mode, 30 ºC, Elmasonic P 120 H model, VWR, Lisbon, Portugal) to achieve full polymer dissolution. To improve the accuracy of encapsulation efficiency measurements, this Naringin-containing acetone solution was freshly prepared. Then, this solution was slowly added dropwise into a 10 mL round-bottom flask containing 5.0 mL deionized water (previously filtered through 0.2 µm syringe filter (cellulose acetate, VWR, Lisbon, Portugal) and stirred for 90 min at 400 rpm, RT. Afterwards, acetone was evaporated under a rotary evaporator during 8 min (37 ºC, 50 mbar). The resultant solution was dialyzed (3500 Da MWCO) against deionized water for 1 h (400 rpm) to remove free Naringin. Blank micelles were prepared following the same procedure minus the unnecessary dialysis step.

To investigate the cellular uptake of the produced nanocarriers, the hydrophobic fluorescent dye Coum-6 was loaded in PMs hydrophobic core. The Coum-6-loaded micelles were prepared according to the above-mentioned nanoprecipitation conditions with minor modifications. For the preparation of fluorescent micelles, acetone solution (1 mL)

containing Coum-6 at 2 % w/v of copolymer was used instead, and the whole nanoprecipitation process was conducted in the dark.

3.2.5 Micelles Physicochemical Characterization

The average hydrodynamic particle radius (H_r), size distribution (PDI) and ζ-potential of the different PMs (1 mg/mL) were determined through dynamic light scattering (DLS), by using a Malvern Zetasizer Nano ZS equipment (Malvern Instruments Ltd., Malvern, United Kingdom). All experiments were carried out at 25 ºC with a 173º backscatter angle, and each sample measurement was repeated three times. The H_r of the micelles was calculated from the Stokes-Einstein equation, while the PDI was obtained by using the cumulants analysis. The ζ-potential values were extrapolated from electrophoretic mobility values using Smoluchowski's equation in Zetasizer v7.11 (Malvern, United Kingdom) [4]. Either disposable capillary cell (DTS1070) for ζ-potential analysis or square polystyrene cuvettes (DTS0012) for size analysis were used accordingly.

In addition, self-assembled micelles morphology was observed by scanning transmission electron microscopy (STEM). The different samples were prepared by careful drop-wise addition of 10 µL of freshly prepared micelles (0.2 mg/mL) on a carbon-film copper grid (400 mesh, EM Resolutions, United Kingdom). The samples were then left to dry overnight, at RT. Nanomicelles micrographs were acquired in a Hitachi SU-70 STEM microscope, operated at an accelerating voltage of 20.0 kV, at various magnifications.

3.2.6 Evaluation of Micelles Colloidal Stability

The colloidal stability of different PMs was investigated by monitoring changes in size, PDI and ζ-potential along time upon storage in solution. For stability studies Naringin-loaded nanocarrier formulations (n=3), were prepared by nanoprecipitation and maintained in deionized water or PBS (pH = 7.4) at 4 ºC. Micelles and their physicochemical properties were then analyzed by DLS at different time intervals: 0, 1, 7 and 14 days.

3.2.7 Drug Loading

The Naringin content loaded into PMs was determined by ultraviolet-visible (UV-VIS) absorbance of the flavanone peak of Naringin (λ= 282 nm) corresponding to the benzoyl moiety. This peak is followed by a another region of smaller intensity to higher wavelengths (300 – 400 nm), associated with the cinnamoyl moiety and is characteristic of flavanones

such as Naringin [5] (Figure 33, Annex I). The UV-VIS absorbance was measured in a microplate reader equipped with a tungsten halogen lamp (Synergy HTX Biotek, Izasa Scientific, Carnaxide, Portugal) by using a quartz microplate (Hella transparent 96-wellplate, VWR, Lisbon, Portugal).

Briefly, a solution of freshly prepared PMs (1 mg/mL) loaded with Naringin was transferred to a dialysis tubing (Float-A-Lyzer G2, 3500 Da MWCO) and dialyzed in sink conditions against deionized water for 1 h, under stirring (400 rpm). After free drug removal, the remaining Naringin-micelles solution (0.2 mg/mL) was analyzed by UV-VIS at 282 nm. Because the mPEG-MS-PLA amphiphilic copolymer contains a slight background signal, blank micelles (0.2 mg/mL) were used to establish the blank for UV-VIS quantification of drug encapsulation. A standard calibration curve of Naringin in deionized water was used to determine the drug encapsulation efficacy (Figure 33, Annex I). Encapsulation efficiency was calculated using the above equation:

Equation 1: Encapsulation Efficiency (%):

$$= \left(\frac{Amount\ of\ Naringin\ within\ the\ micelles)}{Theoretical\ amount\ of\ Naringin\ added}\right) \times\ 100$$

3.2.8 *In vitro* Drug Release Profile

The *in vitro* Naringin release profile from mPEG-MS-PLA micelles was investigated in PBS at various pH conditions to mimic different physiological scenarios: pH 7.4 (physiological pH) and pH 5.5 (endo-lysosomal pH). For this evaluation, 2 mL of freshly prepared Naringin-loaded micelles (1 mg/mL in deionized water) were transferred to a dialysis tubing (3500 – 5000 Da MWCO) and submerged in 15 mL of PBS at 37 ºC at a constant stirring rate (600 rpm). At defined time intervals, 1 mL samples were withdrawn from the dialysate and replaced with the same volume of fresh PBS. Samples were withdrawn at different time points until the plateau phase was achieved. For this study, the standard calibration curve of the drug in water was used (Figure 33, Annex I).

3.2.9 Cell Culture

All cells were manipulated in aseptic conditions within a Class II biological safety cabinet and maintained as per established guidelines in a humidified 5 % CO_2 atmosphere incubator (Binder C-170, VWR, Lisbon, Portugal) with 95 % O_2 and at 37 ºC [6]. MC3T3-E1 and hASCs were routinely cultured in α-MEM supplemented with 10 % (v/v) heat-inactivated FBS and

1 % of antibiotic mixture (basal growth medium, BM) and media was exchanged every 5 days. Cells were subcultured before reaching confluence. All plastic adherent well plates were made of tissue culture treated polystyrene (Sarstedt, Sintra, Portugal). Cells were subcultured before reaching confluence. Culture media was exchanged every 5 days.

For cellular experiments investigating osteogenic differentiation, AA, β-gly and Dex stock solutions were prepared in dPBS and frozen at -20 ºC. Different osteogenic media were prepared from such aliquots. Osteogenic supplements were added to BM in the following concentrations: (i) reduced osteogenic differentiation medium (rOS) - 50 µg/mL AA and 10 mM β-gly; and (ii) OS-Dex – rOS and 100 nM Dex. For preparation of free Naringin concentrations, the drug was initially dissolved in sterile DMSO (50 mg/mL) and subsequently diluted in the respective assay media (basal or osteogenic) and to a final 0.1 % (v/v) DMSO content across all concentrations. Osteogenic assays involving ALP activity and BMP-2 quantifications, as well as OPN and Alizarin Red S visualization followed the below described conditions (Table 1). Osteogenic assays involving Alkaline phosphatase (ALP) activity and BMP-2 quantifications, as well as OPN and Alizarin Red S imaging assays followed the below described conditions (Table 1).

Table 1. Overview of the conditions used in osteogenic differentiation assays.

Assay	Culture medium	Pharmaceutic	Dosing regime	Total incubation time
I, OS-Dex	AA + β-gly + Dex (OS)	Naringin	Single	21 d
II, One dose	AA + β-gly (rOS)	Naringin; Naringin-loaded micelles	Single	7 d
II, Two dose	AA + β-gly (rOS)	Naringin; Naringin-loaded micelles	Double	7 d

Across all experiments, medium was exchanged every 3 days containing the respective osteogenic supplements listed above, except for the Two dose assay, where medium with a second dose of pharmaceutic was added after 3 days. Please see the respective dose regimen schematics in each result panel.

3.2.10 *In vitro* Cellular Uptake Studies

3.2.10.1 Fluorescence Microscopy

The kinetics of PMs cellular uptake in MC3T3-E1 pre-osteoblasts and hASCs was evaluated by using fluorescence microscopy. For this study, fluorescent Coum-6 loaded PMs

were used. Briefly, MC3T3-E1 and hASCs were seeded overnight in µ-Slide 8-well chambers (ibidi GmbH) at a density of 8.0 and 25.0 x 10^3 cells/well, respectively, in 200 µL of free-antibiotic BM. Then, cells were incubated with 250 µg/well of Coum-6-loaded nanocarriers, in free-antibiotic BM for different time intervals (2, 4 and 6 h). After each timepoint, cells were fixed in 4 % formaldehyde solution and washed three times with dPBS. Then, the cells cytoplasm was fluorescently labelled with 50 µL of WGA Alexa Fluor® 594 conjugate dye (0.2 mg/mL) by incubating for 5 min in the dark. Afterwards, the cells were washed three times with dPBS to remove excess dye. Cells were maintained in dPBS until fluorescence microscopy analysis. Confocal laser scanning microscopy (CLSM) and fluorescence microscopy (Axio Imager 2, Carl Zeiss Microscopy GmbH) were used to follow the kinetics of intracellular internalization of the nanocarriers. Image processing was performed using ZEN v2.3 blue edition software.

3.2.10.2 Flow Cytometry

The quantitative measurement of Coum-6 fluorescence intensity was conducted via flow cytometry. MC3T3-E1 and hASCs were seeded overnight in 24-well plates at a density of 50 and 40 x 10^3 cells/well (n=4) respectively, in 500 µL of free-antibiotic BM. Then, medium was replaced with 500 µL of free-antibiotic BM containing the 96-well plate equivalent of 25, 50 and 100 µg of Coum-6- nanocarriers per well. Nanocarriers were previously concentrated by centrifuging for 30 min in Amicon® ultra centrifugal units (3000 Da MWCO) at 16600 g. After 4 h incubation, growth media was aspirated and cells were washed twice with 1 mL dPBS, before being harvested by trypsinization (500 µL, 5 min incubation at 37 ºC), neutralized with equal volume of dPBS and collected by centrifugation at 500 g for 5 min. Then, the supernatant was aspirated and the cells were suspended in 200 µL of dPBS prior to fluorescent intensity measurements.

3.2.11 Cytotoxicity Assays

Assessment of cell metabolism of MC3T3-E1 and hASCs was performed by using the AlamarBlue® Cell Viability assay. This assay is based on the mitochondrial oxidoredutase enzyme metabolic reduction of the blue non-fluorescent resazurin dye to the pink-colored highly fluorescent resorufin within the intracellular reducing environment of metabolically active cells [7].

For evaluation of micelles and free drug possible cell toxicity in MC3T3-E1 cells were initially seeded overnight in a 96-well plate at a density of 5 x 10^3 cells/well, (n=5). Each plate well contained 200 µL of BM. Then, cells were treated with BM containing free Naringin or Naringin-loaded micelles at a final drug concentration of 0 (K-, negative control), 2, 5, 10, 20 and 50 µg/mL of Naringin. For blank and Naringin-loaded micelles cytotoxicity evaluation, nanocarriers were concentrated in BM and diluted according to the different tested concentrations. For blank micelles experiments, cells were incubated with BM containing nanocarrier dosages of 12.5, 25, 50, 75, 100, 200 µg nanocarriers/well.

In addition, cell cytotoxicity assays were also performed in hASCs as these cells are particularly interesting for cell-based therapies, particularly in the bone regeneration context. For these assays, hASCs were seeded at a density of 3.5 x 10^3 cells/well and different Naringin concentrations of 0 (K-, negative control), 5, 10, 20 and 50 µg/mL were used.

During the assays, all cells were incubated for 24, 48 and 72 h. After each timepoint, the BM was exchanged to BM containing AlamarBlue according to manufacturer's instructions. Following an overnight incubation period, the media was then transferred to a black clear bottom 96-well plate for analysis. AlamarBlue fluorescence was detected at an excitation/emission of λ_{ex} = 540 nm/ λ_{em} = 600 nm by using a multi-mode microplate reader. All conditions were normalized to the control group (BM) set at 100 % viability.

3.2.12 Cellular Proliferation Assays

The samples from the previous cytotoxicity assays were washed twice with dPBS and then each well was incubated with 200 µL of 2 % Triton X-100 and sonicated in an ultrasound bath for 7 min (37 Hz, sweep field, 60 % potency) before the plates were frozen at -20 ºC. This freeze-thaw cycle was repeated one more time before determining the double stranded DNA (dsDNA) content of the lysates. Then, in a clear bottom black 96-well plate, 25 µL of each sample was mixed with 25 µL of Tris-EDTA buffer (10 mM Tris-HCl, 1 mM EDTA, pH 7.5) and 50 µL of PicoGreen working solution. DNA content was extrapolated from a high range standard curve of bacteriophage lambda DNA (0, 50, 75, 150, 250 and 500 ng DNA/mL). The plate was gently shaken and incubated for 5 min in the dark at RT. Samples were excited at λ = 485 nm and fluorescence intensity was measured at λ = 520 nm in a microplate reader.

3.2.13 ALP Activity Measurement Assays

The ability of Naringin to induce osteogenic differentiation of hASCs was evaluated in OS-Dex or rOS. hASCs were seeded overnight in a 48-well culture plate at a density of 3.5 x 10^3 cells/well (*n*=5) in 300 µL of BM. After 24 h of cell seeding, medium was replaced with BM and OS-Dex containing free Naringin or Naringin-loaded polymeric nanomicelles at a concentration of 0 (control), 5, 10, 20 and 50 µg/mL of Naringin, accordingly. All cells were incubated for 3, 7, 14 and 21 days and the respective differentiation medium was exchanged every 3 to 4 days.

For ALP quantification cells were initially lysed by using the freeze-thaw technique to release ALP enzyme to the extracellular medium. Initially, cells were washed twice with dPBS and incubated with 300 µL of 2 % Triton X-100 solution in deionized water in an ultrasound bath for 7 min (37 Hz, sweep field, 60 % potency) before being frozen at -20 ºC. This freeze-thaw cycle was repeated one more time before determining ALP activity in the lysates by using 4NPhP ALP-mediated hydrolysis to quantify 4NPh release. For this quantification, 25 µL of each lysate sample were added to 75 µL of a freshly prepared 4NPhP solution (2 mg/mL) in 1 M diethanolamine (DEA) buffer (pH 9.8, with 0.5 mM $MgCl_2$). The samples were incubated in the dark at 37 ºC for 1 h. Enzyme activity was then quantified by UV-VIS analysis at λ = 405 nm. A standard curve of 4NPh was used as reference (0, 15 30, 50, 75, 95 µM in DEA buffer). The ALP activity was normalized according to the total DNA content in cell lysate determined by a PicoGreen® DNA Quantification kit according to the aforementioned protocol, and ALP was expressed as nanomole of p-nitrophenol/pg dsDNA.

3.2.14 ALP Staining Assays

To visualize the ALP activity in the cell monolayer, cells were stained with 1-Step™ NBT/BCIP Substrate Solution. Initially, hASCs were seeded overnight in 48-well plates at a density of 3.5 x 10^3 cells/well (*n*=3) in 300 µL of BM. After, cells were treated with BM and OS-Dex containing free Naringin or Naringin-loaded polymeric nanomicelles at a concentration of 0 (K-, negative control), 5, 10, 20 and 50 µg/mL of Naringin. Cells were incubated for 14 days and differentiation medium was exchanged every 3 to 4 days. After each timepoint, cells were pre-fixed with 4% formaldehyde fixative solution directly added into the culture medium. Afterwards, cells were incubated with 300 µL of 4 % formaldehyde fixative solution for 20 min, at RT. Then, cells were washed two times with dPBS and

incubated with 200 µL of NBT/BCIP for 1 hour at 37 ºC. Stained cells were imaged with a Stemi 508 Stereo Microscope (Zeiss, Taper, Sintra, Portugal).

3.2.15 ELISA Immunoassay Quantification of BMP-2 Secretion

The production of BMP-2 from hASCs was determined by an Enzyme-Linked Immunosorbent Assay (ELISA) kit for human BMP-2 quantification according to the manufacturer's instructions (Thermo Fisher Scientific, Alfagene, Lisbon, Portugal). For this assay, culture medium from the ALP activity experiments with OS-Dex at 14 and 21 days was collected and frozen at -20 ºC. Then, BMP-2 levels were quantified by UV-VIS analysis at λ = 450 nm with the absorbance measured at λ = 550 nm serving as correction factor by using a microplate reader. BMP-2 levels were expressed in pg/mL of BMP-2 normalized to dsDNA content (pg dsDNA).

3.2.16 Osteopontin Immunostaining

Osteopontin (OPN) expression was visualized via fluorescence imaging of the extracellular layer formed during *in vitro* culture. Initially, 13 mm tissue culture polystyrene coverslips (TCPS) (Sarstedt, Sintra, Portugal) were punched with a 3.5 mm biopsy punch (ZMED) to afford smaller coverslips. The coverslips were washed with absolute ethanol and dried in an oven (60 ºC) before undergoing UV sterilization for 30 min. Afterwards, TCPS were placed on the bottom of an adherent 48-well plate, where hASCs were seeded overnight at a density of 3.5 x 10^3 cells/well in 300 µL of BM. After, cells were treated with BM and OS-Dex containing free Naringin or Naringin-loaded polymeric nanomicelles at different concentrations. Cells were incubated for 14 days and differentiation medium was exchanged every 3 to 4 days. After each timepoint, cells were fixed as aforementioned and washed three times with dPBS. For immunostaining, cells were first incubated with 300 µL of 0.5 % Triton-X100 in dPBS for 5 min, at RT. Afterwards, cells were rinsed two times in dPBS and incubated in 300 µL of a 5 % FBS/dPBS blocking solution for 45 min, at RT. Afterwards, the cells were washed in dPBS and incubated with 20 µL of a mouse anti-human OPN antibody solution (dilution 1:100 in 5% FBS/dPBS; Biolegend, Taper, Sintra, Portugal) overnight at 4°C, in the dark. Cells were then washed with dPBS and incubated with 20 µL of an anti-mouse Alexa Fluor 647 conjugate dye solution (dilution 1:100 in 5 % FBS/dPBS; Alfagene, Lisbon, Portugal) for 1 h, at RT, in the dark. Finally, cells were rinsed three times in dPBS before incubating for 5 min with 20 µL of a DAPI solution for nuclei staining

(dilution 1:500, original aliquot at 5 mg/mL in H_2O), in the dark, at RT. Cells were then washed three times and the coverslips were transferred into microscopic slides for fluorescence microscopy analysis (Axio Imager M2, Carl Zeiss Microscopy GmbH). Image processing was performed by using ZEN v2.3 blue edition (Carl Zeiss Microscopy GmbH). For OPN quantification, the coverslips were imaged in 8 random regions using the 10x/0.25 NA Plan-Achromat objective. The OPN mean fluorescence intensity (MFI) of each condition was obtained as the mean value across the respective random fluorescence micrographs. During sample acquisition, light intensity from the HXP200 metal-halide lamp, camera binning and exposure time was maintained constant throughout the entire process.

3.2.17 Alizarin Red S Mineralization Assay

In order to detect mineral accumulation in osteogenic cells, staining with Alizarin Red S dye was performed. Alizarin Red S is an anthraquinone dye commonly used for histological characterization of calcium deposits [8]. For Alizarin Red S staining, hASCs were seeded overnight in 48-well plates on top of punched TCPS coverslips at a density of 3.5 x 10^3 cells/well (*n*=3) in 300 µL of BM. Afterwards, hASCs were treated with BM and OS-Dex containing free Naringin or Naringin-loaded polymeric nanomicelles at different concentrations. Cells were incubated for 21 days and differentiation medium was exchanged every 3 to 4 days. Afterwards, cells were fixed and washed as aforementioned, before being incubated with 300 µL of Alizarin Red S (40 mM, pH = 4.2), for 1 h in the dark at RT. After incubation, the staining solution was removed and cells were rinsed three times with deionized water. Stained monolayers were imaged with a Stemi 508 Stereo Microscope.

3.2.18 Statistical Analysis

The data obtained is expressed as the mean ± standard deviation (s.d.). Significant differences were analyzed by GraphPad Prism version 6.01. One-way ANOVA was used to determine the significant differences among groups, followed by a Newman-Keuls multiple comparison test for pairwise comparison. Two-way ANOVA was used for statistical analysis between two groups, where $P < 0.05$ was used for significance.

4 Results and Discussion

4.1 Synthesis and Characterization of mPEG-PLA Diblock Copolymer via ROP

The diblock copolymer mPEG-PLA aimed to be used as a precursor for the synthesis of self-assembled micellar nanocarriers was synthesized by ROP of the six-membered cyclic diester L-lactide using stannous octoate ($Sn(Oct)_2$) as a catalyst and mPEG-OH as an initiator (Figure 11). Metal alkoxides, such as $Sn(Oct)_2$, contain free d-orbitals and promote lactone polymerization through a coordination insertion mechanism resulting in the addition of two lactic acid monomers to the growing end of the polymer chain [9]. Herein, the Lewis acidic metal alkoxide coordinates with the carbonyl oxygen of the lactone and is followed by alkoxy insertion into the acyl oxygen bond. Cleavage of this acyl bond results in L-Lactide and produces metal alkoxide species that can reinitiate the cycle, this the main reason for the polymerization process to be named 'living polymerization' [10].

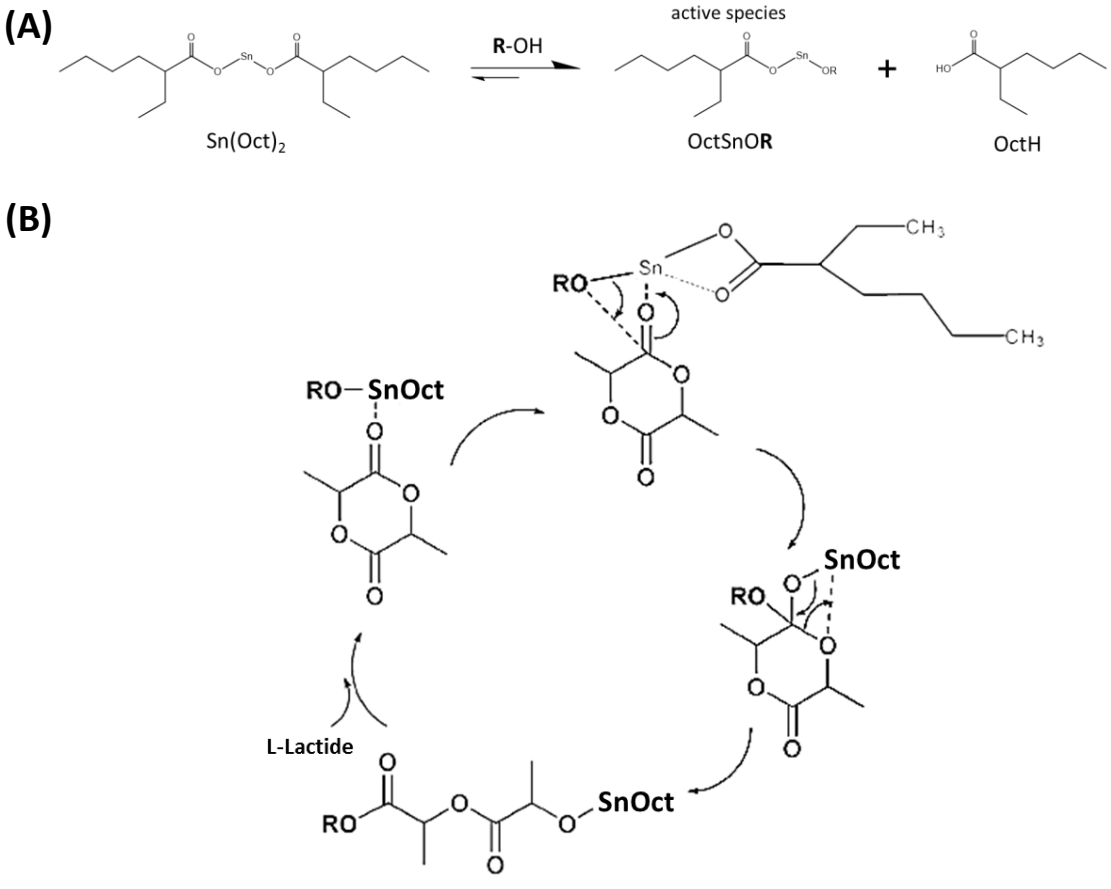

Figure 11. Coordination-insertion mechanism of $Sn(Oct)_2$ for the ROP of L-Lactide. **(A)** Formation of the active species initiator for the coordination-insertion reaction. **(B)** Opening of the lactide ring and insertion into a macroinitiator containing a hydroxyl end group (OR). Adapted from references [10–12].

The synthesis of mPEG-PLA via ROP proceeded as before described in the Methods Section 3.2.1. The resulting mPEG-PLA diblock copolymer and its reaction components were then characterized by ^{1}H NMR and ATR-FTIR. The proton NMR characterization is presented in Figure 12. As the ^{1}H NMR spectrum demonstrates, all the characteristic peaks of the synthesized copolymer are in agreement with those reported in the literature [13–15]. In detail, the peaks with a chemical shift at δ= 3.65 and δ= 3.38 ppm are assigned to mPEG repeating methylene units (c, O-**CH$_2$**-**CH$_2$**) and methoxy end group (d, **CH$_3$**-O), respectively [14]. The multiplet at δ= 5.17 ppm and the singlet at δ= 1.57 ppm are the characteristic protons of the PLA backbone and are attributed to the repeating methenyl (a, CH_3-**CH**-O) and methyl (b, **CH$_3$**-CH-O) units, respectively.[14] In addition, the characteristic chemical shift of the two lactide peaks at δ= 5.03 ppm (**CH**-CH_3) and δ= 1.66 (CH-**CH$_3$**) to PLA peaks δ= 5.17 and δ= 1.57 ppm, respectively, are indicative of a successful polymerization and absence of lactide monomer in the purified copolymer and thus, provide evidence that the obtained spectra does not correspond to a physical mixture of the monomers [16]. Moreover, in the mPEG-PLA copolymer spectrum it is possible to observe the presence of two peaks corresponding to the terminal repeating monomer of the PLA chain. The weak quartet signal obtained at δ= 4.34 ppm and the multiplet obtained at δ= 1.47 ppm are assigned to the methenyl (e, CH_3-**CH**-OH) and methyl (f, **CH$_3$**-CH-OH) protons that are neighbors of the PLA hydroxyl end group [15]. In addition, the characteristic peak of the $CDCl_3$ solvent was present at δ= 7.26 ppm in all spectra as expected.

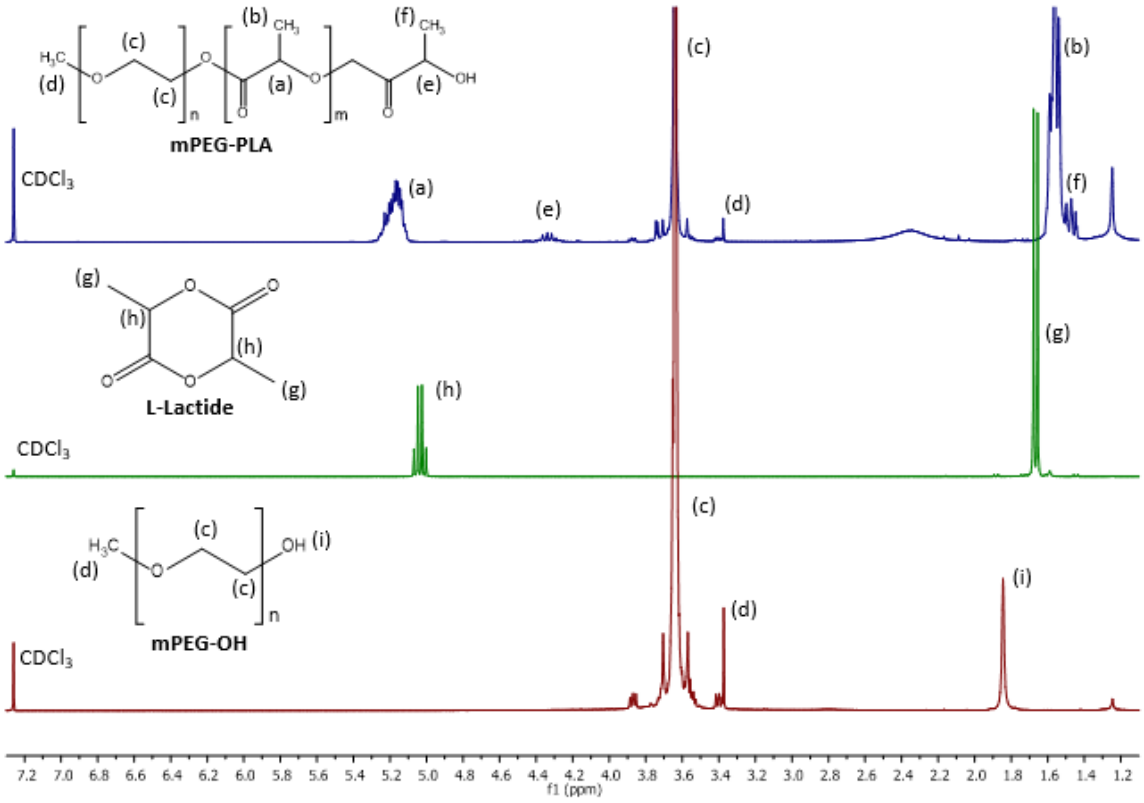

Figure 12. ^{1}H NMR spectra of mPEG-PLA diblock copolymer and its respective reaction reagents in $CDCl_3$.

As a complement to NMR characterization data, the ATR-FTIR spectra corroborated the successful synthesis of the diblock copolymer (Figure 13). Such is evident in the bands observed at 2883 and 2924 cm^{-1} which are assigned to **-C-H** stretching vibrations in mPEG and mPEG-PLA, respectively [13]. In addition, the strong band obtained at 1749 cm^{-1} corresponds to the **-C=O** stretching of lactic acid esters [17]. The bands present at 1545, 1454 and 1186 cm^{-1} correspond to asymmetric **-CH_3** bending and **-C-O-C-** stretching, respectively [18]. Moreover, the ATR-FTIR data obtained for mPEG-OH and mPEG-PLA shows a characteristic **C-O-C** ether asymmetric stretching band at 1095 and 1081 cm^{-1}, respectively [19]. It is important to emphasize that the absorption peak at 930 cm^{-1} for **-CO-O-** ring of lactide was absent from the FTIR spectrum of mPEG-PLA diblock copolymer. This peak is characteristic for the lactide monomer and can be used to differentiate between PLA and unreacted lactide monomers [15]. Taken together, both characterization techniques confirmed the successful synthesis of mPEG-PLA amphiphilic diblock copolymer by ROP.

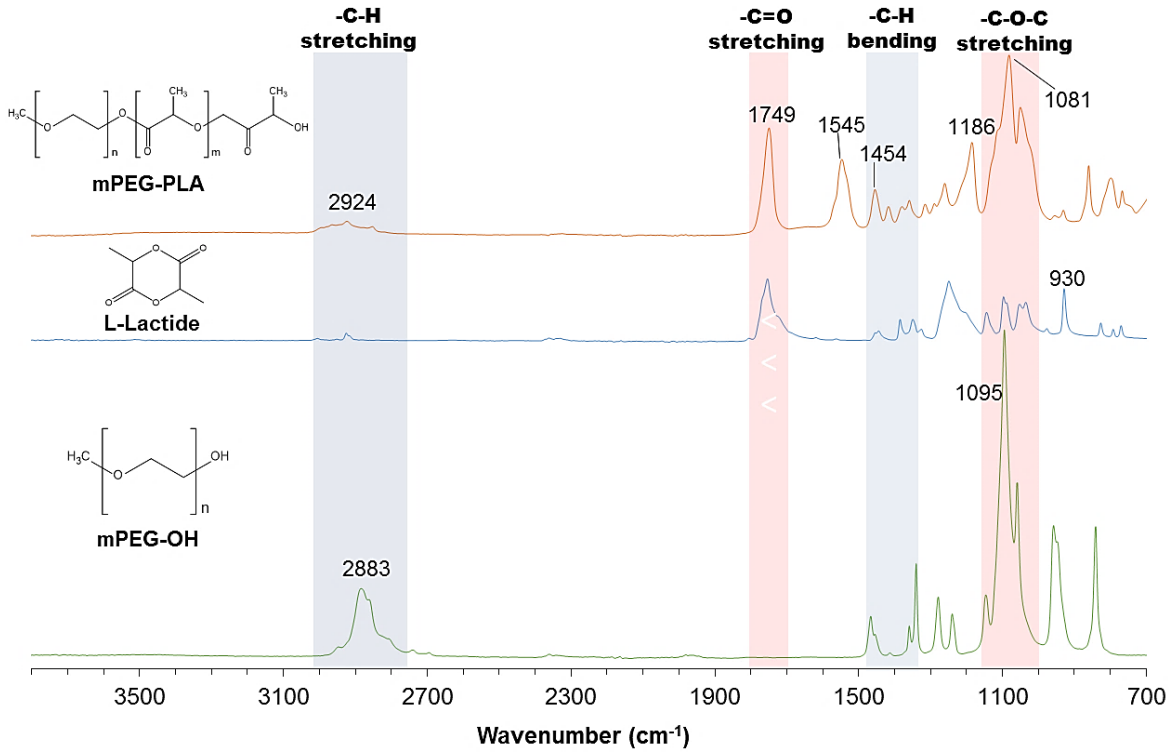

Figure 13. ATR-FTIR spectra of mPEG-PLA diblock copolymer and its respective reaction components.

The ROP of lactones is a widely-established method to produce aliphatic polyesters due to its ease of scale up, yield and cost effectiveness. In addition, its living polymerization nature leads to a better control in polymer chain lengths as well as physicochemical properties [10]. Some drawbacks of this synthesis include the use of toxic solvents (e.g. toluene) and heavy metals catalysts and the difficulty associated with their complete removal as recommended by regulatory agencies [20,21].

To overcome such limitations, novel alternatives have been focusing on the use of non-toxic catalysts containing calcium (e.g. calcium acetylacetonate) or by taking advantage of green chemistry-based enzymatic catalysts (e.g. lipase) to mediate the polymerization process [12,20]. Taking this into consideration, the selected catalyst for mPEG-PLA ROP-based synthesis was $Sn(Oct)_2$. This catalyst has a high activity and is approved by FDA-as a food additive. The main drawback regarding its use is the requirement for high reaction temperatures in order to achieve high monomer-to-polymer conversion rates. Such increases both inter- and intramolecular esterification and consequently contributes to polymer molecular weight polydispersity [11].

The molecular weight of the hydrophobic polymer backbone plays an important role in the context of amphiphilic micelles self-assembly process and on their final physicochemical

properties [22]. The length of the synthesized PLA hydrophobic polymer chain and most importantly, the reproducibility of this polymerization was analyzed by ^{1}H NMR spectroscopy. The ethylene oxide/lactyl (EO/LA) ratio of the copolymers was determined from the integration of NMR proton signals obtained at δ= 3.65 ppm (O-**CH_2-CH_2**) assigned to the repeating mPEG methylene groups, and from the peaks obtained at δ= 5.2 ppm (CH_3-**CH**-O) which correspond to repeating PLA methenyl units. The values of the corresponding integers were obtained after three measurements in MestReNova software. The number average molecular weight (M_n) of the PLA hydrophobic backbone was determined according to Equation 2, where 44 and 72 correspond to the molecular weight of the repeating monomers [23].

$$\text{Equation 2.}\ Mn(PLA) = \frac{72\ \times Mn(PEG)}{44} \times \frac{1}{EO/LA}$$

Self-assembled micelles were prepared as aforementioned in the Methods Section 3.2.4, and the corresponding micelle hydrodynamic radius (H_r), PDI and ζ-potential were obtained via DLS and electrophoretic mobility measurements. Table 2 showcases the resulting PLA hydrophobic block M_n and corresponding H_r, PDI and ζ-potential measurements relatively to each synthesis replicate.

The intra-batch copolymer variation was observed following a ROP synthesis (S2a and S2b). Generally, all reaction conditions and purifying steps were maintained for all replicates, except for S2a and S2b, in which the recovery rate of the purified polymer in the MetOH precipitation step was changed. It is worth noting that both S2a and S2b were obtained from the same synthesis replicate (S2). Basically, while S2a represents the polymer fraction that rapidly precipitated in cold MetOH, S2b corresponds to the slowest forming precipitate recovered after overnight precipitation. In agreement with this, S2a is enriched in PLA segments when compared to the slower forming precipitates in S2b, M_n (PLA) 3512 vs 1719, respectively. These findings may be correlated with mPEG solubility in MetOH and PLA insolubility in this polar solvent. Therefore, the longer the PLA block in the amphiphilic mPEG-PLA copolymer, the more hydrophobic the copolymer becomes, hence leading to faster precipitation rates. These observations show that the M_n range of polymerized PLA segments can potentially be reduced by adjusting the time of recovery after MetOH precipitation: the faster the recovery rate, the higher M_n of the recovered mPEG-PLA diblock copolymer. Regarding the effect of copolymer molecular weight in

nanocarrier formulations, Lebouille and colleagues found that final particle size should not depend on the polymer molar mass, when producing polycaprolactone nanoparticles with different molar masses (2, 4, 8, 25, 37, 50 and 80 kDa), while a theoretical analysis by Whitesides and Ross found that initial polymer PDI did not affect the final particle size [24,25]. Still, one needs to consider the differences between a solid polycaprolactone nanoparticle produced in the presence of a surfactant versus the more flexible PMs self-assembled via nanoprecipitation.

Table 2. Composition of mPEG-PLA diblock copolymer and respective micelle physicochemical properties

Synthesis	EO/LA[a]	M_n(PLA)[b]	H_r, nm[c]	PDI[c]	ζ-potential, mV[c]
S1	5.88	1391	144.9 ± 0.78 126.4 ± 0.31	0.208 ± 0.010 0.173 ± 0.009	-10.8 ± 1.15 -10.6 ± 0.88
S2a	2.33	3512	150.6 ± 5.80	0.355 ± 0.014	-10.1 ± 0.25
S2b	4.76	1719	222.2	0.327	-
S3	4.17	1962	-	-	-

[a] EO/LA ratio calculated from the integration of NMR resonances assigned to repeating mPEG and PLA units at δ= 3.65 and δ= 5.20 ppm, respectively. [b] M_n of PLA segment calculated from Equation 2. [c] PM physicochemical properties determined by DLS.

The ROP-synthesized mPEG-PLA diblock copolymer was then used for the self-assembly of polymeric nanomicelles. Blank PMs were prepared by the solvent exchange technique, also known as nanoprecipitation. In terms of micelle properties, disparities could be observed if micelles were formulated with the different batches of synthesized copolymers (Table 2). Initially, the S1 batch mPEG-PLA diblock copolymer was used to produce two nanomicelles formulations employing the same nanoprecipitation conditions. The results indicate that micelles produced from S1 batch exhibit similar size, PDI and ζ-potential if nanoprecipitation is performed in the optimized conditions described in detail in the Methods Section 3.2.9. However, in comparison to micelles formulated with the other synthesized copolymer batches, there are clear size discrepancies. While S1 copolymer yielded relatively small micelles (ca. Hr 137 nm, PDI 0.191), the copolymers obtained in the second synthesis (S2a and S2b) yielded larger micelles and with a significantly higher PDI.

Hydrodynamic particle size dispersity is an important parameter in nanocarrier formulations as highly polydisperse formulations can have different biological performances in comparison to nanocarrier formulations with narrower size range. Conversely, ζ-potential of the PMs was unaffected by variations in PLA M_n, from S1 (1391) to S2a (3518) exhibiting values of -10.6 mV and -10.1 mV, respectively, suggesting that this parameter is less susceptible to variations in PLA hydrophobic chain length.

The observed variability between micelles size and polymer synthesis affects manufacturing reproducibility and may impair the envisioned use of such nanomicelles for bone drug delivery and tissue engineering. In light of these findings, a simple alternative synthesis route for the mPEG-PLA copolymer was chosen, with the aim to achieve higher reproducibility.

4.2 Bioinstructive Naringin Micelles for Guiding Stem Cells Osteodifferentiation

Subchapter 4.2.

This subchapter is based on the article entitled
"*Bioinstructive Naringin-loaded Micelles for Guiding Stem Cells Osteodifferentiation*"
(manuscript in preparation)

Bioinstructive Naringin-loaded Micelles for Guiding Stem Cells Osteodifferentiation

Lavrador, P.[1], Gaspar, V.M.[1], and Mano, J.F.[1#]
[1]Department of Chemistry, CICECO – Aveiro Institute of Materials, University of Aveiro, Campus Universitário de Santiago, 3810-193, Aveiro, Portugal

[#]Corresponding author:
João F. Mano
E-mail: jmano@ua.pt

Abstract

Naringin is a naturally occurring hydrophobic flavanone with potential to promote the proliferation and osteogenic differentiation of mesenchymal stem cells. In this work, we report for the first time the delivery of Naringin through biodegradable mPEG-MS-PLA diblock polymeric micelles to human adipose-derived stem cells (hASCs) with the aim to explore its pro-osteogenic effect in these cells. The synthesis of the diblock copolymer was performed via Michael-type addition reaction between hydrophilic mPEG-MAL and hydrophobic PLA-SH and its success was confirmed by ^{1}H NMR and FTIR spectroscopy. The resulting mPEG-MS-PLA copolymer self-assembled into monodisperse polymeric micelles via nanoprecipitation (84.48 ± 2.44 nm) and a high Naringin encapsulation efficiency (87.8 ± 4.6 %) was obtained. The characterization of Naringin-loaded nanomicelles *in vitro* drug release profile revealed a sustained cargo release over time up to 7 days. Alongside, pre-clinical data revealed that that upon internalization in 2D cultures of hASCs, Naringin nanomicellar formulations attained a higher pro-osteogenic effect than that of the free drug. Moreover, Naringin-loaded micelles also induced superior osteopontin expression and increased matrix mineralization. Overall, these findings support the use of nanomicelles for Naringin delivery into hard-to-transfect hASCs, as a valid approach for modulating stem cells osteogenic differentiation.

Keywords: Controlled release, human adipose-derived mesenchymal stem cells, Naringin, osteogenic differentiation, polymeric micelles

1. Introduction

The potential of human mesenchymal stem cells (hMSCs) for osteogenic and chondrogenic differentiation has been widely explored for the treatment of various disorders including those related to bone tissues, heart (e.g. myocardial infarction), skin-grafts and hepatic or renal failure [26].

Among the different types of stem cells, human adipose-derived stem cells (hASCs) have been gaining attention as an attractive source of hMSCs for bone tissue engineering and regenerative medicine owing to their low immunogenicity, immunosuppressive and anti-inflammatory activity [27]. Adding to this, these cells are readily available due to their straightforward isolation from adipose tissue using minimally invasive techniques [27]. This unique set of features establishes these cells as promising candidates to be used for stem cell-based therapies. Unfortunately, the success of hASCs as gold standard models for cell-based therapies is limited by the technologies used for their osteogenic differentiation, in particular, pharmaceutical-based approaches.

Current approaches for pro-osteogenic differentiation rely on the use of drugs or recombinant proteins (e.g. Dexamethasone (Dex) and bone morphogenetic protein 2 (BMP-2)). These are often associated with deleterious side effects and low effectiveness. In fact, the glucocorticoid Dex can increase osteoblast differentiation but simultaneously induce adipogenesis even in osteogenic conditions [28]. The alternative use of BMPs for eliciting bone formation is also not without drawbacks as supraphysiological doses are usually needed to obtain the desired osteoinductive outcome [29]. Besides, BMPs have high production costs and could be denatured *in vivo*, which limits their applicability [30].

In light of this, there has been a shift towards the discovery of naturally available compounds with potential for modulating the process of stem cells differentiation. One of such bioinspired drugs is Naringin, a natural flavanone glycoside that can enhance the proliferation and differentiation of osteoprogenitor cells into osteoblasts, as well as inhibit osteoclasts maturation [31]. Naringin offers several advantages in comparison with synthetic pro-osteogenic drugs. For instance, in comparison with Dex, Naringin is capable of repressing adipogenesis while promoting the osteogenic commitment of hMSCs [32–34]. Also, Dex systemic administration is characterized by a plethora of deleterious side-effects [35], while Naringin is reported to possess a wide range of anti-oxidant, anti-inflammatory, anti-cancer and anti-microbial activities [31,36]. Moreover, Naringin is reported to enhance the

secretion of BMP-2 in osteoprogenitor cells [37]. Overall, this makes Naringin a promising candidate for inducing the osteodifferentiattion of hASCs. However, this flavanone has poor *in vivo* bioavailability and can be extensively metabolized upon administration, a factor that limits its clinical efficacy [38,39]. Therefore, Naringin bioactivity could be potentially improved by inclusion in a nanocarrier.

In this study, the potential of mPEG-MS-PLA nanomicelles-mediated Naringin delivery was explored for the first time in the context of flavanone-bioinstructed stem cell osteogenic differentiation. The obtained results indicate that nanomicelles have a high Naringin encapsulation efficacy and achieve a dose-dependent cellular internalization in hard to transfect hASCs. Osteogenesis induction assays demonstrated that Naringin intracellular delivery and spatiotemporal release improves hASCs commitment to osteogenic lineages, with significant calcium mineralization deposits being obtained in nanocarrier transfected stem cells in comparison to free drug controls. These results emphasize the valuable potential of Naringin nanodelivery as a cell-instructive approach that can then be extrapolated for application in bone tissue engineering and regenerative medicine.

2. Materials and Methods

2.1 Materials

Methoxypoly(ethylene glycol)-maleimide (mPEG-MAL) (Mn 5000, > 90 % purity), thiol-poly(L-lactide) (PLA-SH) (Mn 5000, PDI < 1.2); 4-Nitrophenyl phosphate disodium salt hexahydrate (4NPhP), 4-Nitrophenol 10 mM (4NPh), phosphate buffered saline (PBS), formaldehyde, Coumarin-6 (Coum-6), Naringin (> 95 % purity), β-glycerophosphate disodium salt hydrate (β-gly), Alizarin Red S, Triton X-100 and Amicon® Ultra-4 mL (3000 MWCO) were all purchased from Laborspirit (Lisbon, Portugal). Spectra/Por 1 dialysis tubing (6000 - 8000 Da MWCO) and Float-A-Lyzer G2 (3500 - 5000 Da MWCO) dialysis cassettes were purchased from Reagente 5 (Oporto, Portugal). Murine pre-osteoblast cell line subclone-4 (MC3T3-E1, *Mus Musculus*, ATCC® CRL-2593™) and human adipose-derived mesenchymal stem cells (hASCs, *Homo Sapiens*, ATCC® PCS-500-011™) were purchased from LGC Standards S.L.U. (Barcelona, Spain). Minimum Essential Medium α-modification (α-MEM), fetal bovine serum (FBS, E.U. approved, South American origin), antibiotic, TrypLE™ Xpress Enzyme with phenol red (1X), Quant-iT™ PicoGreen® dsDNA Assay Kit, AlamarBlue™, 1-Step™ NBT/BCIP Substrate Solution, and Wheat

Germ Agglutinin (WGA) Alexa Fluor® 594 conjugate dye and DAPI were purchased from Alfagene (Lisbon, Portugal). Dexamethasone (Dex, 96% purity) and Dulbecco's PBS were purchased from Thermo Fisher Scientific (Oeiras, Portugal). L-ascorbic acid 2-phosphate magnesium salt (AA) was purchased from VWR (Lisbon, Portugal).

2.2 Synthesis of mPEG-MS-PLA Copolymer

mPEG-MS-PLA copolymer was synthesized via a Michael-type addition reaction between mPEG-MAL and PLA-SH [1] (Figure 14). Briefly, mPEG-MAL (1.5 mPEG/PLA molar ratio, 0.04 mmol) and PLA-SH (0.0267 mmol) were dissolved in a mixture of acetone (v/v = 0.43) and sodium phosphate buffer (pH = 7.2, 100 mM, v/v = 0.57) containing EDTA (5 mM) and mixed under inert conditions (N_2) for 2 days at room temperature (RT). Afterwards, the resulting crude mixture was completely dried in a rotary evaporator (Buchi, Rotavapor® R-300), dissolved in dichloromethane and then precipitated in cold diethyl ether. The recovered precipitate was then dialyzed (6000 - 8000 Da MWCO) against deionized water for 72 h, before being frozen at -80 ºC and freeze-dried for storage.

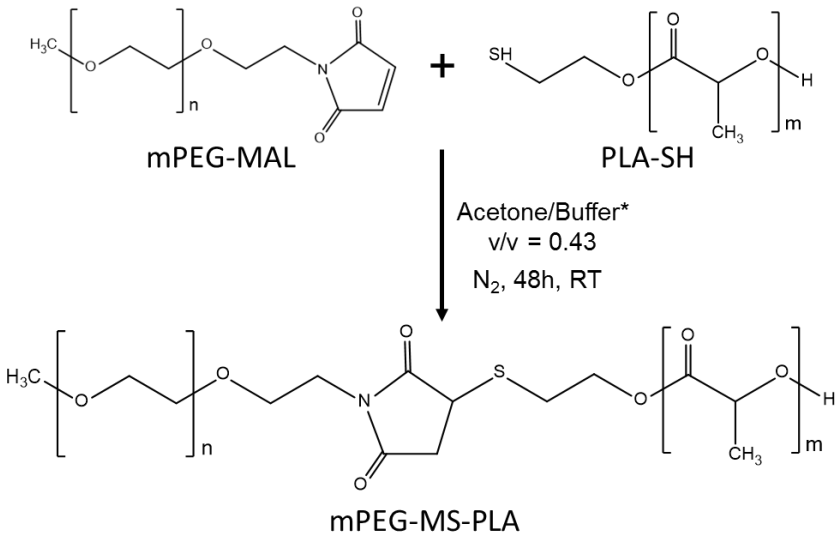

Figure 14. Synthesis route of mPEG-MS-PLA diblock copolymer via a Michael-type addition. *Phosphate buffer 100 mM, pH = 7.2, containing 5 mM EDTA.

2.3 Spectroscopy Characterization of mPEG-MS-PLA Copolymer

The successful synthesis of mPEG-MS-PLA was characterized by different spectroscopy techniques. Proton nuclear magnetic resonance (^{1}H NMR) spectra were recorded on a Bruker Advance III 400 MHz spectrometer. Prior to spectra acquisition, samples were dissolved in $CDCl_3$ and transferred to 300 MHz NMR glass tubes (Sigma-Aldrich, Sintra, Portugal).

NMR spectra were acquired with 18 s relaxation delay, 256 scans and 32 dummy scans. Data processing was performed in the MestReNova v6.0.2 software, and spectra were normalized according to the established $CDCl_3$ solvent peak at 7.26 ppm. Fourier Transformed Infrared spectra were collected on dried powder samples with attenuated total reflectance (ATR-FTIR) by using a Bruker Tensor 27 spectrometer. The spectra of all samples were recorded at a 4 cm^{-1} resolution with a total of 256 scans in the spectral width of 4000 to 350 cm^{-1}. Spectral data was processed in OPUS software.

2.4 Preparation of mPEG-MS-PLA Nanomicelles

Self-assembly of Naringin-loaded or blank mPEG-MS-PLA nanomicelles was performed by nanoprecipitation. First, the copolymer (5 mg) was dissolved in 1 mL of freshly prepared acetone solution containing Naringin (10 % w/w of copolymer) under ultrasound sonication for 5 min. Then, the solution was added dropwise into a 10 mL round-bottom flask containing 5 mL deionized water and stirred for 90 min at 400 rpm, RT. Afterwards, acetone was evaporated under a rotary evaporator during 8 min (37 ºC, 50 mbar). The resultant solution was dialyzed (3500 -5000 Da MWCO) against deionized water for 1 h to remove free Naringin. Blank micelles were prepared following the above-mentioned procedure without dialysis.

2.5 Physicochemical Characterization of Nanomicelles

The average hydrodynamic particle radius (H_r), size distribution (PDI) and ζ-potential of the different micelles (1 mg/mL) were characterized by dynamic light scattering (DLS) with a Zetasizer Nano ZS equipment (Malvern Instruments Ltd., Malvern, UK). All measurements were carried out in triplicate at 25 ºC and with a 173º backscatter angle. Nanomicelles morphology was observed by scanning transmission electron microscopy (STEM). Samples were prepared by drop-wise addition of 10 µL of freshly prepared micelles (0.2 mg/mL) on a carbon-film copper grid and left to dry overnight, at RT. STEM micrographs were acquired in a Hitachi SU-70 STEM microscope, operated at an accelerating voltage of 20.0 kV.

2.6 Evaluation of Nanomicelles Colloidal Stability

Nanomicelles colloidal stability was investigated by monitoring changes in size, PDI and ζ-potential along time upon storage in solution. For stability studies Naringin-loaded nanocarrier formulations (*n*=3), were prepared by nanoprecipitation and maintained in

deionized water or PBS (pH = 7.4) at 4 ºC. Nanomicelles and their physicochemical properties were then analyzed by DLS at different time intervals: 0, 1, 7 and 14 days.

2.7 Drug Loading

Naringin encapsulation efficiency was determined by ultraviolet-visible (UV-VIS) absorbance of the flavanone peak of Naringin (λ= 282 nm) corresponding to the benzoyl moiety. This peak is followed by a another region of smaller intensity to higher wavelengths (300 – 400 nm), associated with the cinnamoyl moiety and is characteristic of flavanones such as Naringin [5] (Figure 33, Annex I). Briefly, after free drug removal, Naringin-loaded nanomicelles solution (0.2 mg/mL) was analyzed by UV-VIS at 282 nm. Blank nanomicelles (0.2 mg/mL) established the blank for UV-VIS quantification. The UV-VIS absorbance was measured in a microplate reader equipped with a tungsten halogen lamp (Synergy HTX Biotek, Izasa Scientific, Carnaxide, Portugal) by using a quartz microplate (Hella transparent 96-wellplate, VWR, Lisbon, Portugal). A standard calibration curve of Naringin in deionized water was used to determine the drug encapsulation efficacy (Figure 33, Annex I). Encapsulation efficiency was calculated using the above equation:

Encapsulation Efficiency (%):

$$= \left(\frac{Amount\ of\ Naringin\ within\ the\ micelles)}{Theoretical\ amount\ of\ Naringin\ added}\right) \times\ 100$$

2.8 *In vitro* Drug Release Profile

The *in vitro* Naringin release profile was investigated in PBS at various pH conditions to mimic different physiological scenarios: pH 7.4 (physiological pH) and pH 5.5 (endo-lysosomal pH). Briefly, 2 mL of freshly prepared Naringin-loaded micelles (1 mg/mL) were transferred to a dialysis tubing (3500 - 5000 Da MWCO) and submerged in 15 mL of PBS at 37 ºC at a constant stirring rate (600 rpm). At defined time intervals, 1 mL samples were withdrawn from the dialysate and replaced with the same volume of fresh PBS. Samples were withdrawn at different time points until the plateau phase was achieved. For this study, the standard calibration curve of the drug in water was used (Figure 33, Annex I).

2.9 Cell Culture

All cells were manipulated within a Class II biological safety cabinet and maintained as per established guidelines in a humidified 5 % CO_2 atmosphere incubator with 95 % O_2 and

at 37 ºC [6]. MC3T3-E1 and hASCs were routinely cultured in α-MEM supplemented with 10 % (v/v) heat-inactivated FBS and 1 % of antibiotic mixture (basal growth medium, BM) and media was exchanged every 5 days. Cells were subcultured before reaching confluence. All plastic adherent well plates were made of tissue culture treated polystyrene (Sarstedt, Sintra, Portugal).

For cellular experiments investigating osteogenic differentiation, AA, β-gly and Dex stock solutions were prepared in dPBS and frozen at -20ºC. Different osteogenic media were prepared from such aliquots. Osteogenic supplements were added to BM in the following concentrations: (i) reduced osteogenic differentiation medium (rOS) - 50 µg/mL AA and 10 mM β-gly; and (ii) OS-Dex – rOS and 100 nM Dex. For preparation of free Naringin concentrations, the drug was initially dissolved in sterile dimethylsulfoxide (50 mg/mL) and subsequently diluted in the respective assay media (basal or osteogenic) and to a final 0.1 % (v/v) dimethylsulfoxide content across all concentrations. Osteogenic assays involving alkaline phosphatase (ALP) activity and BMP-2 quantifications, as well as OPN and Alizarin Red S visualization followed the below described conditions (Table 3).

Table 3. Overview of the conditions used in osteogenic differentiation assays.

Assay	Culture medium	Pharmaceutic	Dosing regime	Total incubation time
I, OS-Dex	AA + β-gly + Dex (OS)	Naringin	Single	21 d
II, One dose	AA + β-gly (rOS)	Naringin; Naringin-loaded micelles	Single	7 d
II, Two dose	AA + β-gly (rOS)	Naringin; Naringin-loaded micelles	Double	7 d

Across all experiments, medium was exchanged every 3 days containing the respective osteogenic supplements listed above, except for the Two dose assay, where medium with a second dose of pharmaceutic was added after 3 days. Please see the respective dose regimen schematics in each result panel.

2.10 *In vitro* Cellular Uptake Studies

2.10.1 Fluorescence Microscopy

Nanomicelles cellular uptake kinetics in MC3T3-E1 pre-osteoblasts and hASCs were evaluated via fluorescence microscopy. Briefly, MC3T3-E1 and hASCs were seeded in µ-Slide 8-well chambers (ibidi GmbH) overnight at a density of 8.0 and 25.0 x 10^3 cells/well, respectively, in free-antibiotic BM. Then, cells were incubated with 250 µg/well of Coum-

6-loaded nanocarriers for different time intervals (2, 4 and 6 h). After each time point, cells were fixed in 4% formaldehyde. After 6h, fixed cells were washed three times with dPBS and then the cells cytoplasm was labelled with 50 µL of WGA Alexa Fluor® 594 conjugate dye (0.2 mg/mL) by incubating for 5 min in the dark. Afterwards, cells were rinsed three times in dPBS and maintained in dPBS until fluorescence microscopy analysis. Confocal laser scanning microscopy (CLSM) and fluorescence microscopy (Axio Imager 2, Zeiss) were used to follow the kinetics of intracellular internalization of the nanocarriers. Image processing was performed using ZEN v2.3 blue edition software (Carl Zeiss Microscopy GmbH).

2.10.2 Flow Cytometry

The quantitative measurement of Coum-6 fluorescence intensity was conducted using a flow cytometer. MC3T3-E1 and hASCs were seeded in 24-well plates overnight at a density of 50 and 40 x 10^3 cells/well (n=4) respectively, in free-antibiotic BM. Then, cells were incubated with the 96-well plate equivalent of 25, 50 and 100 µg of Coum-6- nanocarriers per well. Nanocarriers were previously concentrated by centrifuging for 30 min in Amicon® ultra centrifugal units (3000 Da MWCO) at 16600 g. After 4 h incubation, cells were washed twice with dPBS, trypsinized (500 µL, 5 min incubation at 37ºC), neutralized with equal volume of dPBS and collected by centrifugation at 500g for 5 min. Then, the supernatant was aspirated and cells were suspended in 200 µL of dPBS prior to fluorescent intensity measurements.

2.11 Cytotoxicity Assays

Assessment of MC3T3-E1 and hASCs cell metabolism was performed by using the AlamarBlue® Cell Viability assay. Briefly, MC3T3-E1 cells were seeded in a 96-well plate overnight at a density of 5 x 10^3 cells/well (n=5) in BM. Then, cells were incubated with BM containing free Naringin or Naringin-loaded micelles at a final drug concentration of 0 (K-, negative control), 2, 5, 10, 20 and 50 µg/mL of Naringin. For blank and Naringin-loaded micelles cytotoxicity evaluation, nanocarriers were concentrated in BM and diluted according to the different tested concentrations. For blank micelles experiments, cells were incubated with BM containing nanocarrier dosages of 12.5, 25, 50, 75, 100, 200 µg nanocarriers/well. In addition, cell cytotoxicity assays were also performed in hASCs as these cells are particularly interesting for cell-based therapies, particularly in the bone

regeneration context. For these assays, hASCs were seeded at a density of 3.5 x 10^3 cells/well and different Naringin concentrations of 0 (K-, control), 5, 10, 20 and 50 µg/mL were used.

During the assays, all cells were incubated for 24, 48 and 72 h. After each timepoint, the medium was exchanged to BM containing AlamarBlue according to manufacturer's instructions. Following an overnight incubation period, the media was then transferred to a black clear bottom 96-well plate for analysis. AlamarBlue fluorescence was detected at an excitation/emission of λ_{ex} = 540 nm/ λ_{em} = 600 nm by using a multi-mode microplate reader. All conditions were normalized to the control group (BM) set at 100 % viability.

2.12 Cellular Proliferation Assays

Samples from the previous cytotoxicity assays were rinsed with dPBS, incubated with 200 µL of 2 % Triton X-100 in deionized water and sonicated for 7 min before plates were frozen at -20 ºC. This freeze-thaw cycle was repeated one more time before determining lysates double-stranded DNA (dsDNA) content with the PicoGreen kit according to the manufacturer's instructions. Cell dsDNA content was then determined after incubation for 5 min in the dark at RT. The samples were excited at λ = 485 nm and fluorescence intensity was measured at λ = 520 nm in a microplate reader.

2.13 ALP Activity Measurement Assays

The ability of Naringin to induce osteogenic differentiation of hASCs was evaluated in OS-Dex or rOS. hASCs were seeded overnight in a 48-well plate at a density of 3.5 x 10^3 cells/well (*n*=5) in BM. Then, medium was replaced with BM and OS-Dex containing free Naringin or Naringin-loaded polymeric nanomicelles at a concentration of 0 (control), 5, 10, 20 and 50 µg/mL of Naringin, accordingly. All cells were incubated for 3, 7, 14 and 21 days and the respective differentiation medium was exchanged every 3 to 4 days. After each time point, cells were washed twice with dPBS and incubated with 300 µL of 2 % Triton X-100 solution in an ultrasound bath for 7 min (37 Hz, sweep field, 60% potency) before being frozen at -20 ºC. This freeze-thaw cycle was repeated one more time before determining ALP activity in the lysates by using 4NPhP ALP-mediated hydrolysis to quantify 4NPh release. For this quantification, 25 µL of each lysate sample were added to 75 µL of a freshly prepared 4NPhP solution (2 mg/mL) in 1 M diethanolamine (DEA) buffer (pH 9.8, with 0.5 mM $MgCl_2$). The samples were incubated in the dark at 37ºC for 1 h. Enzyme activity was then quantified by UV-VIS analysis at λ = 405 nm. A standard curve of 4NPh was used as

reference (0, 15 30, 50, 75, 95 µM in DEA buffer). ALP activity was normalized according to the total DNA content in cell lysate determined by a PicoGreen® DNA Quantification kit according to the aforementioned protocol, and ALP was expressed as nanomole of p-nitrophenol/pg DNA.

2.14 ALP Staining

To visualize the ALP activity in the cell monolayer, cells were stained with 1-Step™ NBT/BCIP Substrate Solution. Briefly, hASCs were seeded overnight in 48-well plates at a density of 3.5 x 10^3 cells/well (n=3) in BM. Then, cells were treated with BM and OS-Dex containing free Naringin or Naringin-loaded polymeric nanomicelles at a concentration of 0 (K-, control), 5, 10, 20 and 50 µg/mL of Naringin. Cells were incubated for 14 days and differentiation medium was exchanged every 3 to 4 days. After each timepoint, cells were fixed as aforementioned and rinsed in dPBS before adding 200 µL of NBT/BCIP and incubating for 1 h at 37 ºC. Stained cells were imaged with a Stemi 508 Stereo Microscope (Zeiss, Taper, Sintra, Portugal).

2.15 ELISA Immunoassay Quantification of BMP-2 Secretion

BMP-2 secretion from hASCs was determined via ELISA kit for human BMP-2 according to the manufacturer's instructions. For this assay, culture medium from the ALP activity experiments with OS-Dex at 14 and 21 days was collected and frozen at -20ºC. Then, BMP-2 levels were quantified by UV-VIS analysis at λ = 450 nm with the absorbance measured at λ = 550 nm serving as correction factor by using a microplate reader. BMP-2 levels were expressed in pg/mL of BMP-2 normalized to dsDNA content.

2.16 Osteopontin Immunostaining

Osteopontin (OPN) expression was visualized via fluorescence imaging of the extracellular layer formed during *in vitro* culture. Initially, hASCs were seeded in TCPS coverslips overnight at a density of 3.5 x 10^3 cells/well in BM. After, cells were treated with BM and OS-Dex containing free Naringin or Naringin-loaded polymeric nanomicelles at different concentrations. Cells were incubated for 14 days and differentiation medium was exchanged every 3 to 4 days. After each timepoint, cells were fixed as aforementioned and rinsed in dPBS.

For immunostaining, cells were first incubated with 0.5 % Triton-X100 in dPBS for 5 min, at RT. Afterwards, cells were rinsed in dPBS and incubated with a 5 % FBS/dPBS

blocking solution for 45 min, at RT. Then, cells were washed in dPBS and incubated with 20 µL of a mouse anti-human OPN antibody solution (dilution 1:100 in 5% FBS/dPBS; Biolegend, Taper, Sintra, Portugal) overnight at 4°C, in the dark. Cells were then washed with dPBS and incubated with 20 µL of an anti-mouse Alexa Fluor 647 conjugate dye solution (dilution 1:100 in 5 % FBS/dPBS) for 1 h, at RT, in the dark. Finally, cells were rinsed three times in dPBS before incubating for 5 min with 20 µL of a DAPI solution for nuclei staining (dilution 1:500, original aliquot at 5 mg/mL in H_2O), in the dark, at RT. Cells fluorescence microscopy analysis was performed in a Axio Imager M2 widefield microscope (Carl Zeiss Microscopy GmbH). Image processing was performed by using ZEN v2.3 blue edition. For OPN quantification, 8 random coverslip regions were imaged by using the 10x/0.25 NA Plan-Achromat objective.

2.17 Alizarin Red S Mineralization Assay

In order to detect mineral accumulation in osteogenic cells, staining with Alizarin Red S dye was performed. For Alizarin Red S staining, hASCs were seeded overnight in 48-well TCPS coverslips at a density of 3.5 x 10^3 cells/well (n=3) in BM. Cells were treated with BM and OS-Dex containing free Naringin or Naringin-loaded polymeric nanomicelles at different concentrations. Cells were incubated for 21 days and differentiation medium was exchanged every 3 to 4 days. Afterwards, cells were fixed and washed as aforementioned, before incubation with 300 µL of Alizarin Red S (40 mM, pH = 4.2), for 1 h in the dark at RT. After incubation, the staining solution was removed and cells were rinsed three times with deionized water. Stained monolayers were imaged with a Stemi 508 Stereo Microscope.

2.18 Statistical Analysis

The data obtained is expressed as the mean ± standard deviation (s.d.). Significant differences were analyzed by GraphPad Prism version 6.01. One-way ANOVA was used to determine the significant differences among groups, followed by a Newman-Keuls multiple comparison test for pairwise comparison. Two-way ANOVA was used for statistical analysis between two groups, where $P < 0.05$ was used for significance.

3. Results and discussion

3.1 Synthesis of mPEG-MS-PLA Copolymer

The conjugation of commercially available copolymers, namely methoxypoly(ethylene glycol)-maleimide (mPEG-MAL, 5000 Da, PDI < 1.2) and thiol-poly(L-lactide) (PLA-SH, 5000 Da, PDI < 1.2) was selected as a valid alternative to improve reproducibility in nanomicelles synthesis. By using commercially available polymers the variability associated with the chemical synthesis process was reduced.

A highly selective conjugation was accomplished through Michael-type addition reaction between the thiolated polymer (PLA-SH) and the double bond of the N-substituted maleimide group in mPEG-MAL, that resulted in a succinimidyl thioether adduct [40]. Maleimides are capable of selectively conjugating to thiols in the pH range of 6.5 – 7.5 to afford thiosuccinimide bonds [2]. Whilst at physiological pH the reaction between maleimide and sulfhydryl proceeds at several orders of magnitude (10^3) faster than that with amines, at higher pH values (> 8.0) maleimides will also react with amino groups [2,41]. In addition, it is worth noting that the kinetics of thiol oxidation (15.2 M^{-1} s^{-1})[3] are several orders of magnitude (10^2) slower than the corresponding rates of Michael-type addition (1.3×10^3 M^{-1} s^{-1})[40], which is why significant formation of PLA-SS-PLA dimers was not expected. Nevertheless, since the purification of the synthesized mPEG-MS-PLA copolymer from these dimers can be challenging, the reaction protocol was modified to guarantee negligible formation of these side species (*i*.e. molar excess of mPEG-MAL, inert conditions (N_2) and addition of EDTA to reduce thiol-oxidation). In addition, the maleimide ring can self-hydrolyze in aqueous buffers to a non-reactive cis-maleimide carboxylic acid derivative over long reaction times or moderately basic (> 8.0) pH conditions (Figure 15). [42] Hence, in order to minimize the ring-opening of maleimide prior to thiol-binding, the reaction mixture consisted of phosphate buffer with pH = 7.2 to promote dissolution of hydrophilic MAL-PEG chains, while acetone was subsequently added to slowly promote the dissolution of the PLA-SH hydrophobic block.

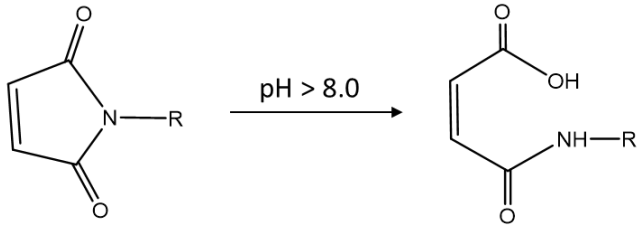

Figure 15. Self-hydrolysis of maleimide ring in aqueous buffer with moderate basic pH (> 8) to a non-reactive cis-maleimide carboxylic acid derivative.

mPEG-MS-PLA diblock copolymer and its reaction components were then characterized by ^{1}H NMR and ATR-FTIR. The obtained ^{1}H NMR spectrum of the synthesized copolymer is in agreement with literature reports and exhibit the characteristic peaks of both hydrophilic and hydrophobic blocks (Figure 16). The resonances assigned to mPEG repeating methylene units (c, O-**CH$_2$-CH$_2$**) and methoxy end group (d, **CH$_3$**-O), respectively at δ= 3.63 and δ= 3.37 ppm, are present in both mPEG-MAL as well mPEG-MS-PLA diblock copolymer spectra [14]. The multiplet obtained at δ= 5.16 ppm and the single peak at δ= 1.57 ppm are characteristic of the PLA backbone and are present in both PLA-SH as well mPEG-MS-PLA spectra [14,15]. These peaks correspond to repeating methenyl (a, CH$_3$-**CH**-O) and methyl (b, **CH$_3$**-CH-O) units, respectively. Regarding the PLA-SH spectrum, two distinct peaks can be distinguished between δ= 4.2 - 4.4 ppm: one corresponding to the methenyl (g, CH$_3$-**CH**-OH) proton neighbor of the hydroxyl end group at δ= 4.34 ppm, and the other corresponding to the methylene protons adjacent to the ester linkage closest to the terminal thiol (f, –O-**CH$_2$**-CH$_2$-SH) at δ= 4.25 ppm [43]. In addition, the peak around δ= 2.75 ppm corresponds to the methylene protons adjacent to the thiol end-group (e, –O-CH$_2$-**CH$_2$**-SH) confirming that PLA-SH was not oxidated to the disulfide form [43]. If the disulfide was present a characteristic peak of methylene protons adjacent to disulfides would be present instead at δ= 2.9 ppm as described by Cunningham and Oh [43]. Finally, the singlet observed at δ= 6.70 ppm on the mPEG-MAL spectrum is assigned to the alkene protons (**CH=CH**) present in the maleimide ring [44]. The successful coupling mPEG-MS-PLA is further supported by the disappearance of this characteristic peak assigned to the maleimide moiety as well as the appearance of PLA-related resonances on the copolymer spectrum.

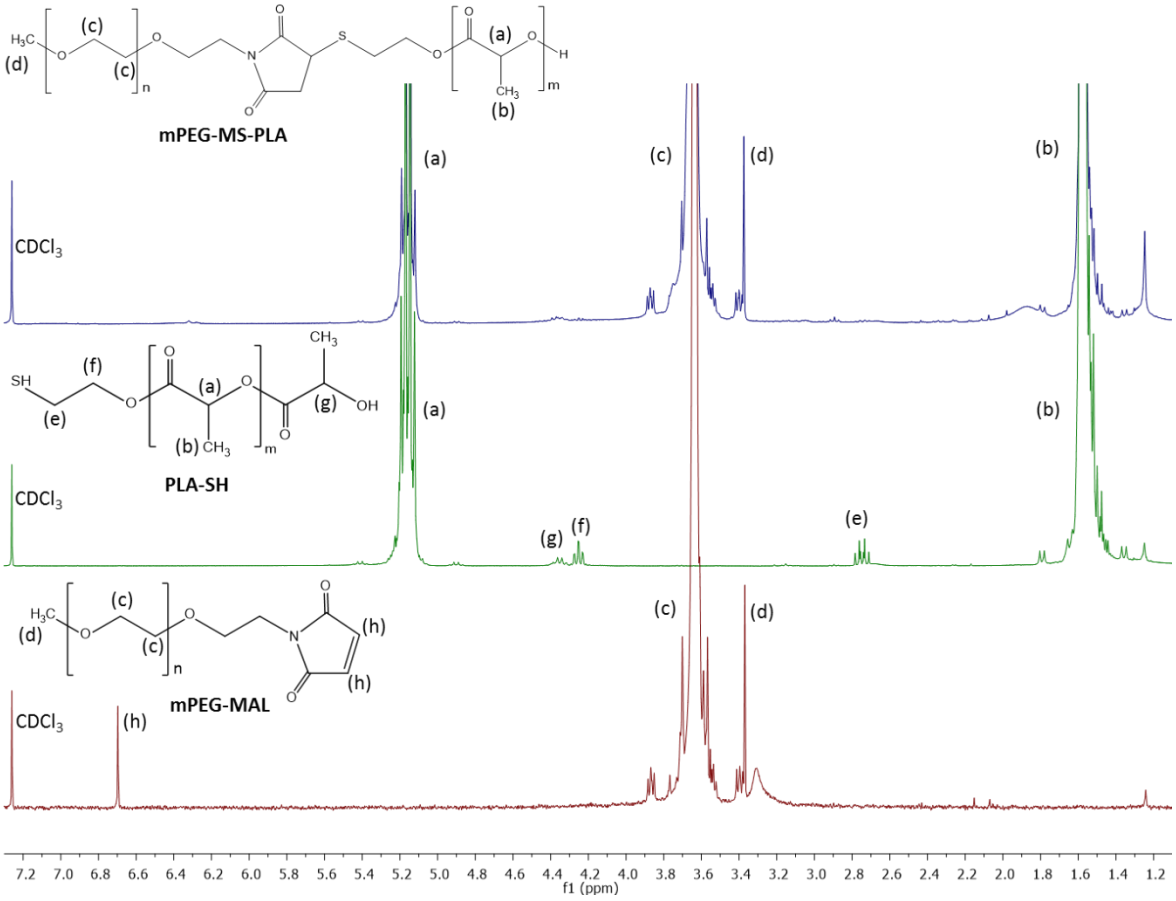

Figure 16. ^{1}H NMR spectra of mPEG-MS-PLA diblock copolymer and its respective reaction components in $CDCl_3$.

Adding to NMR characterization, the ATR-FTIR spectra also corroborated the successful conjugation of mPEG-MAL and PLA-SH polymers (Figure 17). The initial analysis of the individual polymers reveals a band at 2883 cm^{-1}, which is assigned to **-C-H** stretching vibrations (CH_2 symmetric), and is present in both mPEG-MAL and mPEG-MS-PLA spectra [45]. In addition, the strong band obtained at 1755 cm^{-1} corresponds to the carbonyl (**-C=O**) stretching of lactic acid esters in the PLA-SH polymer [18]. This band shifted to 1751 cm^{-1} for the mPEG-MS-PLA copolymer. Regarding mPEG-MAL, the characteristic band obtained at 1711 cm^{-1} is assigned to carbonyl (**-C=O**) stretching of the imide ring [46]. This finding was confirmed by performing a comparison between mPEG-MAL and mPEG-OH as shown in the inset (Figure 17). This maleimide-related band appears as a small shoulder in the copolymer spectrum, corroborating a successful synthesis. Alternatively, the small peak obtained at 696 cm^{-1} in the mPEG-MAL spectrum corresponds to cis-**CH=CH** imide and is reported to be characteristic of unreacted maleimide groups [46,47]. Therefore, it could be useful for further corroborating the conjugation of the two polymers. However, this weak

band is overlapped in the copolymer spectra with the characteristic PLA bands in the region of 760-650 cm^{-1}. Moreover, the peak observed in mPEG-MAL at 1466 cm^{-1} corresponds to **-C-H** deformation (CH_2 scissoring), while the peak at 1456 cm^{-1} is assigned to **-CH_3** bending in the PLA-SH spectrum [18,19]. Indeed, both peaks are visibly overlapped in the 1467-1455 cm^{-1} region in the copolymer spectrum, hence indicating the presence of both polymers (Figure 17).

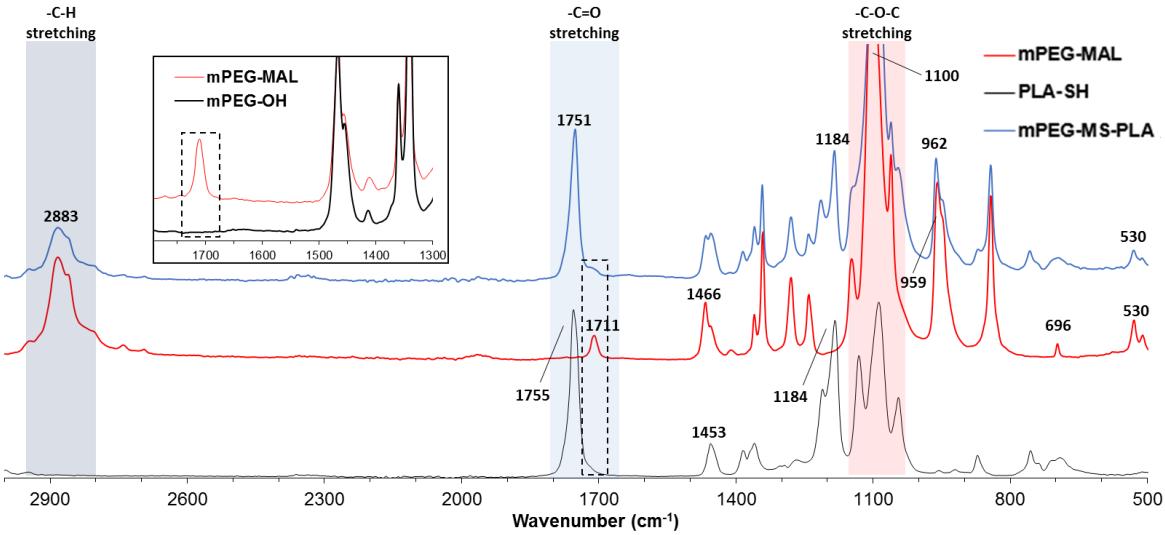

Figure 17. ATR-FTIR spectra of mPEG-MS-PLA diblock copolymer and its respective reaction components.

Adding to this, the spectra of PLA-SH and mPEG-MS-PLA copolymer exhibit a characteristic band at 1184 cm^{-1} which is assigned to **-C-O** bending in lactic acid esters [17]. The **-C-O-C** ether asymmetric stretching vibrations present in both PEG and PLA overlap in the range 1150 to 1040 cm^{-1} [18,45]. Furthermore, the bands at 959 and 962 cm^{-1} correspond to **-CH_2** rocking (**CH_2-CH_2**-O) in mPEG-MAL and mPEG-MS-PLA copolymer, respectively, further confirming the presence of the mPEG backbone in the final copolymer [19]. In addition, the band at 529 cm^{-1} is assigned to the characteristic **-C-C** vibration in mPEG repetitive chains and is present in both the monomer as well as the corresponding copolymer [45]. According to the work of Younes and Cohn, the degree of crystallinity can be roughly appreciated by comparing the two bands related with the crystalline (C, ca. 755 cm^{-1}) and the amorphous (A, ca. 869 cm^{-1}) phases of PLA.[48] In the obtained spectrum, the corresponding C and A bands are located at 756 and 870 cm^{-1} for the copolymer, and at 754 and 872 cm^{-1} for the PLA-SH monomer. Because the absorbance ratio of these two bands is approximately 1, the polymers are amorphous. Taken together, both characterization

techniques establish the successful conjugation of the two monomers, resulting in the mPEG-MS-PLA copolymer. This synthesis alternative not only allows for facile production of a reproducible mPEG-MS-PLA diblock copolymer, but can also be carried out under mild reaction conditions.

3.2 Optimization of Nanomicelles Self-assembly via Nanoprecipitation

mPEG-MS-PLA core-shell type PMs were produced via the nanoprecipitation technique as before described (Methods Section 3.2.5) [49]. Micelles physicochemical properties were optimized by manipulating different formulation parameters including: (i) stirring time, (ii) stirring speed and (iii) type of stirring plate (Table 4).

Table 4. Different formulations and its respective parameter modifications.

Stirring Plate	Formulation	Stirring speed (rpm)	Stirring time (min)
1	F1	600	120
	F2	500	90
2	F3	500	90

Stirring plate used: 1 - magnetic stirrer/hot plate MR Hei-Tec. 2 – Ovan MultiMix D multi-stirrer.

The physicochemical properties of the different nanocarriers produced during this optimization process are shown in Figure 18. The obtained results indicate that mPEG-MS-PLA micelles size decreased across formulations, ranging from an initial size of 111.9 ± 8.6 nm to a final size of 83.0 ± 4.8 nm. The obtained results indicate that decreasing stirring speed led to the formation of slightly smaller micelles, which is consistent with findings of the previous work by Asadi and colleagues studying factors that can influence particle size.[50] Furthermore, by switching to MultiMix D (VWR, Lisbon) multi-stirrer plate consistently smaller micelles were obtained (Formulation F3). This size reduction was accomplished while maintaining the monodisperse character of micellar formulations below the acceptable threshold (PDI < 0.200).

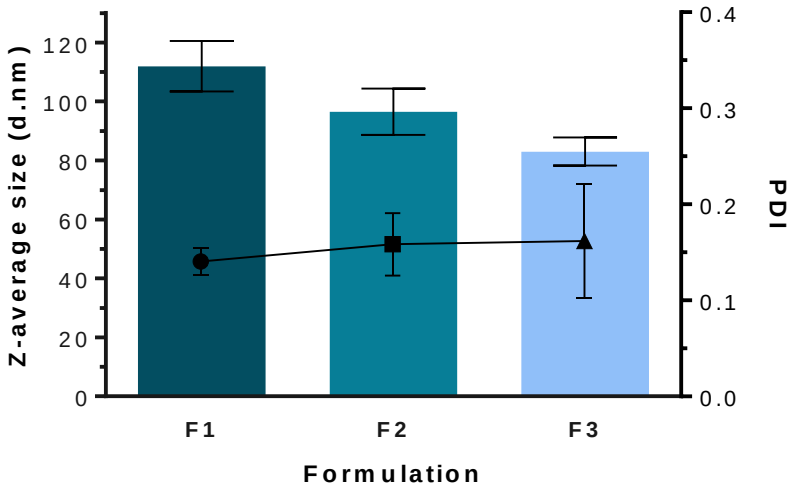

Figure 18. Characterization of different blank mPEG-MS-PLA micellar formulations by DLS. Size (left y axis, bars) and PDI (right y axis, connected dots). Data is represented as mean ± s.d. (*n*=3).

It is important to note that the obtained final particle size is suitable for delivery, because nanomaterials smaller than 5 - 6 nm are rapidly eliminated by the kidneys, whereas nanoparticles with diameters over 150 - 200 nm accumulate significantly in MPS organs such as the spleen and liver, where they are subsequently processed and excreted from the body [51,52]. Furthermore, the literature review (Introduction Section 1.7) performed on the current knowledge of the physiological barriers for bone delivery suggests that maintaining a nanocarrier size between 60 - 100 nm might be valuable for improving both para- and transcellular uptakes into the marrow stroma. From this standpoint, the subsequent experiments to investigate Naringin drug loading were performed with micelles produced with the experimental parameters from formulation F3.

3.3 Formulation of Naringin-loaded Nanomicelles

Naringin drug loading was promoted during nanoprecipitation mediated self-assembly by mixing the drug with the copolymer in the organic phase. Micelles were then formulated as before described via drop-wise addition of drug-copolymer mixture into a determined amount of aqueous solution (V= 5 mL, RT). Naringin-loaded and blank (control) micelles physicochemical properties, such as H_r, PDI and surface charge (ζ-potential) were then characterized by DLS and electrophoretic mobility, respectively. The obtained data presented in Figure 19 shows that blank micelles (75.15 ± 1.06 nm) are smaller than those loaded with Naringin (84.48 ± 2.44 nm). This contrasts with some literature reports which indicate that the encapsulation of hydrophobic drugs reduces particle size [53,54]. The main

driving force for drug loading in micelles is the hydrophobic interaction that is established between the drug and polymer blocks of the polymeric micelle core [53]. In fact, the physical entrapment of lipophilic small molecules generally leads to a decrease in micelle size, but as documented by Wang and colleagues an increase in the size of PEG-PLA core-shell nanomicelles can be observed after entrapping Doxorubicin hydrochloride salt [55]. The authors attributed this finding to the presence of Doxorubicin which increased the volume of the core.

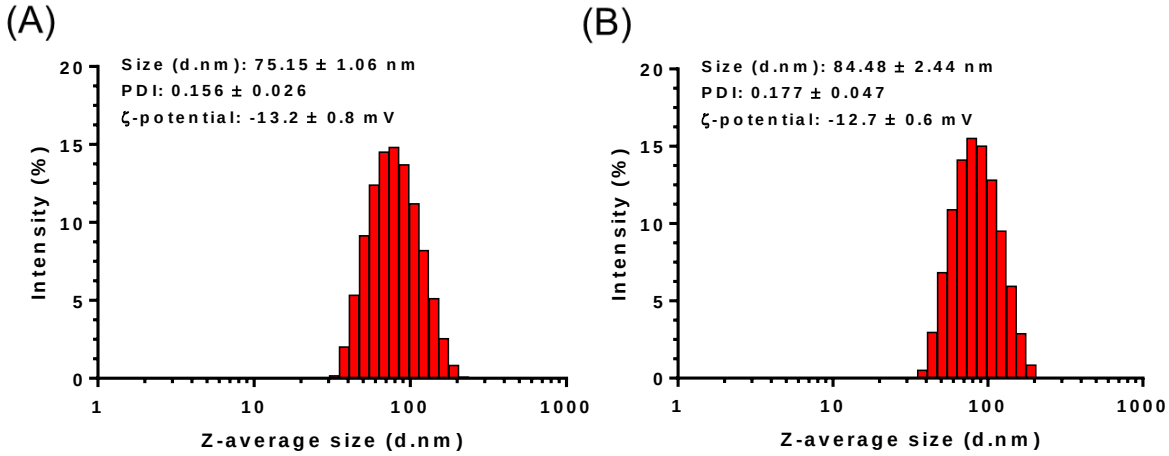

Figure 19. Physicochemical characterization of blank (A) and Naringin-loaded (B) mPEG-MS-PLA micelles via DLS analysis. Each measurement was performed in triplicate and includes at least three different replicates (n=3).

Considering the amphiphilic features of the flavanone glycoside Naringin, this could explain the small increase in hydrodynamic size of the drug-loaded micelles over blank micelles. Indeed, Naringin's bulkier non-planar structure comprised by hydrophobic (aglycone, Naringenin) and hydrophilic (glycoside, Neohesperidose) domains could potentially decrease the hydrophobic interactions with PLA micelles core. This hypothesis is supported by the work of Sanver on experimental modelling of flavonoid membrane interactions, which suggests that flavonoids such as Naringin may partition in the lipid/water interface [56]. Moreover, Yan and his team studied Naringin/β-cyclodextrin (β-CD) inclusion complexes, where computational and experimental simulations indicated that while the benzene ring of Naringin was embedded within the hydrophobic (β-CD) cavity, the glycoside domain was on plane with the relatively hydrophilic outer wide rim [57]. Moreover, it is important to mention that as reported by Kanaze and colleagues, the capacity for PEG to form hydrogen bonds with flavanone glycosides such as Naringin is limited [58], whereas

the PLA repeating lactide units containing carbonyls (-C=O) may provide more opportunities for hydrogen-bonding with the flavonoid hydroxyls (-OH) [59]. Therefore, it would appear that the amphiphilic character of Naringin could play a role in the interactions governing the hydrophobic micelle core, but its specific interaction in this PEG-MS-PLA system should be further explored in the future. These insights are extremely important to optimize nanocarriers properties when encapsulation of flavonoids such as Naringin or others are envisioned.

Another important factor governing the *in-vivo* fate of nanocarriers is their surface charge. Regarding the ζ-potential of mPEG-MS-PLA micelles, both blank and Naringin-loaded displayed similar negative values: -13.2 ± 0.8 mV and -12.7 ± 0.6 mV, respectively. These results are consistent with other studies employing PEG-PLA micelles in the literature [13,60]. The obtained surface charge values are promising for *in vivo* delivery applications, because slightly negative-charged nanoparticles have longer circulation times and are less prone to opsonization and subsequent accumulation in the MPS organs [52].

In addition, it is interesting to note that the ζ-potential of three different replicates of Naringin-loaded micelles was analyzed before and after dialysis against deionized water to remove free drug. The ζ-potential of a Naringin solution in deionized water (0.1 mg/mL) was measured and found to be -25.1 ± 1.3 mV. The initial ζ-potential of the drug-loaded micelles changed from -18.2 ± 1.0 mV to -12.7 ± 0.6 mV upon dialysis, which could indicate that either free Naringin or adsorbed to the micelle surface was removed from the mPEG-MS-PLA solution.

3.4 Morphological Characterization of Nanomicelles

The morphology of mPEG-MS-PLA core-shell micelles was characterized by STEM due to micelles degradation observed in transmission electron microscopy (TEM). Such degradation is a result of the higher voltage used by the TEM equipment (~100 kV) that promotes a local increase in temperature and micelles disruption. The obtained STEM micrographs show that both blank and Naringin-loaded micelles have a spherical morphology (Figure 20).

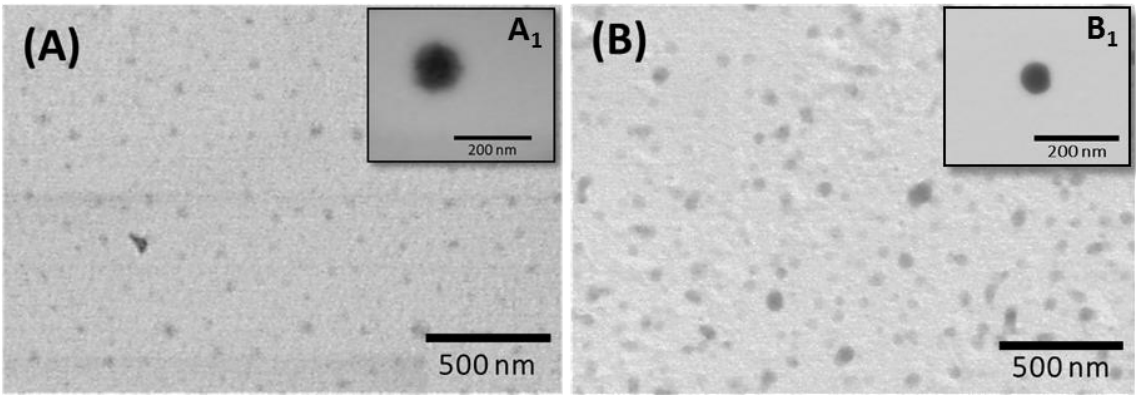

Figure 20. Nanomicelles morphological analysis through STEM at 20 kV. (A) blank micelles (30X) and (B) Naringin-loaded micelles (50X), with each respective inset (200X).

The shape of nanocarriers is known to play a key role in their interaction with cell membrane at the nano-biointerface thus influencing the cellular uptake rate [61]. Typically, for nanoparticles greater than 100 nm there is a clear uptake-shape correlation with particles achieving a higher uptake in the order of rod-shaped > worms > spheres, all exhibiting an increased cellular uptake, especially when compared to cube-shaped nanoparticles [51,62]. On the other hand, spherical particles have a significant uptake potential over rods for sub-100 nm nanoparticles [51]. All these reports emphasize the effect of shape in the efficacy of intracellular therapeutics delivery and may thus influence the overall therapeutic outcome or induce cytotoxicity [63].

It is also important to properly characterize nanocarriers geometry due to its influence in particles interaction with serum proteins [51]. Circulating serum proteins can adsorb on nanocarriers surface, forming a dynamic protein corona (e.g. soft and hard corona)[64] which can dramatically alter their active targeting and biodistribution profile [61]. Therefore, besides altering uptake dynamics, particle morphology can affect their kinetics of accumulation and excretion within the body. This once again highlights the importance of establishing a well-defined characterization of the prepared nanocarriers [65].

3.5 Evaluation of Nanomicelles Colloidal Stability

The colloidal stability of Naringin-loaded mPEG-MS-PLA micelles in aqueous solutions was investigated via DLS by monitoring changes in their physicochemical properties, namely particle size, PDI and ζ-potential, up to 14 days (Figure 21). Overall, the obtained results indicate that micelles are stable after a two-week storage period at 4ºC in both deionized water and PBS buffer at physiological pH =7.4. In particular, the produced

micelles maintained a relatively constant particle size and PDI. Regarding the micelles dispersed in PBS, they presented a slight increase in the final PDI. In addition, ζ-potential remained constant throughout the storage period, which supports the stability of the PEG corona in aqueous solutions. Moreover, considering that particle size remained unchanged over two weeks, this further corroborates the stability of the maleimide-alkylthiol linkage in these conditions. Nevertheless, the above results concerning the stability studies highlight a high colloidal stability of mPEG-MS-PLA nanomicelles and suggest that these nanocarriers may be suitable for *in vivo* applications.

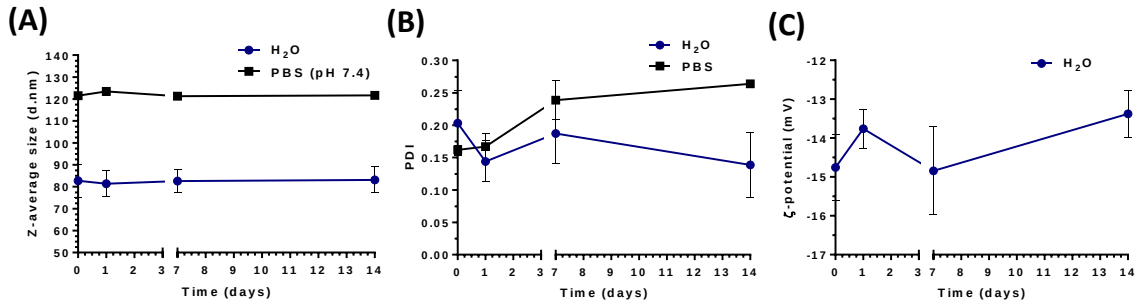

Figure 21. Colloidal stability of mPEG-MS-PLA PMs in aqueous conditions: water (sphere, blue) and PBS at pH 7.4 (square, black). (A) Particle size (nm), (B) PDI and (C) ζ-potential (mV).

3.5 Drug Encapsulation Efficiency and *In vitro* Drug Release

The Naringin encapsulation efficacy in PMs was determined by UV-VIS analysis of the characteristic flavanone peak at λ= 282 nm of Naringin-loaded micelle solutions at a final polymer concentration of 0.2 mg/mL. The amount of encapsulated Naringin was extrapolated from Naringin calibration curve in water (concentration range from 2 - 100 µg/mL, located in Figure 33, Annex I) The obtained data shows that mPEG-MS-PLA micelles achieved a high encapsulation efficiency of Naringin (87.2 ± 4.6 %) (Figure 22A).

So far, the delivery of Naringin was only attempted by impregnation in implantable scaffolds, porous composites or in surface-coatings [66–69]. These works focused on the development of bone graft materials either to enhance the repair of osteoporotic bone defects, or to provide a multifunctional orthopedic coating with inherent antimicrobial and pro-osteogenic properties. In this context, Chang and his team developed a pH-responsive Naringin-loaded hydrogel for inhibiting the bacteria-induced inflammation characteristic of periodontal diseases, namely periodontitis [70].

It is important to emphasize that to date a limited number of literature reports have focused on the encapsulation of Naringin in nanocarriers. One of the few examples is the

recent study performed by Feng and colleagues, in which Naringin establishes an inclusion complex with water-soluble ternary nanoparticles (particle size: 212 nm, PDI: 0.252) [71]. These carriers consisted of amylose, α-linoleic acid and β-lactoglobulin, and the aim of the study was to improve Naringin bioavailability using a food grade carrier, as well as study the physicochemical properties of this particular inclusion complex. Moreover, Naringin encapsulation efficiency within these nanocarriers was 78.7 ± 4.2% as determined via high-performance liquid chromatography. Considering this, the obtained results with mPEG-MS-PLA PMs present a higher encapsulation efficiency. Such is paramount to reduce the dose of nanocarriers that is required to be administered to MSCs in order to promote their osteogenic differentiation as envisioned.

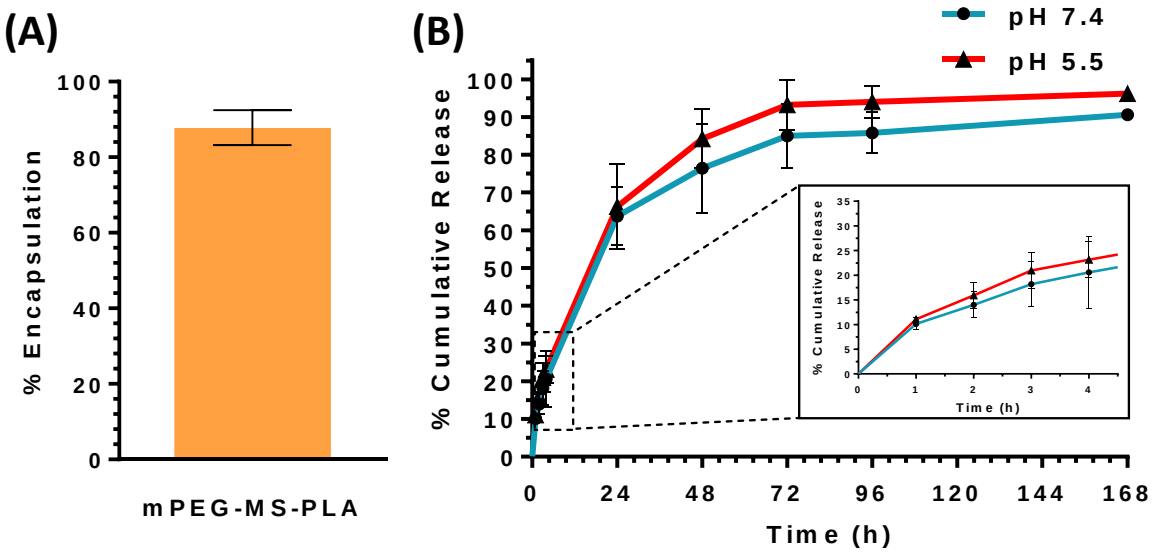

Figure 22. Micelles drug encapsulation efficacy and *in vitro* release profile. (A) Naringin drug loading within self-assembled mPEG-MS-PLA micelles. (B) Cumulative release profile of Naringin from mPEG-MS-PLA micelles in PBS at pH 7.4 (sphere, blue) and 5.5 (triangle, red). Inset represents the cumulative release during the first 4h of the release studies. Data is presented as mean ± s.d. (n=3).

Afterwards, the *in vitro* release profile of Naringin from mPEG-MS-PLA micelles was investigated by using the dialysis method under sink conditions. (Figure 22B). This study was conducted in PBS buffer at different pH values to simulate either physiological conditions (pH = 7.4) or the acidic environment within the lysosomal/endosomal intracellular compartments [72]. The latter was considered important since mPEG-PLA micelles are reported to be internalized via dynamin- and caveolin-dependent but also clathrin-independent endocytosis which results in the formation of endo-lysosomal vesicles [73].

The release profile of these nanocarriers exhibited a similar release for both acidic and physiological conditions. Moreover, the release profile of Naringin from mPEG-MS-PLA micelles appears to follow a biphasic release: (i) a fast release during the first hours (ca. 22% released drug within 4 h), and then (ii) a slower and sustained release over the following days, ca. 65%, 80%, 89%, 89.5% and 93% released drug, respectively for 1, 2, 3, 4 and 7 days.

Drug release kinetics are influenced by several factors, including drug solubility, stability and interaction with the polymeric matrix, as well nanocarrier polymeric composition, structure and biodegradation kinetics [74]. The obtained release profile is relatively similar to other studies in the literature involving the use of mPEG-PLA PMs [75]. In addition, the Naringin release profile herein observed is somewhat similar to the release profile of the recent work by Yu and colleagues, where Naringin was loaded into a mineralized collagen coating, containing or not metal-organic frameworks (MOFs). In this study, the authors observed a burst release, obtaining ca. 65% and 85% of released Naringin at 16 hours for the Collagen/MOFs and Collagen groups, respectively. Moreover, they determined that the Collagen/MOFs coatings could halve the initial burst release. Interestingly, the mPEG-MS-PLA micelles from this work achieved only 65% of released drug after 24 hours, which means that these nanomicelles provide an even more sustained release when compared to the reported Collagen/MOFs coatings. The authors underline the importance of both preventing an initial burst release and guaranteeing a long-term sustained release of Naringin for enhancing its therapeutic potential. One of the main advantages of the PMs here produced is the ability to tune this diffusion-based release profile via testing different polymeric architectures, such as shell or core crosslinking, or by imparting stimuli-responsiveness to the polymeric nanocarrier [76,77].

3.6 Naringin-loaded Nanomicelles Production Scale-up

The switch from laboratory scale to larger scale nanomedicines manufacturing (e.g. pilot or industrial scale) is often a pre-requisite for their foreseeable translation and represents a remarkably challenging task from a technological and logistical perspective [78]. Particles size, surface charge, morphology, monodispersity and high drug loading efficacy are key parameters that need to be maintained following larger scale synthesis. Assuring that the optimized parameters for small scale particles manufacture result in the same

physicochemical properties (size, charge, morphology) upon scale up is crucial to maintain nanocarriers biological performance [79]. Even during the stages of pre-clinical analysis, larger manufacturing of particles is important for *in vivo* validation of such carriers, which normally involves a higher amount of particles than that used in *in vitro* assays.

One of the main advantages of nanoprecipitation is the high throughput potential and facile scale-up production [80]. Considering this, and because pre-clinical *in vitro* cell-based assays require significant quantities of Naringin-loaded mPEG-MS-PLA micelles, a 5-fold scale-up was performed, maintaining all original parameters of formulation F3. Monodisperse nanomicelles (H_r: 84.87 ± 2.19 nm, PDI: 0.114 ± 0.035, ζ-potential: -11.1 ± 0.4 mV), with high Naringin encapsulation efficiency (86.15 ± 4.31%) were obtained (Figure 34, Annex I). Drug entrapment and physicochemical properties for the scale-up nanoprecipitation are in line with previous findings reported for initial formulations (Figure 19), highlighting the reproducible and scalable nature of the nanoprecipitation method.

3.7 Preparation for Cellular Assays

To incubate the formulated mPEG-MS-PLA micelles with cells, they need to be sufficiently concentrated to be administered in multi-well testing plates. Different strategies have been tested to concentrate nanomicelles. Firstly, Amicon® Ultra centrifugal filters were used as an attempt to have a fast concentration procedure. This strategy promoted a reduction from 5 mL initial volume to a final 200 µL in under 30 min at 16600 g. However, UV-VIS analysis of the filtrate versus the concentrated solution indicated that a very significant portion of drug was lost during the process. Possibly, the dynamic stability of the micelles was disrupted during high speed centrifugation against the filter wall, dismantling micelles and releasing large amounts of Naringin through the filtrate.

In light of this finding, a different alternative to concentrate the micelle solution was tested. Blank micelles were concentrated in the rotary evaporator (25 mbar, 37 ºC) for 20 to 35 min depending on initial water volume. Afterwards, the concentrated solution was diluted and micelle stability during this concentration procedure was evaluated via DLS analysis. Pre-rotary evaporation (i) and post-rotary evaporation (ii) samples were analyzed in terms of hydrodynamic size and PDI. The findings demonstrate that micelles maintain their initial properties even after enduring the concentration process: (i) Initial size of 60.78 ± 1.13 nm, PDI: 0.315 ± 0.004; to (ii) Final size of 62.88 ± 0.72 nm, PDI: 0.326 ± 0.035, post-evaporation. These results suggest that the rotary evaporator-mediated concentration method

described is adequate for concentrating nanomicelles suspensions for subsequent cellular assays.

3.8 Nanomicelles Cellular Uptake

Micelles cellular uptake was evaluated in MC3T3-E1 (Figure 23) and hASCs which can be differentiated into bone-resident cells (Figure 24). Nanocarriers cellular uptake kinetics were studied by CLSM. For intracellular visualization of micelle uptake, mPEG-MS-PLA micelles were loaded with the model fluorescent dye Coum-6, with these micelles maintaining similar physicochemical properties than their non-loaded counterparts (H_r of 63.6 ± 1.6 nm, PDI of 0.176 ± 0.003). The physicochemical characterization of these micelles, as well as a fluorescence microscopy image of these micelles in aqueous solution is shown in Figure 35, Annex II.

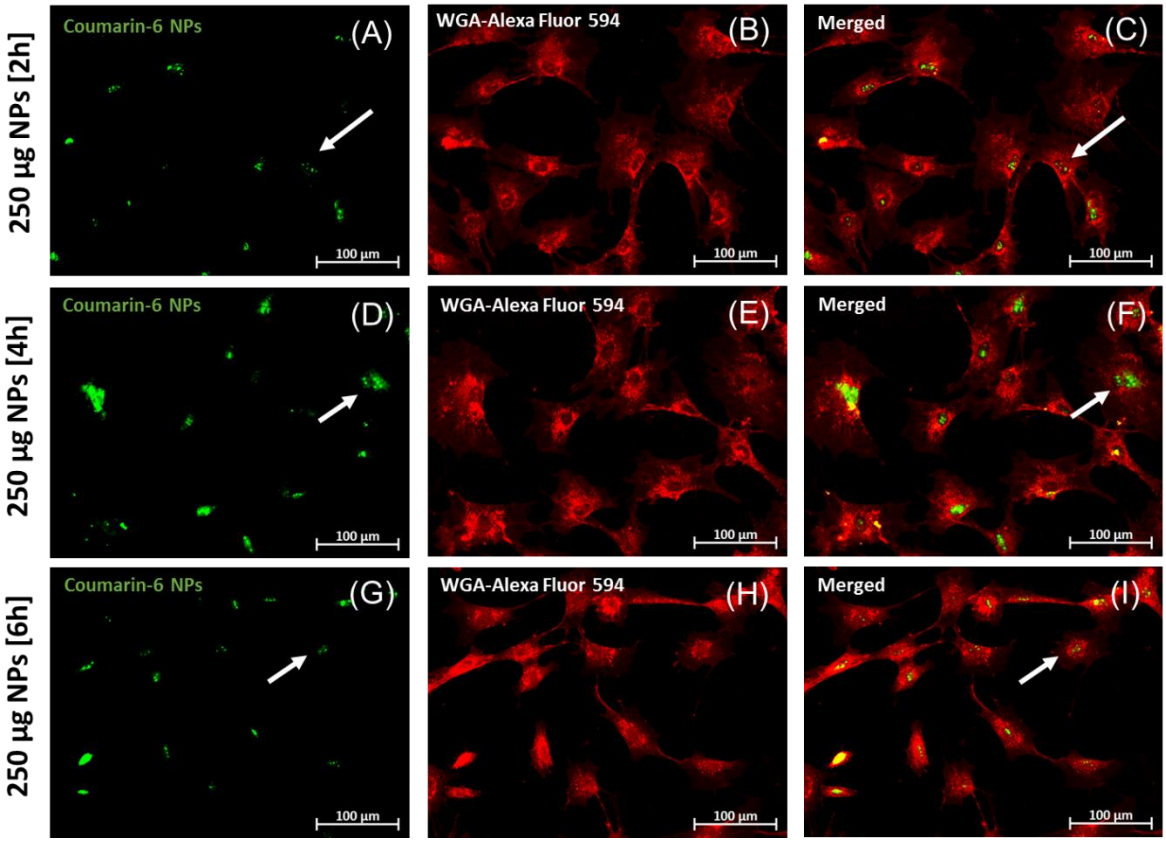

Figure 23. Cellular uptake kinetics of mPEG-MS-PLA micelles in M3C3T3-E1 cells, obtained via CLSM. Green channel: Coum-6-loaded micelles (NPs). Red channel: WGA-Alexa Fluor 594. White arrows indicate micellar carriers.

As shown in Figure 23 and 24, Coum-6-loaded mPEG-MS-PLA micelles successfully transfected both MC3T3-E1 and hASCs cells, showing visible cellular uptake within only 2

hours of micelle incubation. The difficulty of transfecting hASCs is well-known in the scope of intracellular delivery of nucleic acids for cell reprogramming [81]. Therefore, the obtained results show that the developed delivery system has potential in transfecting these cells for application of stem cell-based therapies, and in particular, capable of delivering Naringin intracellularly. Concerning this, the micelles appear to localize to the perinuclear region but not adsorbed on the cells' surface. This is important because successful internalization of the nanocarriers is crucial for increasing the intracellularly available Naringin concentration.

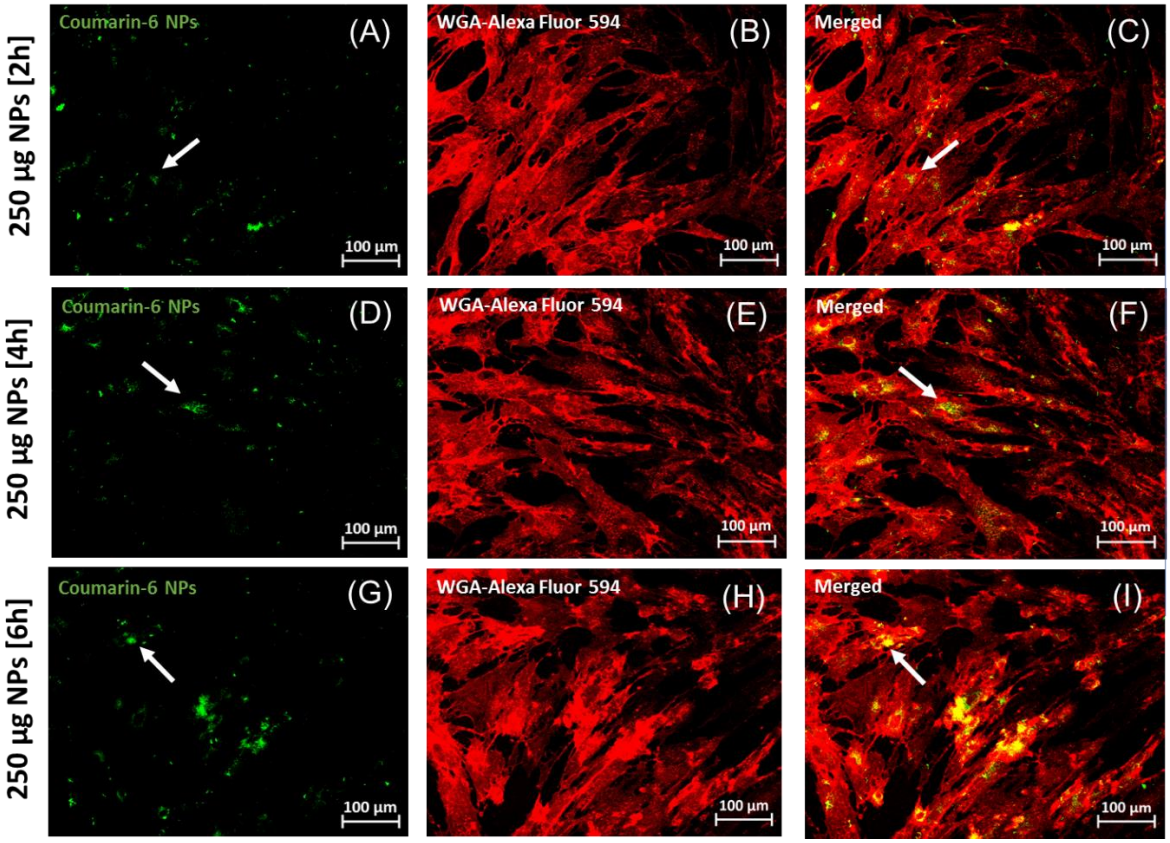

Figure 24. Cellular uptake kinetics of mPEG-MS-PLA micelles in hASCs cells, obtained via CLSM imaging. Green channel: Coum-6-loaded micelles. Red channel: WGA-Alexa Fluor 594 stained cell membrane. White arrows indicate Coum-6-loaded micellar carriers.

Moreover, the characteristic localization of nanomicelles in cell nucleus vicinity is well reported in the literature [82]. The authors suggested that while the endocytosis of nanocarriers did not play a key role in the cellular delivery of Coum-6, the release rate of this drug from the delivery systems was correlated with the obtained intensities. Furthermore, Zhang and his team performed an intracellular trafficking study with PEG-b-PLA micelles loaded with Nile Red and found that most of the internalized micelles were localized in the lysosome, while only a small fraction was present in the endoplasmic reticulum [73]. Overall, these

studies suggest that the stained perinuclear region could be attributed to intracellularly-released Coum-6. Nevertheless, tracking micelles intracellular trafficking into different compartments including acidic compartments (e.g. endo-lysosomes) could be useful to further evaluate the intracellular fate of such particles [73].

In addition to CLSM data, the cellular uptake of Coum-6 loaded micelles in both MC3T3-E1 and hASCs was evaluated by flow cytometry (FCM) analysis. Different nanomicelles dosages (25, 50 and 100 µg) were incubated in all *in vitro* cell models for 4 h prior to analysis. The results obtained are presented in Figure 25.

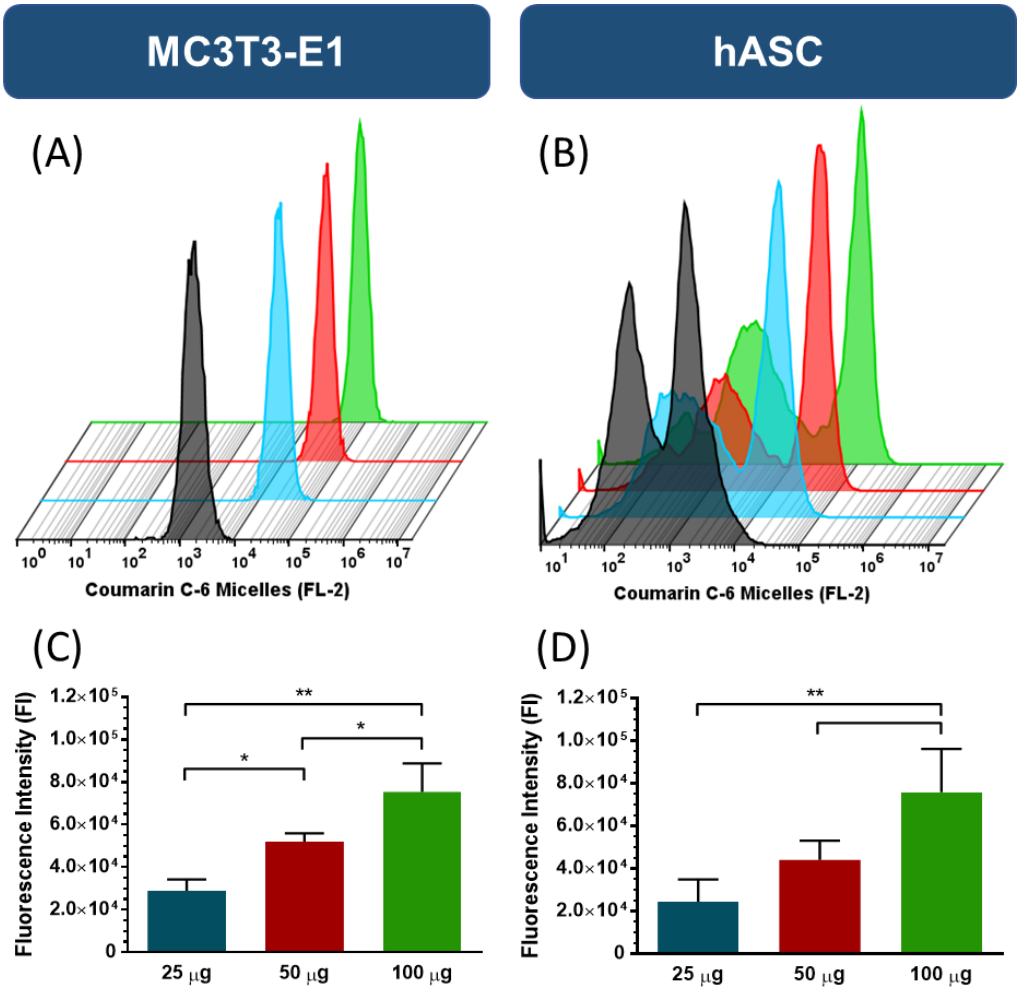

Figure 25. FCM analysis of Coum-6 loaded mPEG-MS-PLA micelles cellular uptake in MC3T3-E1 **(A, C)** and hASCs **(B, D)**. Representative cellular uptake histograms of micelles in MC3T3-E1 **(A)** and hASCs **(B)**. Fluorescent intensity values obtained after transfecting MC3T3-E1 **(C)** and hASCs **(D)** with micelles. Black color represents cell auto-fluorescence; blue: 25 µg; red: 50 µg; and green: 100 µg of incubated micelle dosage. *p < 0.05; **p < 0.01. Data represented in mean ± s.d. (*n*=3).

FCM analysis revealed that micelles cellular uptake increased with increasing nanomicelles dose (in the tested range). Regarding the particular case of MC3T3-E1 cells, a 1.8-fold increase in fluorescence intensity (*$p < 0.05$) was obtained for the 50 µg dose in comparison with the lowest micelle dose (25 µg). Moreover, the highest dose (100 µg) tested achieved a 2.6-fold increase in cellular uptake (**$p < 0.01$).

Likewise, nanomicelles cellular uptake data obtained in hASCs show a 1.8- and 3.1-fold increase in MFI for 50 and 100 µg respectively (**$p < 0.01$), compared to the lowest dose. These findings highlight the transfection capacity of the formulated mPEG-MS-PLA micelles in these generally hard to transfect MSCs, thus showing promise for the intracellular delivery of bioactive molecules with ability to guide their differentiation to specific lineages.

3.9 Cellular Viability and Proliferation Assays

For proper evaluation of the osteogenic potential of the developed delivery system, its biocompatibility must be evaluated. Ideally the carriers must not exert a significant toxic effect in the tested cells (MC3T3-E1, hASCs) and within the concentrations studied, so that no dose-dependent cytotoxicity can influence the interpretation of the obtained results. Although PEG-PLA diblock copolymers are considered highly biocompatible, investigating a possible cytotoxic response due to the drug dosage is a pre-requisite [13]. The Naringin flavanone has already been described as a relatively non-toxic compound in various cell lines (e.g. MC3T3-E1, human osteoblast, UMR-106, bone marrow stromal cells) when administered the range of 1 – 200 µg/mL [31]. However, it is important to emphasize that the upper limit of cytotoxic Naringin concentrations appears to vary among different cell types [33,37]. The Naringin dose range was selected from a thorough analysis of available literature reports in different cells lines (Table 5, Annex III) but since this is the first study to be performed in hASCs evaluating its toxicity is a pre-requisite for further osteogenesis induction studies. In addition, the biocompatibility profile of blank micelles and free Naringin was also evaluated in the MC3T3-E1 cell line and their non-toxic character was confirmed and is in accordance with literature reports (Figure 36, Annex II) [83,84].

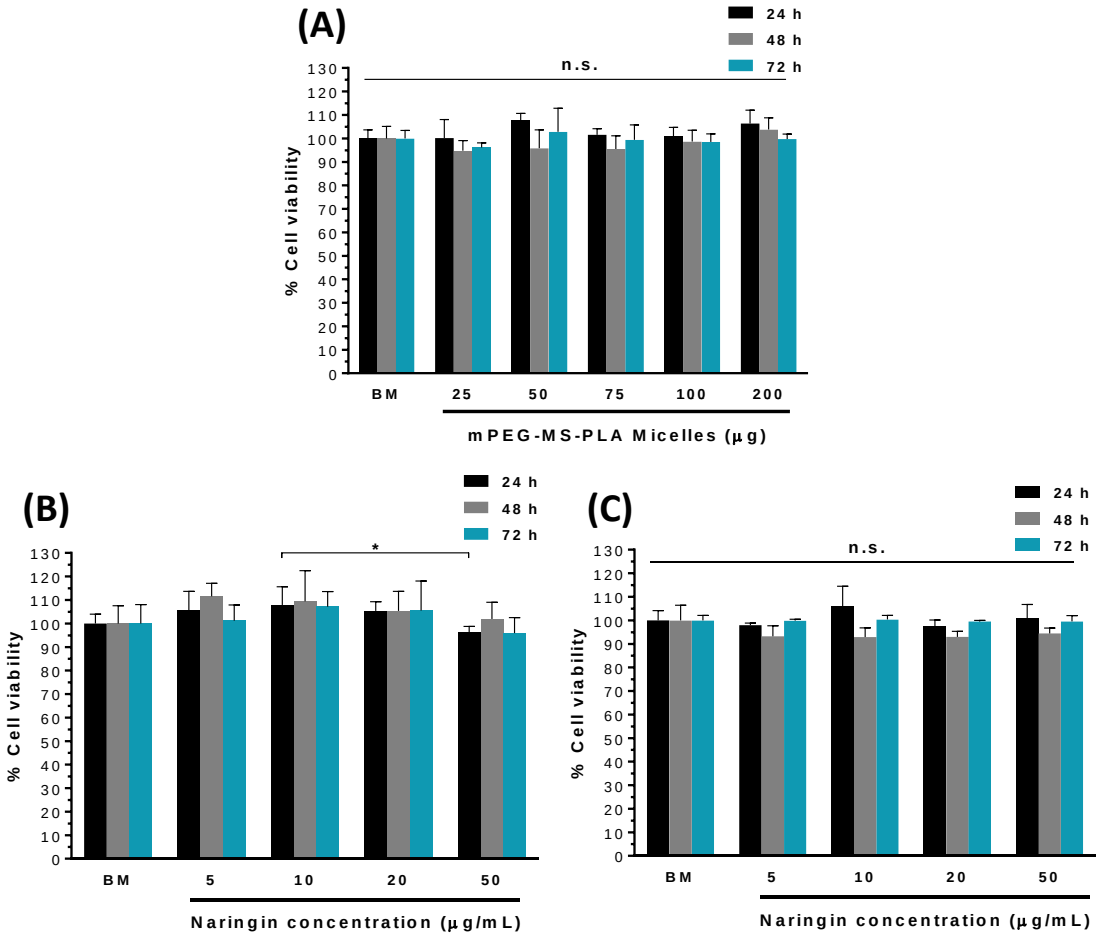

Figure 26. Characterization of blank mPEG-MS-PLA blank micelles **(A)**, free Naringin **(B)** and Naringin-loaded micelles **(C)** effect in hASCs cell viability following incubation at different time points. BM represents basal medium negative cytotoxicity (K-) control. n.s. stands for non-significant, *p < 0.05. Data represented in mean ± s.d. (*n*=5).

The results presented in the cytotoxicity evaluation panel regarding hASCs (Figure 26) show that blank mPEG-MS-PLA micelles elicited no cytotoxic effect in this cell line as compared to basal medium negative control (BM, K-) (Figure. 26A). Moreover, as shown in Figure 26B, the nanocarriers maintained their biocompatible profile upon loading of the Naringin flavanone. In parallel, the administration of free Naringin concentrations ranging from 5 – 50 µg/mL showed no significant changes in cell viability across all studied time points (Figure 26C), suggesting that these doses can be used for osteogenic differentiation purposes. Overall, these results highlight the non-toxic features of blank nanocarriers and both free Naringin and Naringin-loaded micelles in hASCs.

Naringin has been described to significantly enhance cell proliferation of osteoprogenitor cells (e.g. MC3T3-E1 and human/rat BM-MSCs) or with an osteoblastic phenotype (e.g.

osteoblast-like UMR 106 and MG 63 cells or human osteoblasts) [33,37,67,84–87]. Overall, these studies investigated Naringin-induced cell proliferation by performing metabolic assays such as MTT and CCK-8. However, the discrepancy between the metabolic activity and cell numbers is well documented on the literature, where it is shown that these assays may overestimate cell proliferation when compared to DNA-binding fluorophores [88]. Hence quantifying DNA content with specific fluorophores is an important complement to these metabolic assays. Moreover, flavonoids are reported to dose-dependently reduce tetrazolium salts such as MTT even in the absence of cells, which may significantly influence the obtained results in metabolic assays [89]. In fact, some flavonoids inhibit cell growth but show enhanced MTT reduction. As such, to confirm Naringin proliferative properties, the double-stranded DNA (dsDNA) content was quantified via PicoGreen® in the same samples of hASCs used for cytotoxicity assays. By using this strategy, a correlation between metabolic activity and DNA content could be extrapolated. The obtained results are presented in Figure 27.

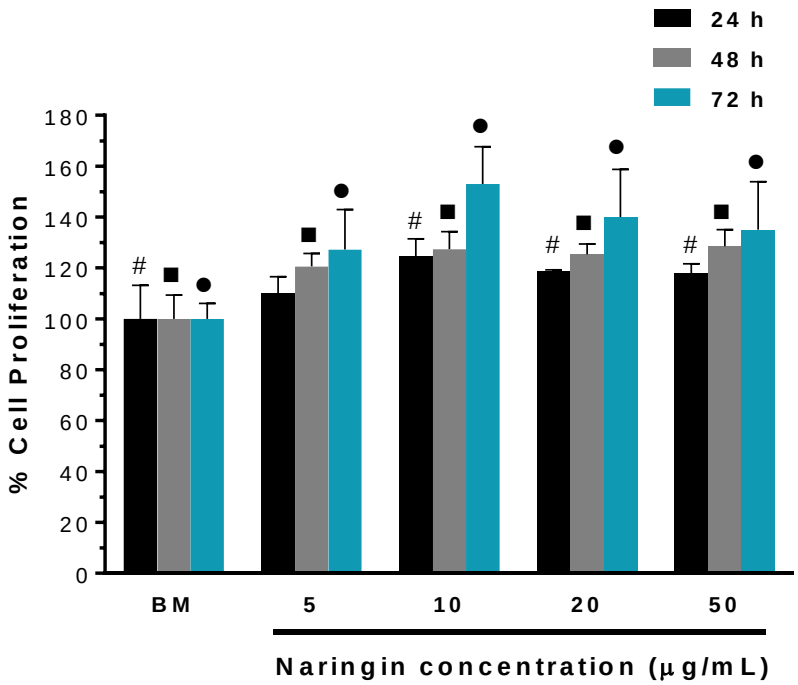

Figure 27. Effect of free Naringin on the proliferation of hASCs relative to the negative control, basal medium (BM). Symbols #, ■, ● correspond to 24, 48 and 72 h of incubation, respectively. They represent statistically significant data relative to control. #: BM vs 10 **p < 0.01, BM vs 20, 50 *p < 0.05. ■: BM vs 5 ***p < 0.001, BM vs 10, 20, 50 ****p < 0.0001. ●: BM vs 5 *p < 0.05. BM vs 10, 20, 50 **p < 0.01. Data is represented as mean ± s.d. (*n*=5).

Overall, free Naringin increased the proliferation of hASCs relatively to control groups on all time points and across the studied concentrations. Interestingly, the obtained data seems to suggest that the effect of Naringin on the rate of proliferation increases over time, accordingly, ca. 115 ± 6 % (24 h), 122 ± 4 % (48 h) and 141 ± 11 % (72 h), with up to 50 % enhanced cell proliferation for 10 µg/mL at the latest time point. However, across the range of concentrations herein studied, no dose-dependent effect could be perceived for these time points, contrary to some previous reports in the literature for other cell lines (Table 5, Annex III) [31].

From herein forward, hASCs were selected for assessing the osteogenic potential of Naringin since to date the effect of this flavanone in these stem cells has not been studied. Moreover, in comparison with murine MC3T3-E1 cells, ASCs extracted from human adipose tissue represent a valuable source of MSCs for cell-based regenerative therapies. Besides their human origin, they can be easily harvested from adult adipose tissue, possess low antigenicity and comparatively to hBM-MSCs, exhibit faster proliferation rates and increased genetic stability in prolonged culture periods, which establishes these cells as promising candidates for driving forward tissue engineering applications [90,91].

3.10 Naringin Stimulatory Activity in OS-Dex in hASCs

3.10.1 Naringin-induced Stimulation of ALP Activity

Alkaline phosphatase (ALP) is widely recognized as an early marker of pre-osteoblastic phenotype and plays an important role in bone mineralization [92]. This effector protein is responsible for providing inorganic phosphate and coordinating bone metabolism towards the mineralization of the extracellular matrix [93,94]. Currently, measurement of its activity represents the most frequently used assay to investigate the progress of stem cells (hBM-MSCs or hASCs) osteogenic differentiation [92]. Typically, in order to induce osteogenesis, stem cells are cultured in specific osteoinductive media and the osteogenic potential attained is then determined by measuring osteogenic markers such as ALP. However, this differentiation potential can vary due to several factors, such as: **(i)** donor or tissue origin, **(ii)** cell passage number, **(iii)** different serum conditions (fetal bovine or human), **(iv)** the type of osteogenic supplements used (ascorbic acid (AA) and β-glycerophosphate (β-gly), dexamethasone (Dex)), as well as the **(v)** concentration of these components (i.e., Dex

administered dose and frequency of administration), which can all play a key role in determining the osteogenic differentiation potential of stem cells [95–98].

Regarding studies on the osteogenic potential of free Naringin, different literature reports indicate different choices for the osteogenic inductive medium. Most of these reports vary between osteoinductive (AA + β-gly or AA + β-gly + Dex) or even BM conditions. As aforementioned, this can lead to different outcomes in the osteogenic differentiation potential of stem cells. Therefore, initially the osteogenic capacity of free Naringin in hASCs was evaluated under different medium conditions (Table 3, Methods Section 2.9): i) osteogenic medium (AA + β-gly) with Dex (OS-Dex), ii) osteogenic medium (AA + β-gly, OS), and iii) basal growth medium (BM).

For the first experiment, hASCs were incubated with different concentrations of free Naringin in OS-Dex medium over 21 days. Throughout the assay, cell culture medium was exchanged every 3-4 days with fresh OS-Dex medium with no Naringin addition other than that at day 0 (Figure 28A). The ALP activity was then quantified by p-nitrophenylphosphate hydrolysis and normalized to dsDNA content by using the PicoGreen® assay. The outcome of this experiment is shown in Figure 28.

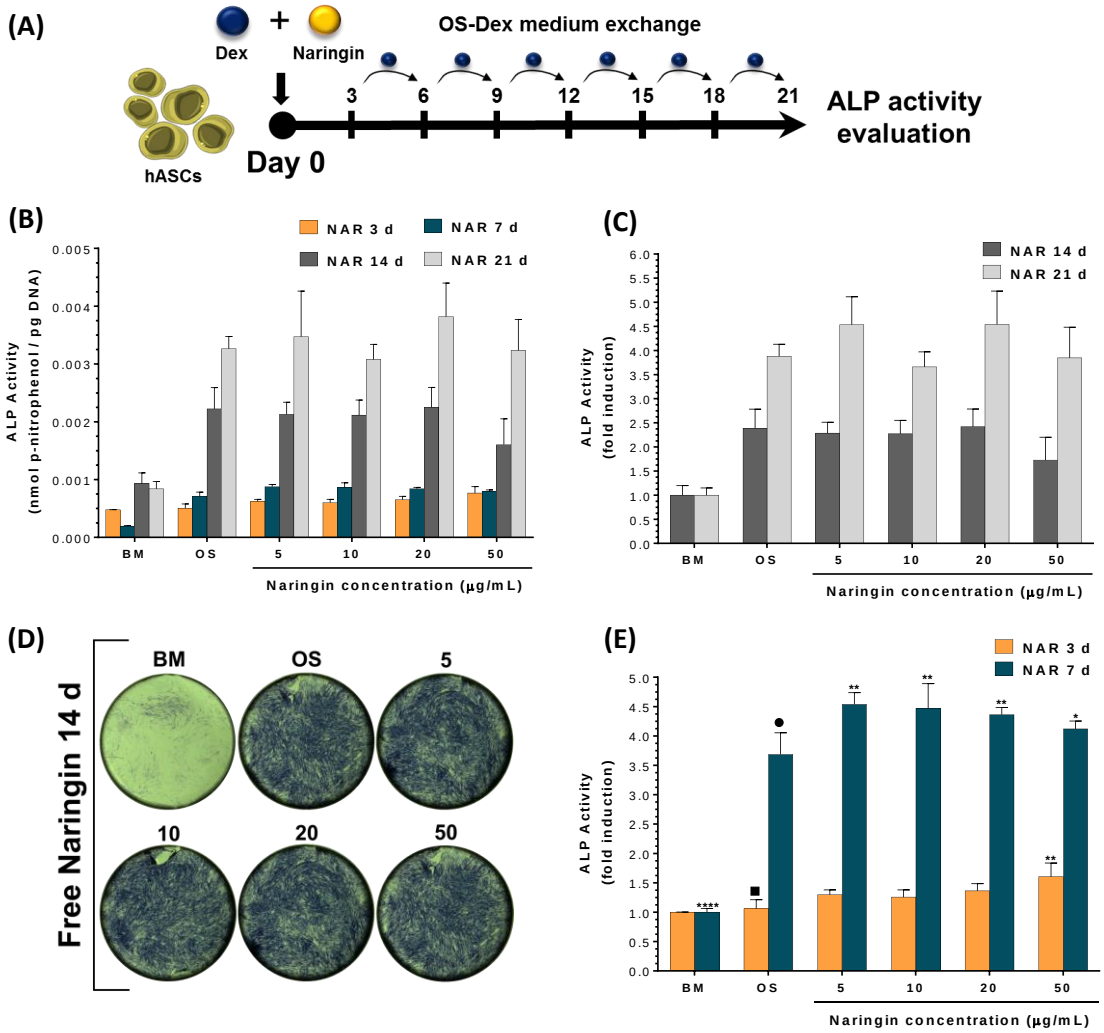

Figure 28. Naringin-induced ALP stimulation in OS-Dex (OS) differentiation medium. **(A)** Dose regime of Dex and Naringin in this experiment. **(B)** ALP activity of hASCs over 21 days in OS-Dex, with different Naringin concentrations, expressed in nmol p-nitrophenol normalized to DNA content. **(C)** ALP activity fold induction over basal medium (BM) at 14 and 21 days. Differences between Naringin doses and OS-Dex are not significant. **(D)** BCIP/NBT ALP-staining at 14 days. **(E)** ALP activity fold induction over basal medium (BM) at 3 and 7 days. Symbols ■ and ● represent the control group used to perform the statistical analysis of each timepoint. Data represented as mean ± s.d. (*n*=5).

The results presented in Figure 28A show the increase in hASCs ALP activity along time after incubation in OS-Dex control group and with different Naringin doses (Figure 28A). The ALP activity is the highest at the final time point of the experiment, *i.e.*, 21 days of incubation, which might suggest that continuously exchanging the osteogenic medium with a renewed Dex dose (100 nM) might lead to continous stimulation of hASCs populations. Alternatively, according to the obtained results shown in Figure 28B, the use of Naringin as an initial stimulation factor to promote osteogenesis is limited to the earlier time points, i.e.,

3 and 7 days of incubation. Indeed, the data presented in Figure 28C shows that, at 14 and 21 days of incubation, no significant differences in ALP activity can be observed among different Naringin doses and the respective OS-Dex control group. Likewise, these findings are supported by Figure 28D, which shows the ALP-dependent staining of hASCs at 14 days via BCIP/NBT substrate. The visual observation of the ALP-stained cells also cannot discern clear differences between the osteogenic control and the various Naringin doses.

However, for the earlier time points, i.e., 3 and 7 days of incubation, the osteogenic effect of Naringin over the OS-Dex control groups is significant, as shown in Figure 28E. At 3 days, a dose-dependent effect of Naringin can be observed, with the highest dose (50 μg/mL) showing a 0.6-fold improved ALP activity induction over the OS-Dex control group (**$p < 0.01$) and a 0.3-fold ALP increase across all studied doses, from 5 to 20 μg/mL (*$p < 0.05$). At 7 days, no significant difference across all Naringin doses could be observed indicating that lower doses are equally beneficial. In comparison with OS-Dex control group, a 0.2-fold increase in ALP activity could be observed across all Naringin doses.

In conclusion, a significant pro-osteogenic effect between different Naringin doses was observed at 3 days, while the osteogenic effect between Naringin and OS-Dex control groups was observed at 3 and 7 days. These findings suggest that perhaps constant long-term stimulation of hASCs with Dex, with only an initial stimulatory dose of Naringin (Figure 28A), might dillute this flavonoid effect on the promotion of ALP levels over the course of the experiment. In fact, for later time points of the experiment, 14 and 21 days, there was no significant difference between the OS-Dex control and different Naringin conditions.

3.10.2 Naringin-induced Expression of BMP-2

Despite previous results on long-term ALP-stimulatory activity mediated by Naringin, the expression levels of other osteogenesis-related markers were evaluated to further investigate the contribution of Naringin in differentiating these stem cells to the osteoblastic lineage.

Naringin has previously been described to promote the secretion of BMPs, extracellularly secreted biomolecules that play a key role in modulating osteogenic differentiation pathways and coordinating bone formation [37]. The quantification of BMP-2 in the culture medium from the previous *in vitro* assays was performed via ELISA at 14 and 21 days of incubation. The obtained results are presented in Figure 29.

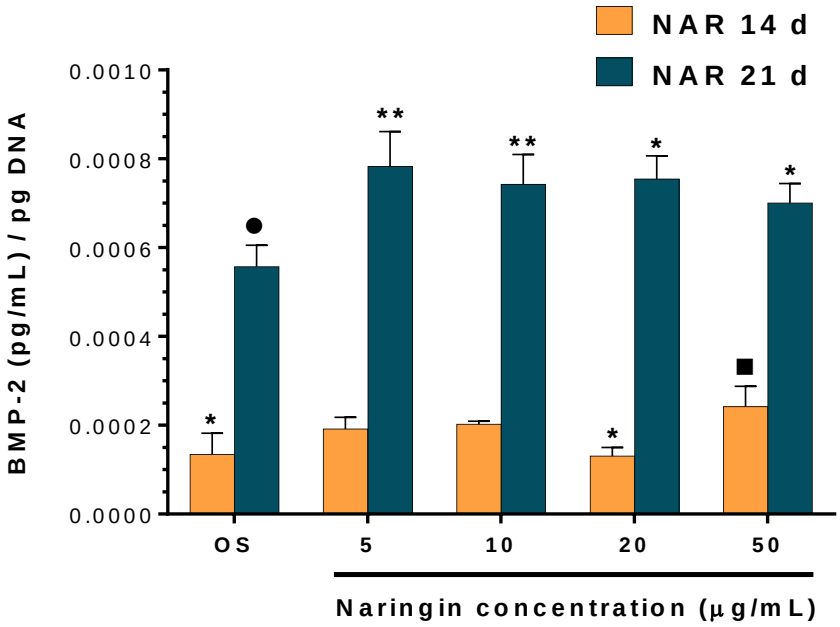

Figure 29. Naringin-induced BMP-2 secretion in hASCs at 14 and 21 days, after incubation with OS-Dex differentiation medium (OS) control group and with Naringin doses. Cumulative BMP-2 levels were normalized to DNA content. Symbols ■ and ● represent the control group used to perform the statistical analysis of each timepoint. Data is represented as mean ± s.d. (*n*=3). *p < 0.05, **p < 0.01.

The results obtained in Figure 29 highlight the contribution of Naringin over the OS-Dex group in improving the secretion of BMP-2. At 14 days, a dose-dependent stimulation of BMP-2 could be observed, with the highest Naringin dose of 50 µg/mL significantly improving BMP-2 levels over OS-Dex and 20 µg/mL dose groups (*p < 0.05). In addition, the cumulative BMP-2 levels at 21 days show a 0.4-fold improvement over OS-Dex control group. Meanwhile, the differences in BMP-2 levels across the range of Naringin doses studied at 21 days are not significant. Overall, these results underline that a single initial dose of Naringin was sufficient to elicit an increased BMP-2 production over OS-Dex treated hASCs at 14 and 21 days. Furthermore, they showcase the importance of evaluating different osteogenic markers, other than ALP activity, because these can convey important findings regarding Naringin effect in hASCS.

It is worth noting that this increased BMP-2 production did not lead to significant differences in ALP activity after 14 or 21 days of OS-Dex stimulation. These findings are in agreement with a previous study by Cruz and colleagues, where they found that exogenous administration of recombinant BMP-2 to hASCs did not increase the levels of ALP [99]. Nevertheless, the enhanced secretion of BMP-2 by Naringin in hASCs is an important finding, in particular because this bone morphogenetic protein is capable of inducing

commitment and differentiation of multipotent stem cell lines into an osteoblastic-phenotype [100]. Moreover, Naringin appears to have a synergistic effect with BMP-2 in the total osteogenic differentiation of MC3T3-E1 pre-osteoblasts [101]. So far, across the literature there is currently only one study describing Naringin-induced BMP-2 secretion, and this effect was observed in murine pOB, i.e., differentiated cells with an already defined osteoblastic phenotype [37]. Therefore, the above findings provide validation of this effect for the first time in hASCs and its importance is supported by the role of BMP-2 in the osteogenic commitment of stem cells.

3.10.3 Naringin-induced Expression of OPN

Osteopontin (OPN) is another classical osteogenic marker that is important to evaluate. OPN, also known as secreted phosphoprotein 1, is a non-collagenous bone matrix protein significantly secreted by MSCs undergoing osteogenic differentation [102]. OPN is present both intracellularly - regulating cytoskeleton dynamics and signalling transduction pathways (e.g. IFNα and MAPK) [103]; and extracellularly, being associated with the bone matrix. The secreted form of OPN preferentially accumulates in mineralized bone matrix, where it influences the cell- and matrix-matrix interactions towards coordinating several cell dynamics involving survival, adhesion and migration [104]. Moreover, OPN-rich interfacial regions have been suggested to mediate mechanical stress response in osteoblasts and minimize microcrack propagation in bone, thus improving the osteointegration properties of intertwined mineralized matrixes [105]. Therefore, more than an osteogenic marker, OPN acts as local signalling molecule bewteen osteoblasts and osteoclasts and its interactions with integrins are associated with osteoclastogenesis and regulate the bone remodeling process [106].

Naringin has been previously described to increase OPN expression in both osteoprogenitor (e.g. BM-MSCs, hAFSCs, hPDLSCs, MC3T3-E1) and osteoblastic cell lines (e.g. hOB and pOB), reflecting the osteogenic potential of this flavanone for bone tissue engineering applications due to the role of OPN in promoting biomechanical osteointegration [37,85,107,108]. In this experiment, hASCs were incubated with different concentrations of free Naringin and also Naringin-loaded nanomicelles in OS-Dex containing medium over 14 days. Throughout the assay, cell culture medium was exchanged every 3 to 4 days with fresh OS-Dex medium with no Naringin addition other than that at

day 0 (Figure 28A). The expression of OPN was then quantified by fluorescence microscopy imaging after staining with mouse anti-human OPN antibody conjugated to anti-mouse Alexa Fluor 647 dye. The outcome of this experiment is shown in Figure 30.

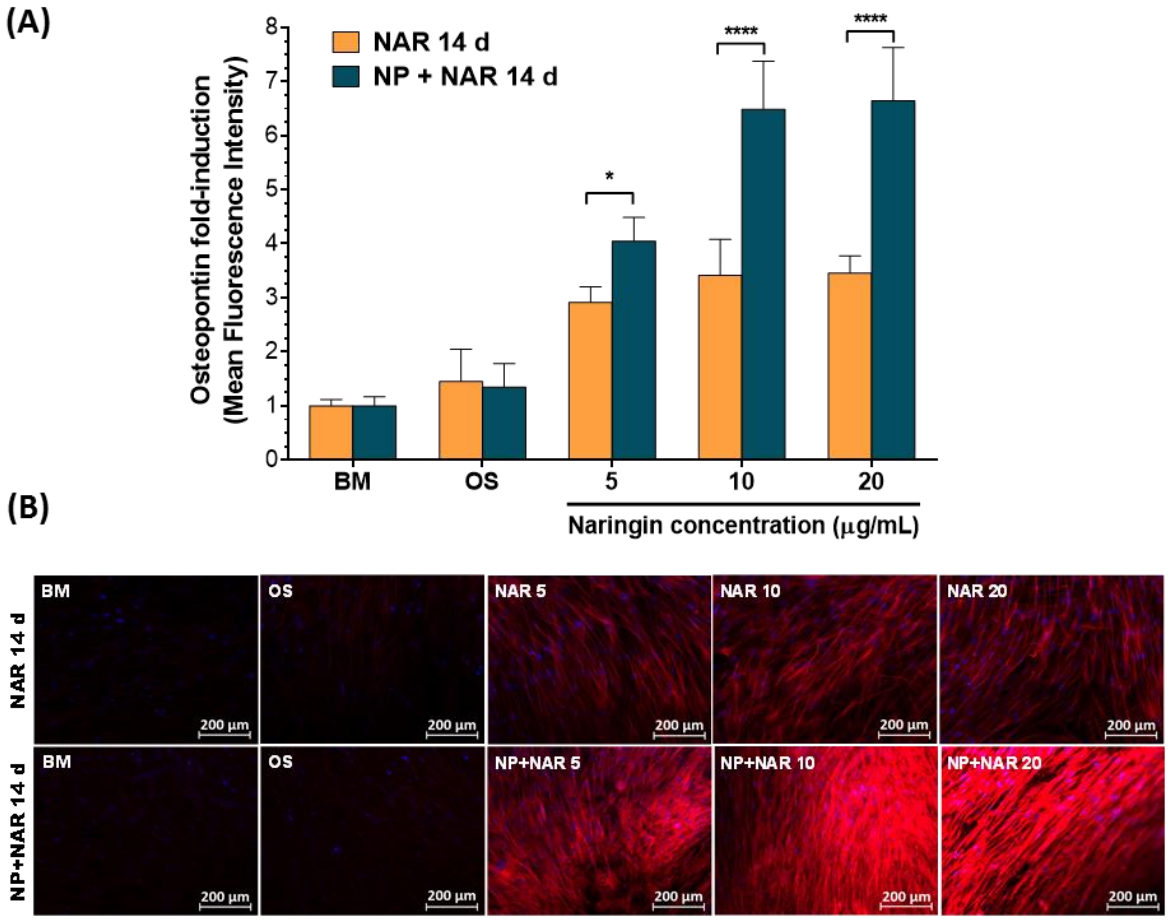

Figure 30. Naringin-induced OPN expression in hASCs at 14 days, after incubation with BM and OS-Dex medium (control groups), and with free Naringin or Naringin-loaded nanomicelles doses. **(A)** OPN expressed as fold-induction in MFI relatively to BM control group. **(B)** Representative fluorescence microscopy imaging of immunostained hASCs at 14 days after incubation with free Naringin or Naringin-loaded nanomicelles at various doses. Blue channel: cell nucleus staining with DAPI. Red channel: OPN staining with anti-mouse Alexa Fluor 647 fluorescent antibody conjugate. Data represented as mean ± s.d. (n=6). *$p < 0.05$, ****$p < 0.0001$.

The obtained results in Figure 30A show the remarkable capacity of Naringin to induce OPN expression in hASCs. In fact, a single stimulatory dose of Naringin was able to significantly enhance OPN expression after 14 days of culture. Regarding stimulation with free drug, all tested doses (5, 10, 20 μg/mL) were able to significantly enhance OPN expression by aproximately 2-fold when compared to both control groups, BM and OS (****$p < 0.0001$). However, the slight differences among the investigated drug dose range

were not statistically significant. On the other hand, incubation with Naringin-loaded nanomicelles elicited a 3-fold at 5 μg/mL and a 6.5-fold increase in OPN expression at the higher doses, accordingly 10 and 20 μg/mL versus both control groups (****$p < 0.0001$). Moreover, the dose-dependent effect of Naringin was evidenced in the loaded-micelles experiment since the highest doses (10 and 20 μg/mL) significantly improved OPN expression by 0.4-fold in comparison to that obtained at 5 μg/mL dosage (****$p < 0.0001$). In addition, it is important to highlight that the controlled delivery of Naringin via nanomicelles led to a higher OPN secretion when compared to free drug at the same doses. The effect of Naringin on OPN expression, as well as the superior performance of the Naringin-loaded nanocarriers are also evidenced by the results in Figure 30B.

The above shown results are in agreement with various literature reports investigating the effect of Naringin in OPN expression. For instance, Wu and colleagues investigated the *in vitro* potential of Naringin in promoting OPN secretion over three different cell lines: MC3T3-E1, hOB and pOB [37]. The authors observed that a 3-day incubation period with 3 μM of Naringin (1.74 μg/mL) elicited a 3-fold increase in extracellular OPN expression over BM control across all cells, as measured via an ELISA immunoassay. Alternatively, Yin and his team evaluated the Naringin-induced pro-osteogenic effect in human periodontal dental ligament stem cells (hPDLSCs) both *in vitro* and upon *in vivo* transplantation of hPDLSCs implanted in nanohydroxyapatite [108]. A preliminary *in vitro* RT-PCR screening assay of OPN-encoding gene expression was performed. After Naringin-induction for 14 days, RT-PCR showed a 0.4 to 0.7-fold OPN induction relatively to BM control in a dose-dependent manner, from 100 nM to 1 μM drug doses. In addition, in the *in vivo* study, hPDLSCs were incubated in BM medium containing Naringin (1 μM) for 7 days and then transplanted into 6 week-old immunocompromised Beige micevia a nanohydroxyapatite scaffold. After 8 weeks, the transplants were harvested and immunohistochemical staining of OPN was performed. The treatment group (Naringin-treated cells) exhibited a 50 % increase in OPN expression compared to the non-treated cells. Overall, these results are consistent with improved OPN expression due to Naringin stimulatory effect on osteogenesis.

Another important study that should be mentioned in the context of hASCs lineage differentiation, is the relation between OPN secretion and adipogenesis. Concerning this, Chen and colleagues investigated the key role of the interaction between OPN and integrin αV/β1 in defining MSCs differentiation in both *in vitro* and *in vivo* mice models [104]. The

authors compared the adipogenic and osteogenic differentiation potential of mouse BM-MSCs derived from wild-type and $OPN^{-/-}$ mice and observed an accelerated adipogenesis in $OPN^{-/-}$ BM-MSCs. Moreover, the OPN blockade not only skewed mouse BM-MSC differentiation towards the adipocyte lineage *in vitro*, but also resulted in impaired bone formation and led to a higher fat to total body weight ratio in OPN-deficient mice. Therefore, this study suggests that increased OPN expression might be valuable for pursuing osteogenic commitment of MSCs. Besides significantly increasing OPN expression, Naringin modulates other pathways (e.g. inhibition of PPARɣ and activation of Notch signaling) that all play a role in ultimately promoting osteogenesis over adipogenesis, which might be important considering the donor tissue of the studied stem cells in this thesis [32,33].

3.10.4 Naringin-induced Mineralization

Insights into the biology of bone formation have demonstrated that the first step consists in MSCs recruitment to target sites, leading to the synthesis of a surrounding cartilaginous matrix template [109]. Then, this proliferating cluster of MSCs differentiate into osteoprogenitor cells which initiates the endochondral ossification process, where the cartilaginous template is continuously replaced by bone, followed by subsequent longitudinal growth, as described in the introductory section 1.2 [110]. Matrix vesicles constitute the nucleation sites for the onset of calcification to propagate to nearby collagen fibrils, both serving as a natural dynamic scaffold responsible for accumulating calcium and inorganic phosphate ultimately leading to the formation of hydroxyapatite crystals [111]. In *in vitro* pre-clinical assays of novel bone therapies, osteoprogenitor cells are routinely induced to form a mineralized monolayer by long-term exposition to osteogenic medium, typically after 21 to 28 days of culture. Alizarin Red S staining is generally used to confirm calcium-rich deposits in these 2D cell cultures.

In the literature, Naringin has been described to promote mineralization of osteoprogenitor cells in a dose-dependent manner, which is ultimately the goal of bone tissue engineering applications, i.e., to produce appreciable mineralization *in vitro* for posterior implantation in patients [33,68].

To evaluate this effect in hASCs, the cells were incubated with different concentrations of free Naringin and also Naringin-loaded nanomicelles in OS-Dex containing medium over 21 days. Throughout the assay, cell culture medium was exchanged every 3 - 4 days with

fresh OS-Dex medium with no Naringin addition other than that at day 0 (Please see dose regime in Figure 28A). The formation of calcium nodes in the mineralized cell monolayer was visualized by Alizarin Red S staining. The outcomes of this experiment are exhibited in Figure 31.

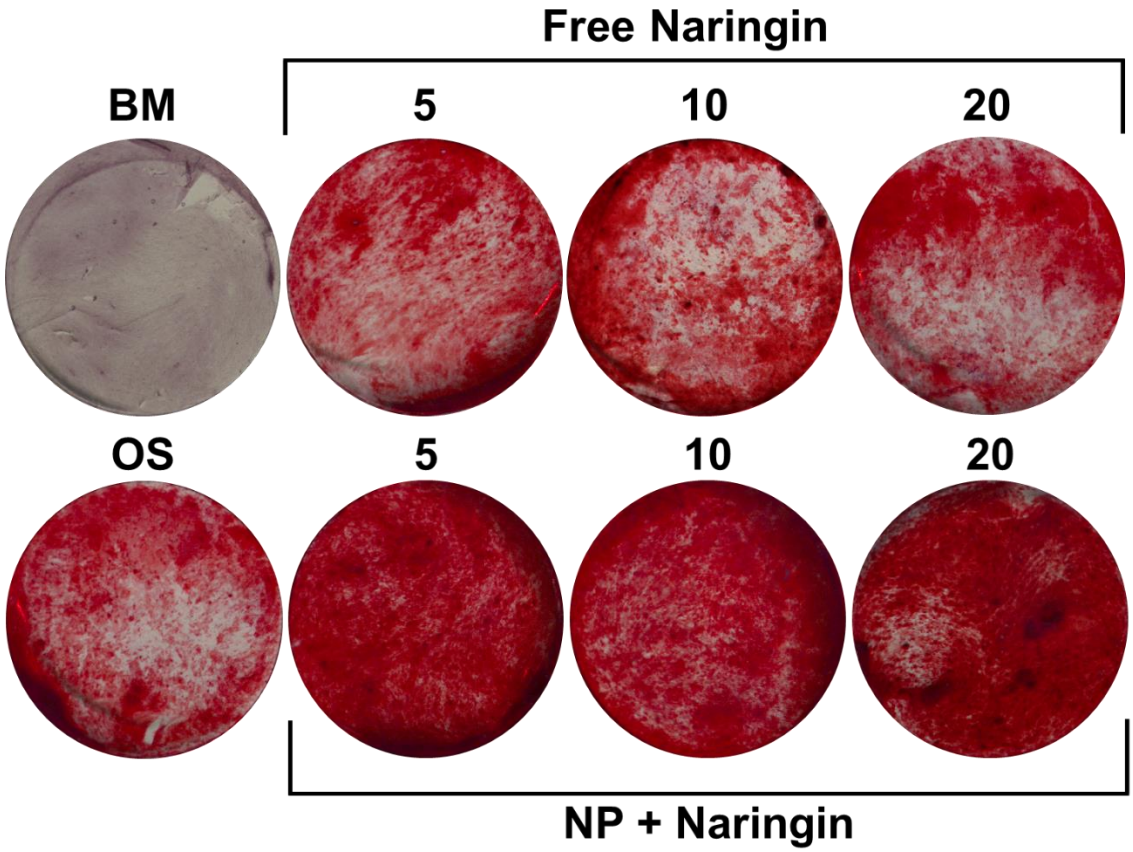

Figure 31. Optical microscopy micrographs of Alizarin Red S staining of calcium deposits in Naringin-treated hASCs cell monolayer after a 21-day induction in OS-Dex medium. BM represents basal medium.

The obtained results in Figure 31 show the potential of a single stimulatory dose of Naringin to induce mineralization in a dose-dependent manner after 21 days of culture. These findings are supported by the work of Yu and colleagues who observed a dose-dependent calcium node deposition from 1, 10 to 50 μg/mL of Naringin in rat BM-MSCs [33]. Notably, the dose-dependent effect of Naringin appears noticeably visible upon Naringin-loaded micelles administration. In comparison to free drug, the controlled delivery of Naringin markedly improved mineralization of the cell matrix. Mineralization data is paramount for pursuing further applications in the future, especially considering the origin of the used stem cells (adipose-derived) and the effect of Dex in their pro-adipogenic/pro-osteogenic differentiation duality. Indeed, a study by Ghali and co-workers found that

addition of Dex at as low as 100 nM in osteogenic medium strongly induced adipogenesis, even exhibiting a higher lipid droplet accumulation than 500 nM of Dex in adipogenic induction medium [28]. Taking into consideration that this was the concentration of Dex used during these experiments, the above findings provide evidence for significant hASCs mineralization elicited by Naringin, with evident matrix osteogenic calcification. Moreover, adipogenic regulator PPARɣ is a nuclear receptor which could help explain the improved mineralization of Naringin-loaded nanomicelles groups [112].

3.11 Effect of Dose Regime of Naringin and Naringin-loaded Micelles on the Stimulation of ALP Activity

Collectivelly, the previous experiments investigating different osteogenic markers reveal the pro-osteogenic potential of Naringin, either in free form or when delivered by micellar carriers as demonstrated by OPN expression and matrix calcium deposition data. However, in the previous assays, Naringin was used in combination with osteogenic medium containing Dex, which appeared to dilute the flavonoid effect on the stimulation of ALP activity. In fact, in OS-Dex experiments quantifying ALP activity, differences among Naringin doses were not significant at 7 days.

Therefore, in this experiment, different dose regimes of free Naringin and drug-loaded micelles in reduced osteogenic medium (absent of Dex, rOS) were studied in order to further investigate Naringin pro-osteogenic effect in hASCs as well as its ALP stimulatory activties (Figure 32A). It was hypothesized that, in rOS induction medium, the addition of a second dosage of free Naringin or Naringin-loaded micelles on the ALP activity of hASCs could elicit different results. Such are important findings for the development of stem cell-based therapies based on the most effective Naringin regime for enhancing osteogenic differentiation.

As such, unlike previous experiments, where only a single initial dose of Naringin was given at the initial incubation time point, this study explored the effect of adding a second dose of the flavonoid or flavonoid-loaded micelles after 3 days incubation. The obtained results are shown in Figure 32.

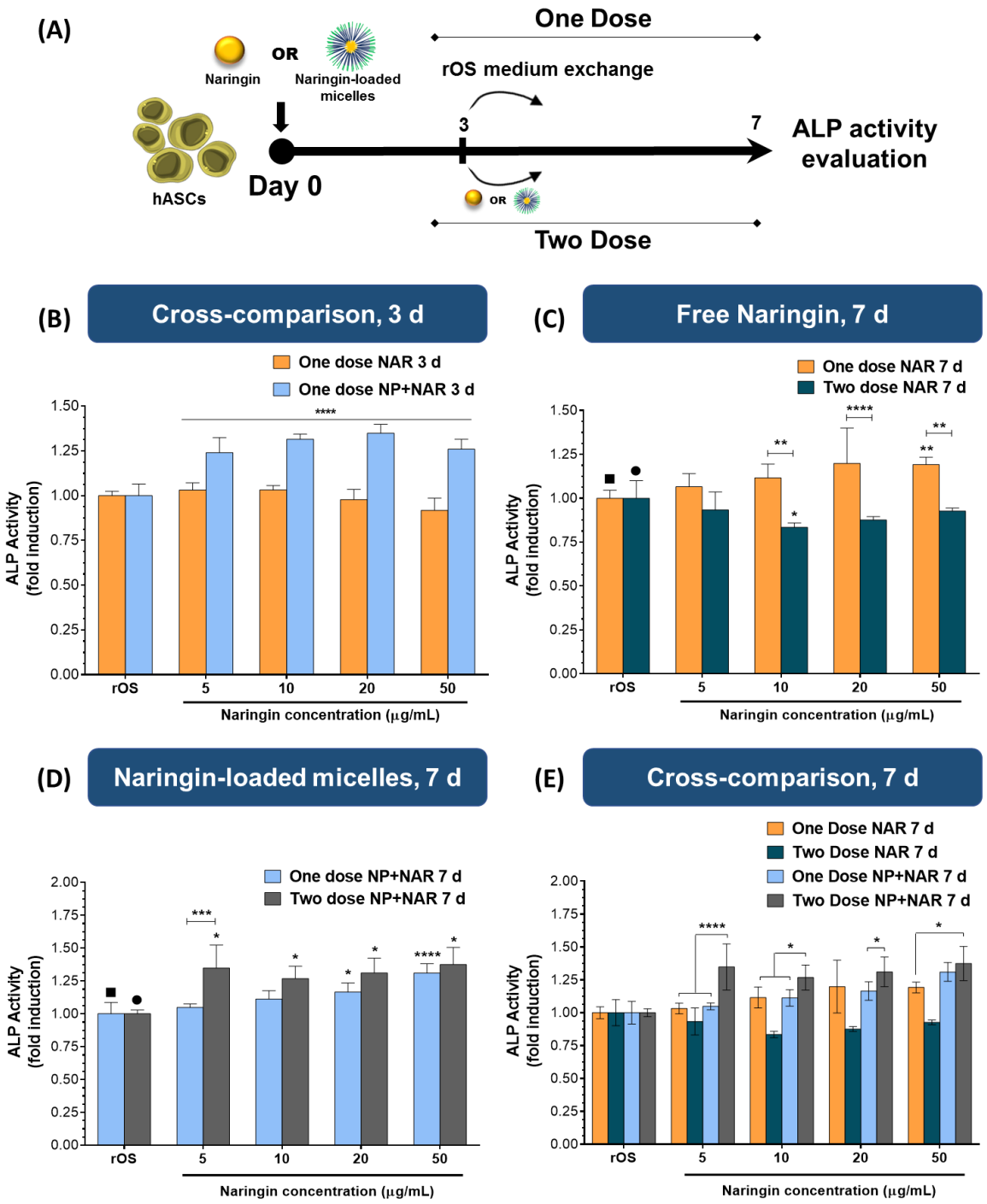

Figure 32. The effect of dose regimen and Naringin-loaded micelles on the stimulation of ALP activity in rOS differentiation medium. **(A)** Dose regime of free Naringin and Naringin-loaded micelles in this experiment. **(B)** Comparison of the effect of Naringin-loaded micelles and free Naringin on the promotion of ALP activity of hASCs at 3 days, expressed in fold induction over rOS control group. Comparison of the dose regimen effect of free Naringin **(C)** and Naringin-loaded micelles **(D)** on the promotion of ALP activity of hASCs at 7 days, expressed in fold induction over rOS control group. **(E)** Comparison of the effect of Naringin-loaded micelles and free Naringin with respective dose regimen on the promotion of ALP activity of hASCs at 7 days, expressed in fold induction over rOS control group. Levels of ALP activity were normalized to DNA

content prior to normalization to rOS control group. Symbols ■ and ● represent the control group used to perform the statistical analysis of each timepoint. Data represented in mean ± s.d. (*n*=4). *p < 0.05, **p < 0.01, ***p < 0.001, ****p < 0.0001.

The obtained results in Figure 32B highlight the superior performance of nanomicelles-delivered Naringin over free drug incubation at 3 days. Naringin-loaded micelles significantly improved ALP activity levels ca. 0.3 fold over the OS control group and across all doses of free Naringin studied. However, there was no significant differences among the various concentrations of Naringin-loaded micelles.

Regarding the 7 day assays, different performances according to the dose regimen could be observed for free drug and drug-loaded micelles. For the free drug assays, a single dose of Naringin in rOS promoted ALP activity in a dose-dependent manner, with the highest dose (50 μg/mL) showing a 0.15 to 0.20 fold improval over 5 μg/mL and the rOS control group. Meanwhile, the administration of a second dose of free Naringin lead to no significant differences among Naringin groups (Figure 32C). Collectively, a single dose of Naringin lead to a 0.2 to 0.3 fold increase in ALP activity when compared to the two-dose regimen, specifically 10, 20 and 50 μg/mL concentrations.

On the other hand, a single dose of drug-loaded micelles originated a pro-stimulatory effect on ALP, with the highest doses (20 and 50 μg/mL) exhibiting a 0.2 to 0.3 fold enhancement in ALP activity over the rOS control group (Figure 32D). In addition, while the 20 μg/mL group was significantly superior to 5 μg/mL, the highest dose (50 μg/mL) of Naringin was significantly 0.15 to 0.3 fold superior across all concentrations tested. Alternatively, for nanocarrier dual administration, the lowest dose (5 μg/mL) achieved ALP activity stimulation equivalent to higher concentrations. In comparison, the lowest dose resulted in a 0.4 fold enhancement in ALP activity relative to the corresponding concentration in the one-dose regimen (***p < 0.001). Also, all Naringin concentrations in the two-dose nanocarrier regimen were capable of significantly improving the ALP activity by 0.3 to 0.4 fold over the rOS control group, which was not observed for the single-dose regimen.

Overall, different performances according to the dose regimen could be observed for free drug and drug-loaded micelles. In the free drug assay, a second dose seemed prejudicial for ALP stimulation, whereas a second dose of Naringin-loaded nanocarriers significantly increased the ALP activity over rOS control group and relatively to the single-dose regimen.

These results indicate that a second dose of free drug seems to slightly inhibit ALP stimulation in hASCs, whereas the controlled release of Naringin benefits from the two-dose regimen leading to increased ALP activity levels. Cytotoxicity inherent to a second dose administration was not proposed here because dsDNA quantifications of both assays showed no significant changes between the two dose regimens (Figure 37, Annex IV). The above findings are supported by the work of Guo and colleagues, where they investigated the double directional adjusting estrogenic effect of Naringin [113]. The authors concluded that Naringin showed estrogenic agonist activity at low concentrations, but acted as estrogenic antagonist at high concentrations. The interaction of Naringin with estrogen receptor (ER) and its role in osteogenesis is well described in the literature, and the obtained results above may suggest that intracellular delivery of Naringin might overcome this limitting effect [113,114].

Figure 32D provides an overall comparison between all the tested dose regimen groups, with both free drug and drug-loaded groups. For one-dose regimen, free Naringin and Naringin-loaded groups exhibited similar enhancements of ALP stimulation at 7 days. However, when comparing two-dose regimens, Naringin-loaded groups were significantly superior across all concentrations studied. In addition, the obtained results show that dual nanocarrier administration requires lower Naringin doses to effectively improve ALP activity versus one-dose regimens.

In summary, for free drug assays, a single initial Naringin dose exhibited improved stimulatory activity of ALP when compared to two-dose, while in the drug-loaded assays, a two-dose regimen was consistently superior compared to single administration. The obtained results indicate the potential of the formulated nanocarriers to deliver Naringin to hASCs and significantly enhance its pro-osteogenic effect over free drug administration, especially at earlier time points and requiring lower doses.

5 General Conclusions and Future Perspectives

Adult adipose derived stem cell-based therapies have shown great potential for tissue engineering applications due the multilineage differentiation potential and facile isolation of these cells.

Throughout this thesis the potential of stem cell-based therapies was explored by using a naturally available drug to guide cells differentiation towards an osteoblastic phenotype. The inclusion of Naringin in micellar nanocarriers resulted in a high encapsulation efficiency and led to a sustained drug release in both physiological and endo-lysosomal conditions. Moreover, these nanocarriers were readily internalized by hASCs as demonstrated by microscopy imaging. The controlled delivery of Naringin elicited a more pronounced ALP expression at the earlier time points over free drug administration. In addition, a single initial stimulatory dose of Naringin-loaded nanocarriers significantly increased OPN expression over free drug after 14 days. Moreover, Naringin delivery via nanomicelles significantly improved hASCs matrix mineralization over free drug at 21 days. Taken together, the findings of this thesis provide evidence that the inclusion of Naringin in biocompatible nanocarriers effectively promotes the osteogenic differentiation of hASCs in vitro.

In the foreseeable future, the design of Naringin micellar delivery system could be enhanced by inclusion of stimuli-responsive moieties into nanocarriers polymeric backbone in order to fine tune the delivery process upon specific stimuli. In fact, there are several interesting biophysiological cues within the bone tissue and alterations found in skeletal disorders that could potentially be exploited for stimuli-responsive delivery of bioactive molecules. The latter is particularly interesting since during the onset and progression of different bone disorders many of skeletal microenvironment hallmarks and cellular functions become profoundly deregulated. Each of these disease-specific features represent unique opportunities for nanocarrier-mediated stimuli-responsive release of therapeutics. This spatiotemporally controlled drug release can result in higher stability in vivo and improved biodistribution of the drug at skeletal sites upon parenteral administration.

Envisioning future advances, the next-generation of such systems could combine also physical and morphological properties such as shape, topography and mechanical properties which are known to influence cellular behavior and nanocarriers biological performance. Moreover, endowing nanocarriers with osteotropic targeting moieties could further improve

bone accumulation and prove to be useful in directing nanocarriers towards specific skeletal surfaces, such as recent fracture sites or high bone turnover regions. A multidisciplinary approach is required for considering the final application of such systems, and guide the formulation of smarter nanocarriers for systemic bone treatments. The combination of bioinspired therapeutics with design advances in nanocarriers performance, will undoubtedly pave the future in providing suitable candidates for future commercialization and realistic clinical application.

6 References

1. Northrop, B. H. *et al.* Thiol–maleimide 'click' chemistry: evaluating the influence of solvent, initiator, and thiol on the reaction mechanism, kinetics, and selectivity. *Polym. Chem.* **6,** 3415–3430 (2015).
2. Hermanson, G. T. in *Bioconjugate Techniques* 229–258 (Academic Press, 2013). doi:https://doi.org/10.1016/B978-0-12-382239-0.00003-0
3. Luo, D., Smith, S. W. & Anderson, B. D. Kinetics and mechanism of the reaction of cysteine and hydrogen peroxide in aqueous solution. *J. Pharm. Sci.* **94,** 304–316 (2005).
4. Varenne, F. *et al.* Towards quality assessed characterization of nanomaterial: Transfer of validated protocols for size measurement by dynamic light scattering and evaluation of zeta potential by electrophoretic light scattering. *Int. J. Pharm.* **528,** 299–311 (2017).
5. Gattuso, G., Barreca, D., Gargiulli, C., Leuzzi, U. & Caristi, C. Flavonoid composition of citrus juices. *Molecules* **12,** 1641–1673 (2007).
6. Geraghty, R. J. *et al.* Guidelines for the use of cell lines in biomedical research. *Br. J. Cancer* **111,** 1021–1046 (2014).
7. Rampersad, S. N. Multiple applications of alamar blue as an indicator of metabolic function and cellular health in cell viability bioassays. *Sensors (Switzerland)* **12,** 12347–12360 (2012).
8. Gregory, C. A., Grady Gunn, W., Peister, A. & Prockop, D. J. An Alizarin red-based assay of mineralization by adherent cells in culture: comparison with cetylpyridinium chloride extraction. *Anal. Biochem.* **329,** 77–84 (2004).
9. Khan, J. H., Schue, F. & George, G. A. Heterogeneous ring-opening polymerization of lactones for biomedical applications. *Polym. Int.* **58,** 296–301 (2009).
10. Williams, C. K. Synthesis of functionalized biodegradable polyesters. *Chem. Soc. Rev.* **36,** 1573 (2007).
11. Labet, M. & Thielemans, W. Synthesis of polycaprolactone: a review. *Chem. Soc. Rev.* **38,** 3484 (2009).
12. Albertsson, A.-C. & Varma, I. K. Recent Developments in Ring Opening Polymerization of Lactones for Biomedical Applications. *Biomacromolecules* **4,** 1466–1486 (2003).
13. Marques, J. G. *et al.* Co-delivery of Sildenafil (Viagra®) and Crizotinib for Synergistic and Improved Anti-tumoral Therapy. *Pharm. Res.* **31,** 2516–2528 (2014).
14. Mert, O., Doganci, E., Erbil, H. Y. & Demir, a S. Surface Characterization of Poly(l-lactic acid)−Methoxy Poly(ethylene glycol) Diblock Copolymers by Static and Dynamic Contact Angle Measurements, FTIR, and ATR-FTIR. *Langmuir* **24,** 749–757 (2008).
15. Boua-In, K., Chaiyut, N. & Ksapabutr, B. Preparation of polylactide by ring-opening polymerisation of lactide. *Optoelectron. Adv. Mater. Rapid Commun.* **4,** 1404–1407 (2010).
16. Chumeka, W., Pasetto, P., Pilard, J.-F. & Tanrattanakul, V. Bio-based triblock copolymers from natural rubber and poly(lactic acid): Synthesis and application in polymer blending. *Polymer (Guildf).* **55,** 4478–4487 (2014).
17. H. Hoidy, W., B. Ahmad, M., Jaffar Al-, E. A. & Bt Ibrahim, N. A. Preparation and Characterization of Polylactic Acid/Polycaprolactone Clay Nanocomposites. *J. Appl. Sci.* **10,** 97–106 (2010).
18. Garlotta, D. A Literature Review of Poly(Lactic Acid). *J. Polym. Environ.* **9,** 63–84 (2001).
19. Wang, D. K. *et al.* FT-IR characterization and hydrolysis of PLA-PEG-PLA based copolyester hydrogels with short PLA segments and a cytocompatibility study. *J. Polym. Sci. Part A Polym. Chem.* **51,** 5163–5176 (2013).
20. Chen, H. Y., Tang, H. Y. & Lin, C. C. Ring-opening polymerization of l-lactide catalyzed by a biocompatible calcium complex. *Polymer (Guildf).* **48,** 2257–2262 (2007).
21. Tanzi, M. C. *et al.* Cytotoxicity of some catalysts commonly used in the synthesis of copolymers for biomedical use. *J. Mater. Sci. Mater. Med.* **5,** 393–396 (1994).
22. Allen, C., Maysinger, D. & Eisenberg, A. Nano-engineering block copolymer aggregates for drug delivery. *Colloids Surfaces B Biointerfaces* **16,** 3–27 (1999).
23. Li, F., Li, S., El Ghzaoui, A., Nouailhas, H. & Zhuo, R. Synthesis and gelation properties of PEG-PLA-PEG triblock copolymers obtained by coupling monohydroxylated PEG-PLA with adipoyl chloride. *Langmuir* **23,** 2778–2783 (2007).
24. Lebouille, J. G. J. L., Stepanyan, R., Slot, J. J. M., Cohen Stuart, M. A. & Tuinier, R. Nanoprecipitation of polymers in a bad solvent. *Colloids Surfaces A Physicochem. Eng. Asp.* **460,** 225–235 (2014).
25. Whitesides, T. H. & Ross, D. S. Experimental and Theoretical Analysis of the Limited Coalescence

Process: Stepwise Limited Coalescence. *J. Colloid Interface Sci.* **169,** 48–59 (1995).
26. Uccelli, A., Moretta, L. & Pistoia, V. Mesenchymal stem cells in health and disease. *Nat. Rev. Immunol.* **8,** 726–736 (2008).
27. Frese, L., Dijkman, P. E. & Hoerstrup, S. P. Adipose Tissue-Derived Stem Cells in Regenerative Medicine. *Transfus. Med. Hemotherapy* **43,** 268–274 (2016).
28. Ghali, O. *et al.* Dexamethasone in osteogenic medium strongly induces adipocyte differentiation of mouse bone marrow stromal cells and increases osteoblast differentiation. *BMC Cell Biol.* **16,** 9 (2015).
29. Dimitriou, R., Jones, E., McGonagle, D. & Giannoudis, P. V. Bone regeneration: current concepts and future directions. *BMC Med.* **9,** 66 (2011).
30. El Bialy, I., Jiskoot, W. & Reza Nejadnik, M. Formulation, Delivery and Stability of Bone Morphogenetic Proteins for Effective Bone Regeneration. *Pharm. Res.* **34,** 1152–1170 (2017).
31. Chen, R., Qi, Q.-L., Wang, M.-T. & Li, Q.-Y. Therapeutic potential of naringin: an overview. *Pharm. Biol.* **54,** 3203–3210 (2016).
32. Fan, J., Li, J. & Fan, Q. Naringin promotes differentiation of bone marrow stem cells into osteoblasts by upregulating the expression levels of microRNA-20a and downregulating the expression levels of PPARγ. *Mol. Med. Rep.* **12,** 4759–4765 (2015).
33. Yu, G. *et al.* Naringin Stimulates Osteogenic Differentiation of Rat Bone Marrow Stromal Cells via Activation of the Notch Signaling Pathway. *Stem Cells Int.* **2016,** 1–8 (2016).
34. Osathanon, T., Subbalekha, K., Sastravaha, P. & Pavasant, P. Notch signalling inhibits the adipogenic differentiation of single-cell-derived mesenchymal stem cell clones isolated from human adipose tissue. *Cell Biol. Int.* **36,** 1161–1170 (2012).
35. Hempen, C., Weiss, E. & Hess, C. F. Dexamethasone treatment in patients with brain metastases and primary brain tumors: do the benefits outweigh the side-effects? *Support. Care Cancer* **10,** 322–328 (2002).
36. Rao, K. *et al.* Gum tragacanth stabilized green gold nanoparticles as cargos for Naringin loading: A morphological investigation through AFM. *Carbohydr. Polym.* **174,** 243–252 (2017).
37. Wu, J. Bin *et al.* Naringin-induced bone morphogenetic protein-2 expression via PI3K, Akt, c-Fos/c-Jun and AP-1 pathway in osteoblasts. *Eur. J. Pharmacol.* **588,** 333–341 (2008).
38. Walle, T. Absorption and metabolism of flavonoids. *Free Radic. Biol. Med.* **36,** 829–837 (2004).
39. Cassidy, A. & Minihane, A.-M. The role of metabolism (and the microbiome) in defining the clinical efficacy of dietary flavonoids. *Am. J. Clin. Nutr.* **105,** 10–22 (2017).
40. Fontaine, S. D., Reid, R., Robinson, L., Ashley, G. W. & Santi, D. V. Long-Term Stabilization of Maleimide–Thiol Conjugates. *Bioconjug. Chem.* **26,** 145–152 (2015).
41. Brewer, C. F. & Riehm, J. P. Evidence for possible nonspecific reactions between N-ethylmaleimide and proteins. *Anal. Biochem.* **18,** 248–255 (1967).
42. Conde, J. *et al.* Revisiting 30 years of biofunctionalization and surface chemistry of inorganic nanoparticles for nanomedicine. *Front. Chem.* **2,** 1–27 (2014).
43. Cunningham, A. & Oh, J. K. New Design of Thiol-Responsive Degradable Polylactide-Based Block Copolymer Micelles. *Macromol. Rapid Commun.* **34,** 163–168 (2013).
44. Zhou, Y., Nie, W., Zhao, J. & Yuan, X. Rapidly in situ forming adhesive hydrogel based on a PEG-maleimide modified polypeptide through Michael addition. *J. Mater. Sci. Mater. Med.* **24,** 2277–2286 (2013).
45. Pramanik, S., Ataollahi, F., Pingguan-Murphy, B., Oshkour, A. A. & Osman, N. A. A. In Vitro Study of Surface Modified Poly(ethylene glycol)-Impregnated Sintered Bovine Bone Scaffolds on Human Fibroblast Cells. *Sci. Rep.* **5,** 9806 (2015).
46. Zeng, C., Seino, H., Ren, J., Hatanaka, K. & Yoshie, N. Bio-Based Furan Polymers with Self-Healing Ability. *Macromolecules* **46,** 1794–1802 (2013).
47. Oishi, T. & Fujimoto, M. Synthesis and Chiroptical Properties of Poly[N -(4- N ′-(α-Methylbenzyl)-Aminocarbonylphenyl)-Mamaleimide]. *J. Macromol. Sci. Part A* **29,** 1187–1205 (1992).
48. Younes, H. & Cohn, D. Phase separation in poly(ethylene glycol)/poly(lactic acid) blends. *Eur. Polym. J.* **24,** 765–773 (1988).
49. Niwa, T., Takeuchi, H., Hino, T., Kunou, N. & Kawashima, Y. Preparations of biodegradable nanospheres of water-soluble and insoluble drugs with D,L-lactide/glycolide copolymer by a novel spontaneous emulsification solvent diffusion method, and the drug release behavior. *J. Control. Release* **25,** 89–98 (1993).
50. Asadi, H., Rostamizadeh, K., Salari, D. & Hamidi, M. Preparation of biodegradable nanoparticles of tri-block PLA–PEG–PLA copolymer and determination of factors controlling the particle size using artificial neural network. *J. Microencapsul.* **28,** 406–416 (2011).

51. Albanese, A., Tang, P. S. & Chan, W. C. W. The Effect of Nanoparticle Size, Shape, and Surface Chemistry on Biological Systems. *Annu. Rev. Biomed. Eng.* **14,** 1–16 (2012).
52. Blanco, E., Shen, H. & Ferrari, M. Principles of nanoparticle design for overcoming biological barriers to drug delivery. *Nat. Biotechnol.* **33,** 941–951 (2015).
53. Kataoka, K., Harada, A. & Nagasaki, Y. Block copolymer micelles for drug delivery: Design, characterization and biological significance. *Adv. Drug Deliv. Rev.* **47,** 113–131 (2001).
54. Shuai, X., Ai, H., Nasongkla, N., Kim, S. & Gao, J. Micellar carriers based on block copolymers of poly(ε-caprolactone) and poly(ethylene glycol) for doxorubicin delivery. *J. Control. Release* **98,** 415–426 (2004).
55. Wang, H. *et al.* Enhanced anti-tumor efficacy by co-delivery of doxorubicin and paclitaxel with amphiphilic methoxy PEG-PLGA copolymer nanoparticles. *Biomaterials* **32,** 8281–8290 (2011).
56. Sanver, D. Experimental Modelling of Flavonoid Membrane Interactions. (The University of Leeds, 2017).
57. Yan, H.-H. *et al.* Experimental and computational studies of naringin/cyclodextrin inclusion complexation. *J. Incl. Phenom. Macrocycl. Chem.* **88,** 15–26 (2017).
58. Kanaze, F. I. *et al.* Dissolution enhancement of flavonoids by solid dispersion in PVP and PEG matrixes: A comparative study. *J. Appl. Polym. Sci.* **102,** 460–471 (2006).
59. Trotta, F., Drioli, E., Baggiani, C. & Lacopo, D. Molecular imprinted polymeric membrane for naringin recognition. *J. Memb. Sci.* **201,** 77–84 (2002).
60. Vila, A., Gill, H., McCallion, O. & Alonso, M. J. Transport of PLA-PEG particles across the nasal mucosa: effect of particle size and PEG coating density. *J. Control. Release* **98,** 231–244 (2004).
61. Nel, A. E. *et al.* Understanding biophysicochemical interactions at the nano–bio interface. *Nat. Mater.* **8,** 543–557 (2009).
62. Toy, R., Peiris, P. M., Ghaghada, K. B. & Karathanasis, E. Shaping cancer nanomedicine: the effect of particle shape on the in vivo journey of nanoparticles. *Nanomedicine* **9,** 121–134 (2014).
63. Pujari-Palmer, S. *et al.* In vivo and in vitro evaluation of hydroxyapatite nanoparticle morphology on the acute inflammatory response. *Biomaterials* **90,** 1–11 (2016).
64. Monopoli, M. P., Åberg, C., Salvati, A. & Dawson, K. A. Biomolecular coronas provide the biological identity of nanosized materials. *Nat. Nanotechnol.* **7,** 779–786 (2012).
65. Talamini, L. *et al.* Influence of Size and Shape on the Anatomical Distribution of Endotoxin-Free Gold Nanoparticles. *ACS Nano* **11,** 5519–5529 (2017).
66. Ji, Y. *et al.* Controlled-release naringin nanoscaffold for osteoporotic bone healing. *Dent. Mater.* **30,** 1263–1273 (2014).
67. Chen, K.-Y., Lin, K., Chen, Y. & Yao, C. A Novel Porous Gelatin Composite Containing Naringin for Bone Repair. *Evidence-Based Complement. Altern. Med.* **2013,** 1–10 (2013).
68. Yu, M. *et al.* Controlled release of naringin in metal-organic framework-loaded mineralized collagen coating to simultaneously enhance osseointegration and antibacterial activity. *ACS Appl. Mater. Interfaces* **9,** 19698–19705 (2017).
69. Guo, Z. *et al.* Sequential controlled-released dual-drug loaded scaffold for guided bone regeneration in a rat fenestration defect model. *J. Mater. Chem. B* **5,** 7701–7710 (2017).
70. Chang, P.-C. *et al.* Inhibition of Periodontitis Induction Using a Stimuli-Responsive Hydrogel Carrying Naringin. *J. Periodontol.* **88,** 190–196 (2017).
71. Feng, T. *et al.* Structural characterization and bioavailability of ternary nanoparticles consisting of amylose, α-linoleic acid and β-lactoglobulin complexed with naringin. *Int. J. Biol. Macromol.* **99,** 365–374 (2017).
72. Schmaljohann, D. Thermo- and pH-responsive polymers in drug delivery. *Adv. Drug Deliv. Rev.* **58,** 1655–1670 (2006).
73. Zhang, Z. *et al.* Cellular uptake and intracellular trafficking of PEG-b-PLA polymeric micelles. *Biomaterials* **33,** 7233–7240 (2012).
74. Fu, Y. & Kao, W. J. Drug release kinetics and transport mechanisms of non-degradable and degradable polymeric delivery systems. *Expert Opin. Drug Deliv.* **7,** 429–444 (2010).
75. Hans, M. L. *et al.* Evaluation of in vitro release and in vivo efficacy of mPEG-PLA-haloperidol conjugate micelle-like structures. *J. Biomed. Mater. Res. Part B Appl. Biomater.* **83B,** 422–430 (2007).
76. Kedar, U., Phutane, P., Shidhaye, S. & Kadam, V. Advances in polymeric micelles for drug delivery and tumor targeting. *Nanomedicine Nanotechnology, Biol. Med.* **6,** 714–729 (2010).
77. Zhang, Q., Re Ko, N. & Kwon Oh, J. Recent advances in stimuli-responsive degradable block copolymer micelles: synthesis and controlled drug delivery applications. *Chem. Commun.* **48,** 7542 (2012).

78. Desai, N. Challenges in Development of Nanoparticle-Based Therapeutics. *AAPS J.* **14,** 282–295 (2012).
79. Paliwal, R., Babu, R. J. & Palakurthi, S. Nanomedicine Scale-up Technologies: Feasibilities and Challenges. *AAPS PharmSciTech* **15,** 1527–1534 (2014).
80. Liu, D. *et al.* A Versatile and Robust Microfluidic Platform Toward High Throughput Synthesis of Homogeneous Nanoparticles with Tunable Properties. *Adv. Mater.* **27,** 2298–2304 (2015).
81. Park, E., Cho, H.-B. & Takimoto, K. Effective gene delivery into adipose-derived stem cells: transfection of cells in suspension with the use of a nuclear localization signal peptide–conjugated polyethylenimine. *Cytotherapy* **17,** 536–542 (2015).
82. Sun, X., Li, F., Wang, Y. & Liang, W. Cellular uptake and elimination of lipophilic drug delivered by nanocarriers. *Pharmazie* **65,** 737–742 (2010).
83. Jeong, J. *et al.* Stimulative effects of Drynariae Rhizoma extracts on the proliferation and differentiation of osteoblastic MC3T3-E1 Cells. *J. Ethnopharmacol.* **96,** 489–495 (2005).
84. Li, L., Zeng, Z. & Cai, G. Comparison of neoeriocitrin and naringin on proliferation and osteogenic differentiation in MC3T3-E1. *Phytomedicine* **18,** 985–989 (2011).
85. Peng-Zhang *et al.* Effects of naringin on the proliferation and osteogenic differentiation of human bone mesenchymal stem cell. *Eur. J. Pharmacol.* **607,** 1–5 (2009).
86. Wang, H. *et al.* Naringin enhances osteogenic differentiation through the activation of ERK signaling in human bone marrow mesenchymal stem cells. *Iran. J. Basic Med. Sci.* **20,** 407–413 (2017).
87. Li, F. *et al.* Stimulative activity of Drynaria fortunei (Kunze) J. Sm. extracts and two of its flavonoids on the proliferation of osteoblastic like cells. *Pharmazie* **61,** 962–965 (2006).
88. Quent, V. M. C., Loessner, D., Friis, T., Reichert, J. C. & Hutmacher, D. W. Discrepancies between metabolic activity and DNA content as tool to assess cell proliferation in cancer research. *J. Cell. Mol. Med.* **14,** 1003–1013 (2010).
89. Talorete, T. P. N., Bouaziz, M., Sayadi, S. & Isoda, H. Influence of medium type and serum on MTT reduction by flavonoids in the absence of cells. *Cytotechnology* **52,** 189–198 (2007).
90. Leto Barone, A. A., Khalifian, S., Lee, W. P. A. & Brandacher, G. Immunomodulatory Effects of Adipose-Derived Stem Cells: Fact or Fiction? *Biomed Res. Int.* **2013,** 1–8 (2013).
91. Zhu, X., Du, J. & Liu, G. The comparison of multilineage differentiation of bone marrow and adipose-derived mesenchymal stem cells. *Clin. Lab.* **58,** 897–903 (2012).
92. Granéli, C. *et al.* Novel markers of osteogenic and adipogenic differentiation of human bone marrow stromal cells identified using a quantitative proteomics approach. *Stem Cell Res.* **12,** 153–165 (2014).
93. Orimo, H. The Mechanism of Mineralization and the Role of Alkaline Phosphatase in Health and Disease. *J. Nippon Med. Sch.* **77,** 4–12 (2010).
94. Marom, R., Shur, I., Solomon, R. & Benayahu, D. Characterization of adhesion and differentiation markers of osteogenic marrow stromal cells. *J. Cell. Physiol.* **202,** 41–48 (2005).
95. Liao, H.-T. Osteogenic potential: Comparison between bone marrow and adipose-derived mesenchymal stem cells. *World J. Stem Cells* **6,** 288 (2014).
96. Wall, M. E., Bernacki, S. H. & Loboa, E. G. Effects of Serial Passaging on the Adipogenic and Osteogenic Differentiation Potential of Adipose-Derived Human Mesenchymal Stem Cells. *Tissue Eng.* **13,** 1291–1298 (2007).
97. Kyllönen, L. *et al.* Effects of different serum conditions on osteogenic differentiation of human adipose stem cells in vitro. *Stem Cell Res. Ther.* **4,** 17 (2013).
98. de Girolamo, L., Sartori, M. F., Albisetti, W. & Brini, A. T. Osteogenic differentiation of human adipose-derived stem cells: comparison of two different inductive media. *J. Tissue Eng. Regen. Med.* **1,** 154–157 (2007).
99. Cruz, A. C. C., Silva, M. L., Caon, T. & Simões, C. M. O. Addition of bone morphogenetic protein type 2 to ascorbate and β-glycerophosphate supplementation did not enhance osteogenic differentiation of human adipose-derived stem cells. *J. Appl. Oral Sci.* **20,** 628–635 (2012).
100. Wang, E. A., Israel, D. I., Kelly, S. & Luxenberg, D. P. Bone Morphogenetic Protein-2 Causes Commitment and Differentiation in C3Hl0T1/2 and 3T3 Cells. *Growth Factors* **9,** 57–71 (1993).
101. Gaoli, X. *et al.* Effect of naringin combined with bone morphogenetic protein-2 on the proliferation and differentiation of MC3T3-E1 cells. *West China J. Stomatol.* **35,** 275–280 (2017).
102. Rickard, D. J., Sullivan, T. A., Shenker, B. J., Leboy, P. S. & Kazhdan, I. Induction of Rapid Osteoblast Differentiation in Rat Bone Marrow Stromal Cell Cultures by Dexamethasone and BMP-2. *Dev. Biol.* **161,** 218–228 (1994).
103. Inoue, M. & Shinohara, M. L. Intracellular osteopontin (iOPN) and immunity. *Immunol. Res.* **49,** 160–172 (2011).

104. Chen, Q. *et al.* An Osteopontin-Integrin Interaction Plays a Critical Role in Directing Adipogenesis and Osteogenesis by Mesenchymal Stem Cells. *Stem Cells* **32,** 327–337 (2014).
105. Mckee, M. D. & Nanci, A. Osteopontin: An Interfacial Extracellular Matrix Protein in Mineralized Tissues. *Connect. Tissue Res.* **35,** 197–205 (1996).
106. Uemura, T. *et al.* Osteopontin involvement in bone remodeling and its effects on in vivo osteogenic potential of bone marrow-derived osteoblasts/porous hydroxyapatite constructs. *Mater. Sci. Eng. C* **17,** 33–36 (2001).
107. Liu, M., Li, Y. & Yang, S.-T. Effects of naringin on the proliferation and osteogenic differentiation of human amniotic fluid-derived stem cells. *J. Tissue Eng. Regen. Med.* **11,** 276–284 (2014).
108. Yin, L. *et al.* Effects of Naringin on Proliferation and Osteogenic Differentiation of Human Periodontal Ligament Stem Cells In Vitro and In Vivo. *Stem Cells Int.* **2015,** 1–9 (2015).
109. Milner, P. I., Clegg, P. D. & Stewart, M. C. Stem Cell–based Therapies for Bone Repair. *Vet. Clin. North Am. Equine Pract.* **27,** 299–314 (2011).
110. Mackie, E. J., Ahmed, Y. A., Tatarczuch, L., Chen, K.-S. & Mirams, M. Endochondral ossification: How cartilage is converted into bone in the developing skeleton. *Int. J. Biochem. Cell Biol.* **40,** 46–62 (2008).
111. Golub, E. E. Role of matrix vesicles in biomineralization. *Biochim. Biophys. Acta - Gen. Subj.* **1790,** 1592–1598 (2009).
112. Takada, I., Kouzmenko, A. P. & Kato, S. Wnt and PPARγ signaling in osteoblastogenesis and adipogenesis. *Nat. Rev. Rheumatol.* **5,** 442–447 (2009).
113. Guo, D. *et al.* Double directional adjusting estrogenic effect of naringin from Rhizoma drynariae (Gusuibu). *J. Ethnopharmacol.* **138,** 451–457 (2011).
114. Cai, C. *et al.* Estrogen-related receptor α is involved in the osteogenic differentiation of mesenchymal stem cells isolated from human periodontal ligaments. *Int. J. Mol. Med.* **31,** 1195–1201 (2013).
115. Li, N., Jiang, Y., Wooley, P. H., Xu, Z. & Yang, S. Y. Naringin promotes osteoblast differentiation and effectively reverses ovariectomy-associated osteoporosis. *J. Orthop. Sci.* **18,** 478–485 (2013).
116. Wong, R. W. K. & Rabie, A. B. M. Effect of naringin on bone cells. *J. Orthop. Res.* **24,** 2045–2050 (2006).

7 Annexes

7.1Annex I

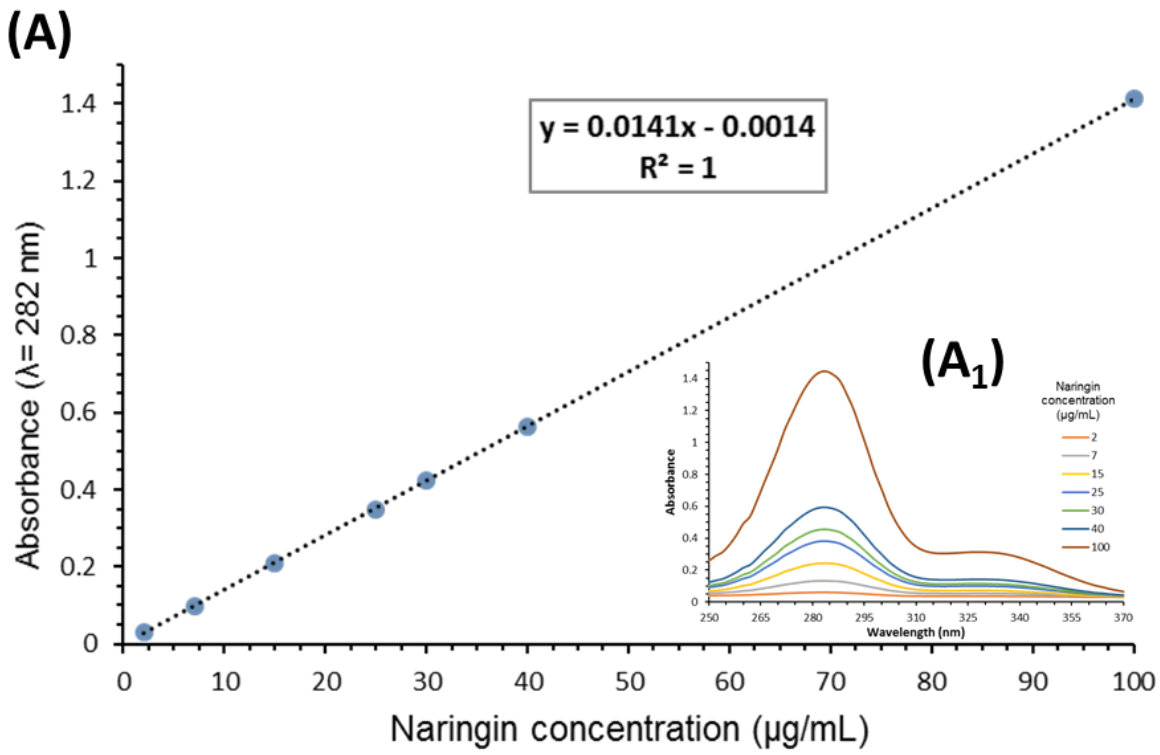

Figure 33. (A) Naringin calibration curve in water calculated by measuring the absorbance peak at λ =282 nm, ranging from 2 – 100 µg/mL. **(A1)** Inset represents the absorbance spectrum of Naringin within a spectral window of 250 to 370 nm.

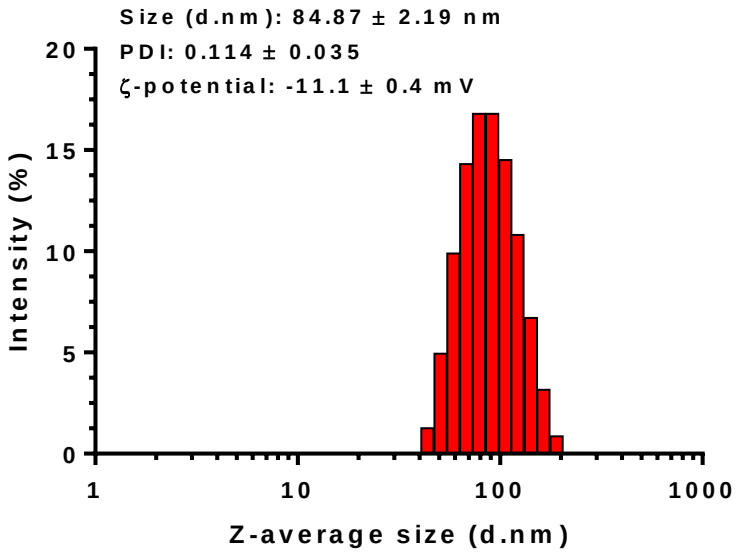

Figure 34. DLS physicochemical characterization of Naringin-loaded mPEG-MS-PLA micelles produced upon a 5-fold scale-up of the nanoprecipitation procedure.

7.2Annex II

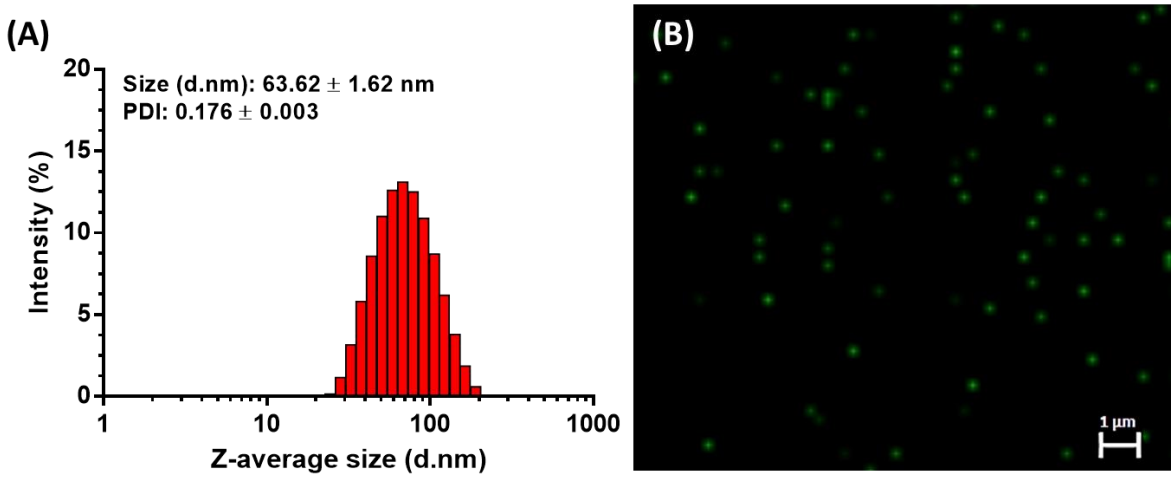

Figure 35. Characterization of Coum-6 loaded mPEG-MS-PLA micelles. **(A)** Physicochemical characterization of Coum-6 loaded micelles via DLS analysis. **(B)** Fluorescence microscopy micrographs of Coum-6 loaded micelles. Green channel: Coum-6.

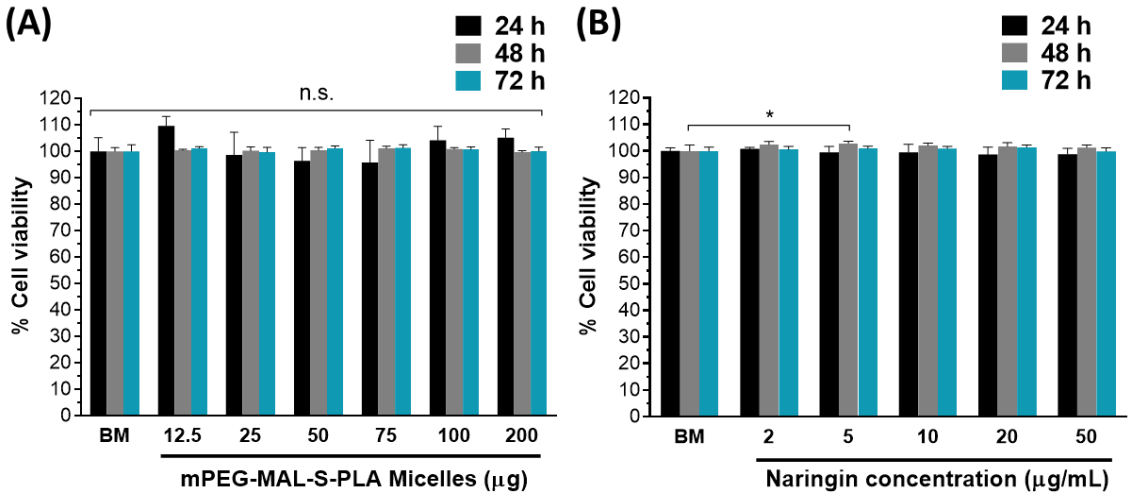

Figure 36. Characterization of blank mPEG-MS-PLA micelles **(A)** and free Naringin **(B)** effect in MC3T3-E1 cell viability following incubation at different time points. BM represents basal medium negative cytotoxicity control (K-). *p < 0.05. Data represents mean ± s.d. (*n*=5).

7.3Annex III

Table 5. Overview of literature studies investigating the osteogenic potential of Naringin and reported proliferative abilities determined via cell viability / metabolic assays *(Table continued over next page).*

Assay	Cell line	Timepoints	Naringin Dose	Main Results	Ref.
BrdU	MC3T3-E1, pOB, hOB	72 h	0.3, 1, 3, 10 µM	Increased proliferation (180-200 %) across all doses	Wu et al (2008).[37]
MTT	hBM-MSC	12, 24, 36, 48, 60, 72, 96 h	1, 10, 100, 200 µg/mL	Dose-dependent increase in proliferation up to 100 µg/mL. After 36 h, 200 µg/mL was cytotoxic.	Peng-Zhang et al (2009).[85]
MTT	UMR-106	48 h	0.01, 0.1, 1, 10, 100 µM	Dose-dependent increase in proliferation (105-130 %) up to 10 µM; 115% proliferation for 100 µM	Li et al (2006).[87]
MTT	MG-63	48 h	0.1, 1, 10, 100 µg/mL; 1, 10, 20 and 50 mg/mL	Dose-dependent increase in proliferation (120-160 %) up to 10 mg/mL. Proliferation decreased to 110% for 20 mg/mL and was not significant at 50 mg/mL.	Chen et al. (2013).[67]
CCK-8	ratBM-MSC	12, 24, 48, 72, 96 h	1, 10, 50, 100 µg/mL	Dose-dependent increase in proliferation up to 50 µg/mL. After 48h, 100 µg/mL group was cytotoxic.	Yu et al. (2016).[33]
MTT	rabbitBM-MSC	48h 3, 5, 7, 10 d	0.01, 0.1, 1, 10, 100 µM 0.1, 1, 10 µM	Dose-dependent increase in proliferation (110-125 %) up to 100 µM. 120 % proliferation for 0.1 - 10 µM	Fan et al. (2015).[32]
MTT	MC3T3-E1	72 h	2, 4, 8, 10, 20 µg/mL	140 % proliferation for 2 µg/mL, not significant for remaining dose groups	Li et al. (2011).[84]
MTT	ratBM-MSC	1, 3, 5, 7, 9 d	1, 10; 100 ng/mL; 1, 10, 100 µg/mL	Dose-dependent increase in proliferation up to 10 µg/mL. After 9 d, proliferation of 100 µg/mL group was superior to control but inferior to all other dose groups.	Li et al. (2013).[115]
MTT	hPDLSC	1, 2, 3, 4, 5 d	0.01; 0.1; 1; 10; 100 µM	Dose-dependent increase in proliferation (120–140 % at 5 days) up to 1 µM. After 3 d, both 10 and 100 µM groups were cytotoxic.	Yin et al. (2015).[108]

Assay	Cell line	Timepoints	Naringin Dose	Main Results	Ref.
Alamar Blue	hAFSC	1, 2, 3, 4 d	1, 10, 100, 200 µg/mL	Dose-dependent increase in proliferation up to 100 µg/mL. Across all time points, proliferation of 200 µg/mL group was similar or inferior to control, indicating a possible cytotoxicity.	Liu et al. (2014).[107]
MTT	hBM-MSC	1, 3, 7, 14 d	10, 50, 100 µg/mL	Differences between Naringin groups and controls significant after 3 d of culture. Dose-dependent increase in proliferation up to 100 µg/mL.	Wang et al. (2017).[86]
MTT	UMR-106	24, 48, 72 h	0.001, 0.01, 0.1 µM	Dose-dependent increase in proliferation up to 0.1 µM	Wong et al. (2016).[116]

Murine pre-osteoblastic (**MC3T3-E1)**, murine primary fetal osteoblastic (**pOB)**, human fetal osteoblastic (**hOB)**, human/rat/rabbit bone marrow stem cells (**hBM-MSC/ratBM-MSC/rabbitBM-MSC)**, rat osteosarcoma osteoblast-like **(UMR-106)**, human osteosarcoma osteoblast-like **(MG-63)**, human periodontal dental ligament stem cells **(hPDLSC)**, human amniotic fluid-derived stem cells **(hAFSC)**. Naringin ($C_{27}H_{32}O_{14}$) average mass: 580.53 g/mol. Conversion of Naringin concentrations: 1 µM = 0.58 µg/mL.

7.4Annex IV

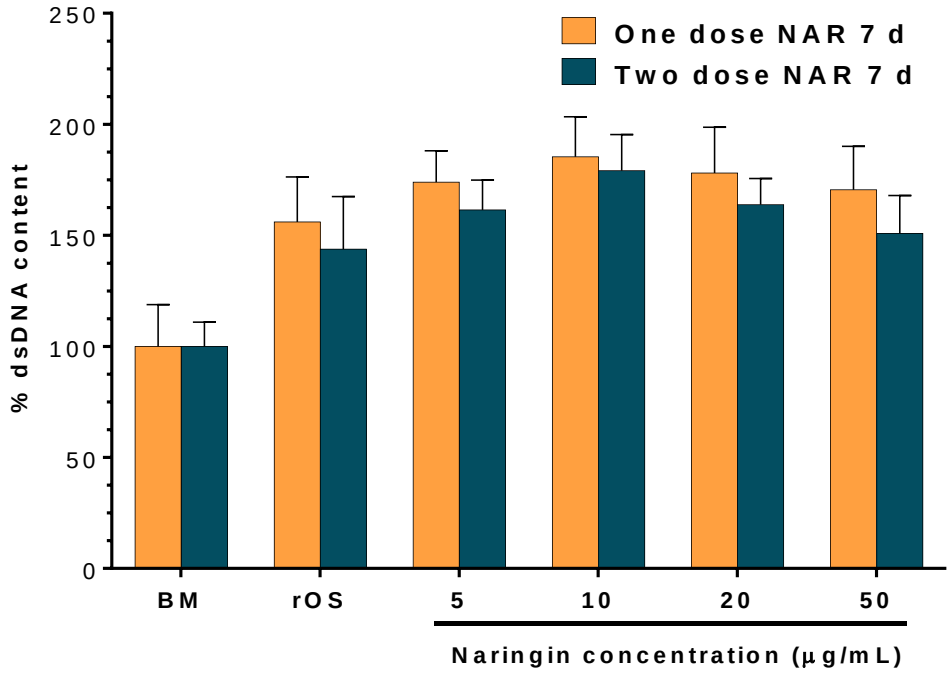

Figure 37. Quantification of dsDNA content after One dose and Two dose free Naringin regimen experiments, normalized to BM control group. BM represents basal medium. rOS represents the osteogenic control group. Data represented in mean ± s.d. (*n*=4).